Dynamics of the Indian monsoon onset

Lucy Grace Recchia

Submitted in accordance with the requirements
for the degree of Doctor of Philosophy

The University of Leeds
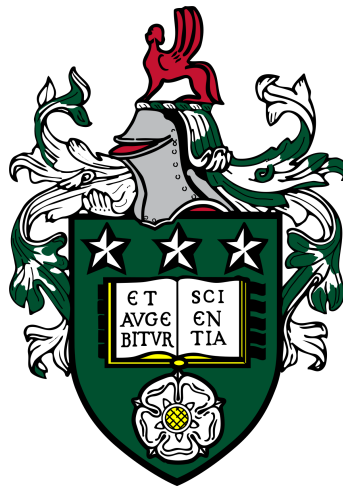
School of Mathematics

August 2020

Declaration

The candidate confirms that the work submitted is her own and that appropriate credit has been given where reference has been made to the work of others. This copy has been supplied on the understanding that it is copyright material and that no quotation from the thesis may be published without proper acknowledgement.

This copy has been supplied on the understanding that it is copyright material and that no quotation from the thesis may be published without proper acknowledgement.

Acknowledgments

Abstract

The Indian monsoon is a globally significant meteorological event, bringing widespread precipitation annually between May and September. The monsoon first onsets at the beginning of June in the southeastern state of Kerala, then propagates to the northwest, against the mean mid-level wind field. Low-level moist inflow from over the Arabian sea moistens the lower troposphere over southeast India, enabling shallow convection and then supporting deep convection. Recent theory has argued that the spatial distribution of monsoon onset is controlled by the action of convection, which erodes the dry layer at mid-levels from below. This in turn allows the monsoon onset to progress to the northwest.

Accurate forecasting of the onset and progression of the monsoon is important for Indian farmers, which constitute a large portion of the population and economy. In particular, the prediction of the spatial pattern, intensity and timing of precipitation is key. It is difficult to represent the physical processes and dynamical interactions associated with the Indian monsoon in numerical weather and climate prediction models, as these processes are imperfectly parameterised. Additionally, the complexity of the system, involving a number of balancing processes, is difficult to represent computationally. Current weather and climate prediction models have large biases for monsoon rainfall, and the root causes of these biases are not known. Idealised modelling studies can increase understanding regarding the roles of different processes and allow testing of their effects on the Indian monsoon onset.

To investigate the propagation mechanisms, an idealised model that reproduces the onset and propagation of the Indian monsoon is developed. It is a two-layer model of moisture dynamics, based on conservation laws, for a vertical plane representing a transect from the India-Pakistan border in the northwest to southeast India). In the model, the balance between low-level moist inflow, mid-level dry advection and the rate of convection, controls the onset of the monsoon. For a prescribed low and mid-level wind field, the coupled ordinary differential equations describing the evolution of water vapour content can be studied both analytically and numerically, enabling monsoon onset fronts to be identified and an onset front speed to be calculated. The dependence of these front speeds on the assumed (parameterised) representations of evaporation, precipitation and convection is investigated. It is found that a realistic onset speed can be obtained from a highly idealised setup, for a particular range of convective-mixing timescales.

The Weather Research and Forecasting (WRF) model is used to simulate the 2016 sea-

son, validating performance against reanalysis and observational data. The WRF model is examined in the framework of the two-layer idealised model, focusing on the evolution of moisture content over lower and upper atmospheric layers, increase in low-level moisture flux at onset and the decrease in the mid-level northwesterly wind. The parallels between the WRF model and idealised model lend support to the theory of monsoon onset. A moisture budget analysis is also conducted for the WRF model, enabling a vertical convective flux to be a diagnosed and through its correlation with total column moisture, a convective timescale is derived. In the idealised model, a range of 0.5–7 days is initially assumed, which is verified by the WRF model results of 1–2 days. The methodology used to derive a convective timescale in the WRF model can be applied to other models, building a more complete picture of the range of possible convective timescales associated with the Indian monsoon.

Contents

List of Figures

Chapter 1

Introduction

The Indian monsoon is one of the most poorly forecast meteorological events on the global scale, despite major advances in modelling techniques and computing. Rainfall brought by the Indian monsoon is crucial for the agricultural sector, which is linked with the economy (Gadgil and Gadgil, 2006). It is important to predict the dates that the monsoon onsets over different parts of the Indian continent. A delayed or an early onset can mean droughts or flooding, which have consequences on economic and humanitarian levels.

Representing the physical processes and dynamical interactions that characterise the onset of the Indian monsoon in weather and climate models is a continuing challenge. Some of the aspects that contribute to the complexity of the problem are soil-moisture interaction, orographic influence and convective cloud transports of moisture. A better understanding of the underlying processes driving the onset and progression of the Indian monsoon, coupled with knowledge of the relative importance of these processes, can help inform model development and thus improve forecasting skill.

1.1   Description of the Indian monsoon

A monsoon is defined as a seasonal reversal of winds near the surface, with the summer season bringing rain and the winter season being dry. The definition is based on the Asian monsoon, a significant event of the global circulation, and refers to atmospheric flow over the Indian Ocean. In the summer season, May–September, the prevailing winds are from the southwest and in the winter season, October–April, the winds are northeasterly. A more detailed discussion of the large-scale circulation, monsoon dynamics and factors impacting the timing and severity of the Indian monsoon is covered in Chapter 2.

Globally, monsoons occur over Africa, Asia and Australia. North and South America also experience similar events, although as there is not a complete reversal of winds they are arguably not true monsoons. The unique topography of India, which is bounded by the Himalayas to the north, Arabian Sea to the west and Bay of Bengal to the east, distinguishes it from other monsoon systems. The Asian monsoon is split into the Indian monsoon and the East Asian monsoon, as the processes driving these events are

dynamically different. The Indian monsoon refers to the summer monsoon, which is the main subject of discussion in this thesis. The winter monsoon is less important for the majority of India compared with for East Asia, due to the Himalayas blocking cold flow from the semi-permanent high pressure system over Siberia, meaning that the majority of the Indian continent experiences drier weather. Notable exceptions being Sri Lanka and the southeast coast of India, for which the winter monsoon can bring as much rainfall as the summer monsoon. The Indian monsoon is characterised by active, neutral and break phases, where active phases are associated with increased rainfall and break phases are associated with reduced or no rainfall. Break phases in particular can be prolonged, leading to droughts (Rajeevan et al., 2010), consequently affecting crop productivity and the economy.
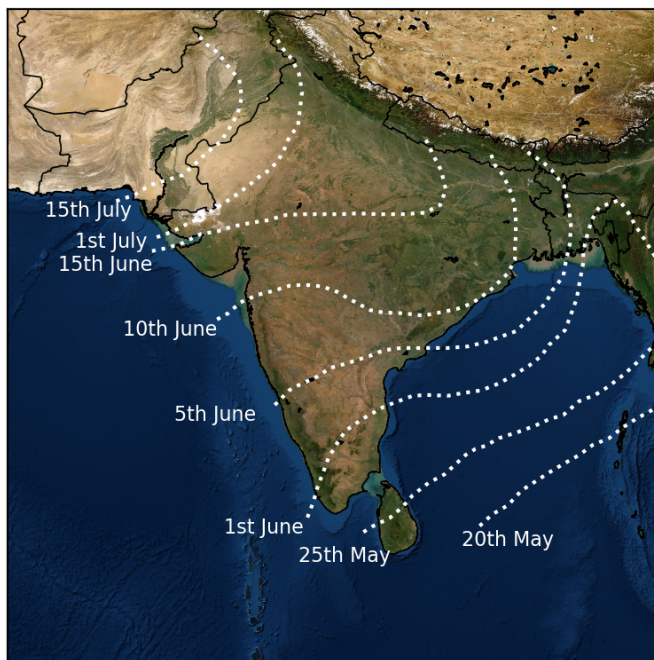
Figure 1.1: *Isochrones showing normal onset dates, as per India Meteorological Department (2016), across regions of India.*

The Indian monsoon onsets in the southern state of Kerala at the beginning of June (Figure 1.1, 1st June isochrone). Over the following six weeks, the onset progresses in a northwesterly direction, covering all of India by mid-July. Declaration of monsoon onset across Indian states is typically based on exceeding a threshold of rainfall within a time period of several days. The full monsoon continues from mid-July through to September, when the monsoon begins to withdraw in a reverse pattern to the onset. The onset of the Indian monsoon is particularly unusual compared to other monsoons, in that it progresses against the prevailing wind field. In this thesis, the focus of the research relates to the

mechanisms driving the onset and progression of the Indian monsoon.

The Indian monsoon is initiated by a thermal contrast between the land and sea, modifying the large-scale circulation. A low-level southwesterly wind, also referred to as the monsoonal flow, brings an influx of moisture from the Arabian Sea to the southern peninsula of India. The atmosphere in the southeast becomes favourable for moist convection, encouraging the development of cumulus and congestus clouds and leading to increased rainfall over the region. Once the monsoon has onset in the southeast, it propagates to the northwest towards Pakistan, against the mid-level wind field. Thus, the progression of monsoon onset cannot be explained by advection of moisture in the direction of travel.

The theory proposed by Parker et al. (2016) presents the onset as a balance between low-level southwesterly moist inflow, convective activity and mid-level dry northwesterly wind, explaining the progression by moisture arguments. Taking a vertical cross-section along a northwest–southeast transect of India, the mid-level wind is pictured as a wedge of dry air, becoming shallower towards the southeast. At the start of June, when the monsoon has first onset in southern India, the increased convective activity and growth of clouds moistens the dry wedge of air from below, eroding it. The dry layer becomes thinner at the southeastern edge, allowing the onset to progress northwestwards. At mid-onset, around the middle of June, the northwesterly winds weaken, aiding the erosion of the dry wedge of air by moist convection and hastening the advance of the onset to the northwest. One of the aims of this thesis is to investigate and test the conceptual model suggested by Parker et al. (2016) for the propagation of the Indian monsoon onset.

1.2 Modelling & forecasting the Indian monsoon

Accurately forecasting the Indian monsoon is especially important for the agricultural sector, where the timing, duration and intensity of monsoonal rainfall can have a significant impact on crop planting schedules. Additionally, predicting active and break phases of the monsoon is crucial for minimising the effects of flooding and droughts. Forecasting weather typically involves interpreting and analysing the output of models, which attempt to predict the future state of the atmosphere based on current weather conditions. The Indian monsoon is difficult to forecast accurately because it is hard to represent the interplay of the physical driving forces in models across different time and spatial scales. The key variable to output from a numerical weather prediction (NWP) model that is useful to the population of India is the rainfall, but this is dependent on and sensitive to the atmospheric dynamics. Representation of the circulation, microphysics, vertical transport, cloud formation, surface fluxes, radiative effects and other aspects can all contribute to how rainfall is produced in numerical weather prediction models. Clearly, understanding of the dynamics is required before attempting to model them in the framework of the Indian monsoon.

1.2.1   Forecasting the Indian monsoon

Forecasting the Indian monsoon on a range of timescales is important for both regional weather and global climate operations. There is a high level of uncertainty with regards to the future climate and its influence on rainfall patterns and intensity in the tropics, with large changes being predicted (Chadwick et al., 2015). The Indian monsoon is one of the key sources of uncertainty. It is classed as a tipping element (Lenton et al., 2008), meaning that the system is at risk of transitioning into a different state under small changes. Examples of other tipping elements are the Greenland ice sheet, the El Niño Southern Oscillation, the Amazon rainforest and the West African monsoon. For the Indian monsoon, this could be a more intense monsoon, or the complete collapse of the large-scale circulation and thus the monsoon itself. It is not known how competing factors will influence the Indian monsoon in the long term. For instance, higher levels of black carbon act to suppress the monsoon, whilst warmer sea surface temperatures act to increase the intensity of the monsoon. Similarly, the El Niño Southern Oscillation can become enhanced or damped under different future climate scenarios (Collins et al., 2010), affecting the intensity and timing of the Indian monsoon. Although many simulations show that precipitation extremes intensify in an increasingly warming climate, it is unclear whether this effect will be felt more strongly in the tropics (O'Gorman, 2015). Improving the understanding of the physical mechanisms driving and affecting systems such as the Indian monsoon can help reduce uncertainty in modelling and predicting future climate scenarios.

There are a range of phenomena, mostly acting on sea surface temperature, that influence the Indian monsoon on interseasonal and interannual timescales. Extent of Himalayan snow cover, El Niño Southern Oscillation phase and sign of the Indian Ocean Dipole are examples of such phenomena that can modify the intensity of the monsoon. Figure 1.2 summarises the various regional and global components acting to influence the Indian monsoon on hourly–decadal timescales. These are further discussed in the following chapter. A lack of understanding of the effects and variability of some of these features, coupled with complications of modelling them, makes long-range forecasting of the Indian monsoon a challenge. To predict the monsoon accurately on seasonal timescales, the climatic components that vary more slowly need to be correctly represented (Sperber et al., 2000). There is a lack of data for sea surface temperature, momentum fluxes and other ocean parameters and a need for integration of observations from satellites and reference sites and model simulations and analysis (Bollasina and Benedict, 2004). A more coherent observational network, taking multiple atmospheric and oceanic measurements at regular intervals, would aid forecasters.

The skill of prediction for the onset of the monsoon and precipitation on sub-seasonal timescales is particularly poor when compared to other global monsoon systems (Bombardi et al., 2017). Forecasts are accurate to approximately two weeks ahead in mid-latitude regions, but this is reduced to about two days in the Tropics (e.g. Wallace and Hobbs (2006)). The predictability is partly limited by the internal variability inherent in the

dynamical nature of the monsoon. Tropical storms and monsoon depressions are especially hard to predict and model, possibly due to the small-scale dynamics and microphysics that are not generally resolved explicitly. These typically bring intense, localised bursts of rain over a short time, which can have a significant impact, particularly with regards to flood risk. As previously noted, active and break phases in the monsoon, lasting up to a week, can also lead to flooding or periods of drought. Similarly, a delayed onset can lead to a heatwave and an onset that progresses at a faster rate than normal can bring rainfall earlier than expected. For instance, a delayed onset in 2014 led to extended dry conditions over northern India, and a rapid advancement of the onset in 2013 contributed to flooding in Uttarakhand, a northern state of India. In the case of the latter, the monsoon onset arrived 1–2 weeks earlier than normal.
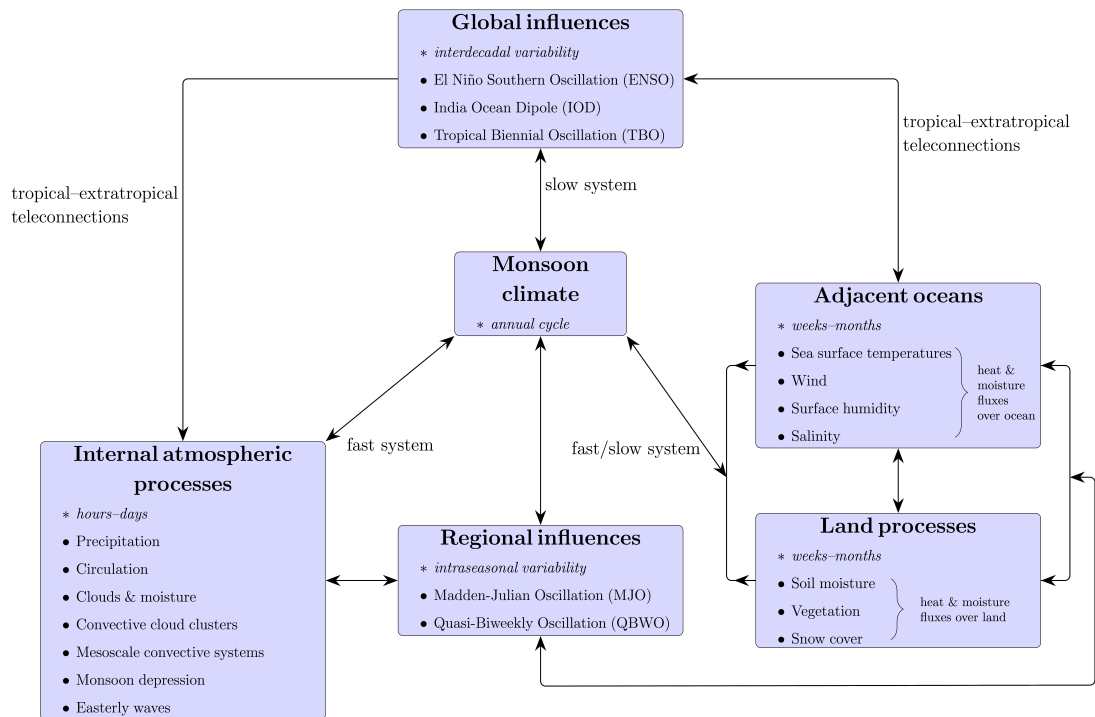
Figure 1.2: *Schematic adapted from (Lau et al., 2000) showing the various components and their contributions to a monsoon climate and its variability.*

1.2.2 Modelling the Indian monsoon

There are many different types of models to represent weather and climate, ranging in complexity and scale. The choice of model type is dependent on the extent of the application and the project aims. Often, the decision is a compromise between model intricacy and computational cost. For long, climatic simulations, typically spanning hundreds of years, General Circulation Models (GCMs) are employed, usually including ocean and sea ice components. These types of model runs provide a large-scale picture of global climate trends, incorporating atmospheric and oceanic oscillations that occur on longer timescales. Generally, a longer simulation has a larger horizontal grid size, upwards of 50 km, due

to computational limits. To investigate certain areas in more detail and provide weather forecasting services, Regional Climate Models (RCMs) are utilised. The capability of a finer horizontal resolution of the range 4–30 km is offset by a shorter simulation time of the order of weeks–years. Another class of model that is used primarily for research purposes is Large Eddy Simulation (LES). They are used to simulate small-scale features of fluid flows, such as turbulent moist convection. A much finer horizontal grid size of several hundred metres is required to resolve these features, meaning that simulations are hours–days, with the time period being limited by computational resources.

Finally, simplified mathematical models are considered. These are used as research tools to analyse a subset of processes in a larger system, or to model whole systems in alternative ways, using ideas from other areas of mathematics including statistics and dynamical theory. A simplified, or toy, model usually consists of several equations that can be solved analytically, or numerically with a minimal amount of computation cost. There is greater transparency in a toy model due to a reduced number of variables and processes. This allows effects of perturbations to be more easily traced back and attributed to a cause. In contrast, with complex climate models, there is a lack of clarity with the results, which can be difficult to interpret and analyse.

Despite substantial progress in the field of atmospheric science, particularly with regards to taking meteorological measurements and computing technology, the Indian monsoon is still poorly forecast on all timescales, with numerical weather prediction models struggling to emulate the complex dynamics. The forecasting of the monsoon on a range of timescales, the challenges, and the advances in modelling techniques are discussed in more depth in the following subsections.

1.2.3   Challenges in modelling the Indian monsoon

The physical processes driving the Indian monsoon onset and progression are difficult to model as there are dynamical interactions occurring simultaneously across multiple time and spatial scales. The set of equations governing the time evolution of the atmosphere, including the Navier-Stokes equations, cannot be solved analytically. Thus, they are instead solved numerically on a three-dimensional grid. The size of the grid and the time-step are determined by a compromise of accuracy and computing power. A more coarse horizontal grid size, as used by climate models, is less expensive computationally, allowing longer simulations. However, this means that certain processes occur within the space of a grid cell, and are unable to be resolved explicitly. These sub-grid scale processes are parameterised in terms of resolved variables, giving an average effect for the cell. Convection, which is instrumental in cloud formation and development, is one of the key mechanisms needing to be parameterised. Improving representation of convection in models is one of the main areas of active research, due to its important role in weather dynamics and particularly because clouds are a significant source of uncertainty in future climate scenarios. Another issue of having a more coarse horizontal grid size is that some orographic detail is

lost. The presence of the Himalayas, the largest mountain range in world, has a significant impact on the large-scale circulation which influences the genesis of the Indian monsoon. Thus, it is vital for models to accurately represent mountain ranges and their effect on weather.

1.2.4 Advances in modelling the Indian monsoon

Over the last 40 years, substantial improvements in computing technology have allowed for progressively more complex models at increasingly fine horizontal resolution. A greater range of dynamical processes from different constituents of the Earth system are now included. This in turn means that physical features can be modelled more accurately, contributing to research efforts and leading to increased understanding, in a continuing cycle. Generally, the large-scale circulation and temperature is well represented in models, but improvements need to be made with regards to vertical transport and rainfall patterns. For the Indian monsoon, it is suggested that parameterisations in convection and land-surface processes have the most potential for development. Although the rainfall timing and location is often incorrectly simulated, some advancement has been made with reproducing the correct intensity of rainfall in convection-permitting models. Over a seasonal timescale, it is possible to predict, by using statistical methods applied to early predictors over the winter and spring months, whether the monsoon will have a wet or dry rainfall anomaly.

It has been noted that a lack of measurements over tropical regions is an issue, as observations are needed to validate and calibrate weather and climate models. Collins et al. (2013) suggest that the lack of accurate observations may be a greater barrier to model development than the horizontal resolution or the parameterisation of physical processes. Several field campaigns in recent years, such as the African Monsoon Multidiscipline Analysis (AMMA, 2006) and the INteraction of Convective Organisation with Monsoon Precipitation, Atmosphere, Surface and Sea (INCOMPASS, 2016), which took a range of atmospheric measurements during the West African and Indian monsoons respectively, have helped to further knowledge in the field and facilitate collaborations across the globe.

1.3 Research aims

The goal of meteorology research is to increase understanding of the role and effect of physical processes associated with weather, stimulating model development and leading to improved forecast skill. Here, the focus is the onset and progression of the Indian monsoon, which is a key element in the global climate system. Rainfall associated with the arrival of the monsoon is crucial for agriculture, which constitutes a significant part of the Indian economy. The most advanced numerical weather prediction models do not reproduce the correct timing of monsoon onset or the intensity or duration of rainfall. Part of the issue

is that the mechanism by which the monsoon onset travels from southeast to northwest India, against the mean wind field, is not clear. To help address this, the monsoon onset and progression is examined in a novel way, combining a classical fluid dynamics and a meteorological perspective in a bottom-up/top-down approach. The former consists of developing a simplified mathematical model, based on a system of partial different equations, that can be analysed analytically. The equations will be derived from moisture budget arguments, focusing on a few key variables such as low-level southwesterly inflow, convective activity and northwesterly mid-level advection, which reproduce a monsoon onset and replicate its travel across India. Within a simple framework, the balance and interplay of these variables and their effect on the onset and progression of the Indian monsoon can be investigated in a transparent manner. The results should make clear which process has the most important role to play. Additionally, the theory of onset proposed by Parker et al. (2016) is hoped to be supported in a quantitative way.

The alternative angle of approach, at the other end of the complexity scale, is using an existing Regional Climate Model to produce simulations of the Indian monsoon. Here, the Weather Research and Forecasting (WRF) model is used, although the method would be applicable to other numerical weather prediction models. Part of the work with the Weather Research and Forecasting model will involve validating its performance against reanalysis data and observations. To compare the two models, equivalent variables will be identified and their effects evaluated. The results of the Weather Research and Forecasting model simulations should inform improvements to the simplified model, allowing additional layers of complexity to be added. Beginning with a one-dimensional model with two vertical layers, the primary variable is defined as a measure of atmospheric moisture. Initially, a steady-state of the two-layer system will be analysed, before allowing time evolution of quantities. From the Weather Research and Forecasting simulations, it might be discovered that land-surface processes or the horizontal wind field are of key importance for the monsoon onset and progression. Thus, the simplified model is extended to include either a surface layer or a second spatial dimension. Each version of the simplified model provides understanding, with the adding of additional factors in stages providing clarity on their individual impacts.

Using this novel method of comparing a simplified mathematical model to a complex numerical weather prediction model, it is hoped that the relative importance and contribution of several key processes involved in the onset and progression of the Indian monsoon can be stated. Thus, recommendations concerning future model development can be made.

1.4   Thesis structure

The following chapter will give some background relating to the Indian monsoon and its variability, including a detailed description of the large-scale circulation, temperature differentials and pressure gradients. A brief review of simplified and numerical weather

prediction models of the Indian monsoon follows, highlighting common biases and expanding on the level of detail presented thus far. Influences on the monsoon are loosely grouped into sections on rainfall and clouds, sea surface temperatures, topography and monsoon depressions.

Chapter 3 presents the conceptual multi-layer model, using moisture budget arguments to derive a set of linked equations. For processes requiring parameterisation, such as vertical moisture flux and surface forcing, the merits and drawbacks of different ways of achieving this are debated. Chapters 4 and 5 show the results of testing two simplified versions of the multi-layer model derived in Chapter 3. Firstly, in Chapter 4, the simplest version of the model is considered, consisting of two layers where the lower layer is fixed in time. The next iteration of this, allowing the lower to be dynamic, is the subject of Chapter 5. Here, solutions are derived both analytically and numerically for the system at equilibrium and incorporating temporal advancement. The sensitivity of the model to the choice of initial conditions and timescale parameters is tested. In Chapter 5 several experiments are developed to investigate the effect of changing a particular variable, such as the rate or depth of low-level moist inflow, the rate of convection or the strength of the mid-level dry advection.

A different approach is taken in Chapter 6, wherein a numerical weather prediction model is used to simulate the onset and progression of the Indian monsoon. Features of the model are briefly covered, followed by a description of the simulation and evaluation of model performance. Chapter 7 compares the dynamic lower layer model (Chapter 5) with the numerical weather prediction model (Chapter 6). This is done by undertaking a moisture budget analysis with the numerical weather prediction model, then identifying equivalent variables and contrasting their evolution throughout the monsoon season. Finally, Chapter 8 summarises the main results of this thesis, in relation to the research aims, and outlines suggestions for further work.

Chapter 2

Background of the Indian monsoon

This chapter begins with a detailed description of the Indian monsoon (Section 2.1), focusing on large-scale processes such as the low, mid and high level winds, temperature differentials and pressure gradients. The definition of monsoon onset and its progression is also covered, in greater depth than in the previous chapter (Subsection 2.1.4). A range of simplified and advanced weather models are reviewed with regards to their performance in accurately representing aspects of the Indian monsoon in Section 2.2. The challenges of modelling are expanded on, comparing deficiencies between models and their causes. The spatio-temporal representation of rainfall and cloud cover, indicating areas with deep convective potential, will be described from observations in Section 2.3. Sections on how the variation of sea surface temperatures (2.4) and the topography (2.5), including land-surface interactions, affect the monsoon will follow. There will be a focus on monsoon depressions (Section 2.6), which are a frequent feature of the Indian monsoon, as these have a high potential for human impact.

2.1 Description of the Indian monsoon

The following subsections will describe the conditions observed during the Indian summer monsoon, with the large-scale flow in winter given for comparison. Historical explanations for the occurrence of the Indian monsoon will be given, followed by the current understanding of monsoon processes. The criteria for the onset of the Indian monsoon is stated, along with a description of how it progresses to cover the entire Indian peninsula and then subsequently withdraws. The factors contributing to the variability of the Indian monsoon, including reference to active and break phases, are discussed within the text.

2.1.1 Summer circulation

The low-level wind circulation over Asia during the summer monsoon (June–September) and the winter circulation (December–February) is given by Figure 2.1, whilst Figure 2.2

shows the high level currents. The main monsoon flow originates as a southeasterly flow
(Trade Winds) below the equator, from an area of high pressure known as the Mascarene
high which is situated at 30°S, 50°E in the Indian Ocean off the east coast of South Africa.
There is a line of convergence at the equator as this flow moves northwards and becomes
southwesterly, deflected because of the Coriolis effect (McGregor and Nieuwolt, 1998).
Moisture is transferred across the equator; Saha (1970) gives magnitudes of equatorial
fluxes for air and water vapour, although the amounts are debated. The presence of
African orography partially determines the speed of this air mass and controls the vertical
structure. Without the orography, the low-level westerly jet over the Arabian Sea and
Indian monsoon would be stronger (Chakraborty et al., 2009). The flow continues over
the warm Indian Ocean, becoming unstable with respect to moist convection, passes over
the Indian continent then curves northeast over the Bay of Bengal. This air current,
known as the Somali Jet (also called the Findlater Jet, East African Low Level Jet or
Cross-Equatorial Low Level Jet), is a low level flow with a mean speed of 12–15 ms^{-1}
and speeds of 25–50 ms^{-1} in the core at around 1500m (McGregor and Nieuwolt, 1998).
There is a diurnal cycle, with the highest speeds being reached in the early morning and
the lowest in the afternoon (McGregor and Nieuwolt, 1998). There is a rapid deepening
of the air current close to the west coast of India, where the hill range of the Western
Ghats forms a barrier. The principle weather influences on the Indian summer monsoon
are illustrated schematically in Walker (1972), Figure 7.
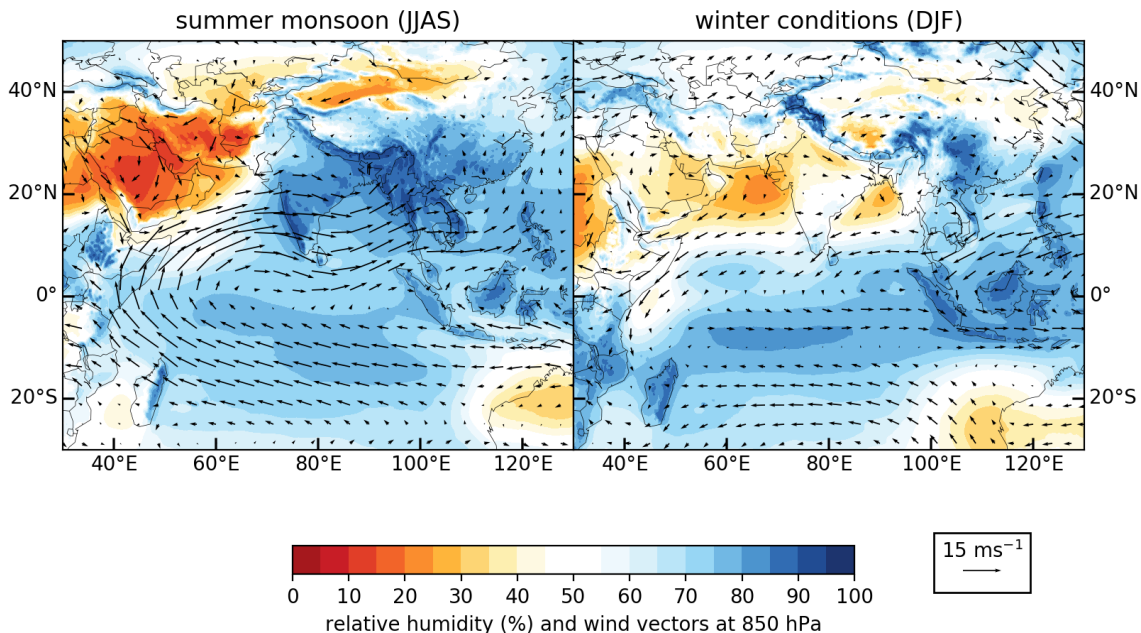
Figure 2.1: *Relative humidity (shading, %) and wind (vectors, ms^{-1}) at 850 hPa level,
for the Indian summer monsoon (June–September) and the winter season (December–
February). Produced from ERA5 reanalysis data (Copernicus Climate Change Service,
2017), averaged over years 1988–2017.*

Findlater (1969); Cadet and Ovarlez (1976); Findlater (1974) describe the observed flow of the Somali Jet from balloon experiments, illustrated in Figure 2.1 as the strong, low-level air current originating in the south, passing along the east coast of Africa and turning towards the western coast of India. Also described is the bifurcation of the jet during June/July into two branches over northern India and the southern peninsula respectively. It should be noted that the more northern branch of the Somali Jet has since been found to be closer to latitude 25° than 17° (Joseph and Sijikumar, 2004). Another balloon experiment (Ethé et al., 2002) collected data on velocity, humidity and temperature of the Somali Jet, comparing results with European Centre for Medium-Range Weather Forecasts (ECMWF) analyses. Generally, there was found to be good agreement between the balloon measurements and the weather forecasts. The velocity of this air mass is linked with active and break monsoon periods, which has implications for forecasting precipitation events. Stronger convective heating in the Bay of Bengal region is linearly correlated with the high-level zonal wind component, potentially initiating an active monsoon phase after a time lag of several days (Joseph and Sijikumar, 2004). Subrahmanyam et al. (2014) have investigated the variations of the Somali Jet with changes in sea surface temperature, which is discussed further in Section 2.4. Also, Hannachi and Turner (2013) have linked sea level pressure anomalies with active/break phases of the monsoon and the strengthening/weakening of the Somali Jet. In terms of potential vorticity, string cyclonic shear in the Somali Jet is linked with large positive potential vorticity (Yang and Krishnamurti, 1981). The generation of this positive potential vorticity by large-scale convergence and large-scale vertical advection is balanced by horizontal advection and cumulus mass flux (Yang and Krishnamurti, 1981). More detailed discussion of the potential vorticity, absolute vorticity and dry static stability budgets is given by Yang and Krishnamurti (1981).

To the northwest of India and into Pakistan is the Thar desert, which receives a large amount of solar radiation during the summer months. This causes the surface layer to heat and expand with a corresponding reduction in density. Locally, the increased thickness of the pressure layer corresponds with an area of high pressure aloft and an area of low pressure at the surface. This layer of dry air that forms, known as a heat or thermal low, is stable and reaches to the mid-troposphere. It is influenced by regional and remote forcing, with the orography (Hindu Kush mountains) having a greater role than surface thermal forcing (Bollasina and Nigam, 2011). The heat low forms during the onset of the monsoon and is strongest in July. It plays a role in the progression of the monsoon onset, competing against moisture inflow at low levels from the southwest, as observed by Parker et al. (2016). When the heat low extends to the east, a mass of hot, dry air intrudes into the mid–high level easterly flow occurring south of the Tibetan Plateau. Krishnamurti et al. (2010) links these dry intrusions to break periods in the monsoon that are associated with reduced precipitation.

There is a moist flow at low–mid levels over the Bay of Bengal, curving from the

southwest to the northwest, continuing south of the Himalayas. This flow is orographically
and thermally influenced by the Tibetan Plateau, with synoptic systems in the flow being
related to areas of organised precipitation (Luo and Yanai, 1983). A line of convergence
exists northwest of the Pakistan border where the moist flow from the Bay of Bengal
meets the northwesterly dry air coming off the continent from the heat low. At high
levels, the dry flow, known as the Subtropical Jet, is westerly and flows north of the
Tibetan Plateau. The Subtropical Jet encircles the globe, with the maximum intensity
being reached during winter and the location being further south than its summer position
(McGregor and Nieuwolt, 1998), which is shown in Figure 2.2.
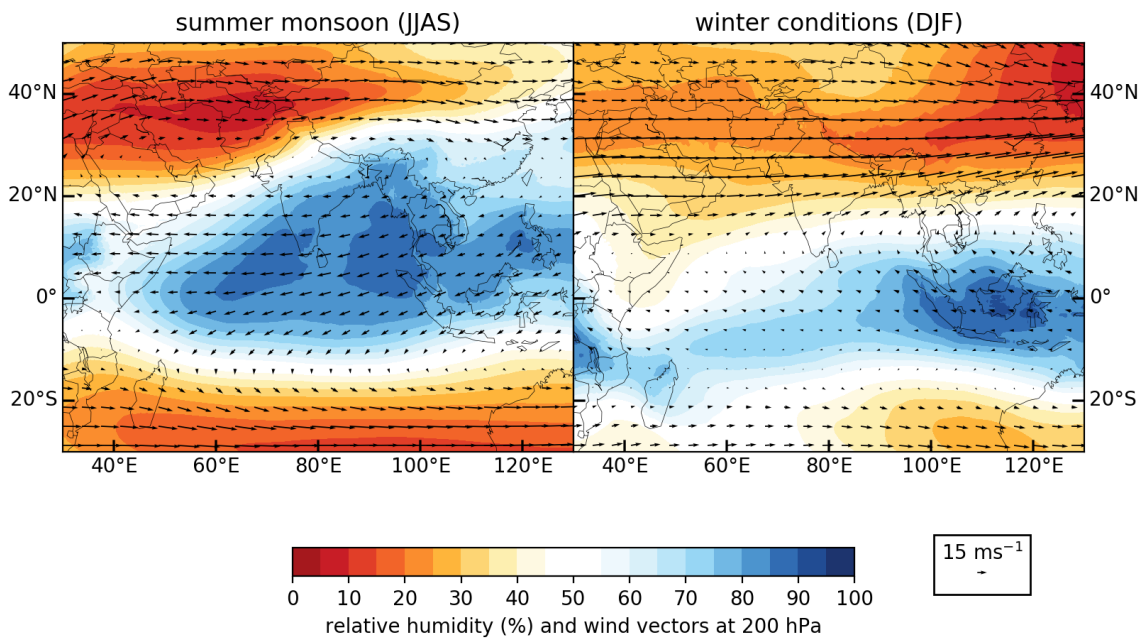
Figure 2.2: *Relative humidity (shading, %) and wind (vectors, ms^{-1}) at 200 hPa level,*
for the Indian summer monsoon (June–September) and the winter season (December–
February). Produced from ERA5 reanalysis data (Copernicus Climate Change Service,
2017), averaged over years 1988–2017.

South of the Tibetan highlands during summer, due to the heating of the land, an area
of low pressure develops at the surface as the warmed air expands and the layer increases
in thickness. This seasonal low pressure region to the northeast of India is known as
the monsoon trough. It is characterised by a convergence of winds and indicated by
increased cloudiness. Unlike over the Thar desert, there is an influx of moisture from
over the Bay of Bengal, reducing the stability of the atmosphere. This allows triggering
of convection, leading to the characteristic cloudiness and a higher probability of rainfall
occurring. Convergence at the surface is linked with divergence in the upper levels, as
the warm air is pushed outwards and begins to cool. At high levels of about 200 hPa
over the Tibetan highlands, where the risen warm air leads to a zone of high pressure, an
anticyclone forms known as the Tibetan high. Associated with the outflow of the Tibetan

high is the Tropical Easterly Jet (or Equatorial Easterly Jet). This high level easterly flow is a thermal wind reaching speeds of over 40 ms^{-1} (Galvin, 2008) and is present in the months June–September. It extends from Southeast Asia to Africa (50–80°E) and is centred on 15°N (McGregor and Nieuwolt, 1998).

The intertropical convergence zone (ITCZ), which is associated with cloudiness and rainfall due to convergence of air masses, is less defined during the summer as it moves north over the Asian continent. The thermal equator is also located north of India in the summer, whereas in winter it is to the south over the Indian Ocean (Nieuwolt, 1977). This movement is due to having more land mass to the north, which heats quicker than the oceans during summer, creating a temperature and pressure differential so that air flows from the sea towards the land at the surface. The land surface temperature follows a diurnal cycle, varying 10–15°C between day and night. This cycle is linked to the formation of clouds and triggering of deep convection, culminating in rainfall that peaks at mid-afternoon/evening. Galvin (2008) states that this development of the monsoon trough over the Arabian Sea and the movement of several low pressure systems from the Bay of Bengal by tropical easterly waves are the two main mechanisms responsible for bringing the monsoon rains over India.

Over northern India, the ITCZ forms the monsoon trough; a region of low surface pressure experiencing strong horizontal wind shear. This band of low pressure stretches from the India-Pakistan border in the northwest to the northeastern coastline, following the line of the Himalayan foothills which are located further north. When the Indian monsoon is in a break period, the monsoon trough is located further north, closer to Nepal and slightly to the east. The monsoon trough can extend into the Bay of Bengal, lowering the surface pressure which allows monsoon depressions to form. Section 2.6 will discuss monsoon depressions and their effect on rainfall pattern and intensity in greater depth. Vertical wind shear associated with the monsoon trough inhibits the formation of vortices, reducing the likelihood of tropical cyclones developing during peak monsoon season (McGregor and Nieuwolt, 1998).

2.1.2 Winter circulation

In the winter months, the temperature gradient reverses, with the seas being relatively warmer than the land which receives less solar insolation during this time (Jaswal et al., 2012). The ITCZ and the thermal equator are both located south of India in the winter, changing the spread of precipitation so that it is greater over the Indian Ocean than the continent (Nieuwolt, 1977). The Arabian Sea cools faster and to a lower temperature than the Bay of Bengal due to increased mixing and higher speed surface winds over the Arabian Sea. The Somali jet weakens, allowing a reversal of the low level flow from southwest to northeast, as can be seen in Figure 2.1. The dry low–mid level flow from northwest India/Pakistan pushes further into India now that it is not restricted by the monsoon circulation, contributing to northeast India becoming drier. Easterly low level

winds from over the Bay of Bengal bring moisture to the southern peninsula and eastern coast. At mid and higher levels, westerly flow dominates as the Subtropical Jet strengthens and moves further south, so that the flow to the north and south of the Tibetan Plateau is now westerly (Figure 2.2).

2.1.3   Monsoon theory

Early explanations of the Indian monsoon are based around the classical thermal theory, first presented by Edmund Halley in 1686, which describes the monsoon as a giant sea breeze (Walker, 1972). As the Asian land mass receives more solar radiation and becomes hotter, a temperature gradient develops between the land and the sea, as the sea is relatively cooler than the land. The layer of air above the surface becomes thicker locally, expanding as it is heated, creating a vertical pressure gradient with low pressure at the surface and high pressure aloft. Moist sea air is drawn in over land and convergence at the surface can initiate convective processes, leading to cloud cover and potentially precipitation. There is a north-south temperature gradient throughout the Indian landmass. The land-sea contrast intensifies the southwesterly monsoonal flow, but is not sufficient to account for the high wind speeds over the Arabian Sea. The Somali Jet is also required to account for the change in large-scale circulation during the monsoon.
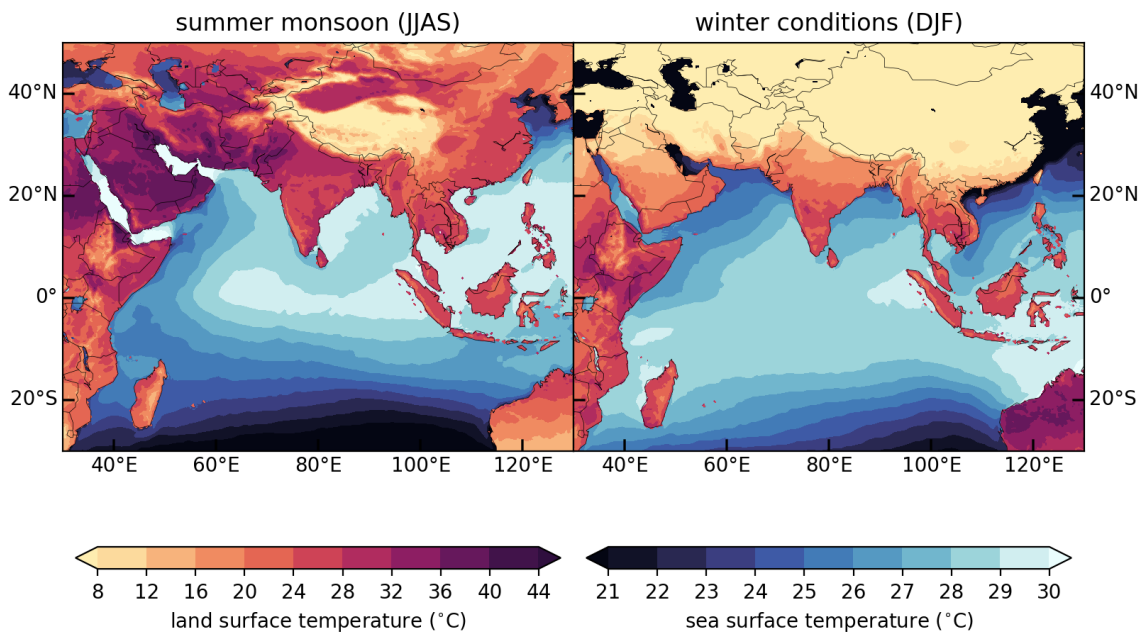
Figure 2.3: *Land surface temperature (warm colours, °C) and sea surface temperature (cool colours, °C), for the Indian summer monsoon (June–September) and the winter season (December–February). Produced from ERA5 reanalysis data (Copernicus Climate Change Service, 2017), averaged over years 1988–2017.*

The difference in land temperature between summer and winter months is shown in Figure 2.3. With the exception of the mountainous region of Tibet, the Eurasian landmass

in summer is very warm, reaching temperatures of over 36°C in some areas. Conversely, in the winter months, surface temperatures are below 10°C for the majority of the landmass. For India, a temperature gradient of around 8°C is observed in summer, with the north being warmer than the south. This gradient is reversed in winter.

Orography enhances the south-north pressure gradient (Park and Hong, 2004) with the area of surface low pressure in the north becoming the monsoon trough, which is part of the discontinuous ITCZ in summer. Gadgil (2003) emphasises the role of ITCZ migration in the development of the Indian monsoon, linking intraseasonal variations to poleward propagations of the ITCZ at 2–6 week intervals. The length of the monsoon season is strongly related to its overall strength (Gadgil, 2003).

More recently, the traditional sea-breeze theory has been challenged, with the temperature gradient thought to be a response of a seasonally migrating ITCZ, rather than the driver. An aspect in direct disagreement with the sea-breeze theory is the correlation of strong monsoon years with a decreased meridional temperature gradient near the surface (Walker et al., 2015), and drought years being associated with increased land surface temperatures (Geen et al., 2020). Walker et al. (2015) also notes that the interannual variability in precipitation is related to changes in the large-scale circulation, rather than changes in moisture. Several studies have investigated the role of the large-scale circulation in setting up monsoon systems. Bordoni and Schneider (2008) use aquaplanet simulations to demonstrate that monsoons can develop without land-surface effects or an active hydrological cycle. Land is necessary only to provide a surface of sufficiently low thermal inertia, to allow rapid adjustment of the moist static energy. This supports earlier work by Privé and Plumb (2007a), who show the existence of Hadley circulation in an axisymmetric atmosphere. Bordoni and Schneider (2008) describe the monsoon onset as a Hadley cell transition from an equinox regime controlled by eddy momentum fluxes, to a monsoon regime controlled by thermal driving. The regime transition involves the ITCZ moving polewards from a position near the equator. Schneider et al. (2014) say that the seasonal migration of the ITCZ cannot be explained by insolation or temperature differences between hemispheres alone, and that the ITCZ shifts with the moist static energy maximum. The seasonal changes in the large-scale circulation and the energy budget can explain the migration of the ITCZ, which initiates a regime change to monsoon conditions. Further work is needed to unite the energetics and dynamics perspectives in order to develop a comprehensive monsoon theory (Geen et al., 2020).

2.1.4   Onset & withdrawal

The Indian monsoon first onsets in the southeast at the start of June, then progresses in a northwesterly direction, as mentioned previously in Section 1.1. After approximately six weeks, the monsoon covers all of India, bringing a significant proportion of the annual rainfall over about two months. Figure 1.1, in Chapter 1, shows the normal onset dates for the monsoon progression.

The Indian Meteorological Department formally defines the monsoon onset with criteria for rainfall, wind speed and outgoing longwave radiation over the southeastern state of Kerala (India Meteorological Department, 2016). The depth of westerlies from the equator to latitude 10 °N and longitude 55°E to 80°E should be maintained up to 600 hPa and the zonal wind speed in the region between latitude 5–10°N and longitude 70–80°E should be around 15–20 Kts (7.5–10.5 ms^{-1}) at 925 hPa. The outgoing longwave radiation in the region latitude 5–10°N and longitude 70–75°E should be below 200 Wm^{-2}. Winds are derived from satellite or root-mean-square covariance wind analysis and outgoing longwave radiation is derived from the Indian National Satellite System (INSAT). The rainfall criterion requires that at least 2.5 mm is recorded for two consecutive days after 10th May at 60% of 14 stations located around the coast of the southwestern state of Kerala. If the amount and spread of rainfall is achieved and the conditions on wind field and outgoing longwave radiation are also met, then the onset of the monsoon is declared over Kerala on the second day. This usually occurs around the start of June, although there is high interannual variability. Joseph et al. (2016) describes this method for determining the onset date over Kerala in more depth. It has been suggested that local onset dates provide more meaningful information to forecasters - Fitzpatrick et al. (2016b) has developed a method with Local Onset Regions to determine regions where local onset variability is consistent. This method has previously been applied to the West African monsoon (Fitzpatrick et al., 2016a). The interannual variability of rainfall is fairly low, with a standard deviation of around 10% of the total summer rainfall (Turner and Annamalai, 2012). The intraseasonal variability, determined by active and break phases of the monsoon, is more critical for agriculture and water supply than the interannual variability. Fasullo and Webster (2003) offer an alternative method of assessing the onset and withdrawal dates using vertically integrated moisture transport instead of rainfall, which is typically more poorly modelled and measured.

The theory behind the onset of the monsoon is described as a 3-stage process by Zhang et al. (2004). Firstly, sensible and latent heat fluxes over the land lead to the formation of a cyclonic vortex over the Bay of Bengal. Low-level southwesterly winds strengthen and become more dominant due to the rapid increase of land-sea contrast between East Africa and the Indian Ocean, enhanced by the Somali Jet, as described above. These low level flows are linked with the ITCZ, which moves northwards, and can have a significant influence on the rainfall over India, with a time lag of a few days (Findlater, 1969). In the second stage, high level easterlies to the north of India strengthen, forming the Tropical Easterly Jet (Galvin, 2008). The (westerly) Subtropical Jet becomes weaker and moves further north. Subsequently, thermal forcing of the eastern Tibetan Plateau occurs and there is active convection over the Bay of Bengal. In the third stage, a low-level cyclonic vortex forms over the east coast and the northwest pressure gradient intensifies. A more in depth description is given by Raju et al. (2005), who discusses the evolution of heat, moisture and kinetic energy over India, the Arabian Sea and the Bay of Bengal.

From the onset over Kerala, the monsoon progresses to the whole southern peninsula and also to the north east states near Bangledesh. It is complicated by the presence of the Himalayan barrier (Galvin, 2008). The northeast-southwest orientated progression band continues to the northwest, reaching Pakistan around mid-July. This is illustrated by the dashed white lines in Figure 1.1. The mechanism of onset, as noted in Section 1.1, is described as a balance between the low-level southwesterly monsoon flow and the mid-level dry air extending east from the heat low over northwest India/Pakistan (Parker et al., 2016), supported by Menon et al. (2018); Volonté et al. (2019). The theory is illustrated schematically in Figure 13 of Parker et al. (2016). The mid-level dry layer suppresses convection in the northwest but further southeast where the profile is shallower, the conditions for convection become favourable. Shallow cumulus and congestus clouds moisten the dry layer from below, making the profile closer to moist adiabatic (Parker et al., 2016; Menon et al., 2018). As the level of moisture increases and onset advances, the northern limit of convection moves towards the northwest. Rains associated with the onset front wet the surface which maintains the amount of moisture through evapotranspiration. Parker et al. (2016) point out that the propagation of the monsoon cannot be directly explained by moisture fluxes to the northwest, and Volonté et al. (2019) emphasise the importance of local diabatic processes on the non-steady nature of the progression of monsoon onset.

Towards the end of the summer season, as the amount of solar radiation decreases, the thermal contrast is reversed so that the sea is relatively warmer than the land. The ITCZ reforms and migrates south of the Indian peninsula. The winds revert back to their winter patterns (as described in Subsection 2.1.2) and the withdrawal process begins around the start of September. This occurs in reverse to the progression, but over a longer period of time. The monsoon has usually withdrawn over the entire Indian peninsula by mid-December and over Sri Lanka by January. The India Meteorological Department (2016) defines criteria for the withdrawal, including a lack of rainfall activity over the specified region, reduction of moisture content and establishment of an anticyclone in the lower troposphere over northern and central India.

2.2   Modelling the Indian monsoon

Models of the Indian monsoon are broadly split into two categories: simplified, mathematical models that may reproduce only some features, and numerical weather prediction models which attempt to reconcile all physical processes. The former give the opportunity to study certain features in greater detail and transparency. Numerical weather prediction models are more realistic as they include full atmospheric dynamics. However, they can be difficult to analyse and are susceptible to biases, particularly over the Indian region. The best research approach would be to utilise a combination of modelling techniques, to gain the benefits from each perspective. There is a need to define the various processes that can influence monsoon onset and to quantify the effects on the speed of onset progression and

precipitation distribution, through modelling studies and comparison with observations.

2.2.1   Simplified monsoon models

Various simplified models have been developed to simulate the main features of the Indian monsoon in order to test sensitivity to different forcings and to analyse the dynamical processes. Godbole (1973) uses a two-dimensional model of zonally symmetric motion to reproduce the large-scale circulation and temperature gradients observed during the Indian monsoon. Experiments both with and without the Himalayas demonstrate their important role in the establishment of the monsoon flow. The contribution from the presence of two oceans and the development of a horizontal thermal gradient in the upper troposphere, are also highlighted. A model with full hydrology, an interactive ocean and heated continent was put forward by Webster and Chou (1980) to reproduce some key aspects of the monsoon. The importance of hydrology, not just orography, is emphasised and thermodynamics were used to gain insight into the scale of motion of moist processes. An idealised model with the geometry but not the topography of the Indian subcontinent is presented by Chou (2003), which induces a positive meridional tropospheric temperature gradient and thus a weak Asian summer monsoon circulation. Also shown was that a higher prescribed heating with weaker surface albedo over Eurasia and the Tibetan Plateau strengthens the temperature gradient, and consequently a stronger monsoon, in agreement with the theory outlined above.

Rodwell (1993) introduces a simple primitive equation model to simulate the time-mean monsoonal flow and accurately represent the Somali Jet. Thermodynamic balances, potential vorticity analysis and response to different heating regimes are undertaken. The basis of this model is expanded upon in Hoskins and Rodwell (1995), where it is also found that a linear version of the model with no orography can reproduce the upper tropospheric circulation, although the accuracy is improved when mountains are included. A more detailed investigation of the mechanisms of the Somali Jet and the potential vorticity behaviour was a further application of this model (Rodwell and Hoskins, 1995).

Gill (1980) demonstrates that a simple analytic model based on linear theory for small perturbations to the atmosphere can produce a circulation similar to that of the Indian monsoon in July, given a diabatic heating source located north of the equator. Rossby wave dynamics govern the response of the atmosphere to heating (Lau et al., 2000). The anomalous circulation of the Indian monsoon generates divergence, which is inversely related to the advection of planetary-scale vorticity along longitudinal lines, in accordance with the Sverdrop balance (Lau et al., 2000). Based on some of the work by Rodwell-Hoskins, Saini et al. (2011) find that strong diabatic heating in summer produces a Rossby wave response that thermodynamically interact with the midlatitude westerly jet to produce subsidence over north Africa, the Mediterranean and the Middle East, with reduced rainfall to the west of the monsoon.

Rácz and Smith (1999) have investigated the dynamical structure of heat lows and look at the distributions of relative and potential vorticity. They found that the relative vorticity is strongest in the early morning and that there is an anticyclonic potential vorticity anomaly throughout most of the lower troposphere. At the surface, the potential vorticity anomaly is cyclonic and corresponds to the maximum surface temperature. The numerical model used to investigate heat lows is based on an idealised flow pattern with a square region of land surrounded by sea. It would be interesting to apply a similar model and experiment to a triangular area of land and modify the boundary conditions to represent a simplified India. A more theoretical experiment is set up in a general circulation model by Privé and Plumb (2007a,b). Axisymmetric studies and the impact of eddies and forcing geometry were investigated.

Another theme of models relates to the moist static energy budget. Srinivasan (2001) derives a single equation to show that the seasonal variation in rainfall depends primarily on evaporation, net radiation at the top of the atmosphere and the integrated water vapour. Focusing on the energy budget, Muller and O'Gorman (2011) consider how it can explain the spatial variability in precipitation change. They find that the precipitation response at large scales, and over land at small scales, is guided by the changes in radiative and surface sensible heat fluxes. However, over the ocean at small scales, the precipitation response is inhibited by cloud and water vapour feedbacks. On the other hand, some studies use the moisture budget to develop simplified models. For example, Masunaga and Sumi (2017) use a time-dependent model that is zero-dimensional in space, to predict the vertical integral of vertical moisture advection. The vertical profile is degenerated into modes representing deep convection and convective heating by congestus/stratiform clouds. Using a closure to represent consumption efficiency of water vapor into precipitation, the results show that the congestus/stratiform vertical mode is highly inefficient, whilst the deep convective mode is efficient. This suggests that congestus clouds do not involve an efficient mechanism to produce rainfall despite a column moistening by vertical moisture advection (Masunaga and Sumi, 2017).

There a number of studies using the shallow water equations, involving many modifications to suit the application. For instance, Kent et al. (2017) uses rotating shallow water equations, adapting to include simplified dynamics of cumulus convection and precipitation. A conditional instability leads to a convective updraft, and coupled with moisture transport, can produce downdrafts and precipitation. Similarly, Bouchut et al. (2009) uses a simplified form of the shallow water equations, with moisture and convection, to reproduce the propagation of precipitation fronts. This is particularly relevant for modelling monsoon onset, which can be thought of as a propagating moisture front.

A final model to note is the two-layer formulation describing the affinity between precipitation and column water vapour in the Tropics, by Muller et al. (2009). Here, a stability threshold relating to boundary layer water vapour determines the occurrence of precipitation. Likewise, Schewe et al. (2012) describes modelling the transition from pre-

onset to full monsoon by a threshold of atmospheric specific humidity over the ocean. A more detailed comparison of monsoon models is beyond the scope of this work but it is evident that a simple model is sufficient to reproduce the main features of the monsoon and to investigate specific aspects in greater detail.

2.2.2   Numerical weather prediction models

In meteorology, numerical weather and climate prediction models are the primary tools for forecasting weather and climate respectively. Although many advances have been made in recent years, such models have difficulty in accurately simulating complex dynamical systems, such as the Indian monsoon. In particular, the primary output of interest, the spatial and temporal structure of rainfall, is not captured well compared to observations. Typically, over the Tropics, rain falls too extensively and is insufficiently intense, compared with observations (Stephens et al., 2010; Lucas-Picher et al., 2011; Bollasina and Ming, 2013a; Sperber et al., 2013; Karmacharya et al., 2015; George et al., 2016; Johnson et al., 2017; Martin et al., 2017; Goswami and Goswami, 2017). The large-scale circulation in the Tropics is also an area that needs revising. Note that such deficiencies are common to an array of General Circulation Models (Sperber et al., 2013; Ashfaq et al., 2017), and Regional Climate Models (Lucas-Picher et al., 2011), but aspects have been improved over recent years, as can be seen by looking back at Gilchrist (1977); Sperber and Palmer (1996).

Specifically for the Indian region, a dry bias to the northwest persists in models throughout the monsoon season (Sahana et al., 2018). Additionally, monsoon onset is usually late in model simulations (Sperber et al., 2013). However, on a positive note, research by Menon et al. (2018) show that models are capable of reproducing the mechanism of monsoon onset, as described in Parker et al. (2016). The simulation with a coupled atmosphere-ocean model shows the moistening of the free troposphere, competition against a mid-level dry intrusion and shallow convection occurring ahead of the onset, aiding the progression to northwest India.

Part of the issue of modelling rainfall accurately is the presence of biases in sea surface temperature. For example, cold sea surface temperature biases over the Arabian Sea weaken moisture fluxes and reduce the amount of rainfall (Levine et al., 2013). Another flaw in models is the assumption that the atmosphere reacts to the ocean, rather than the existence of a two-way dynamic between the atmosphere and ocean. Kumar et al. (2005) suggests that coupled atmosphere-ocean models perform better than models forced by sea surface temperature. After the onset of the summer monsoon, it seems that it is the monsoon that is influencing the Indian Ocean (Krishnamurthy and Kirtman, 2003). Furthermore, the patterns and dynamics of oscillations such as El Niño Southern Oscillation, Madden-Julian Oscillation and others, are not fully understood and it is an ongoing challenge to capture their effects accurately in models. The importance of Indian Ocean coupled dynamics and teleconnections is highlighted by George et al. (2016), who relates

the model skill in representing these phenomena to the prediction of India's summer rainfall. To help improve models, more sea surface temperature observations in the Indian Ocean are required, particularly to quantify variability over seasonal and yearly timescales (Vecchi and Harrison, 2004).

Models have difficulty in accurately representing the diurnal cycle, which is necessary for correct timing of precipitation. This is not just an issue for the Indian monsoon - Birch et al. (2014) state the need for improved schemes to capture the diurnal cycle better and to be able to trigger convection in high convection inhibition conditions with regards to the West African monsoon. Cloud resolving models with a high horizontal resolution of 1 km represent the diurnal cycle more accurately than global convective parameterised models, which tend to peak too early (Bechtold, 2015). Similarly, models with an explicitly resolved convection also reproduce a more realistic diurnal cycle (Dirmeyer et al., 2012). The development and implementation of improved convection schemes with different parameterisations is an important area of current research.

The spatial resolution, choice of boundary conditions and the physical representation of convection - explicit or parameterised - are possible limitations of modelling the onset and progression of the monsoon (Mishra et al., 2014; Dirmeyer et al., 2012; Holloway et al., 2012; Birch et al., 2015; Willetts et al., 2017; Johnson et al., 2017). It has been suggested that more simulations across all timescales with individual models would help address systemic errors, such as tropical circulation and precipitation pattern (Martin et al., 2010). Additional observations, particularly over tropical regions, would also aid model development.
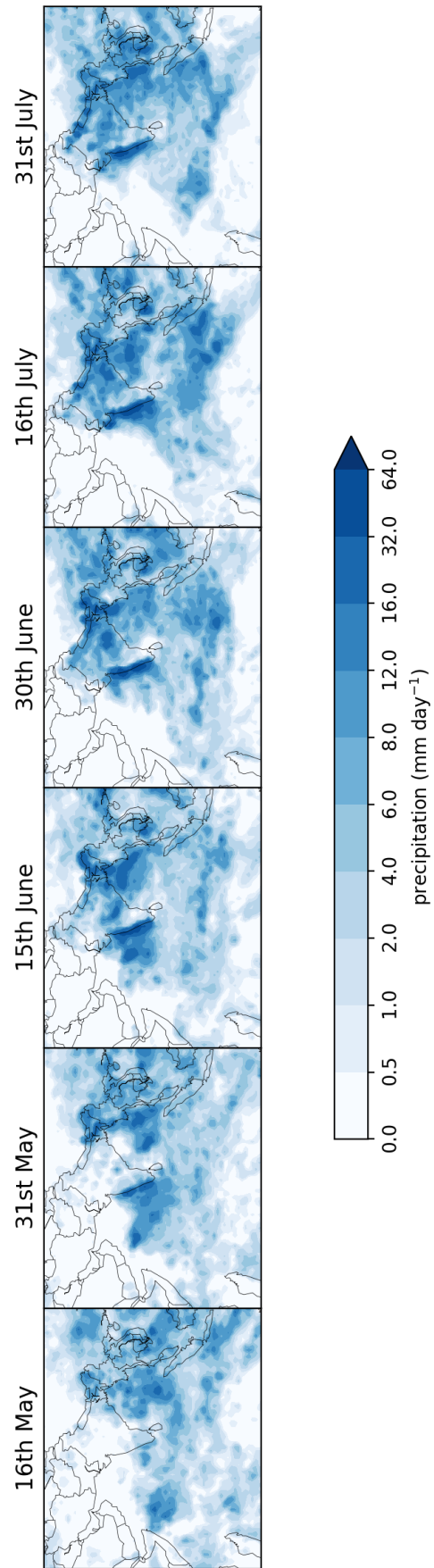
Figure 2.4: *Observed precipitation (mm day^{-1}), for for various dates during the Indian summer monsoon, averaged over years 1998–2011. Derived from merged rain gauge and TRMM satellite data as described in Mitra et al. (2009, 2013).*

2.3   Rainfall and Clouds

The summer monsoon brings 80% of India's annual rainfall (Turner and Annamalai, 2012), half of which results from monsoon depressions (Yoon and Chen, 2005) - these are discussed further in Section 2.6. During the summer months, central India receives 800–1500 mm rain, compared with less than 50 mm over winter (India Meteorological Department, 2016). The states of Kerala in the southwest and the northeastern states surrounding Assam have the highest amounts of rainfall. Cherrapunji and Mawsynram, located in the northeast state of Meghalaya, are deemed the wettest places on earth. Cherrapunji holds the record for the most rainfall in a month - 9300 mm - whilst Mawsynram holds the record for the most rainfall annually, with a yearly average of 11873 mm (Guinness World Records, 2017).

Figure 2.4 shows the climatological observed rainfall for several dates throughout the monsoon period. Looking at the rainfall over land, which is of primary interest, there is a marked increase in rainfall between May and July, particularly noticeable over central India. Areas receiving significant amounts of rainfall are the western coast and northeastern states, consistent with the above. Associated with the summer rainfall is extensive cloud cover. The northwest state of Rajastan is largely dry, due the to presence of the Thar desert, with the majority of rainfall coming from monsoon depressions. The distribution of rainfall is strongly influenced by the orography. Specifically, the Western Ghats in southeast Kerala and the Khasi Hills in the northeast.

In the tropics, there are high rates of evapotranspiration due to warmer air temperatures being able to hold more moisture and high insolation. This leads to the formation of clouds and the advection of this moist air over land produces rainfall. Referring back to Subsection 2.1.1, Saha (1970) attempts to quantify the moisture fluxes into the Arabian Sea from across the equator. In a similar theme, Sadhuram and Kumar (1988) and Kumar and Sadhuram (1989) examine how evaporation rates over the Arabian Sea impacts rainfall on the western coast of India, finding no significant correlation. There is a two-way link between clouds and the oceans. The sea surface temperature controls humidity and thermodynamic processes in the marine boundary layer, which is the moisture source, whilst the clouds influence radiative and mass exchange, convection, evaporation and mesoscale convergence (McGregor and Nieuwolt, 1998). See Houze (1982) for a more detailed description of how tropical cloud clusters modify the vertical atmospheric profile through mesoscale stratiform and radiative processes. Generally, there is more of most cloud types closer to the equator, especially in the ITCZ which is associated with cumulus and cumulonimbus clouds. There is widespread cirrus and altostratus throughout the tropics region. In contrast to the midlatitudes, stratiform clouds are less frequent and limited to areas of convergence or linked to waves/disturbances (McGregor and Nieuwolt, 1998). Cloud bands form in areas of convergence or horizontal shear, becoming rain bands. These are evident over India during the summer monsoon.

In terms of convection, some observations have been made by Houze et al. (2007)

based on the TRMM precipitation radar, with three different mechanisms for western, central and eastern regions around the Himalayas. These are shown schematically in Houze et al. (2007), Figure 29. The most intense deep and wide convection occurs in northwest India (western Himalayan region), where the low level moist monsoonal flow from over the Arabian Sea is capped by an inversion as it under-runs mid-high level dry air advected from the Afghan or Tibetan Plateaus (Houze et al., 2007). The orographic effect on convective precipitation is greatest just upstream of the mountains. The central Himalayan region is characterised by wide intense convection, linked with depressions originating from the Bay of Bengal, which can be enhanced by the steep topography, and presence of deep convective cores over the Tibetan Plateau. A broad area of stratiform precipitation is the signature mechanism of the eastern region of the Himalayas, driven by moist inflow from the Bay of Bengal. Deep convective cores over the Tibetan Plateau are also present. To the east of India, towards the Bay of Bengal, the convection is more likely to be maritime and to the west, of continental origin. Convection is more intense over the lower elevations, such as the Himalayan foothills and the Western Ghats.

Associated with most of the convection types is a diurnal cycle. Deep convective cores form preferentially in the evening. Wide convective cores of continental origin also form preferentially in the evening, with an additional smaller nocturnal/early morning peak due to the convergence of katabatic winds from the Himalayas. Moist monsoonal flow over the foothills and wide convective cores of maritime origin have a midday maximum, although this is a less pronounced diurnal cycle than for the other types (Romatschke et al., 2010).

A characteristic of rainfall in the topics is persistence, which can lead to prolonged droughts or flash flooding. McGregor and Nieuwolt (1998) describes three types of rainfall: convectional, cyclonic and orographic. The first of these is widespread particularly over northern and central India during the monsoon and is formed by rapid uplift of air which produces intense bursts of rainfall. Cyclonic rainfall is associated with horizontal convergence in an area of low pressure with a vorticity maximum, such as the depressions originating mainly from the Bay of Bengal. Close to the Himalayas to the north of India, the Western Ghats along the west coast, the Khasi Hills in the northeast and the hills bordering the Ganges Basin, orographic rainfall where moist air is forced over a topographical barrier can be observed (McGregor and Nieuwolt, 1998). The leeward side of most of these ranges experiences a rain shadow. Two main mechanisms, multi-layer inversion stratification and moist adiabatic stratification, have been identified over the Western Ghats to give low and high rainfall spells respectively (Maheskumar et al., 2014). The former involves advection of warm dry air which inhibits convection and the latter allows efficient warm and mixed phase processes to occur so that shallow and deep convective clouds coexist. This is further developed by Fletcher et al. (2018), who refers to coastal and offshore phases of rainfall, characterised by the strength and moisture content of onshore winds.

2.4   Sea surface temperatures

Variations in sea surface temperature affect the moisture flux which influences the extent
of cloud and can lead to more or less convective conditions. Figure 2.3 shows the long-term
mean sea surface temperature and land surface temperatures for the summer and winter
seasons from reanalysis data.

There is a marked change between summer and winter close to the coastline of the
Eurasian landmass. As the land warms in summer, so does the sea near the coastline,
particularly around India. In winter, the reverse is observed, creating a temperature
gradient, with the sea around southern India being several degrees warmer than the sea
near the southern coast of Pakistan and Bangladesh. The warmest month is May, with
temperatures exceeding 28° during the summer months. The Arabian Sea cools down
earlier and more rapidly than the Bay of Bengal after August. This is due to strong surface
winds over the Arabian Sea increasing vertical transport through turbulent mixing and
transferring heat to deeper layers (Shenoi et al., 2002). There is little correlation between
sea surface temperature and surface air temperatures in the Bay of Bengal during the
monsoon season, in contrast to the Arabian Sea (Jaswal et al., 2012). The Bay of Bengal
experiences weaker surface winds so there is less overturning and heat is transferred only
by diffusion (Shenoi et al., 2002). Contributing to this is the high degree of stratification,
with freshwater inflow from rain and rivers (e.g. the Ganges) creating a low salinity
layer near the surface which inhibits vertical mixing to shallow depths of less than 20 m
(Kumar et al., 2002). The warmer temperatures of the Bay of Bengal are more conducive
to large-scale deep convection, explaining why more low pressure systems form in this
region compared with the Arabian Sea.

There are several phenomena recurring on various timescales that can affect the sea
surface temperature and hence surface pressure and winds. These include the Madden-
Julian Oscillation (30–60 days) in the Indian and Pacific oceans and the El Niño Southern
Oscillation (ENSO) which affects most of the tropics over several months every 3–7 years.
The El Niño Southern Oscillation has three phases: neutral, El Niño and La Niña. El
Niño is associated with warmer sea surface temperature, and higher surface pressures,
while La Niña is linked with cooler sea surface temperature and lower surface pressures
over parts of the Pacific ocean. In terms of the Indian monsoon, El Niño correlates with
a drier monsoon whilst La Niña is linked with a wetter monsoon. There is also the Indian
Ocean Dipole (IOD), which affects the sea surface temperature in the Indian Ocean and
is difficult to predict as it has an irregular pattern, occurring every few years and lasting
for several months. A further example is the Tropical Biennial Oscillation (TBO), which
describes the tendency for a fairly strong monsoon in one year to be followed by a fairly
weak one the next year and vice versa. In addition, an oscillation on similar scale to the
MJO exists: the Quasi Biweekly Oscillation (QBWO). This has a period of 12–20 days and
contributes to tropical intraseasonal variability. The schematic (Figure 1.2) in the previous
chapter summarises the oceanic influences, and others, on the Indian monsoon, grouping

by spatial scale. A more detailed discussion of phenomena and oscillations affecting sea surface temperature is beyond the scope of this thesis.

Warmer oceans generally mean greater sensible heat exchange, and thus a more favourable environment for deep convection. This in turn leads to increased precipitation. The reverse situation, with colder sea surface temperatures, correlates with reduced precipitation. Using a numerical model, Shukla (1975) shows that a cold sea surface temperature anomaly over the central Arabian Sea leads to an increase in sea surface pressure and a decrease in moisture flux, leading to drier conditions and less rainfall over India. A second study (Shukla and Misra, 1977) conducted further research into the link between sea surface temperature and rainfall using observational data. They found that warmer sea surface temperature of the Arabian Sea in July was associated with greater rainfall over central and western India during August, and cooler sea surface temperature was correlated with reduced rainfall. Rao and Goswami (1988); Clark et al. (2000); Krishnamurthy and Kirtman (2003); Jaswal et al. (2012) are mostly in agreement, although Clark et al. (2000) say that it is the preceding winter's sea surface temperature over the Arabian Sea that affects the summer monsoon. Another study (Vecchi and Harrison, 2004) has investigated the correlation between sea surface temperature anomalies and rainfall on a regional scale, finding that warm sea surface temperature over the Arabian Sea increases the amount of evaporation and atmospheric circulation, leading to greater rainfall over the Western Ghats area. The difficulties with robustness and the quality of data available on the results are highlighted, possibly explaining the discrepancies between various studies - for example, Vecchi and Harrison (2004) could not reproduce Clark et al. (2000)'s results.

The relation between sea surface temperature and surface wind speeds has been investigated, with Shukla and Misra (1977) finding an inverse correlation over the Arabian Sea in July. This is complementary to the results discussed in the preceding paragraph, as stronger surface winds are associated with cooler sea surface temperature, which is linked to reduced rainfall. Correspondingly, weaker surface winds are linked with warmer sea surface temperature and increased rainfall. Note that these findings are on a monthly timescale for the specific months of July and August at the peak of the monsoon, when the large-scale circulation is quasi-steady. On shorter timescales of hours–days, stronger winds can lead to larger heat fluxes at the surface, reinforcing the circulation as convection acts as a heat transport mechanism. This process of wind-induced surface heat exchange can lead to localised increases in rainfall. Subrahmanyam et al. (2014) show a similar result, finding a negative correlation with the wind speed of the flow known as the Somali Jet and sea surface temperature anomalies in the Arabian Sea during summer months. Furthermore, Subrahmanyam et al. (2014) conclude that in El Niño years, the sea surface temperature anomaly is greater, there is less cloud cover and the speed of the Somali Jet is slightly reduced. For La Niña years, the sea surface temperature anomaly is less and the speed of the Somali Jet is relatively high. The minor fluctuations in sea surface temperature influence the strength of the Somali Jet so that there are periods of higher and lower

velocity, determining how active the monsoon is. The moisture flux and cloudiness are affected, which determines the intensity of rainfall over India (discussed in Section 2.3).

2.5   Topography

The unique topography of the Indian continent influences the onset of the monsoon and is responsible for regional variations in rainfall intensity. The presence of ocean to the east, south and west, allows moisture to be drawn up into the atmosphere over India to form clouds and provide conditions for deep convection and precipitation. Bordering India to the north and the northwest are the Himalayas, the highest mountain range in the world. The average height of the Himalayas is 6100 m, with the tallest peak, Mount Everest, reaching 8848 m. Beyond the Himalayas to the northeast is a high, flat region known as the Tibetan Plateau. This has a significant influence on atmospheric circulation and hence the monsoon. Another aspect that can affect the strength of the monsoon is the depth and extent of snow cover over the mountains.

Further north, where the boundaries of India, Pakistan, Afghanistan and Tajikistan converge, are the Hindu Kush mountains. Heights of the peaks in this range vary from around 4500 m to 6000 m, decreasing from east to west. Extending down the western coast of India are the Western Ghats, a smaller mountain range with an average elevation of around 1200 m. As mentioned in Subsection 2.1.1, the Western Ghats act as a barrier to the southwesterly monsoon winds and consequently they receive a large amount of rainfall during the monsoon season. Incidentally, some of the highest levels of biodiversity are found in this area. Along the eastern coast of India lie the Eastern Ghats, although this range is not continuous. Between both ranges of the Ghats is the Deccan Plateau, a raised area the shape of a downwards pointing triangle. This is bordered to the north by the Satpura and Vindhya hill ranges. East of Bangledesh in the state Meghalaya are the Khasi Hills. The orography in this region is partly responsible for it being one of the wettest areas on the planet. Northeastern India (and most of Bangledesh) is characterised by the low lying, fertile Gangetic Plain of the Ganges river. Most monsoon depressions pass over this plain tracking northwest, bringing rain to the dry state of Rajasthan, which is a desert region.

The following subsections will focus on the effects of snow cover over Eurasia and the presence of the Tibetan Plateau on the Indian monsoon. Rainfall mechanisms over the mountain ranges have been described in Section 2.3.

2.5.1   Snow cover

It is generally accepted that there is an inverse relationship between the snow cover over Eurasia and the Indian monsoon; winters with little snow cover over Eurasia are followed by summer monsoons with a greater amount of rainfall over India and vice versa (Hahn and Shukla, 1976). More extensive snow cover is associated with colder ground tempera-

tures that cause the monsoon to be weaker. Equally, less extensive snow cover is linked with warmer ground temperatures, leading to a stronger monsoon. A faster snow melt is also conducive for a stronger monsoon and arguably more important than the snow cover (Kripalani et al., 2003). Bamzai and Shukla (1999) found that this inverse correlation is only statistically significant for the western Eurasian region. Unlike previous investigations, no relationship between the seasonal Himalayan snow cover and the Indian monsoon was discovered. This is possibly due to differing methods of analysis and use of different data sets. Over recent years, the relationship between snow cover and the Indian monsoon rainfall appears to have weakened, possibly as a result of global warming (Kripalani et al., 2003). In general, other factors such as oceanic phenomena have a greater influence on the Indian monsoon. For example, the effect of the El Niño Southern Oscillation can dominate the snow cover-rainfall relationship (Fasullo, 2004).

2.5.2   Tibetan Plateau

The presence of the Himalayan mountains are the dominant effect on developing the monsoon circulation (Godbole, 1973). Exploring this further, Hahn and Manabe (1975) conducted an experiment to determine the extent of the influence of the Himalayan mountains on the Indian monsoon. They ran model simulations with and without the mountains. They found that when the mountains were included, the monsoon climate extended further north with a low pressure envelope over the mountains and that moist and latent heating processes dominate over dry and sensible heating processes. There were a few issues with the simulations, such as the Tibetan high being located too far south and the monsoon trough and associated depressions being underestimated, although these do not detract from the key differences observed in the two runs. The Tibetan Plateau plays an important role in atmospheric circulation. Luo and Yanai (1983) describes the orographic and thermal effect on the low level wind field and highlights the relation of synoptic systems at 850 hPa level with organised precipitation in this area. The diurnal cycle over the plateau is pronounced, with more vertical uplift in the evening than the morning, in contrast to surrounding areas (Luo and Yanai, 1983). There are regional differences in vertical motion, the depth of the moist layer and precipitation intensity. In particular, there is greater inflow to the eastern part of the plateau and a higher rate of moisture transfer from the lower to the upper troposphere (Luo and Yanai, 1983). Also, it becomes more humid over the eastern side after the monsoon onset compared with the drier western side. A more detailed analysis of the heat and moisture budgets of the Tibetan Plateau is given by Luo and Yanai (1984). Bollasina and Benedict (2004) outlines key physical mechanisms relating to the Tibetan Plateau that require further investigation. The interaction of the mountain-valley circulation on the monsoon flow at large scales can have a significant effect on the feedback mechanisms of convection, heat fluxes and precipitation. There is some disagreement with Boos and Kuang (2010), who believe that the importance of the Tibetan Plateau for thermal forcing of the monsoon is overstated. Instead, they

find that it is the presence of the Himalayas as an insulating orographic barrier that is key, whilst suggesting that the Tibetan Plateau may play a greater role in the East Asian monsoon.

2.5.3 Land-surface effects

The soil moisture can affect the progression and variability of the Indian monsoon, with the presence of surface water speculated to induce a preferential location for precipitation, potentially acting as a positive feedback. This is evident over the Sahel region with respect to the African monsoon and for northern India (Douville et al., 2001; Taylor et al., 2011). Barton et al. (2019) note that deep convection is initiated over regions with sharp wet-dry soil moisture gradients. Soil moisture has also been shown to induce mesoscale atmospheric circulations in the Sahel region (Taylor et al., 2007) and India (Barton et al., 2019). For the rest of India, the more dynamical nature of this monsoon and the competition of surface evaporation with moisture convergence means that the soil moisture feedback is less significant (Douville et al., 2001). Despite the sea surface temperature being a larger driver for the monsoon (Douville, 2002), it has been shown that similar rain patterns evolve when the external forcings (insolation, sea surface temperature) are fixed and the model depends on the internal dynamics (Bollasina and Ming, 2013b). The model used by Bollasina and Ming (2013b) includes a multi-layer soil parameterisation and it shows the migration of the monsoonal rain band to the northwest by surface hydrology processes. Conditions at the surface of the land, such as snow cover, vegetation and amount of soil moisture, are important for determining the contrast of the land temperature to the sea. It has been suggested that vegetation cover can have an impact, by creating heat and moisture gradients (e.g. Hartley et al. (2016)). Park and Hong (2004) found that this did not have a significant affect on the seasonal rainfall but did contribute to the variability of the Indian monsoon.

2.6   Monsoon depressions

Throughout the summer season, cyclonic systems known as monsoon depressions can develop over the Bay of Bengal, near the edge of the monsoon trough. They can also originate over the Arabian Sea, although this is less common. Once formed, monsoon depressions track approximately northwest, to the south of the Himalayas. The outer diameter of a depression is about 2000 km (Boos et al., 2015) and they move with a propagation speed of 6 ms^{-1} (Yoon and Chen, 2005). Monsoon depressions usually last 2–5 days and there are 3–6 monsoon depressions occurring in the average summer (Hunt et al., 2016a). They bring strong winds and heavy precipitation events, accounting for approximately 50% of total rainfall over India (Yoon and Chen, 2005).

Low pressure systems around India are classified according to India Meteorological Department (2016). When located over the sea, the associated wind speed is used. Systems

with wind speeds of less than 8.5 ms^{-1} are lows and systems with speeds over 16.5 ms^{-1} are cyclonic storms, severity increasing with associated wind speeds. The criteria for depressions are associated wind speeds of 8.5–16.5 ms^{-1}. For systems located over land, the pressure deficit is used to classify these systems. If there is one closed isobar in the interval of 2 hPa then it is a low; if there are two closed isobars it is a depression; if there are four or more closed isobars then it is a cyclonic storm. The focus in this section is on depressions.

A small percentage of monsoon depressions have their origin locally in the Bay of Bengal, whilst 85% develop from the re-genesis of lows from around the South China Sea to the east (Chen, 2009). Some of these residual lows can be traced back to tropical cyclones. The west/northwest propagation across north India goes against the mean surface winds, which are predominantly easterly. A recent paper by Hunt and Parker (2016) suggests a simple explanation for this, based on interaction of vortices at low levels (850 hPa). Modelling a depression as a point vortex and the Himalayan barrier as a cylindrical wall, image vortices are invoked behind the barrier so that the point vortex (depression) propagates parallel to the barrier. Also explained is the observed intensification of flow on the Himalayan side of the depression, as there is a contribution to the flow from the image vortex. Higher speed flow leads to increased moisture advection and more intense rainfall events.

Previously, it has been suggested that the direction of propagation is a result of dynamical lifting west of the vortex centre with vortex stretching as it ascends; however, Boos et al. (2015) has shown that the spatial structure is inconsistent with observations. This could be due to quasi-geostrophy being a poor assumption when high Rossby numbers are involved. Instead, Boos et al. (2015) describes nonlinear, horizontal adiabatic advection (beta drift) of potential vorticity maxima as the propagating mechanism. The potential vorticity core is bimodal and located in the mid-troposphere (Hunt et al., 2016a; Hurley and Boos, 2015). The results of Boos et al. (2015) and Hunt and Parker (2016) appear to be complementary. The maximum rainfall and cloud cover is found to the southwest of the centre (Hunt et al., 2016a; Hurley and Boos, 2015; Yoon and Chen, 2005), which is suggested to be a result of cyclonic mixing of warm, moist air from over the sea with the cooler monsoonal flow. Hunt et al. (2016b) have shown that the area of peak rainfall is linked to deep convection to the south of the centre.

During La Niña years, there may be less depressions than in El Niño years but they are associated with higher intensity rainfall events, possibly due to having more moist, vortical cores (Hunt et al., 2016a). Depressions occurring in an active monsoon phase are stronger. They have a lower central pressure, greater vertical temperature gradient and higher moisture levels that result in higher intensity rainfall events (as for La Niña years). Hunt et al. (2016b) have shown that monsoon depressions exhibit diurnal variability in the rainfall cycle, which could have future implications for modelling and forecasting these systems.

2.7   Concluding remarks

There are many physical processes that affect the onset and progression of the Indian monsoon, from global-scale influences such as the El Niño Southern Oscillation, to internal atmospheric dynamics, acting on a range of spatial and temporal scales. Despite an increase in understanding how these processes interact, there are still many aspects that cannot be fully explained. There has been significant development in numerical weather prediction models, improving forecasting of the precipitation duration, intensity and spread, but there remains a gap between model simulations and observations. Research into using an explicit representation of convection, with high horizontal resolution is promising, although the computational cost remains too high for most applications. Thus, parameterisation of convection, land-surface interactions and boundary layer processes will remain a feature of weather models in the foreseeable future. Simplified models are a useful research tool for providing recommendations to improve parameterisation schemes.

Chapter 3

Two-layer model of moisture dynamics

3.1 Introduction

The first part of this thesis focuses on building an idealised model using a moisture budget approach to represent the onset and advance of the Indian monsoon. The model will then be used to test mechanisms of monsoon onset. A successful outcome to this stage would be that the processes of the monsoon advance can be explained in accordance with observations. Currently, advanced models do not reproduce the advance of the monsoon accurately and there is a large amount of uncertainty, particularly regarding convection. The benefits of using an idealised model are that you can explicitly specify the processes and easily modify the form of functions, whilst the model is also computationally cheap and quick to run. Furthermore, there is greater clarity of the physics within the model so that any phenomena occurring can be more readily interpreted.

3.2 Two-layer model

The formulation of the model is based on the advance of the monsoon onset being a balance between low-level, moist, southwesterly monsoonal flow and mid-tropospheric dry flow intruding from the northwest, as described in Parker et al. (2016). The model describes the evolution of moisture over two atmospheric layers in a vertical cross-section along a transect from northwest to southeast India. Figure 3.1 illustrates the approximate location of this transect (dashed line) and the key wind flows contributing to monsoon onset. A schematic of the vertical cross-section along the transect, highlighting the processes described in the model, is shown in Figure 3.2. The x direction is taken along the transect, starting over northwest India ($x = 0$), with increasing x representing travel in a southeasterly direction. The height into the atmosphere is z, which is split into lower (1) and upper (2) layers of the troposphere. The mid-level dry flow (red in Figure 3.1) is in the x direction and the low-level moist flow (blue in Figure 3.1) is going into the page in what would be the y

direction, where two spatial dimensions are included.

The southwesterly flow becomes more dominant as the monsoon onsets, bringing a greater flux of moisture and expediting the progression of the monsoon. Over time, the wedge of dry air is moistened from below, encouraging shallow convection and sustaining conditions for deep convection to occur at the southeastern limit. In the model, a convective flux describes the vertical transport of moisture from the lower to the upper layer, representing the effects of cumulus clouds. Evaporative fluxes at the surface increase after onset, providing a greater source of moisture to aid the formation of shallow cumulus and congestus clouds. These help to moisten the wedge of dry air, eroding it from the southeast so that the dry intrusion gradually recedes, advancing the northwest progression of the monsoon (Parker et al., 2016; Menon et al., 2018). This process becomes increasingly efficient, possibly aided by a positive feedback of convective rainfall. With the retreat of the dry flow, more pockets of deep convection can form.
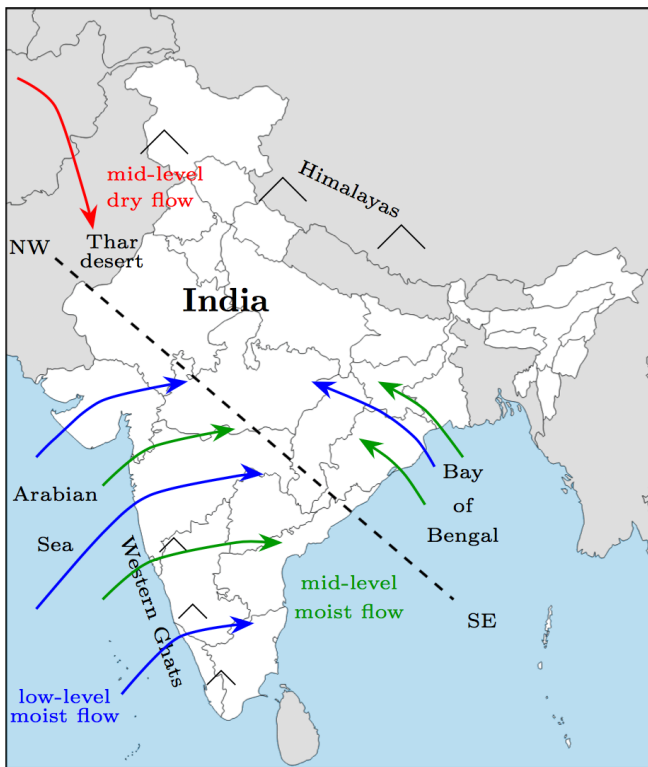
Figure 3.1: *Schematic showing wind flows and some of the topographical features over India. The dashed line shows the northwest–southeast transect which the vertical section is taken along.*

In terms of modelling, the moisture content of the upper tropospheric layer will be investigated, given a moisture profile in the lower tropospheric layer and a moisture flux function between the layers. Solutions for steady and dynamic states will be evaluated and related to the advance of the monsoon. Different moisture profiles and forms of the vertical moisture flux will be analysed and the sensitivity of certain variables tested. By comparing the results to observations, a realistic form for the moisture flux and moisture

profile of the lower layer can be determined, leading to recommendations for weather model improvements.
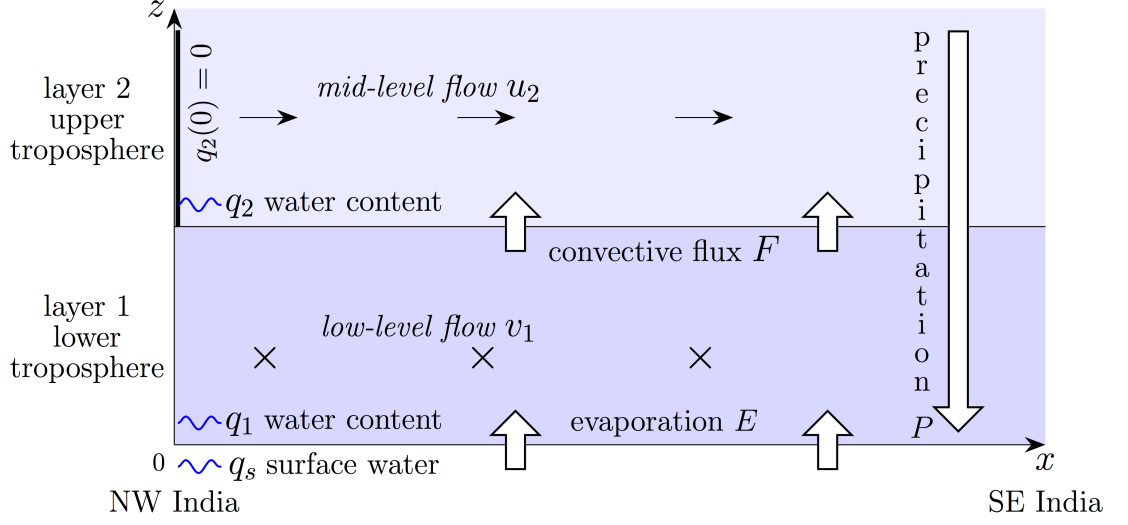
Figure 3.2: *Simplified layer model of the vertical section of the NW-SE transect.*

3.2.1 Equations of motion

The full two-layer moisture model is described by the system of equations 3.1a–3.1c:

$$\frac{\partial q_2}{\partial t} + \mathbf{u_2} \cdot \nabla q_2 = +F - P, \tag{3.1a}$$

$$\frac{\partial q_1}{\partial t} + \mathbf{u_1} \cdot \nabla q_1 = -F + E, \tag{3.1b}$$

$$\frac{\partial q_s}{\partial t} = +P - E + S. \tag{3.1c}$$

A summary of the parameters used in Figure 3.2 and the equations above are:

- $\mathbf{u_i} = (u_i, v_i)$ is the horizontal flow in layer i.

- $q_i(x, t)$ is the column integrated moisture content in layer i and $q_s(x, t)$ is the surface water.

- $F(q_1, q_2)$ is the net vertical flux of water vapour from layer 1 to layer 2.

- P and E are precipitation and evaporation terms respectively.

- S represents surface forcing such as river inflow or outflow.

where the flow is in ms^{-1}, column integrated moisture content is in kg m^{-2} and the flux, precipitation, evaporation and forcing terms are in kg m^{-2} s^{-1}. Each of F, P, E and S will need to be specified or parameterised, possibly in terms of q_1, q_2 and/or q_s. It is assumed that there are no variations across each layer, meaning the equations are depth-averaged. The column integrated moisture contents q_1 & q_2 should be divided by the respective layer

heights to give the concentration (or mixing ratio), but as it is assumed the layer heights are equal, then these are interchangeable.

At the surface, the change in moisture content over time is equal to precipitation adding moisture and evaporation taking moisture away from the lower layer, plus a term to account for additional sources of moisture such as inflow from rivers and outflow to the sea. If the surface forcing term S is zero, then the total moisture content $(q_s + q_1 + q_2)$ is conserved. The lower tropospheric layer equation consists of the time evolution of the moisture content plus an advection term on the left, with a flux and evaporative term on the right. The flux, driven by convection, is negative because moisture is moving down a gradient from the moist lower layer to the drier upper layer. Moisture is being evaporated from the surface and rising to the lower layer, giving a positive term. The form of the upper tropospheric layer is similar, but with the convective flux positive as it represents moisture moving into the upper layer. Moisture condenses into clouds which eventually leads to rainfall, wetting the surface which completes the cycle. Precipitation is restricted to occur only in the upper layer, so there is no shallow rainfall.

3.2.2   Vertical moisture flux

The flux of water vapour F from the lower layer (1) to the upper layer (2), due to convection, must be parameterised in terms of q_1 and q_2 alone. Here, the fluxes due to updrafts (linked with cloud formation) and the compensating subsidence and downdrafts (for mass continuity), need to be accounted for. The exact form of this flux function is unknown because it depends upon the highly complex process of turbulent moist convection. When $q_1 = q_2$, these two processes cannot lead to any net moisture flux, and so $F = 0$. Otherwise, there will be a down-gradient flux, i.e., $F > 0$ when $q_1 > q_2$ and $F < 0$ when $q_2 > q_1$, although the strength of this flux will depend upon q_1 and q_2 in a nontrivial way. Thus, the relatively simple parameterisation is proposed:

$$F = \frac{1}{T_c}(q_1 - q_2)\Phi(q_1, q_2) \begin{cases} \text{where} \qquad \Phi(q_1, q_2) = 1 & \text{(3.2a)} \\[2mm] \text{or} \qquad \Phi(q_1, q_2) = \frac{1}{2}\left(1 + \tanh\left(\frac{q_1 + q_2 - \psi_c}{\Delta q_c}\right)\right) & \text{(3.2b)} \end{cases}$$

where T_c is the timescale for convective adjustment, and $\Phi(q_1, q_2)$ is a positive non-dimensional function representing cloud activity after Yanai et al. (1973), who imply that shallower cumulus clouds are required to supply moisture in order to facilitate the growth of deep, precipitating cumulus clouds. For much of this study, the simple option of $\Phi = 1$ (Equation 3.2a) is selected, implying that convection is always active (and producing a deep moisture flux) whenever $q_1 > q_2$. However, for part of this study a more realistic form (Equation 3.2b) is used, where Δq_c is a width parameter, controlling the steepness of the tanh curve, which determines how rapidly deep convection onsets, and ψ_c is a critical moisture threshold for initiation of deep convection. Here, Φ remains zero when the total column moisture is below a critical threshold, and increases monotonically with total column moisture thereafter, consistent with observations as described in Neelin

et al. (2009) (particularly Figures 1 and 2). Similarly, Holloway and Neelin (2009) notes a sharp increase in precipitation after a particular critical value of total column moisture is reached.
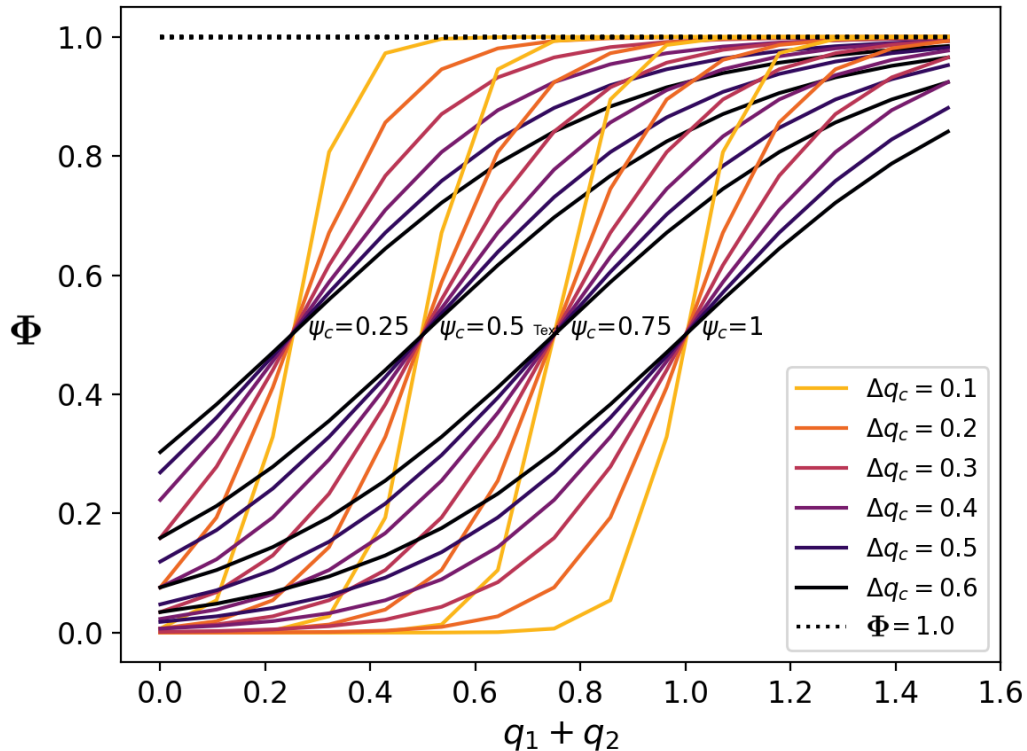
Figure 3.3: *Line plot showing $K(q_1+q_2)$ ($\equiv$ flux F), against total moisture q_1+q_2 for varying width parameter Δq_c and varying ψ_c, which represents the initiation of deep convection via a critical moisture threshold.*

The observed relationship between precipitation and total column water vapour is well documented (e.g. Neelin et al. (2009); Muller et al. (2009); Holloway and Neelin (2009, 2010); Schiro and Neelin (2019)). The importance of lower tropospheric humidity in convective onset is emphasised by Schiro and Neelin (2019). The form of the parameterisation for the convective flux is comparable to Neelin et al. (2009) and Muller et al. (2009), where a two-layer model is used to examine the relationship between precipitation and total column moisture. They parameterise precipitation, P, in terms of the sum of the moisture content over lower and upper layers in the troposphere, with a trigger based on a critical threshold of moisture (q_c) in the lower layer: $P = (q_2 + q_1) H (q_1 - q_c)$. H is the Heaviside function. This form of parameterisation, linked to total column moisture, can be taken as a basis for the form of the convective flux presented in this chapter, where the total column moisture is used as a proxy for precipitation. The correlation of the convective flux and the sum and difference of lower and upper layer moisture content is examined further with a numerical weather prediction model in Chapter 7, specifically Section 7.6.

The choice of Equation 3.2b for Φ is comparable to the profiles in Figure 1 of Neelin

et al. (2009) which shows the relationship of precipitable water against column water
vapour for the eastern Pacific ocean. The forms of the convective flux parameterisation
are shown in Figure 3.3. The parameters Δq_c and ψ_c can be varied: taking Δq_c close to
zero gives a near vertical profile, whilst taking a value closer to one gives a more horizontal
profile and ψ_c moves the plot along the x-axis. A steeper vertical profile (smaller Δq_c)
means a more sudden switch-on of convection, thus increasing the upper layer moisture
at a faster rate, and contributing to a more rapid monsoon onset. This is seen as more
realistic in terms of the real-world monsoon. A lower ψ_c indicates that a lower threshold
of total column moisture is required for convection to switch on, i.e. the environment
is more favourable for (deep) convection. For particular choices of ψ_c and Δq_c so that
$\Phi(q_1, q_2) \approx 1$, the flux of 3.2a can be retrieved from 3.2b.

3.2.3   Wind field

In the lower layer the horizontal wind field, $\mathbf{u}_1 = (u_1, v_1)$, representing the winds along and
perpendicular to the transect, is predominantly determined by the low-level southwesterly
wind, associated with the arrival of the monsoon. This means the main contributor to
advection in the lower layer is approximately perpendicular to the transect (y-direction),
so $\mathbf{u}_1 \approx v_1$. In the upper layer, the prevailing winds are strong northwesterlies, linked with
the dry intrusion. These are in the x-direction, along the transect, giving $\mathbf{u}_2 = (u_2, v_2) \approx$
u_2. Higher level winds, at around 200 hPa, are not incorporated into the model. The
horizontal wind field is allowed to vary with direction, but not time, so that $v_1 = v_1(y)$
and $u_2 = u_2(x)$.

3.2.4   Lateral boundary condition

A boundary condition of dry inflow is imposed for the upper layer at the northwestern
limit, so that $q_2 = 0$ at $x = 0$. This is justified as the moisture content at small x in
the upper layer is very low. The northwesterly winds at mid-levels in northwest India
are predominantly dry because they pass over the Thar desert, which receives very little
rainfall, even during the monsoon. At the northwestern limit of the domain, the air remains
sufficiently dry throughout the monsoon period that the lateral condition is considered
appropriate. A boundary condition is not required for high x, as downstream there is only
advection acting.

3.2.5   Precipitation

The precipitation is removed from the upper layer and added to the surface. This could
be assumed to be an instantaneous process, or else occurring over some timescale of the
order of minutes–hours. The trigger for a precipitation event would be based on a criti-
cal threshold of total column moisture being reached, which has a basis in observations
(Muller et al., 2009; Holloway and Neelin, 2009, 2010). A more complex implementation
could incorporate stability criteria and relation to boundary-layer water vapour. Here the

precipitation has been confined to the upper layer, as separate treatment of rainfall resulting from shallow processes would over-complicate the model and make interpretation more difficult.

The addition of precipitation, without explicitly considering temperature and other thermodynamic properties, has been implemented by Kent et al. (2017), who modifies the rotating shallow water equations. Switches for convection and precipitation are based on critical heights of the fluid layer, indicating positive buoyancy and representative of conditional instability. The rain produced in the model also requires positive wind convergence. The methods used by Kent et al. (2017) for modifying an idealised model to incorporate precipitation process are relevant in the context of the two-layer moisture model described above.

3.2.6 Evaporation

The evaporation term in the two-layer model would be determined by many factors in the real world, including surface temperature, wind speed and shear, soil moisture and vegetation. A simple way of specifying the evaporation in the two-layer model is as a fraction of the precipitation, which could be multiplied by an index in the range 0–1, representing the aridity of the land (e.g. Bowen ratio). There are large areas of irrigated crops in central and northwest India, which may influence patterns of convection and rainfall locally. A more complex parameterisation would be $E = (1 - \sigma) \Theta_s E_p$, where σ is an index for the amount of vegetation, Θ_s is the contribution from soil moisture and E_p is the potential evaporation (Stensrud, 2009). The latter is a measure of the evaporation that could occur given a sufficient source of moisture, for a particular land type and amount of vegetation. It is typically calculated from the Penman–Monteith equations. In the two-layer model, the soil moisture term would need to account for the precipitation (from the upper layer). It is worth noting that soil moisture has short-term and long-term memory, with the surface soil moisture typically retaining a small fraction (10–15%) of precipitation after several days (McColl et al., 2017).

3.2.7 Surface forcing

The surface forcing term accounts for any additional surface mechanisms that bring or remove moisture into the domain from hydrological processes, for example, from river inflow or outflow or surface run-off. There are several major rivers in India, including the Indus, Ganges and Brahmaputra. Each of these is associated with a river drainage basin, which extend over significant areas in northern and central India. Additional sources of surface run-off could be from snow or glacier melting in the Himalayas, or from reservoirs letting water.

3.3   Reduced two-layer model

Substantial insight into the fundamental dynamics of monsoon onset can be gained by focusing on the key processes of low-level moist inflow, upper layer advection and convection. In order to achieve this, the following simplifications are adopted from the full two-layer model:

- Neglect precipitation and evaporation.

- Assume no surface interaction, so q_s and S are not needed.

- Spatially 1D model, with dependencies in x direction only.

- The upper level flow in the x direction, u_2, is prescribed and constant.

- The lower level flow in the y direction, v_1, has no effect in the equations, so $d/dy = 0$.

Thus, the set of three equations (3.1a–3.1c) becomes a coupled set of two equations (3.3a–3.3b), representing a reduced model of moisture dynamics with lower and upper layers that evolve in time.

$$\frac{\partial q_2}{\partial t} + u_2 \frac{\partial q_2}{\partial x} = +F, \tag{3.3a}$$

$$\frac{\partial q_1}{\partial t} \qquad\qquad = -F. \tag{3.3b}$$

However, without inflow, the lower layer moisture (q_1) would be gradually depleted by the convective flux (F). To account for the lower layer moisture being continually refreshed by lateral inflow, evaporation and other forcings, an extra term is added to the lower layer equation, giving:

$$\frac{\partial q_2}{\partial t} + u_2 \frac{\partial q_2}{\partial x} = +F, \tag{3.4a}$$

$$\frac{\partial q_1}{\partial t} \qquad\qquad = -F - \frac{1}{T_\mathrm{m}}(q_1 - q_\mathrm{e}). \tag{3.4b}$$

The $\frac{1}{T_\mathrm{m}}(q_1, q_\mathrm{e})$ term represents a relaxation on a timescale T_m, towards a prescribed lower layer profile $q_\mathrm{e}(x)$, where $q_\mathrm{e}(x)$ is interpreted as a state of equilibrium in the absence of convection. The initial condition for the lower layer moisture (q_1) is dependent on $q_\mathrm{e}(x)$ and is one of the aspects to be investigated further. For example, different multiples of the lower layer profile q_e could be taken to correspond to an initial lower layer profile that is drier, wetter or the same as the background state.

3.3.1   Timescales

The resulting behaviour of the reduced two-layer model is highly dependent upon the assumed timescales T_m and T_c for moisture replenishment and mixing due to convection. However, it is not clear how these timescales should be chosen. For example, assuming that the lifetime of these processes is approximately determined by the efficiency of mixing due

to convection, a single convective cloud might last about an hour, a cluster of convective clouds has a lifetime of several hours, and dry intrusions and storms can persist for several days. Shorter events such as convective updrafts/downdrafts have a high mixing efficiency, whereas longer events with numerous elements such as a multi-cell cluster have a lower mixing efficiency, as there is renewed influxes of moisture over a greater area. The timescale for water vapour to become vertically mixed in the clean-air environment surrounding convection is of the order of days, compared to the convective-scale vertical transport of moisture in clouds taking minutes to an hour (Tompkins and Craig, 1998). Hence, acknowledging that the real timescale for adjustment of moisture may range from the convective timescale to the timescale of large-scale flow, the two-layer model is used to explore a range of values:

$$1/2 \quad \leq \quad T_{\mathrm{c}} \quad \leq 7 \text{ days.} \tag{3.5}$$

There is similar uncertainty in setting T_{m}. In the absence of convection, the assumed lower layer profile q_{e} is replenished by evaporation from a saturated surface. For shallow standing water, evaporation is estimated to occur on a timescale of hours, whereas for moist vegetated layers the timescale would be longer, i.e. several days. Again in the absence of convection, changes to the strength or humidity of the inflow from the Arabian Sea might adjust q_{e} on a timescale of days to a week. Thus, the range for the timescale of replenishment is taken as:

$$1/2 \quad \leq \quad T_{\mathrm{m}} \quad \leq 7 \text{ days.} \tag{3.6}$$

The moisture gain in the upper layer is determined by the rate of convection T_{c}, relative to dry advection. More moisture is transported to the upper layer if the rate of convection is high, given that the rate of moisture inflow to the lower layer T_{m} is sufficiently large. The variation of the rate of convection or replenishment, in connection with strength of the dry intrusion, yields complex dynamical behaviour. However, we highlight the uncertainty in these assumed ranges of T_{c} and T_{m}, and part of our motivation is to understand the sensitivity linked to these assumptions. Chapter 7 aims to quantify the values of these timescales in a numerical weather prediction model.

3.3.2   Low-level moisture inflow

Here, the mathematical basis of the parameterisation of the lower layer inflow is presented. The importance of the lower layer moisture content in relation to the total moisture content across layers and the onset of convection has already been mentioned (e.g. Holloway and Neelin (2009, 2010); Schiro and Neelin (2019)). The term describing lower layer relaxation on a timescale T_{m}, towards a prescribed lower layer profile $q_{\mathrm{e}}(x)$ (a state of non-convective equilibrium), represents lower layer inflow. This is primarily an incoming moisture flux associated with the transverse (southwesterly) wind (v_1). It is impossible to formulate this precisely for an (x, z) transect of infinitesimal width, for which incoming

and outgoing moisture fluxes would be identical. Instead, a transverse domain of finite width is considered, over the range $-L < y < +L$, where L is a length.

The lower layer equation (3.4b), which incorporates the down-gradient flux (Equation 3.2a) described in Subsection 3.2.2 with $\Phi = 1$, can be written in two-dimensional terms where $q_1 = q_1(x, y, t)$ and $q_2 = q_2(x, y, t)$:

$$\frac{\partial q_1}{\partial t} + v_1 \frac{\partial q_1}{\partial y} = -\frac{1}{T_c} (q_1 - q_2). \tag{3.7}$$

The transverse (southwesterly) wind is positive, so $v_1 > 0$, and is assumed to be constant. Note that the along transect flow, $u_1 \partial q_1 / \partial x$, could be included if desired. At $y = -L$, there is a prescribed moisture inflow (Equation 3.8), but the outflow at $y = +L$ is unknown.

$$q_1 (x, y = -L, t) = q_{1_{in}} (x, t). \tag{3.8}$$

To make an effective description of Equations 3.7 and 3.8, a transverse average can be defined for an arbitrary quantity, $a(x, y, t)$:

$$\bar{a}(x, t) = \frac{1}{2L} \int_{-L}^{+L} a(x, y, t) \, dy. \tag{3.9}$$

Applying this averaging operator to Equation 3.7, and substituting Equation 3.8 for the inflow term, gives:

$$\frac{\partial \bar{q}_1}{\partial t} = -\frac{v_1}{2L} \Big[q_1 \Big]_{-L}^{+L} - \frac{1}{T_c} (\bar{q}_1 - \bar{q}_2),$$

$$= -\frac{v_1}{2L} \Big(q_1(x, y = +L, t) - q_1(x, y = -L, t) \Big) - \frac{1}{T_c} (\bar{q}_1 - \bar{q}_2),$$

$$= -\frac{v_1}{2L} \Big(q_1(x, y = +L, t) - q_{1_{in}} \Big) - \frac{1}{T_c} (\bar{q}_1 - \bar{q}_2). \tag{3.10}$$

Note that the outflow (at $y = +L$) is still unknown. This sort of indeterminacy is normal for averaged equations, and the system must be resolved (or closed) by some sort of approximation. If convection is active, q_1 will be depleted from $q_{1_{in}}(x, t)$ as the domain is moved across. For a sufficiently narrow domain, it is supposed that this depletion can be modelled linearly. Thus, given some q_{10} and q_{12}, the approximation is made that:

$$q_1(x, y, t) \approx q_{10}(x, t) + y q_{11}(x, t). \tag{3.11}$$

The terms q_{10} and q_{12} can be rewritten with $\bar{q}_1$ and $q_{1_{in}}$. On applying the averaging operator in Equation 3.9, it is found that $\bar{q}_1 \approx q_{10}$, as the $+y q_{11}(x, t)$ term is odd in terms of powers of y, meaning that it disappears under averaging. Knowledge of q_{10} and the value of $q_1(x, y, t)$ at $y = -L$ can help to determine q_{11}. Using the inflow condition in Equation 3.8:

$$q_1(x, y = -L, t) = q_{1_{in}}(x, t) \approx q_{10}(x, t) - L q_{11}(x, t),$$

$$\approx \bar{q}_1(x, t) - L q_{11}(x, t),$$

$$\Rightarrow q_{11} \approx \frac{\bar{q}_1 - q_{1_{in}}}{L}.$$

Substituting the expressions for q_{10} and q_{11} into Equation 3.11 gives a linear approximation of the moisture in the lower layer:

$$q_1(x, y, t) \approx \bar{q}_1 + \frac{y}{L} \left(\bar{q}_1 - q_{1_{\text{in}}} \right).$$ (3.12)

Now the outflow, at $y = +L$, can be determined:

$$q_1 \left(x, y = +L, t \right) = 2\bar{q}_1 \left(x, t \right) - q_{1_{\text{in}}} \left(x, t \right).$$ (3.13)

Using the inflow and outflow equations (3.8, 3.13) in the transverse averaged equation (3.10):

$$
\begin{aligned}
\frac{\partial \bar{q}_1}{\partial t} &= -\frac{1}{T_{\text{c}}} \left(\bar{q}_1 - \bar{q}_2 \right) - \frac{v_1}{2L} \left(2\bar{q}_1 - q_{1_{\text{in}}} - q_{1_{\text{in}}} \right), \\
&= -\frac{1}{T_{\text{c}}} \left(\bar{q}_1 - \bar{q}_2 \right) - \frac{1}{L/v_1} \left(\bar{q}_1 - q_{1_{\text{in}}} \right).
\end{aligned}
$$ (3.14)

Equation 3.14 is equivalent to Equation 3.4b (with $\Phi = 1$) where:

- The quantities $q_1(x, t)$, $q_2(x, t)$ along a transect line have been replaced with $\bar{q}_1(x, t)$, $\bar{q}_2(x, t)$ which have been averaged over a finite width strip in the transverse direction.

- The replenishment timescale is the length of half the width of the transverse strip divided by the low-level wind speed, so $T_{\text{m}} = L/v_1$.

- The prescribed non-convective equilibrium is the inflow condition, meaning that $q_{\text{e}} = q_{1_{\text{in}}}$.

This gives a clear mathematical basis for interpreting the linear relaxation term, $- \left(q_1 - q_{\text{e}} \right) / T_{\text{m}}$, in terms of a prescribed moist inflow.

3.3.3   Choice of relaxation profile q_{e}

The quantity $q_{\text{e}}(x)$ now represents an equilibrium state of the lower layer, in the absence of convection. Changing q_{e} will alter the equilibrium humidity, effectively increasing or decreasing the depth of the lower layer. We prescribe q_{e} as a function of x:

$$q_{\text{e}}(x) = 1,$$ (3.15a)

$$q_{\text{e}}(x) = 1 - e^{-x/L_{\text{e}}}.$$ (3.15b)

where L_{e} represents the length-scale of the monsoon system in non-convective equilibrium. Profiles of q_{e} against x are shown in Figure 3.4 for several L_{e} values. The form of q_{e} incorporates the dryness present in northwest India ($q_{\text{e}}(0) = 0$) and the greater availability of moisture in the southeast ($q_{\text{e}}(1) = 1$). Taking a smaller value of L_{e} emphasises the transition from dry (intrusion) to wet (monsoon) as we move from northwest to southeast India, and thus we will use $L_{\text{e}} = 1000$ km for our experiments.
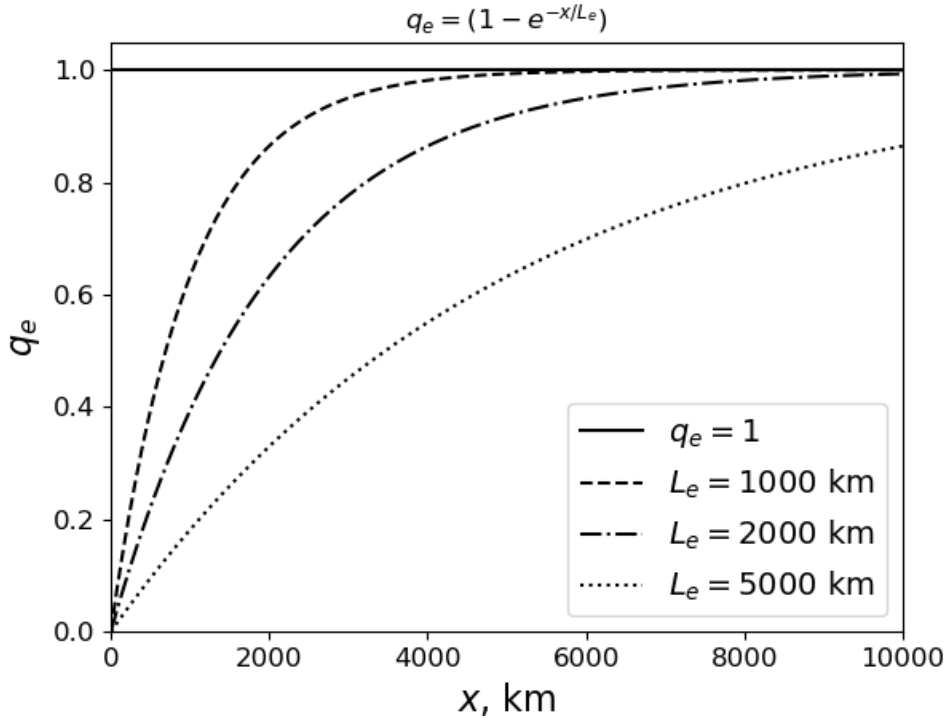
Figure 3.4: *Profile of equilibrium state $q_e(x)$ for the lower layer q_1 in the absence of convection. Cases $q_e = 1$, $q_e = 1 - e^{-x/L_e}$, shown with $L_e = 1000$, 2000, & 5000 km.*

3.4   Concluding remarks

A two-layer moisture model based on mass conservation has been developed, incorporating surface processes, horizontal advection, and explicit treatment of evaporation and precipitation. There are open questions on how to parameterise the terms that cannot be represented explicitly. For example, it is not clear what form the convective flux should take. Here, a simple down-gradient flux is considered, as well as a more complex function that incorporates a tanh-style profile of the total water vapour. There is a basis for parameterising the convective flux in terms of total column moisture, e.g. Neelin et al. (2009); Muller et al. (2009), with emphasis on the role of lower layer moisture. Representing convection as a function of the large-scale environment is very difficult, and remains a major challenge for numerical weather prediction models.

A reduced version of the two-layer model has also been presented, focusing on the key processes of low-level moist inflow, upper layer advection and convection, neglecting precipitation and explicit surface terms. The model is expected to reproduce a monsoon onset that propagates to the northwest, against a prescribed wind in the upper layer. Once the reduced two-layer model has been tested and the interaction between the three key processes has been understood, the model can be modified to include other processes involved in the onset and progression of the Indian monsoon. It is important to understand how a few processes act within the confines of the model and in terms of the implications for the real-world monsoon, before introducing additional complexity.

Chapter 4

Fixed lower layer model

4.1 Introduction

In this chapter, the simplest possible version of the reduced two-layer model is considered, by fixing the lower layer in time. This allows a focus entirely on the upper layer, with competing processes of advection and convection. Moisture is transported from a fixed moist lower layer to the upper layer, via the convective flux. Simultaneously, an imposed northwesterly flow in the upper layer acts to advect dry air into the domain in the northwest, and moist air out of the domain in the southeast. Specifically, the case where the upper layer begins as completely dry, is considered. The lower layer is held at constant relative humidity. Moistening of the upper layer is initiated by the switch-on of convection (at $t = 0$), which continues to act for all $t > 0$. The sudden switch-on of convection can correspond, for example, to a change in surface from arid desert to moist vegetation, or from a change in topography, where convection is triggered by orographic forcing.

In terms of the real-world monsoon, the interaction between the dry intrusion and convective activity has been shown to have an effect on the progression of onset. Over periods of several days, the dry intrusion can weaken, acting to enable convection, which in turn allows the monsoon onset to progress to the northwest. The reverse is also true, where a strengthening dry intrusion suppresses convection and slows or halts the progression of the onset. The dynamic interplay between the upper level advection and convection is illustrated by the onset which progresses in a non-steady nature, moving in more active "bursts" or stalling for several days at a time (Volonté et al., 2019).

Using the fixed lower layer model, the final equilibrium, a balance between advection and convection, will be examined. The sensitivity of the final equilibrium to the form of the parameterised convective flux will be assessed. Furthermore, several different profiles for the prescribed lower layer moisture and the assumed spatial dependence, are investigated. Given that a monsoon onset, likened to a moisture front, can be identified, the speed of the propagation will be derived. The time taken for the upper layer to adjust to an equilibrium state will be considered in terms of the real-world monsoon onset, which takes about six weeks to propagate from southeast to northwest India.

Starting from the reduced two-layer model in the previous chapter (Section 3.3, Equations 3.4a–3.4b), it is assumed that T_m is zero, meaning instantaneous relaxation such that $q_1 = q_e$ and the flux $F(q_1, q_2) = F(q_e, q_2)$. Note that within this section q_1 is used interchangeably with q_e, as a dynamic lower layer is not incorporated into the model at this stage. The coupled equations are reduced to a single equation for the upper layer. This is solved as an initial value problem with $q_2 = 0$ at $t = 0$, i.e. on an initially dry upper layer. At the northwestern boundary ($x = 0$), the model is subject to an inflow of dry air ($q_2 = 0$). The equations, where F represents the parameterisation of the convection flux, become:

$$\frac{\partial q_2}{\partial t} + u_2 \frac{\partial q_2}{\partial x} = F, \quad q_2(x = 0, t) = 0, \quad q_2(x, t = 0) = 0, \quad \text{on} \quad 0 < x < x_{\max}. \quad (4.1)$$

In the following Section (4.2), a non-dimensionalisation of Equation 4.1 is introduced. The options for the parameterisation of the convective flux, F, are discussed. This leads to a system with a single nondimensional parameter, which is convenient for the remaining analysis. Analytical solutions can be derived for the steady-state (Section 4.3) and time-evolving solutions (Section 4.4), for various choices of lower layer profiles and convective fluxes. A numerical scheme is also derived for the time-evolving solutions, which can be validated against the analytical solutions (Section 4.5). Going forward, the system will be too complex to be easily solved analytically, thus a numerical scheme will be required. Further analysis, including determination of onset speeds, is presented in Sections 4.6 and 4.7. The sensitivity of the system to variation of the non-dimensional parameters is assessed in the context of the derived onset speeds.

4.2   Non-dimensionalised system

Equation 4.1 will be non-dimensionalised before further analysis, using a length scale L (so $\hat{x} = x/L$), a timescale T (so $\hat{t} = t/T$) and a moisture scale q_{ref} typical of q_1 (so $\hat{q}_2 = q_2/q_{\text{ref}}$, $\hat{q}_1 = q_1/q_{\text{ref}}$). L is chosen as the length of the transect over India, equal to $x_{\max}$. Note that the form of the convective flux (presented in Subsection 4.2.1) involves a convective timescale T_c and depends on a combination of the lower (q_1) and upper layer (q_2) moisture, so that $F = F(1/T_c, q_1, q_2)$.

4.2.1   Vertical moisture flux

Due to the simplicity of the fixed lower layer model, the choice of flux function is more restricted than the options presented in Section 3.2.2. The down-gradient flux (Equation 3.2a with $\Phi = 1$) is maintained from Chapter 3 - as per Equation 4.2a, but an even simpler flux based on the lower layer moisture is also considered (Equation 4.2b). Mathematically, the simpler flux allows analytical solutions to be readily determined. In terms of the real-world monsoon, the importance of lower tropospheric humidity in determining the total column moisture has already been noted (Muller et al., 2009; Holloway and Neelin,

2009, 2010). More relevantly for this section, the lower tropospheric humidity has also been shown to play a role in convective onset (Schiro and Neelin, 2019). The two non-dimensional fluxes to be considered are defined as:

$$F = \gamma q_1, \tag{4.2a}$$

$$F = \gamma(q_1 - q_2). \tag{4.2b}$$

Equation 4.2a is the simplest possible choice. The upwards flux is determined solely by the water content below. This might apply when the upper layer is sufficiently dry, so the downward transport of upper level dry air, required by the conservation of mass, has no signature in F. Equation 4.2b takes account of the downward transport of upper level moist air, required by the conservation of mass, when q_2 is not small. This gives a classic down-gradient flux. The former is referred to as the "simple" flux and the latter the "down-gradient" flux.

4.2.2 Non-dimensionalised equations

Non-dimensionalising Equation 4.1 with the scalings at the beginning of the Section (4.2) gives:

$$\frac{\partial \hat{q}_2}{\partial \hat{t}} + \frac{T u_2}{L} \frac{\partial \hat{q}_2}{\partial \hat{x}} = \frac{T}{T_c} \left(\frac{F T_c}{q_{\text{ref}}} \right) = \hat{F} \qquad \text{for} \quad 0 < \hat{x} < 1,$$

where $\hat{F} = (TFT_c)/(T_c q_{\text{ref}})$ is a non-dimensional flux. The timescale T is chosen as the advective timescale L/u_2. Taking x_{max} (and therefore L) as 3000 km and u_2 as 5 ms^{-1}, $T = 3000\,000$ m $\div$ 5 ms^{-1} = 6×10^5 s, which is approximately 7 days. The non-dimensional flux incorporates a non-dimensional parameter, γ (see Subsection 4.2.1), which is derived from the convective timescale T_c. The system is now defined in terms of this single parameter, where γ is defined as per Equation 4.3:

$$\gamma = \frac{T}{T_c} = \frac{L}{T_c u_2}. \tag{4.3}$$

From Section 3.3.1, it is expected that T_c is in the range 1/2–7 days, giving a range for γ: 1–14. Dropping the hats for convenience, the system becomes:

$$\frac{\partial q_2}{\partial t} + \frac{\partial q_2}{\partial x} = F, \quad q_2(x = 0, t) = 0, \quad q_2(x, t = 0) = 0, \quad \text{on} \quad 0 < x < 1. \tag{4.4}$$

The fixed lower layer model is now defined in terms of the upper layer moisture $q_2(x, t)$ and a convective flux F which incorporates the non-dimensional parameter γ, as defined in Equation 4.2a or Equation 4.2b. It can now be seen that the switch-on in convection at $t = 0$ is really a switch-on in γ at $t = 0$. Since $\gamma = L/(T_c u_2)$, this can either be viewed as moving from $T_c = \infty$ (i.e., infinite timescale for convection to act, meaning no convection) to finite T_c (with u_2 held fixed and finite), or from $u_2 = \infty$ (i.e., very strong upper level flow) to finite u_2 (with T_c held fixed and finite). The parameter γ essentially measures the efficiency of convection relative to advection, with $\gamma = 0$ corresponding to advection

dominating over convection. The initial situation with $\gamma = 0$ is where convection is ineffective relative to upper-level advection. As the system moves to a new scenario where $\gamma \neq 0$, the convection becomes effective at moistening the upper layer.

4.2.3 Profiles for the fixed lower layer

The non-dimensionalised fixed lower layer system (Equation 4.5) is solved for the two flux options, and for low-level profiles of the form $q_1 = a + bx$. Specifically, choices of 1, x and $1 + x$ for the low-level profile are investigated.

   The lower layer choice of $q_1 = 1$ represents a system in equilibrium, with a constant influx of humid air coming from over the ocean. The lower layer profile $q_1 = x$ is reflecting the increase in moisture content from northwest to southeast India. $q_1 = 1 + x$ is similar, but accounting for the possible presence of some low-level moisture at low x, towards northwest India.

4.3 Analytical steady-state solutions

Equation 4.4 is solved first in the steady-state limit, which turns out to be a key component of the time-dependent solution. Setting $\partial/\partial t = 0$ in Equation 4.4 gives:

$$\frac{dq_2}{dx} = F, \qquad q_2(x = 0) = 0. \tag{4.5}$$

The term on the left represents the change in moisture content in the upper layer, advected by the flow, and the term on the right is the moisture flux between lower and upper layers. This is a clear balance between advection and forcing. There is an evident dependency of q_2 on the flow u_2, via γ; a decrease in γ (which could be from an increase in u_2) means that the convective flux F becomes smaller, so q_2 reduces. Since q_2 is expected to be increasing upwards from zero, this corresponds to greater advection of the upper layer moisture, so q_2 is shifted in the positive x direction. Similarly, an increase in γ (which could be as a result of a reduction in u_2) leads to less advection and q_2 moves in the negative x direction. Where analytic solutions have been calculated, the behaviour of q_2 as u_2 approaches the extreme limits of zero and infinity will investigated. Note that although the changes in γ are generally interpreted here in terms of upper layer advection, u_2, they could equivalently be interpreted in terms of the convective timescale, T_c. The non-dimensional parameter γ can be regarded as either a switch-on of convection ($\gamma \propto 1/T_c \propto F$), or a reduction in upper layer advection (as $\gamma \propto 1/u_2$).

   Equation 4.5 is solved for the two fluxes and for low-level profiles of $q_1 = a + bx$, with cases numbered as indicted in Table 4.1. Case 1 refers to the simple flux, case 2 the down-gradient flux, and the letters a, b, c, refer to three options for the lower layer profile. The lower layer choice of $q_1 = 1$ represents a system in equilibrium, with a constant influx of humid air coming from over the ocean. The lower layer profile $q_1 = x$ is reflecting the increase in moisture content from northwest to southeast India. $q_1 = 1 + x$ is similar,

but accounting for the possible presence of some low-level moisture at low x, towards northwest India.

Table 4.1: *Labelling of flux cases for results.*

Flux	Lower layer $q_1 =$		
	1	x	$1 + x$
$F = \gamma q_1$	case 1a	case 1b	case 1c
$F = \gamma(q_1 - q_2)$	case 2a	case 2b	case 2c

4.3.1 Cases 1a–1c: simple flux

The flux choice $F = \gamma q_1$ is computed with prescribed water content profiles of 1, x and $1+x$ for the lower layer. Analytical solutions for these three cases are given below, applying the boundary condition to determine the constant of integration.

Case 1a: $F = \gamma q_1, \; q_1 = 1$

$$\frac{dq_2}{dx} = \gamma \quad \Rightarrow \quad q_2 = \gamma x. \tag{4.6}$$

Case 1b: $F = \gamma q_1, \; q_1 = x$

$$\frac{dq_2}{dx} = \gamma x \quad \Rightarrow \quad q_2 = \frac{\gamma x^2}{2}. \tag{4.7}$$

Case 1c: $F = \gamma q_1, \; q_1 = 1 + x$

$$\frac{dq_2}{dx} = \gamma(1 + x) \; \Rightarrow \; q_2 = \gamma \left(x + \frac{x^2}{2} \right). \tag{4.8}$$

The physical consistency of the solutions can be checked by inspection. First, if advection vanishes so $u_2 \to 0$ (i.e. $\gamma \to \infty$), then q_2 should grow without bound - and, indeed, $q_2 \propto \gamma$ as expected. Second, if advection becomes strong (i.e. $\gamma \to 0$), then q_2 should be continually transported out of the domain and thus $q_2 \to 0$ - and, indeed, $q_2 \propto \gamma$.

4.3.2 Cases 2a–2c: down-gradient flux

The second flux case $F = \gamma(q_1 - q_2)$ is now computed with the prescribed water content profiles for the lower layer. The standard Taylor expansion: $e^x = 1 + x + \frac{1}{2!}x^2 + \cdots + \frac{1}{n!}x^n + \ldots$ will be used in some of the calculations.

Case 2a: $F = \gamma(q_1 - q_2), \; q_1 = 1$

$$\frac{dq_2}{dx} = \gamma(1 - q_2) \quad \Rightarrow \quad \frac{d}{dx}(q_2 e^{\gamma x}) = \gamma e^{\gamma x} \quad \Rightarrow \quad q_2 = 1 - e^{-\gamma x}. \tag{4.9}$$

As $\gamma \to 0$ (i.e. $u_2 \to \infty$), $q_2 \to 1 - \left(1 - \gamma x + O(\gamma^2) \right) \to 0$.

Case 2b: $F = \gamma(q_1 - q_2), \ q_1 = x$

$$\frac{dq_2}{dx} = \gamma(x - q_2) \quad \Rightarrow \quad \frac{d}{dx}\left(q_2 e^{\gamma x}\right) = \gamma x e^{\gamma x} \Rightarrow \quad q_2 e^{\gamma x} = \gamma \left[\frac{x e^{\gamma x}}{\gamma} - \int \frac{e^{\gamma x}}{\gamma} \, dx\right]$$

$$\Rightarrow \quad q_2 = x - \frac{1}{\gamma} + \frac{e^{-\gamma x}}{\gamma}. \tag{4.10}$$

As $\gamma \to 0$ (i.e. $u_2 \to \infty$), $q_2 \to x - \dfrac{1}{\gamma} + \dfrac{1}{\gamma}\left(1 - \gamma x + \dfrac{\gamma^2 x^2}{2} + O(\gamma^3)\right) \to 0.$

Case 2c: $F = \gamma(q_1 - q_2), \ q_1 = 1 + x$

$$\frac{dq_2}{dx} = \gamma(1 + x - q_2) \quad \Rightarrow \quad q_2 = 1 + x - \frac{1}{\gamma} + \left(\frac{1}{\gamma} - 1\right)e^{-\gamma x}. \tag{4.11}$$

As $\gamma \to 0$ (i.e. $u_2 \to \infty$), $q_2 \to 1 + x - \dfrac{1}{\gamma} + \left(\dfrac{1}{\gamma} - 1\right)\left(1 - \gamma x + \dfrac{\gamma^2 x^2}{2} + O(\gamma^3)\right),$

$$= 1 + x - \frac{1}{\gamma} + \frac{1}{\gamma} - x + \frac{\gamma^2 x^2}{2} - 1 + \gamma x - \frac{\gamma^2 x^2}{2} + O(\gamma^3),$$

$$\to 0.$$

Again, checking the physical consistency of the solutions, it can be seen by inspection that as the flow becomes very small (i.e. $\gamma \to \infty$), the upper layer moisture q_2 tends towards the prescribed lower layer moisture q_1. On the other hand, if the flow becomes very large (i.e. $\gamma \to 0$), it can be shown by expanding the exponential term as a Taylor series that $q_2 \propto \gamma$. Here the advection term dominates so that moisture in the upper layer is being transported downstream faster than it is being replenished, leading to a drying of the upper layer $(q_2 \to 0)$.
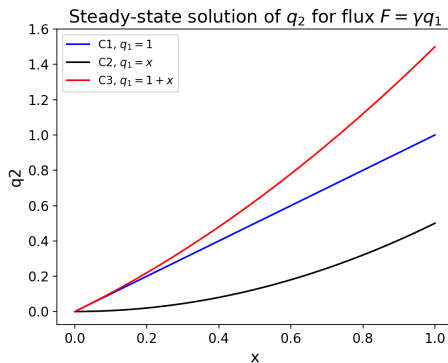
(a) *Cases 1a–1c:* $F = \gamma q_1$
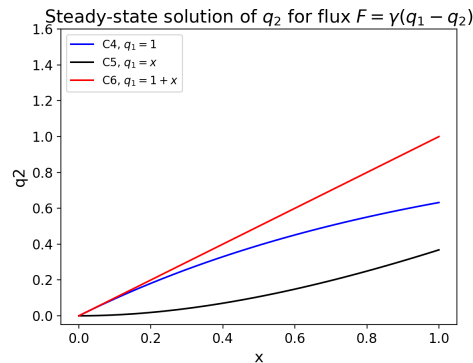
(b) *Cases 2a–2c:* $F = \gamma(q_1 - q_2)$

Figure 4.1: *Steady state solution at $\gamma = 1$: q_2 against x for simple $(F = \gamma q_1)$ and down-gradient $(F = \gamma(q_1 - q_2))$ flux cases with a prescribed lower layer profile of $q_1 = 1$ (blue), $q_1 = x$ (black) or $q_1 = 1 + x$ (red).*

4.3.3 Analysis

Figure 4.1 shows the plots of q_2 against x for the two flux cases with prescribed lower layer profiles of $q_1 = 1$, $q_1 = x$ and $q_1 = 1 + x$ shown in the colours blue, black and red respectively. These plots have been produced from the analytical solutions.

Considering cases 1a–1c with the simple flux (Figure 4.1a), case 1c gives the highest values of upper level moisture q_2, followed by case 1a and finally case 1b. From the analytical solutions it can be seen that $q_2 \propto x$ for case 1a and $q_2 \propto x^2$ for case 1b, which is reflected in the plot. Case 1a represents a stable system with constant moisture influx from the lower layer being offset by horizontal transport in the upper layer due to the flow u_2. Case 1b has a low moisture content in lower layer at low x (i.e. northwest India), which is reflected in the upper layer moisture q_2. At higher x (i.e. southeast India), q_1 is higher, representing the increase in humidity from the land to the sea. Case 1c is a combination of the first cases.

Looking at Figure 4.1b, the highest values of q_2 are given for case 2c, followed by cases 2a and 2b. Here no cases give a linear profile for q_2, as the form of the down-gradient flux leads to an exponential term in the solution for q_2. Cases 2b and 2c are similar in shape to cases 1b and 1c, but containing less moisture in the upper layer, which is also true for case 2a. This can be explained by the form of the flux: rather than a constant moisture input, the flux is governed by the difference in moisture content between the layers. The shape of the plot for case 2a is more concave than the others, which could be representative of the dry northwesterly air encountering the moist low level flow from the ocean (the Somali Jet) and experiencing a more rapid uptake of moisture which is advected towards higher x.

Case 2a is particularly interesting since there is no spatial structure in the forcing (as $q_1 = 1$), but a natural length-scale emerges in the solution ($q_2 = 1 - e^{-\gamma x}$). In dimensional terms:

$$1 - e^{-\gamma \hat{x}} = 1 - e^{-\hat{x}L/(u_2 T_c)} = 1 - e^{-x/L_{\mathrm{mon}}},$$

where $\mathrm{L_{mon}} = u_2 T_c.$ (4.12)

So the solution transitions from dry ($q_2 = 0$ at $x = 0$) to wet ($q_2 = 1$) over the monsoon length-scale L_{mon}. This turns out to be a simple balanace between advection and the rate of moisture transport from below (convection). Increasing advection means increasing monsoon length-scale L_{mon}, and thus decreasing upper layer moisture q_2, as expected. Increasing the strength of convection (i.e. by a smaller convective timescale T_c), means a smaller monsoon length-scale L_{mon}, and thus increasing upper layer moisture q_2, as expected.

In terms of the experiment of switching on convection (or equivalently, reducing u_2 from infinity), the monsoon length-scale L_{mon} describes how close the moisture front (which represents monsoon onset) can travel relative to the dry inflow in northwest India. If upper layer wind speeds of $u_2 = 5$–10 ms^{-1} and a convective timescale T_c in the range

1/2–7 days are considered, the monsoon length-scale L_{mon} can be calculated, giving 200–6000 km. This clearly covers a range of length-scales of relevance for monsoon dynamics. Specifically, with $u_2 = 5$ ms^{-1} and $T_{\mathrm{c}} = 7$ days, $L_{\mathrm{mon}} = 3000$ km, which is approximately the length of a transect running from northwest to southeast India.

4.4 Analytical time-evolving solutions

The unsteady-state problem is now considered, where monsoon onset is modelled for an initial configuration with no upper level moisture ($q_2 = 0$ at $t = 0$). Thus, Equation 4.4 is solved, with the boundary and initial conditions as derived at the beginning of the chapter (repeated here for convenience).

$$\frac{\partial q_2}{\partial t} + \frac{\partial q_2}{\partial x} = F, \quad q_2(x = 0, t) = 0, \quad q_2(x, t = 0) = 0, \quad \text{on} \quad 0 < x < 1. \tag{4.4}$$

Table 4.1 (repeated): *Labelling of flux cases for results.*

	Lower layer $q_1 =$		
Flux	1	x	$1 + x$
$F = \gamma q_1$	case 1a	case 1b	case 1c
$F = \gamma(q_1 - q_2)$	case 2a	case 2b	case 2c

The cases 1a–2c as used in the steady-state formulation, shown in Table 4.1 and repeated above, are now used in the solution of the time-evolving system. Remarkably, this system can be solved analytically. Firstly, the analytical solution for cases 1a,b,c with the simple flux is derived. Secondly, for cases 2a,b,c with the down-gradient flux, the analytical theory from the steady-state solutions for the simple flux needs to be extended. To do this, the q_2 solution is written as the sum of its steady and dynamic (time-evolving) parts:

$$q_2(x, t) = q_{2s}(x) + q_{2d}(x, t). \tag{4.13}$$

Hence, Equation 4.4 can be split:

$$\frac{\partial q_{2s}}{\partial t} + \frac{\partial q_{2s}}{\partial x} + \frac{\partial q_{2d}}{\partial t} + \frac{\partial q_{2d}}{\partial x} = \gamma q_1.$$

The first term on the left is zero as the steady state solution q_{2s} is time independent by definition. The second term from the left cancels with the right hand side; by the steady state equation in section 4.3 these terms are equal. This leaves a first order linear homogeneous partial differential equation with solution $q_{2d} = A(x - t)$, where A is an arbitrary function. Thus:

$$q_2(x, t) = q_{2s}(x) + A(x - t). \tag{4.14}$$

To determine A, the initial condition $q_2(x,0) = 0$ is used, which makes $q_{2s}(x) + A(x) = 0 \Rightarrow A = -q_{2s}$, so that:

$$q_2(x,t) = q_{2s}(x) - q_{2s}(x-t). \tag{4.15}$$

Here $q_{2s}(x)$ is a steady-state solution that is zero for $x < 0$. To make this explicit, $q_{2s}(x)$ is rewritten as $q_{2s}(x)H(x)$, where H is the Heaviside step function, so that Equation 4.15 becomes Equation 4.16. So the lateral boundary condition $q_2(0,t) = 0$ is satisfied for all $t > 0$, since $q_{2s}(x=0, t=0) = 0$.

$$q_2(x,t) = q_{2s}(x)H(x) - q_{2s}(x-t)H(x-t) = \begin{cases} q_{2s}(x), & \text{for } 0 < x < t, \\ q_{2s}(x) - q_{2s}(x-t), & \text{for } x > t. \end{cases} \tag{4.16}$$

The calculation for cases 2a,b,c, with the down-gradient flux, is slightly more complicated. Equation 4.4 is multiplied by an integrating factor $e^{\gamma x}$ and then rewritten:

$$\frac{\partial q_2}{\partial t} + \frac{\partial q_2}{\partial x} + \gamma q_2 = \gamma q_1 \quad \Rightarrow \quad \frac{\partial}{\partial t}(q_2 e^{\gamma x}) + \frac{\partial}{\partial x}(q_2 e^{\gamma x}) = \gamma q_1 e^{\gamma x}.$$

Now let $\tilde{q}_2 = q_2 e^{\gamma x}$ and $\tilde{q}_1 = q_1 e^{\gamma x}$, so that:

$$\frac{\partial \tilde{q}_2}{\partial t} + \frac{\partial \tilde{q}_2}{\partial x} = \gamma \tilde{q}_1. \tag{4.17}$$

Thus, the solutions for the time-evolving case with the down-gradient flux can now be determined in a similar way to the simple flux, using the conversion $q_2 = \tilde{q}_2 e^{-\gamma x}$ at the final stage. Explicitly:

$$\tilde{q}_{2s}(x) = \int_0^x \gamma \tilde{q}_1(\chi)\, d\chi = \gamma \int_0^x e^{\gamma \chi} q_1(\chi)\, d\chi. \tag{4.18}$$

Now Equation 4.16, after multiplication by $e^{-\gamma x}$, becomes:

$$q_2(x,t) = \gamma e^{-\gamma x} \times \begin{cases} \int_0^x e^{\gamma \chi} q_1(\chi)\, d\chi, & \text{for } x < t, \\ \int_{x-t}^x e^{\gamma \chi} q_1(\chi)\, d\chi, & \text{for } x > t. \end{cases} \tag{4.19}$$

4.4.1 Cases 1a–1c: simple flux

The analytical solutions are derived for the time-evolving equations for the flux $F = \gamma q_1$ with prescribed profiles of $q_1 = 1, q_1 = x$ and $q_1 = 1 + x$.

Case 1a: $F = \gamma q_1, \ q_1 = 1$

$$q_2(x,t) = \gamma x H(x) - \gamma(x-t)H(x-t) = \begin{cases} \gamma x, & \text{for } 0 < x < t, \\ \gamma t, & \text{for } x > t. \end{cases} \tag{4.20}$$

Case 1b: $F = \gamma q_1, \ q_1 = x$

$$
q_2(x,t) = \frac{\gamma x^2}{2} H(x) - \frac{\gamma}{2}(x-t)^2 H(x-t) \ = \ \begin{cases} \dfrac{\gamma x^2}{2}, & \text{for } \ 0 < x < t, \\[4mm] \gamma x t - \dfrac{\gamma t^2}{2}, & \text{for } \ x > t. \end{cases} \tag{4.21}
$$

Case 1c: $F = \gamma q_1, \ q_1 = 1 + x$

$$
q_2(x,t) = \gamma x \left(1 + \frac{x}{2}\right) H(x) - \gamma(x-t) \left(\frac{(x-t)^2}{2}\right) H(x-t),
$$

$$
= \begin{cases} \gamma x \left(1 + \dfrac{x}{2}\right), & \text{for } 0 < x < t, \\[4mm] \gamma t \left(1 + x - \dfrac{t}{2}\right), & \text{for } x > t. \end{cases} \tag{4.22}
$$

4.4.2   Cases 2a–2c: down-gradient flux

Similarly to the previous section, analytical solutions are calculated for the three prescribed q_1 profiles, but for the flux $F = \gamma(q_1 - q_2)$. The steady state formulation is solved for $\tilde{q}_1$ and $\tilde{q}_2$, where the boundary condition $(\tilde{q}_2(0) = 0)$ is applied. This solution is used in Equation 4.16, which is converted to an expression in terms of q_2 to give the final solution.

Case 2a: $F = \gamma(q_1 - q_2), \ q_1 = 1$

$$
\frac{d\tilde{q}_{2s}}{dx} = \gamma e^{\gamma x} \ \Rightarrow \ \tilde{q}_{2s} = e^{\gamma x} - 1,
$$

$$
\tilde{q}_2 = (e^{\gamma x} - 1) H(x) - \left(e^{\gamma(x-t)} - 1\right) H(x-t),
$$

$$
q_2(x,t) = \left(1 - e^{-\gamma x}\right) H(x) - \left(e^{-\gamma t} - e^{-\gamma x}\right) H(x-t) \ = \ \begin{cases} 1 - e^{-\gamma x}, & \text{for } \ 0 < x < t, \\[3mm] 1 - e^{-\gamma t}, & \text{for } \ x > t. \end{cases}
$$

$$\tag{4.23}$$

Case 2b: $F = \gamma(q_1 - q_2), \ q_1 = x$

$$
\frac{d\tilde{q}_{2s}}{dx} = \gamma x e^{\gamma x} \ \Rightarrow \ \tilde{q}_{2s} = x e^{\gamma x} - \frac{e^{\gamma x}}{\gamma} + \frac{1}{\gamma},
$$

$$
\tilde{q}_2 = \left(x e^{\gamma x} - \frac{e^{\gamma x}}{\gamma} + \frac{1}{\gamma}\right) H(x) - \left((x-t)e^{\gamma(x-t)} - \frac{e^{\gamma(x-t)}}{\gamma} + \frac{1}{\gamma}\right) H(x-t),
$$

$$
q_2(x,t) = \left(x - \frac{1}{\gamma} + \frac{e^{-\gamma x}}{\gamma}\right) H(x) - \left((x-t)e^{-\gamma t} - \frac{e^{-\gamma t}}{\gamma} + \frac{e^{-\gamma x}}{\gamma}\right) H(x-t),
$$

$$
= \begin{cases} x - \dfrac{1}{\gamma} + \dfrac{e^{-\gamma x}}{\gamma}, & \text{for } \quad 0 < x < t, \\[4mm] x - \dfrac{1}{\gamma} + \dfrac{e^{-\gamma t}}{\gamma} - (x-t)e^{-\gamma t}, & \text{for } \quad x > t. \end{cases} \tag{4.24}
$$

Case 2c: $F = \gamma(q_1 - q_2), \; q_1 = 1 + x$

Using the principle of superposition :

$$
q_2(x,t) \;=\; \begin{cases} 1 + x - \dfrac{1}{\gamma} + \left(\dfrac{1}{\gamma} - 1\right) e^{-\gamma x}, & \text{for} \quad 0 < x < t, \\[4mm] 1 + x - \dfrac{1}{\gamma} + \left(\dfrac{1}{\gamma} - 1 - x + t\right) e^{-\gamma t}, & \text{for} \quad x > t. \end{cases} \tag{4.25}
$$
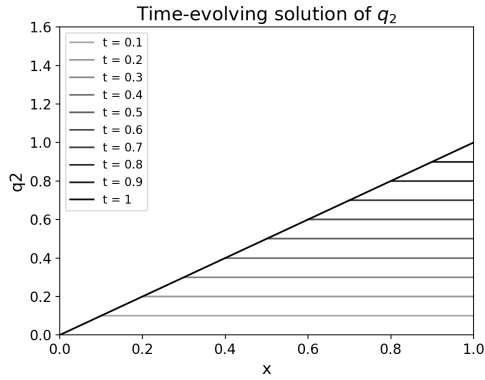
(a) *Case 1a:* $F = \gamma q_1, q_1 = 1$
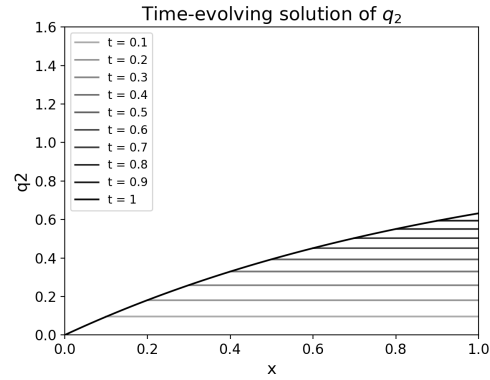
(b) *Case 2a:* $F = \gamma(q_1 - q_2), q_1 = 1$
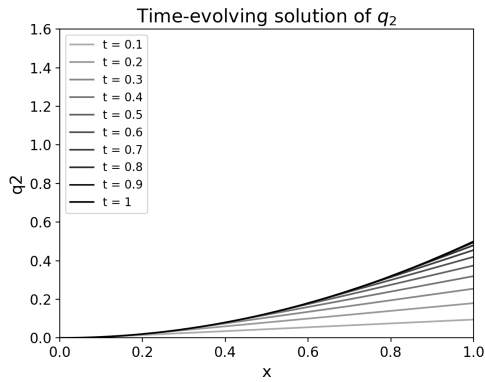
(c) *Case 1b:* $F = \gamma q_1, q_1 = x$
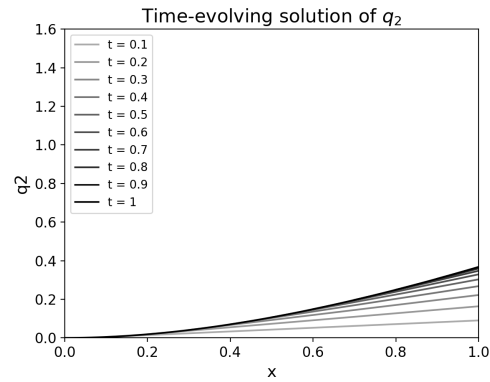
(d) *Case 2b:* $F = \gamma(q_1 - q_2), q_1 = x$
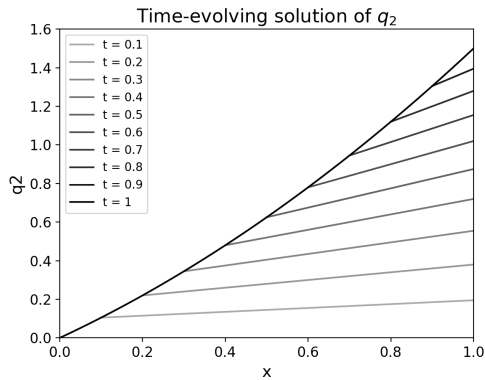
(e) *Case 1c:* $F = \gamma q_1, q_1 = 1 + x$
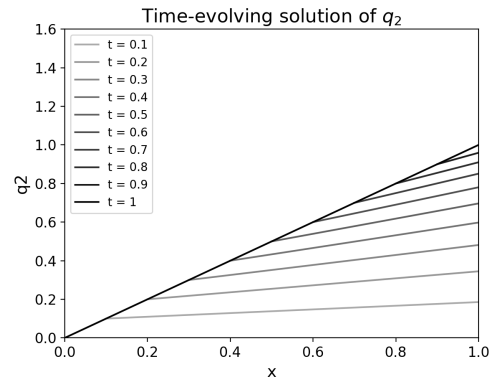
(f) *Case 2c:* $F = \gamma(q_1 - q_2), q_1 = 1 + x$

Figure 4.2: *Time-evolving solution at $\gamma = 1$: q_2 against x for cases 1a–2c. Increasing gradient from light grey to black represents forward time-stepping. Units are non-dimensional.*

4.4.3   Analysis

The two flux cases are computed with three different prescribed water content profiles for the lower layer, $q_1(x) = 1$, $q_1(x) = x$ and $q_1(x) = 1 + x$. Figure 4.2 shows the plots of q_2 against x for each case, with increasing time shown by the darkening gradient. These plots have been generated using the analytical solutions.

For each case, as time progresses, the solution for q_2 tends towards the steady-state solution (Figure 4.1). This is a linear relation in case 1a. Note that for all flux cases the time taken to reach steady-state on $0 < x < 1$ is 1 (non-dimensional units), or $T \sim 7$ days for this choice of timescale. As in the steady-state formulation, the simple flux cases (1a, 1b, 1c) lead to higher values of q_2, compared with the down-gradient flux cases (2a, 2b, 2c). Where the lower layer profile is prescribed as a constant, the upper layer moisture q_2 increases at a constant rate for each time-step. For the other prescribed profiles $q_1 = x$ and $q_1 = 1 + x$, q_2 increases proportionally to x and $1 + x$ respectively.

In dimensional terms, the time taken to reach steady-state (1 in nondimensional units) is L/u_2 in dimensional units. Taking $L = 10\,000$ km and $u_2 = 5$ ms^{-1}, this gives a time of approximately 23 days. This is roughly consistent with the timescale of monsoon onset, which takes approximately 6 weeks to transition from first onset to full monsoon, although the model adjusts slightly faster and requires a longer length-scale to be comparable to the real-world system.

4.5   Numerical solutions

Although the fixed lower layer system can be solved analytically for all cases, solutions from a numerical solver, coded in Python, are also determined. As the model complexity increases, for instance incorporating a dynamic lower layer, the system may not be solvable analytically and the numerical solver will be essential. Thus, it is appropriate to test the numerical code at a stage where it can be verified against the analytical solutions.

A fourth order Runge-Kutta scheme is used to solve Equation 4.4 numerically for the upper level moisture content q_2, with the given boundary condition. The spatial derivative is approximated using a centered finite difference method with uniform grid spacing. Initially, a fourth order accurate differential matrix was used but this led to errors, possibly due to the non-smooth solutions. Hence, a second order accurate differential matrix is applied. The number of grid-points used to represent the domain $0 < x < 1$ is 128 and the code is run for 100 time-steps with step size $\Delta t = 0.01$ (i.e. over $0 < t < 1$).

It can be seen from the analytical expressions and plots (for example, Figure 4.2a) that although the solutions are continuous, the first derivative $\partial q_2/\partial x$ can discontinuous, as can higher order derivatives. If the general case of $q_1 = x^n$ is considered, where $n \in \mathbb{N}$ for the simple flux $F = \gamma q_1$, the solutions for q_2, the first derivative in x, q_{2_x}, and the

second derivative in x, $q_{2_{xx}}$, are:

$$q_2(x,t) = \begin{cases} \dfrac{\gamma x^{n+1}}{n+1}, & \text{for } 0 < x < t, \\[2ex] \dfrac{\gamma}{n+1}\left(x^{n+1} - (x-t)^{n+1}\right), & \text{for } x > t. \end{cases} \tag{4.26}$$

$$q_{2_x}(x,t) = \begin{cases} \gamma x^n, & \text{for } 0 < x < t, \\[2ex] \gamma x^n - \gamma(x-t)^n, & \text{for } x > t. \end{cases} \tag{4.27}$$

$$q_{2_{xx}}(x,t) = \begin{cases} n\gamma x^{n-1}, & \text{for } 0 < x < t, \\[2ex] n\gamma x^{n-1} - n\gamma(x-t)^{n-1}, & \text{for } x > t. \end{cases} \tag{4.28}$$

Table 4.2: *Summary of continuity of the first and second derivatives in x of q_2 for each of the test cases.*

	Case 1a	Case 1b	Case 1c	Case 2a	Case 2b	Case 2c
q_{2_x}	discont.	continuous	discont.	discont.	continuous	discont.
$q_{2_{xx}}$	continuous	discont.	discont.	discont.	discont.	discont.

Because of the discontinuities associated with the spatial derivatives, high-order finite difference schemes are unlikely to be useful. Thus, a second order finite difference scheme is deemed sufficient, in conjunction with a standard high-order (fourth-order) Runge-Kutte scheme for time-stepping.

4.5.1 Error testing

Here, the accuracy of the Python code is tested, computing the error between analytical and numerical solutions. This is a test for the code, giving confidence in the numerical scheme for when the model complexity progresses and analytical solutions cannot be found. Note that the analytical solutions are discontinuous in x, so it is advisable to investigate convergence in grid spacing (h).

The error $E(t)$ is defined as per Equation 4.29. Given that the spatial derivatives are of second order accuracy and the time derivatives are of fourth order accuracy, the error E can be written as a function of these (Equation 4.30).

$$E(t) = \max |q_{2_{\text{num}}} - q_{2_{\text{exact}}}|. \tag{4.29}$$

$$E = O(h^2) + O(\Delta t^4). \tag{4.30}$$
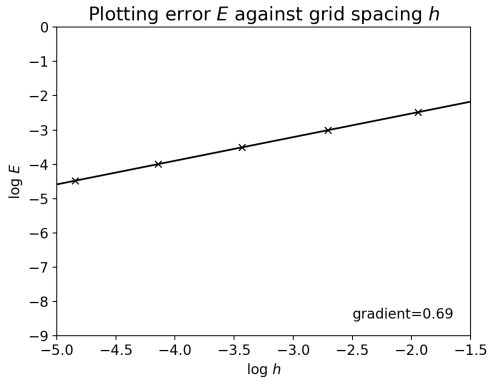
(a) *Case 1a: $F = \gamma q_1, q_1 = 1$.*
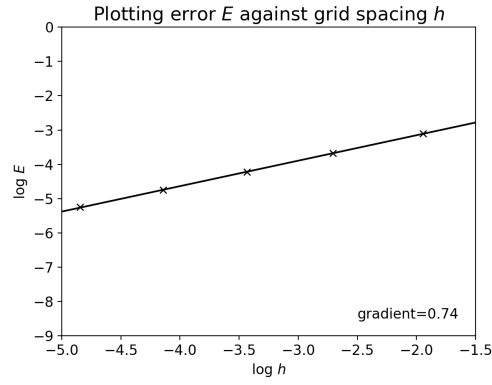
(b) *Case 2a: $F = \gamma(q_1 - q_2), q_1 = 1$.*
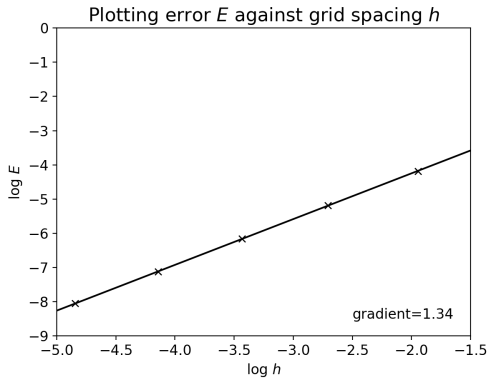
(c) *Case 1b: $F = \gamma q_1, q_1 = x$.*
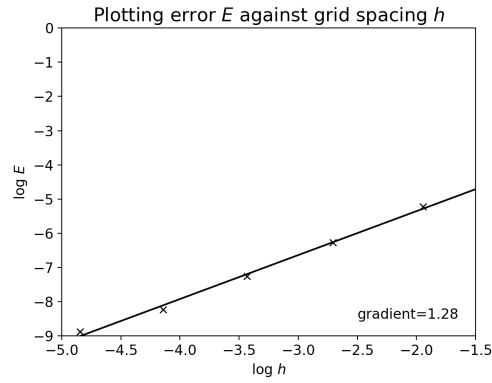
(d) *Case 2b: $F = \gamma(q_1 - q_2), q_1 = x$.*
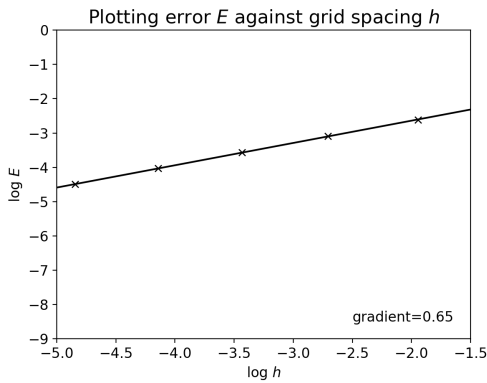
(e) *Case 1c: $F = \gamma q_1, q_1 = 1 + x$.*
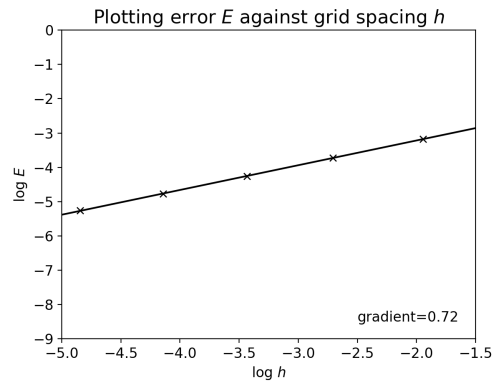
(f) *Case 2c: $F = \gamma(q_1 - q_2), q_1 = 1 + x$.*

Figure 4.3: *Plotting the grid spacing h against the error $E(t)$ for an increasing number of grid points in x (8, 16, 32, 64, 128).*

To isolate the effect of the grid spacing (h) error, the size of the time-step (Δt) is taken as 10^{-5} and the number of steps is correspondingly increased to $100\,000$. Plotting $\log h$ against $\log E$ for several different grid sizes would give a line with a gradient of 2 for a sufficiently smooth underlying solution. Note that for Figure 4.3, E refers to $\max{(E(t))}$ over the run $0 < t < 1$. Looking at Figure 4.3, the discrepancies in cases 1b and 2b are smaller, presumably due to the continuous first derivative and discontinuous second derivative. Likely because of the discontinuity of the first derivative for the other cases, the convergence rate is slower than expected, at around 0.7 compared with 2.

Both the first and second x derivatives of q_2 are continuous when $n \geq 2$. This means that if a lower layer profile of $q_1 = x^2$ is taken, there is much better agreement between analytical and numerical methods when solving for q_2 over time, achieving the desired gradient of 2. Similarly, if $q_1 = x^4$ is taken with a fourth order accuracy differential matrix for the first derivative, the gradient is 4, as expected. Runs with higher orders of x for the lower layer profile have been tested to confirm this, although the figures are not presented here. Thus, it is concluded that the discrepancies in cases 1a, 1c, 2a and 2c are due to discontinuities in the first derivative.

4.6   Analytical derivation of onset speeds

From Parker et al. (2016) and India Meteorological Department (2016), the average speed at which the onset advances over most of India is about 1.6 ms^{-1}. The analytical solutions are used to probe how the speed depends on γ. The onset speed is denoted by v. The critical threshold value of q_2 for monsoon onset is denoted q_c, meaning that when $q_2 \geq q_c$, the monsoon onsets in the model.

As $t \to \infty$, q_2 tends towards the steady-state solution. Thus, $q_2 = q_c$ can only be solved for $x > x_c$, where x_c is the critical distance associated with q_c, characterising the change in regime from time-varying to steady-state. Provided $x > x_c$, monsoon onset by can defined by setting $q_2(x, t) = q_c$. To do this, the expression for $q_2(x, t)$ is used for $x > t$, since monsoon onsets for large x where q_2 is largest. The first time that the onset front appears is when $x = 1$, where the speed is greatest. When $x = x_c$, the onset front has its minimum speed and is last seen at this point. t_1 and t_{xc} are denoted as the first and last times respectively. The exceptions are cases 1a and 2a, where onset occurs instantaneously across the domain when q_2 reaches the threshold value q_c.

The process to determine minimum, maximum and average speeds of the propagation of the onset front is summarised below, followed by the analytical expressions for each distinct case. The method is as follows:

1. Find x_c by substituting $q_2 = q_c$ and $x = x_c$ into the steady state solution (Subsection 4.3, Equations 4.6–4.11) then rearranging.

2. From the time-dependent solution (Subsection 4.4, Equations 4.20–4.25), substitute $q_2 = q_c$ and then rearrange for t in term of x and x_c, using the first result.

3. Differentiate with respect to time to find an expression for the onset speed, $v(x, t)$, where $v \equiv dx/dt$. Note that a positive speed is taken as travelling from right ($x = 1$) to left ($x = 0$).

4. The minimum speed of propagation occurs when $x = x_c$, at time t_{xc}, which can be determined from the expression in stage 2.

5. The maximum speed of propagation occurs when $x = 1$, at time t_1, which can be determined from the expression in stage 2.

6. The average speed of propagation is found from $\Delta x/\Delta t$, where $\Delta x = 1 - x_c$ and $\Delta t = t_{xc} - t_1$.

Note that the results of the method will be numbered in accordance with each stage, so that 1. refers to the value of x_c, 2. refers to the value of t, and so on.

4.6.1   Cases 1a–1c: simple flux $F = \gamma q_1$

Case 1a: $F = \gamma q_1, \; q_1 = 1$

1. $x_c = q_c/\gamma$.

2. $t = q_c/\gamma = x_c$.

3. $v = 0$.

Onset occurs for all $x > x_c$ instantaneously, so there is no front propagation.

Case 1b: $F = \gamma q_1, \; q_1 = x$

1. $x_c = \sqrt{(2q_c)/\gamma}$.

2. $t^2 - 2xt + x_c^2 = 0 \;\Rightarrow\; t = x - \sqrt{x^2 - x_c^2}$.

3. $\dfrac{dt}{dx} = 1 - \dfrac{x}{\sqrt{x^2 - x_c^2}} \;\Rightarrow\; v = \dfrac{\sqrt{x^2 - x_c^2}}{\sqrt{x^2 - x_c^2} - x}$.

4. $v_{\min} = 0$.

5. $v_{\max} = \dfrac{\sqrt{1 - x_c^2}}{1 - \sqrt{1 - x_c^2}}$.

6. $v_{\mathrm{av}} = \dfrac{1 - x_c}{x_c - 1 + \sqrt{1 - x_c^2}}$.

The negative root for t is taken, as $x \to \infty \Rightarrow t \to 0$. The minimum and maximum speeds occur at time $t_{xc} = x_c$ and $t_1 = 1 - \sqrt{1 - x_c^2}$ respectively.

Case 1c: $F = \gamma q_1, \; q_1 = 1 + x$

1. $x_c^2 + 2x_c - (2q_c)\gamma = 0 \;\Rightarrow\; x_c = -1 + \sqrt{1 + 2q_c/\gamma}$.

2. $t^2 - 2(1+x)t + x_c\,(2 + x_c) \;\Rightarrow\; t = (1 + x) - \sqrt{(1+x)^2 - x_c(2 + x_c)}$.

3. $\dfrac{dt}{dx} = 1 - \dfrac{1 + x}{\sqrt{x^2 - x_c^2 + 2(x - x_c) + 1}} \;\Rightarrow\; v = \dfrac{\sqrt{x^2 - x_c^2 + 2(x - x_c) + 1}}{-1 - x + \sqrt{x^2 - x_c^2 + 2(x - x_c) + 1}}$.

4. $v_{\min} = \dfrac{1}{x_c}$.

5. $v_{\max} = \dfrac{\sqrt{4 - 2x_c - x_c^2}}{2 - \sqrt{4 - 2x_c - x_c^2}}$.

6. $v_{\mathrm{av}} = \dfrac{1 - x_c}{x_c - 2 + \sqrt{4 - 2x_c - x_c^2}}$.

Here, the positive root for x_c is taken, as key point of interest is the onset at locations $x_c > 0$. The negative root is for t taken, as $x \to \infty \Rightarrow t \to 0$. The minimum and maximum speeds occur at time $t_{xc} = x_c$ and $t_1 = 2 - \sqrt{4 - x_c(2 + x_c)}$ respectively.

4.6.2   Cases 2a–2c: down-gradient flux, $F = \gamma(q_1 - q_2)$

Case 2a: $F = \gamma(q_1 - q_2), \ q_1 = 1$

1. $x_c = -\ln(1 - q_c)/\gamma$.

2. $t = -\ln(1 - q_c)/\gamma = x_c$.

3. $v = 0$.

Onset occurs for all $x > x_c$ instantaneously, so there is no front propagation.

Case 2b: $F = \gamma(q_1 - q_2), \ q_1 = x$

1. $q_c = x_c - \dfrac{1}{\gamma} + \dfrac{e^{-\gamma x_c}}{\gamma}$.

2. $q_c = x - \dfrac{1}{\gamma} + \dfrac{e^{-\gamma t}}{\gamma} - (x - t)e^{-\gamma t} \ \Rightarrow \ x = \dfrac{e^{-\gamma t} + \gamma t e^{-\gamma t} - e^{-\gamma x_c} - \gamma x_c}{\gamma\left(e^{-\gamma t} - 1\right)}$.

3. $v = \dfrac{e^{-\gamma t}\left(\gamma t + e^{-\gamma t} - e^{-\gamma x_c} - \gamma x_c\right)}{\left(e^{-\gamma t} - 1\right)^2}$.

In this case, the equation in step 2 cannot be rearranged for t, so analytic expressions for the minimum, maximum and average speeds cannot be determined. They can, however, be calculated numerically.

Case 2c: $F = \gamma(q_1 - q_2), \ q_1 = 1 + x$

1. $q_c = 1 - e^{-\gamma x_c} + x_c - \dfrac{1}{\gamma} + \dfrac{e^{-\gamma x_c}}{\gamma}$.

2. $q_c = 1 - e^{-\gamma t} + x - \dfrac{1}{\gamma} + \dfrac{e^{-\gamma t}}{\gamma} - (x - t)e^{-\gamma t}$,

$$\Rightarrow \ x = \dfrac{e^{-\gamma t} + \gamma t e^{-\gamma t} - \gamma e^{-\gamma t} - e^{-\gamma x_c} + \gamma e^{-\gamma x_c} - \gamma x_c}{\gamma\left(e^{-\gamma t} - 1\right)}.$$

3. $v = \dfrac{e^{-\gamma t}\left(-\gamma + \gamma t + e^{-\gamma t} - e^{-\gamma x_c} + \gamma e^{-\gamma x_c} - \gamma x_c\right)}{\left(e^{-\gamma t} - 1\right)^2}$.

As in case 2b, analytic expressions for the minimum, maximum and average speeds cannot be determined, but these values could be calculated numerically.

For the cases where onset is not instantaneous (1b, 1c, 2b and 2c), a q_c value can be chosen. Of course, the speed of onset depends upon the chosen value for the critical moisture content q_c, but it is not clear what value of q_c should be chosen. So results are presented using two values of q_c — one low (0.2) and one high (0.8) — in an attempt to bound the likely range of onset speeds. Thus, x_c, t_{xc}, t_1 and speed v can be calculated, as in Table 4.3, with $\gamma = 1$. A positive speed is indicative of the onset front moving from right to left, i.e. southeast to northwest India, as in observations. With a timescale T of L/u_2, we can dimensionalise the speeds by multiplying by u_2, which has default value 5 ms^{-1}. This shows that most of the cases can reproduce a realistic speed for the movement of the monsoon onset front, with the exception of case 1b, although it should be noted that a higher prescribed q_c threshold would give a lower average speed.

Table 4.3: *Example values for various parameters including a representative average onset speed, given a prescribed upper level moisture threshold for onset q_c.*

	Case 1b	Case 1c	Case 2b	Case 2c
q_c	0.2	0.8	0.2	0.8
x_c	0.63	0.61	0.71	0.80
t_{xc}	0.63	0.61	0.71	0.80
$v_{\min}$	0	1.63	0	0.82
t_1	0.23	0.45	0.26	0.63
$v_{\max}$	3.44	3.44	2.50	0.99
v_{av}	0.90	2.40	0.66	1.15
v_{av}	4.5 ms^{-1}	12.0 ms^{-1}	3.30 ms^{-1}	5.75 ms^{-1}

4.7   Numerical determination of onset speeds

In this section we compare results between the numerical code and the analytic expressions, regarding the onset front x_f. This is done as a check, because at later stages the model complexity will increase so that the system cannot be solved analytically. Hence, we test the numerical elements here so we can have confidence in later results.

The position and speed of the onset front over time is one of the most critical metrics, as this can be directly related and compared to observations. Cases 1a and 2a are not considered in this section as the onset occurs instantaneously across the domain, nullifying analysis of onset propagation. Figure 4.4 shows the propagation of the onset front for the remaining cases 1b, c, and 2b, c, beginning at $x = 1, t = t_1$ and stalling at $x = x_c, t = t_{xc}$. Numerical results are plotted as red crosses overlaying the analytical results (black

(a) *Case 1b: $F = \gamma q_1$ and $q_1 = x$, for $q_c = 0.2$.*

(b) *Case 2b: $F = \gamma(q_1 - q_2)$ and $q_1 = x$, for $q_c = 0.2$.*

(c) *Case 1c: $F = \gamma q_1$ and $q_1 = 1 + x$, for $q_c = 0.8$.*

(d) *Case 2c: $F = \gamma(q_1 - q_2)$ and $q_1 = 1 + x$, for $q_c = 0.8$.*
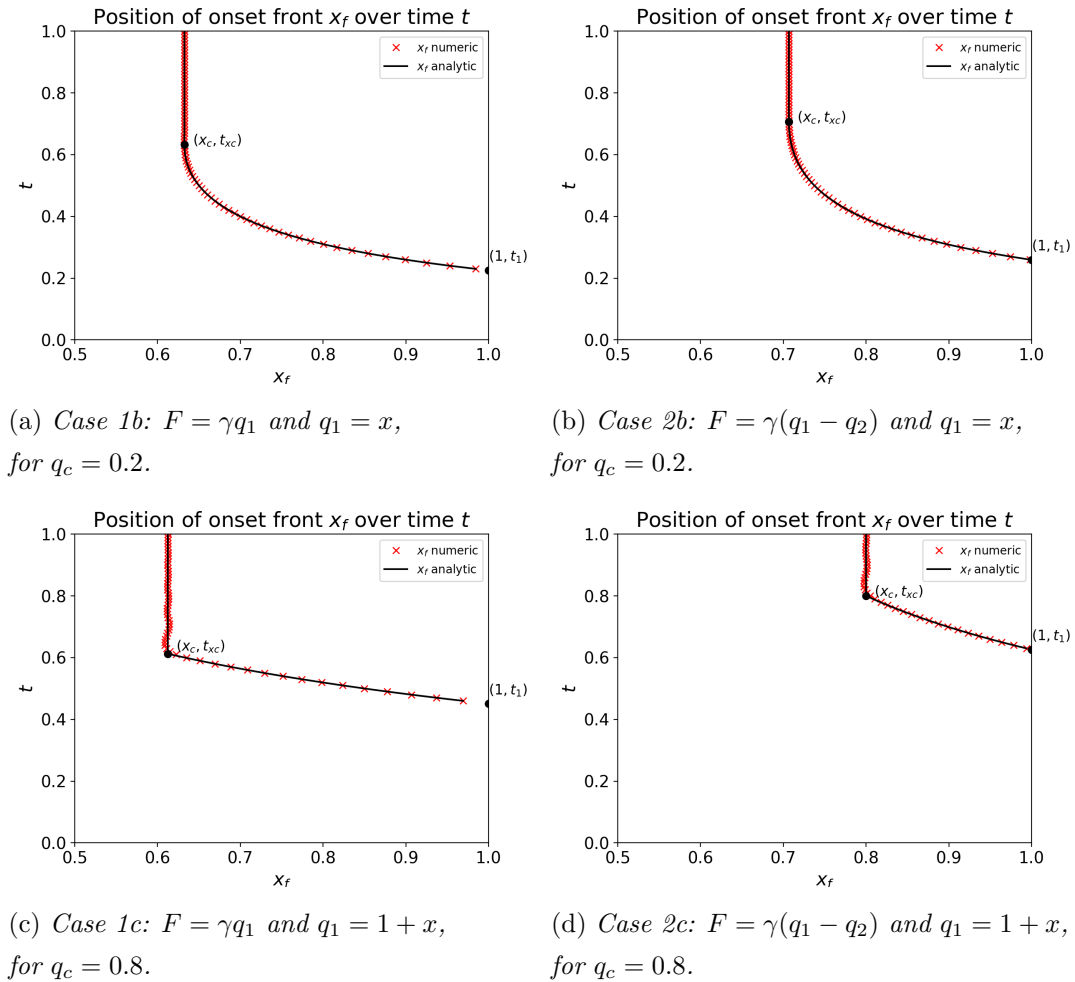
Figure 4.4: *Movement of onset front position x_f over time t for cases 1b, 1c, 2b & 2c, with $\gamma = 1$. The first and last points where the onset front is seen in the domain are marked by $(1, t_1)$ and (x_c, t_{xc}) respectively.*

line, from Section 4.6). The onset front progresses from right to left over time, as in observations. There is also good agreement between numerical and analytical results, although it is slightly better for cases 1b and 2b, where the first derivative in q_2 in x is continuous. Oscillations can be seen above the threshold in the numerical solutions for cases 1c and 2c. It should be noted that the moisture threshold for onset q_c has been chosen arbitrarily and a different choice would give a correspondingly different value for x_c.

The speed of the onset front dx_f/dt over time is plotted in Figure 4.5, again with numerical results in red crosses overlaying the analytical results (black line, derived in Section 4.6). The greatest speed of propagation occurs initially, then the speed decays as time increases. There is good agreement between numerical and analytical results for cases 1b and 2b, but poorer agreement for cases 1c and 2c, particularly around the time t_{xc}.

Continuing to move forward in time beyond the threshold (i.e. after about 0.6 for case 1c and 0.8 for case 2c), oscillations about zero can be observed, most likely due to the
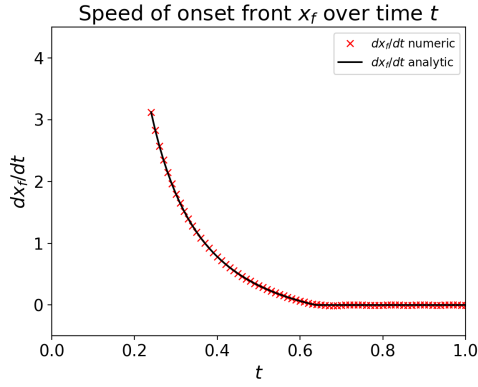
(a) *Case 1b: $F = \gamma q_1$ and $q_1 = x$, for $q_c = 0.2$.*
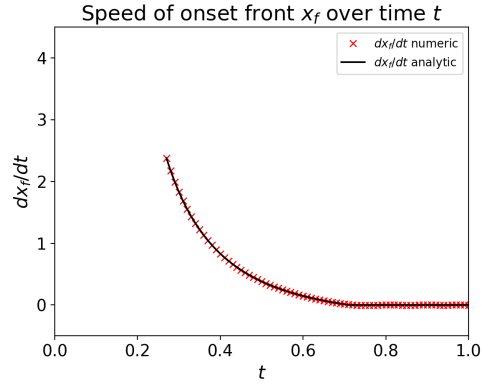
(b) *Case 2b: $F = \gamma(q_1 - q_2)$ and $q_1 = x$, for $q_c = 0.2$.*
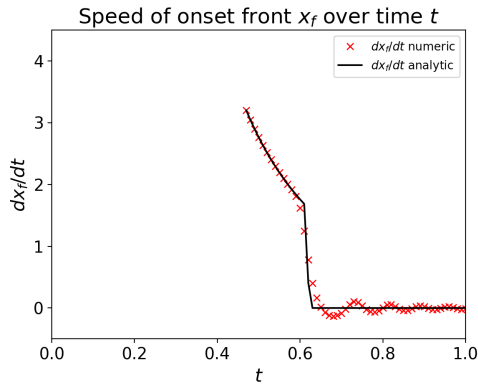
(c) *Case 1c: $F = \gamma q_1$ and $q_1 = 1 + x$, for $q_c = 0.8$.*
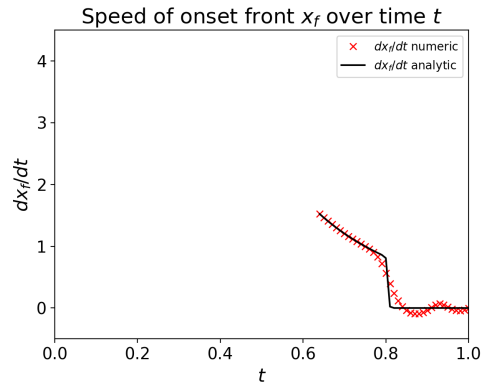
(d) *Case 2c: $F = \gamma(q_1 - q_2)$ and $q_1 = 1 + x$, for $q_c = 0.8$.*

Figure 4.5: *Speed of onset front x_f against time t for cases 1b, 1c, 2b & 2c, with $\gamma = 1$. Cases where the low level profile is constant ($q_1 = 1$) are not included as there is no progression of onset front: onset is simultaneous over x for these cases.*

discontinuous nature of the first derivative q_{2_x}. This demonstrates that the form of lower layer profile q_1 has an impact on the accuracy of determining the onset speed and should be chosen carefully.

4.8   Onset speed dependence on γ

In this section, the effects of varying γ, x_c and q_c on the average and maximum speeds of onset are investigated. Analytical expressions describing the relation between these parameters and the onset "front" speed can be derived for a range of flux and lower layer profile options, disregarding cases 1a and 2a where the onset is instantaneous. Since analytical expressions of the onset speed are available (from Section 4.6 and Table 4.3), it is easy to test a wide range of parameters; this would be much harder if a correspondingly large number of numerical experiments had to be performed. The analytical expressions

are used to produce the following Figures (4.6–4.8).

Firstly, the moisture threshold for onset in the upper level, q_c, is fixed at 0.2 for cases 1b and 2b and 0.8 for cases 1c and 2c, to keep consistent with previous sections. A range of γ values of 0.5 to 9.5 are taken, corresponding to mixing timescales of hours to days. The large range is due to lack of knowledge and observations of mixing processes and timescales. Figure 4.6 illustrates the results, with subplot 4.6a showing of the sensitivity of the average onset speed and subplot 4.6b showing the sensitivity of the maximum onset speed. A low average speed of $v_{av} < 1$, corresponding to about < 5 ms^{-1}, is desired to match observations. For all cases, this occurs when γ is small (< 2), meaning less mixing. In terms of average speed, Cases 1b and 2b are much less sensitive to the choice of γ than cases 1c and 2c, where the average speed increases rapidly with γ. Looking at the maximum speed, it increases linearly and very rapidly with γ to unrealistically high values for all cases.
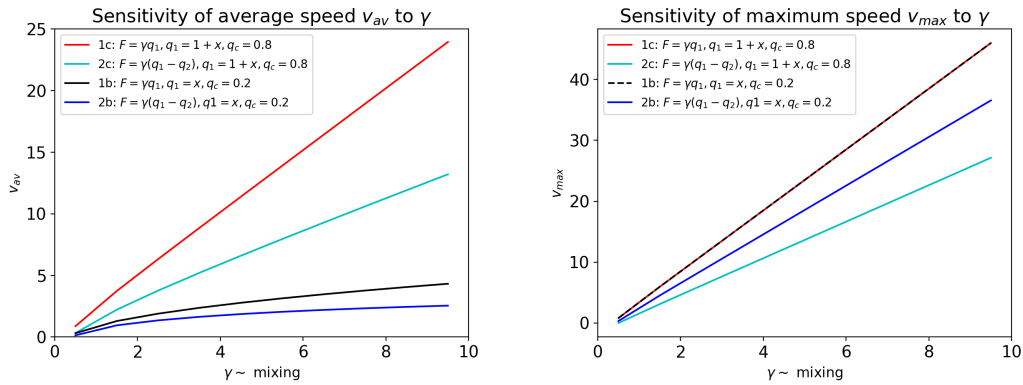
(a) *Average onset speed against γ.*   (b) *Maximum onset speed against γ.*

Figure 4.6: *Cases 1b, 1c, 2b & 2c: Sensitivity of average and maximum speeds to choice of γ within the range 0.5–9.5, fixing q_c at 0.2 for cases 1b & 2b and at 0.8 for cases 1c & 2c.*
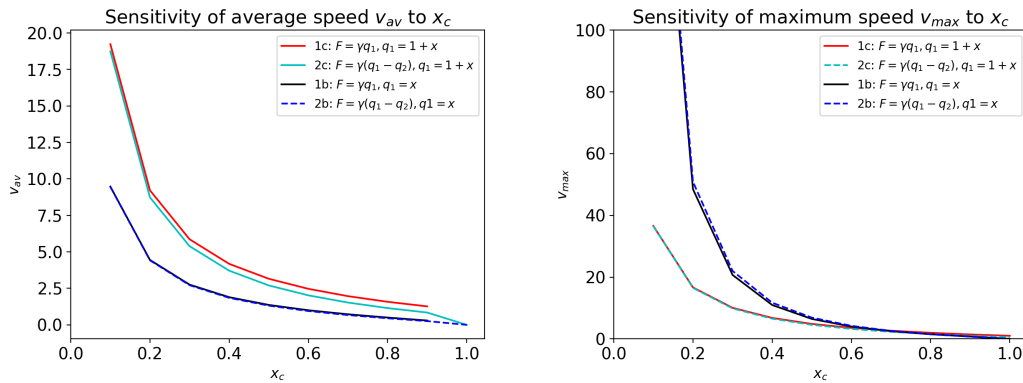
(a) *Average onset speed against x_c.*   (b) *Maximum onset speed against x_c.*

Figure 4.7: *Cases 1b, 1c, 2b & 2c: Sensitivity of average and maximum speeds to choice of x_c within the range 0–1, with $\gamma = 1$.*

Secondly, the parameter x_c, based on q_c, is varied, keeping γ fixed at the default value of one. The range for x_c is derived from the domain for x, where $0 < x < 1$. Figure 4.7a shows that for all cases, a low value of x_c corresponds to higher average speeds. Cases 1c and 2c reach higher average speed values when $x_c < 0.2$ than cases 1b and 2b. For the maximum speed plot in 4.7b, a similar pattern is seen but with cases 1b and 2b having the highest maximum speeds at low x_c. Comparing average and maximum speeds, the maximum speeds are roughly double the magnitude of the average speeds.
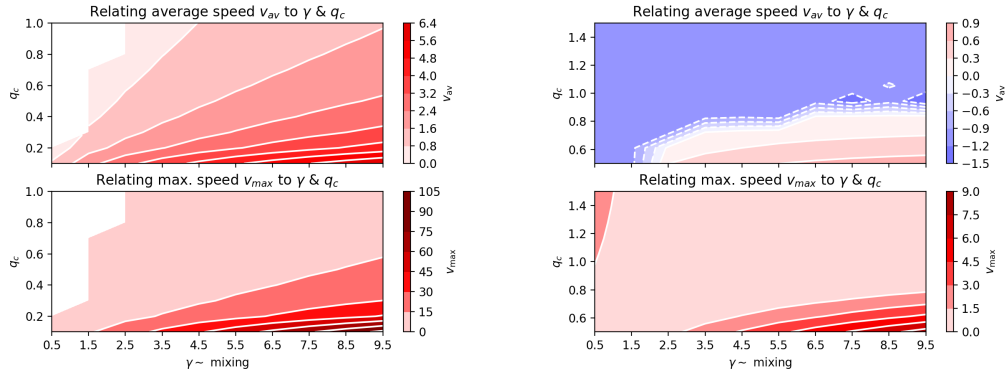
(a) *Case 1b: $F = \gamma q_1, q_1 = x$.* (b) *Case 2b: $F = \gamma(q_1 - q_2), q_1 = x$.*
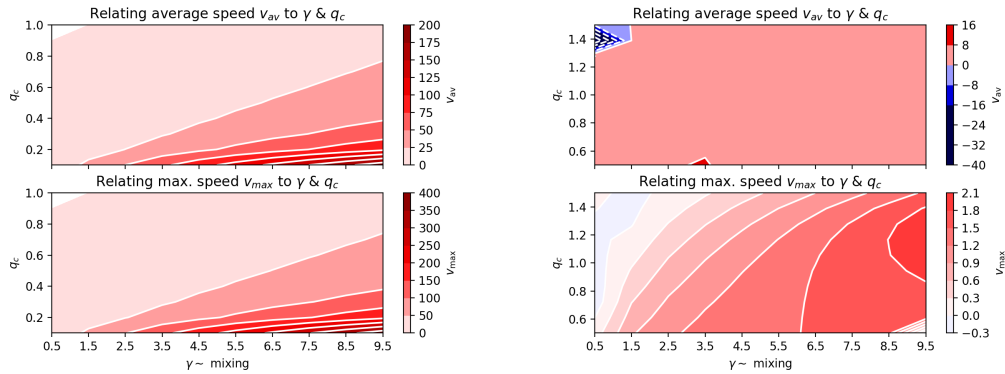
(c) *Case 1c: $F = \gamma q_1, q_1 = 1 + x$.* (d) *Case 2c: $F = \gamma(q_1 - q_2), q_1 = 1 + x$.*

Figure 4.8: *Contours of average and maximum onset front speeds for a range of γ (mixing timescale) values and varying moisture threshold q_c.*

Thirdly, both γ and q_c are varied, with the average and maximum speeds plotted as contours in Figure 4.8. The expressions relating x_c and q_c for each case can be found in section 4.6. There is a large variation in speed for each case, as can be seen from the colour-bars. Cases 1b and 1c show a similar pattern for average and maximum speeds, with the greatest speeds at high γ and low q_c. However, the maximum speeds have values much greater than the average speeds, becoming unrealistic, so going forward the average speed would be a better metric to use for comparison. For case 2b, the plot for maximum speed is similar to cases 1b and 1c, but the average speed plot is noticeably different. Here the onset speed is in fact negative (i.e. propagating from left to right, in contrast with

observations) for a large range of γ and q_c, becoming positive only at high mixing and a very low moisture threshold. Finally for case 2c, there is a large range of γ and q_c values that give a reasonable average speed, with an anomalous zone of higher average speeds at very low q_c for $\gamma = 3.5$ and an area giving negative onset speeds at high q_c for $\gamma < 1.5$. The maximum speed plot for this case is noticeably different from other cases, possibly due to the non-linear nature of the flux. The highest maximum speeds occur when γ and q_c are both high. In general, the average and maximum speeds appear more sensitive to the choice of the mixing parameter γ than the specification of the moisture threshold q_c.

4.9 Conclusions

It has been shown that the simplified version of the reduced two-layer model from Chapter 3, with a fixed lower layer, can reproduce the occurrence of the Indian monsoon onset and its propagation from southeast to northwest India, against the mean upper layer wind field, at a realistic speed. The system reduces to a single partial differential equation, with parameters describing upper level advection and the timescale of convection, with a forcing term relating to the prescribed lower layer moisture profile. Solutions for the steady-state and time-evolving system have been determined both analytically and numerically, allowing testing of the numerical scheme. This is of importance for the next chapter, which will consider a dynamic lower layer, where analytical solutions are unlikely to be as readily available.

Experiments are considered where the upper layer is initialised as dry, corresponding to either a state of no convection or where the upper level advection is so strong that the upper layer remains dry via the northwest boundary condition of dry inflow. Once convection is switched on, the upper layer moistens, with the rate of moistening dependant on the amount of convection, strength of advection and the choice of the lower layer profile. The evolution continues until a balance between the processes is reached. The distance over which the upper layer adjusts to an equilibrium state is characterised by a monsoon length-scale, $L_{\mathrm{mon}} = u_2 T_{\mathrm{c}}$. A simple and a down-gradient vertical flux is considered, with choices of 1, x or $1 + x$ for the lower layer moisture (q_1).

A propagating moisture front, interpreted as monsoon onset, can be observed in the model, moving from southeast to northwest India. The speed of the onset for the difference parameter choices has been determined, with calculated values in the range 3–6 ms^{-1} being consistent with observations. The system is sensitive to certain parameters, such as the choice of γ and the grid spacing, but less sensitive to the arbitrary selection of moisture threshold q_c. Despite the model neglecting several important physical processes such as precipitation and evaporation, it is remarkable that such a simple formulation can reproduce the advance of the monsoon onset against the mean upper layer wind, moreover, at realistic onset speeds.

Chapter 5

Dynamic lower layer model

5.1 Introduction

The reduced two-layer model from Chapter 3, Section 3.3, is now investigated. This is an extension from the fixed lower layer model in Chapter 4, in that dynamic interaction of the lower layer is allowed. The moistening of the upper layer by convection from the lower layer is investigated, with advection in the upper layer acting to dry the upper layer from the northwest. A relaxation in the lower layer is used as a proxy for moisture replenishment, which could be from moist inflow from over the oceans or evaporation. A coupled set of equations with boundary and initial conditions describe the evolution of moisture in the lower and upper layers. The key parameters are the timescale T_c for convection, the timescale T_m for replenishment of the lower-layer humidity, and the upper-layer advection speed u_2. Another parameter, q_e, represents a state of equilibrium in the absence of convection. The lower layer relaxes to the prescribed profile q_e on the timescale T_m, as detailed in Chapter 3, Subsection 3.3.2. The interaction between these processes is examined, with the effects of varying each one independently being evaluated in the context of monsoon onset.

Compared to the fixed lower layer model in Chapter 4, four modifications are made. Firstly, the analysis is undertaken in dimensional terms, which makes the dependence on various parameters become more transparent and is easier to interpret. Secondly, only the down-gradient parameterisation of the convective flux is considered, with $F \propto (q_1 - q_2)/T_c$. This has a greater basis in reality than the simple flux and leads to richer results than in Chapter 4. Thirdly, although a simple, spatially consistent profile $q_e = 1$ is considered for much of the analysis, a non-linear, exponential profile $q_e = 1 - e^{-x/L_e}$ is also explored. Here, L_e represents the length-scale of the monsoon system in non-convective equilibrium. Setting $L_e \to \infty$, the simple profile can be recovered from the exponential one.

Finally, and most importantly, the experiments are designed to investigate the transition from one equilibrium state to a new equilibrium state, given a change in one of the key parameters. Specifically, the experiments consider varying the upper level advection (corresponding to a strengthening or weakening dry intrusion), increasing the low-level

moist inflow (southwesterly monsoon flow intensifies and deepens around onset) and increasing the rate of convection (representing the development of cumulus clouds associated with the monsoon). Each process is varied in isolation, to understand the individual role of each process in the monsoon onset. Once these experiments are interpreted, it would be interesting to vary both the low-level inflow and the rate of convection simultaneously, for example. The transition from an initial to a new equilibrium state is representative of moving from a pre-onset phase to the full monsoon. Note that many of the results of Chapter 4, specifically those for a down-gradient convective flux and with a spatially-constant lower layer moisture profile, can be recovered from those in this chapter by setting $T_\mathrm{m} = 0$, which corresponds to instantaneous lower-layer replenishment, i.e., a fixed lower-layer.

The equations for the dynamic lower layer model are given in Section 5.2, including discussion of the mathematical approaches used to derive solutions to the system. The nature of the equilibrium solutions is determined in Section 5.3. This will be a balance between advection, convection and replenishment, unlike in Chapter 4, where the equilibrium only depended on advection and convection. The time-dependent solutions, notably including derivation of expressions for the onset speed and adjustment timescale, are presented in Section 5.4. Sections 5.5–5.7 give the results of the experiments for increasing low-level moist inflow, increasing the rate of convection, and varying the upper layer advection. Conclusions are summarised in Section 5.8.

5.2   Dimensional system of equations

The system of Equations 3.4a–3.4b from the reduced two-layer model presented in Chapter 3 is the basis of the dynamic lower layer model. The flux is taken as $F = (q_1 - q_2)/T_\mathrm{c}\Phi$, which is the down-gradient flux described in Subsection 3.2.2, Equation 3.2a. In this chapter, $\Phi = 1$. The timescales for convection (T_c) and lower layer moisture replenishment (T_m) are as in Subsection 3.3.1, both with assumed ranges of 1/2–7 days (Equations 3.5, 3.6). The choices of relaxation profile are discussed in Subsection 3.3.3. Following this, choices $q_\mathrm{e}(x) = 1$ and $q_\mathrm{e}(x) = 1 - e^{-x/L_\mathrm{e}}$ are investigated (Equations 3.15a, 3.15b). The parameter L_e represents the length-scale of the monsoon system in non-convective equilibrium. Additionally, the lateral boundary condition of dry inflow upstream (Subsection 3.2.4) is taken. The system of equations for the dynamic lower layer then becomes:

$$\frac{\partial q_2}{\partial t} + u_2 \frac{\partial q_2}{\partial x} = +\frac{1}{T_\mathrm{c}}(q_1 - q_2), \tag{5.1a}$$

$$\frac{\partial q_1}{\partial t} = -\frac{1}{T_\mathrm{c}}(q_1 - q_2) - \frac{1}{T_\mathrm{m}}(q_1 - q_\mathrm{e}), \tag{5.1b}$$

$$q_2(x = 0, t) = 0. \tag{5.1c}$$

In the absence of advection and moisture replenishment, the layers mix at a rate of e^{-2t/T_c}. This can be seen by setting $u_2 = T_\mathrm{m} = 0$ in Equations 5.1a–5.1c:

$$\frac{\partial q_2}{\partial t} = \frac{F}{T_\mathrm{c}}, \quad \frac{\partial q_1}{\partial t} = -\frac{F}{T_\mathrm{c}}.$$

Combining these and rewriting gives:

$$\frac{\partial}{\partial t}(q_1 - q_2) = -\frac{2}{T_c}(q_1 - q_2) \quad \Rightarrow \quad \frac{\partial}{\partial t}\left(e^{-2t/T_c}(q_1 - q_2)\right) = 0.$$

On integration with respect to t, the term for the rate of mixing between layers is derived:

$$e^{-2t/T_c}(q_1 - q_2) = f(x).$$

5.2.1 Mathematical approaches

For the dynamic lower layer model presented in this chapter, it is difficult to derive solutions analytically (unlike the fixed lower layer model in Chapter 4), except for the steady-state case. Some provisional work attempting to solve the time-dependent system is included in Appendix A, employing classical partial differential equation techniques. These suggest that the Green's function for the system would involve a Bessel function $J_0(z) \times e^{(-(\beta t + \alpha x))}$.

Due to the complexity of deriving solutions analytically, particularly in the time-dependent case, the solutions presented are mainly derived numerically. There is, however, an alternative analytical approach which can be considered, namely the small-time evolution.

The development of the system after a small amount of time is considered. Writing q_2, q_1 as Taylor series (Equations 5.2a, 5.2b), the lateral boundary condition (Equation 5.1c) is applied and arbitrary initial conditions are set (Equations 5.3a, 5.3b). The small-time deviation from $(q_1, q_2) = (q_{10}, q_{20})$ implies the initial direction of the monsoon onset, defined as a threshold of total moisture, which may take the form of a front. The initial speed that the monsoon onset propagates over India can also be determined. To do this, q_1, q_2 are written:

$$q_2 = q_{20}(x) + tq_{21}(x) + \frac{t^2}{2}q_{22}(x) + \dots \tag{5.2a}$$

$$q_1 = q_{10}(x) + tq_{11}(x) + \frac{t^2}{2}q_{12}(x) + \dots \tag{5.2b}$$

$$q_2 = q_{20}(x), \quad \text{at} \quad t = 0, \tag{5.3a}$$

$$q_1 = q_{10}(x), \quad \text{at} \quad t = 0, \tag{5.3b}$$

$$q_{20} = 0, \quad \text{at} \quad x = 0. \tag{5.3c}$$

By substituting these into Equations 5.1a, 5.1b, and equating powers of t, we find:

$\underline{O(1)}$:

$$q_{21}(x) = \frac{1}{T_c}\left(q_{10}(x) - q_{20}(x)\right) - u_2 q'_{20}(x), \tag{5.4a}$$

$$q_{11}(x) = -\frac{1}{T_c}\left(q_{10}(x) - q_{20}(x)\right) - \frac{1}{T_m}\left(q_{10}(x) - q_e(x)\right). \tag{5.4b}$$

$O(t)$:

$$q_{22}(x) = \frac{1}{T_c}\Big(q_{11}(x) - q_{21}(x)\Big) - u_2 q'_{21}(x),$$

$$= -\frac{2}{T_c^2}\Big(q_{10}(x) - q_{20}(x)\Big) - \frac{1}{T_c T_m}\Big(q_{10}(x) - q_e(x)\Big)$$

$$- \frac{u_2}{T_c}\Big(q'_{10}(x) - 2q'_{20}(x)\Big) + u_2^2 q''_{20}(x), \tag{5.5a}$$

$$q_{12}(x) = -\frac{1}{T_c}\Big(q_{11}(x) - q_{21}(x)\Big) - \frac{1}{T_m}\Big(q_{11}(x)\Big),$$

$$= \left(\frac{2}{T_c^2} + \frac{1}{T_c T_m}\right)\Big(q_{10}(x) - q_{20}(x)\Big)$$

$$+ \left(\frac{1}{T_c T_m} + \frac{1}{T_m^2}\right)\Big(q_{10}(x) - q_e(x)\Big) - \frac{u_2 q'_{20}(x)}{T_c}. \tag{5.5b}$$

Thus, the series 5.2a, 5.2b, dropping the (x), can now be written:

$$q_2 = q_{20} + t\left(\frac{1}{T_c}(q_{10} - q_{20}) - u_2 q'_{20}\right)$$

$$+ \frac{t^2}{2}\left(-\frac{2}{T_c^2}(q_{10} - q_{20}) - \frac{1}{T_c T_m}(q_{10} - q_e) - \frac{u_2}{T_c}(q'_{10} - 2q'_{20}) + u_2^2 q''_{20}\right) \tag{5.6a}$$

$$+ \dots$$

$$q_1 = q_{10} + t\left(-\frac{1}{T_c}(q_{10} - q_{20}) - \frac{1}{T_m}(q_{10} - q_e)\right)$$

$$+ \frac{t^2}{2}\left[\left(\frac{2}{T_c^2} + \frac{1}{T_c T_m}\right)(q_{10} - q_{20}) + \left(\frac{1}{T_c T_m} + \frac{1}{T_m^2}\right)(q_{10} - q_e) - \frac{u_2 q'_{20}}{T_c}\right] \tag{5.6b}$$

$$+ \dots$$

Note that unless $q_{10}(0) = 0$ and $q'_{20}(0) = 0$, the terms of order t (i.e., $q_{11}(x)$, $q_{21}(x)$) imply $q_2(0, t) \neq 0$, thus violating the lateral boundary condition (Equation 5.3c). Even if $q_{21}(0) = 0$, it is likely that $q_{22}(0) \neq 0$, due the non-zero q_e term, implying $q_2(0, t) \neq 0$. This anomaly can be rectified by performing a separate analysis for the combined limit of small x and small t, revealing the existence of a thin boundary layer which matches Equations 5.6b, 5.6a, to the lateral boundary condition (Equation 5.3c). The boundary layer analysis remains valid provided x is not small. Additional material relating to the boundary layer analysis is included in Appendix B. The small-time solutions presented here are revisited in Section 5.4, in order to derive a monsoon onset speed and a time of adjustment between the initial and final equilibrium states.

5.3 Equilibrium solutions

Analytical solutions can be found for long timescales when the system has reached a state of convective equilibrium. A parameter L_{mon}, which represents the length-scale of the monsoon system, is defined in terms of the speed u_2 and timescales T_{c}, T_{m}.

$$L_{\mathrm{mon}} = u_2 \left(T_{\mathrm{c}} + T_{\mathrm{m}}\right). \tag{5.7}$$

Putting $\partial/\partial t = 0$, the coupled set of equations 5.1a, 5.1b become:

$$u_2 \frac{dq_2}{dx} = +\frac{1}{T_{\mathrm{c}}}(q_1 - q_2), \tag{5.8a}$$

$$0 = -\frac{1}{T_{\mathrm{c}}}(q_1 - q_2) - \frac{1}{T_{\mathrm{m}}}(q_1 - q_{\mathrm{e}}). \tag{5.8b}$$

Rearranging Equation 5.8b to get an expression for q_1, then substituting into Equation 5.8a:

$$q_1 = \frac{q_2 T_{\mathrm{m}} + q_{\mathrm{e}} T_{\mathrm{c}}}{T_{\mathrm{c}} + T_{\mathrm{m}}}. \tag{5.9}$$

$$\frac{dq_2}{dx} = \frac{q_{\mathrm{e}} - q_2}{u_2\left(T_{\mathrm{c}} + T_{\mathrm{m}}\right)} = \frac{q_{\mathrm{e}} - q_2}{L_{\mathrm{mon}}}.$$

Taking an integrating factor of $e^{x/L_{\mathrm{mon}}}$, an expression is written for q_2 in terms of q_{e}, with the lateral boundary condition (Equation 5.1c):

$$q_2 = \frac{e^{-x/L_{\mathrm{mon}}}}{L_{\mathrm{mon}}} \int_0^x q_{\mathrm{e}} \cdot e^{x/L_{\mathrm{mon}}} \, dx. \tag{5.10}$$

5.3.1 Equilibrium solution for $q_{\mathrm{e}} = 1$

Taking the simplest case of $q_{\mathrm{e}} = 1$, substituting into equation 5.10 and integrating:

$$q_2 = \frac{e^{-x/L_{\mathrm{mon}}}}{L_{\mathrm{mon}}} \int_0^x e^{x/L_{\mathrm{mon}}} \, dx = \frac{e^{-x/L_{\mathrm{mon}}}}{L_{\mathrm{mon}}} \left[L_{\mathrm{mon}} e^{x/L_{\mathrm{mon}}}\right]_0^x.$$

Thus, the solution for q_2 in the case $q_{\mathrm{e}} = 1$ can be written, and thus the solution for q_1 from equation 5.9:

$$q_2 = 1 - e^{-x/L_{\mathrm{mon}}}, \tag{5.11a}$$

$$q_1 = 1 - e^{-x/L_{\mathrm{mon}}} \left(\frac{T_{\mathrm{m}}}{T_{\mathrm{c}} + T_{\mathrm{m}}}\right), \tag{5.11b}$$

$$q_1 + q_2 = 2 - e^{-x/L_{\mathrm{mon}}} \left(\frac{T_{\mathrm{c}} + 2T_{\mathrm{m}}}{T_{\mathrm{c}} + T_{\mathrm{m}}}\right). \tag{5.11c}$$

The relative sizes of T_{c} and T_{m} only affect the upper layer q_2 as part of the monsoon length-scale L_{mon}. If $T_{\mathrm{c}} \gg T_{\mathrm{m}}$, then the solution for the lower layer can be reduced to $q_1 \approx 1 - T_{\mathrm{m}} e^{-x/L_{\mathrm{mon}}}/T_{\mathrm{c}} \approx 1$. Here the first term is small, so the solution is dominated by 1. Conversely, if $T_{\mathrm{m}} \gg T_{\mathrm{c}}$, then $q_1 \approx 1 - e^{-x/L_{\mathrm{mon}}} \approx q_2$. The term $T_{\mathrm{c}}/T_{\mathrm{m}}$ is small, so $q_1 \approx q_2$ and the solutions for the upper and lower layers are similar. When $T_{\mathrm{m}} = T_{\mathrm{c}}$, the

upper layer solution remains unchanged, but the lower layer and total moisture solutions simplify to:

$$q_1 = 1 - \frac{1}{2}e^{-x/L_{\text{mon}}},$$

$$q_1 + q_2 = 2 - \frac{3}{2}e^{-x/L_{\text{mon}}}.$$

At the location $x = 0$, when $T_{\text{c}} = T_{\text{m}}$, the value of both the lower layer q_1 and the total moisture $q_1 + q_2$ is simply $1/2$, and the value of the upper layer q_2 is zero.

Another aspect to consider is the limiting behaviour, i.e. when $x \to \infty$. For Equations 5.11a–5.11c, as $x \to \infty$, then $e^{-x/L_{\text{mon}}} \to 0$ and thus:

$$q_2 \to 1,$$

$$q_1 \to 1,$$

$$q_1 + q_2 \to 2.$$

Note that L_{mon} describes the lengthscale over which the solution transitions from low humidity at $x = 0$ ($q_2 = 0$, $q_1 = T_{\text{c}}/(T_{\text{c}} + T_{\text{m}})$) to the limiting values of 1.

5.3.2   Equilibrium solution for $q_{\text{e}} = 1 - e^{-x/L_{\text{e}}}$

Now the more complex case of $q_{\text{e}} = 1 - e^{-x/L_{\text{e}}}$ is considered, where L_{e} is the prescribed length-scale of the monsoon system in non-convective equilibrium. If $L_{\text{e}} \to 0$, then $q_{\text{e}} \to 1$, and similar results to the previous case of q_{e} would be expected. Again, substituting q_{e} into equation 5.10 and integrating:

$$q_2 = \frac{e^{-x/L_{\text{mon}}}}{L_{\text{mon}}} \int_0^x \left(1 - e^{-x/L_{\text{e}}}\right) e^{x/L_{\text{mon}}} \, dx,$$

$$= \frac{e^{-x/L_{\text{mon}}}}{L_{\text{mon}}} \left[L_{\text{mon}} \cdot e^{x/L_{\text{mon}}} - e^{-x/L_{\text{e}} + x/L_{\text{mon}}} \left(-\frac{1}{L_{\text{e}}} + \frac{1}{L_{\text{mon}}}\right)^{-1} \right]_0^x,$$

$$= \frac{e^{-x/L_{\text{mon}}}}{L_{\text{mon}}} \left(L_{\text{mon}} \cdot e^{x/L_{\text{mon}}} - e^{-x/L_{\text{e}} + x/L_{\text{mon}}} \left(\frac{L_{\text{e}} L_{\text{mon}}}{L_{\text{e}} - L_{\text{mon}}}\right) - L_{\text{mon}} + \left(\frac{L_{\text{e}} L_{\text{mon}}}{L_{\text{e}} - L_{\text{mon}}}\right) \right).$$

It is assumed that $L_{\text{e}} \neq L_{\text{mon}}$; else, a different integration would be required. Then, the solution for q_2 in the case $q_{\text{e}} = 1 - e^{-x/L_{\text{e}}}$ can be written, the solution for q_1 from equation 5.9 and thus the solution for the total moisture $q_1 + q_2$:

$$q_2 = 1 - e^{-x/L_{\text{mon}}} \left(\frac{L_{\text{mon}}}{L_{\text{mon}} - L_{\text{e}}}\right) + e^{-x/L_{\text{e}}} \left(\frac{L_{\text{e}}}{L_{\text{mon}} - L_{\text{e}}}\right), \tag{5.12a}$$

$$q_1 = 1 - e^{-x/L_{\text{mon}}} \left(\frac{u_2 T_{\text{m}}}{L_{\text{mon}} - L_{\text{e}}}\right) - e^{-x/L_{\text{e}}} \left(\frac{u_2 T_{\text{c}} - L_{\text{e}}}{L_{\text{mon}} - L_{\text{e}}}\right), \tag{5.12b}$$

$$q_1 + q_2 = 2 - e^{-x/L_{\text{mon}}} \left(\frac{u_2 \left(T_{\text{c}} + 2T_{\text{m}}\right)}{L_{\text{mon}} - L_{\text{e}}}\right) - e^{-x/L_{\text{e}}} \left(\frac{u_2 T_{\text{c}} - 2L_{\text{e}}}{L_{\text{mon}} - L_{\text{e}}}\right). \tag{5.12c}$$

At the edge of the domain, $x = 0$, $q_1 = q_2 = 0$, and so $q_1 + q_2 = 0$. Setting $L_e = 0$, the terms in e^{-x/L_e} disappear, and the terms involving $e^{-x/L_{mon}}$ simplify to Equations 5.11a–5.11c.

For this case of q_e, considering when either T_c or T_m is much larger than the other does not give further information, as the expressions are too complex to clearly see the relations between parameters. For $T_c = T_m$, the upper layer solution is written the same as equation 5.12a, but the lower layer and total moisture solutions become:

$$q_1 = 1 - \frac{e^{-x/L_{mon}}}{2}\left(\frac{L_{mon}}{L_{mon} - L_e}\right) - \frac{e^{-x/L_e}}{2}\left(\frac{L_{mon} - 2L_e}{L_{mon} - L_e}\right),$$

$$q_1 + q_2 = 2 - \frac{3e^{-x/L_{mon}}}{2}\left(\frac{L_{mon}}{L_{mon} - L_e}\right) - \frac{e^{-x/L_e}}{2}\left(\frac{L_{mon} - 4L_e}{L_{mon} - L_e}\right).$$

If $L_{mon} \gg L_e$ is taken, then $L_{mon}/(L_{mon} - L_e) \to 1$. Equations 5.12a, 5.12b, 5.12c, become:

$$q_2 \approx 1 - e^{-x/L_{mon}} + e^{-x/L_e}\left(\frac{1}{L_{mon}}\right), \tag{5.13a}$$

$$q_1 \approx \begin{cases} 1 - e^{-x/L_{mon}}\left(\dfrac{T_m}{T_c + T_m}\right) - e^{-x/L_e}\left(\dfrac{T_c}{T_c + T_m}\right) & \text{for } T_c \neq T_m, \\[3mm] 1 - \dfrac{1}{2}e^{-x/L_{mon}} - \dfrac{1}{2}e^{-x/L_e} & \text{for } T_c = T_m, \end{cases} \tag{5.13b}$$

$$q_1 + q_2 \approx \begin{cases} 2 - e^{-x/L_{mon}}\left(\dfrac{T_c + 2T_m}{T_c + T_m}\right) - e^{-x/L_e}\left(\dfrac{u_2 T_c + 1}{u_2(T_c + T_m)}\right) & \text{for } T_c \neq T_m, \\[3mm] 2 - \dfrac{3}{2}e^{-x/L_{mon}} - \dfrac{1}{2}e^{-x/L_e} & \text{for } T_c = T_m. \end{cases} \tag{5.13c}$$

On the other hand, if $L_{mon} \ll L_e$ is taken, then $L_e/(L_{mon} - L_e) \to -1$. Equations 5.12a, 5.12b, 5.12c, become:

$$q_2 \approx 1 + e^{-x/L_{mon}}\left(\frac{1}{L_e}\right) - e^{-x/L_e}, \tag{5.14a}$$

$$q_1 \approx 1 + e^{-x/L_{mon}}\left(\frac{u_2 T_m}{L_e}\right) - e^{-x/L_e}\left(1 - \frac{u_2 T_c}{L_e}\right), \tag{5.14b}$$

$$q_1 + q_2 \approx 2 + e^{-x/L_{mon}}\left(\frac{u_2 T_m + 1}{L_e}\right) - e^{-x/L_e}\left(2 - \frac{u_2 T_c}{L_e}\right). \tag{5.14c}$$

Looking at the limiting behaviour $(x \to \infty)$ in Equations 5.12a–5.12c, $e^{-x/L_{mon}} \to 0$ and $e^{-x/L_e} \to 0$, giving:

$$q_2 \to 1,$$

$$q_1 \to 1,$$

$$q_1 + q_2 \to 2.$$

So the behaviour of q_1, q_2 and $q_1 + q_2$ as $x \to \infty$ is the same for both cases of q_e.

(a) $q_e = 1$, $T_c = T_m = 1$ *day.*

(b) $q_e = 1 - e^{-x/L_e}$, $T_c = T_m = 1$ *day.*

(c) $q_e = 1$, $T_c = T_m = 4$ *days.*

(d) $q_e = 1 - e^{-x/L_e}$, $T_c = T_m = 4$ *days.*

(e) $q_e = 1$, $T_c = T_m = 7$ *days.*

(f) $q_e = 1 - e^{-x/L_e}$, $T_c = T_m = 7$ *days.*
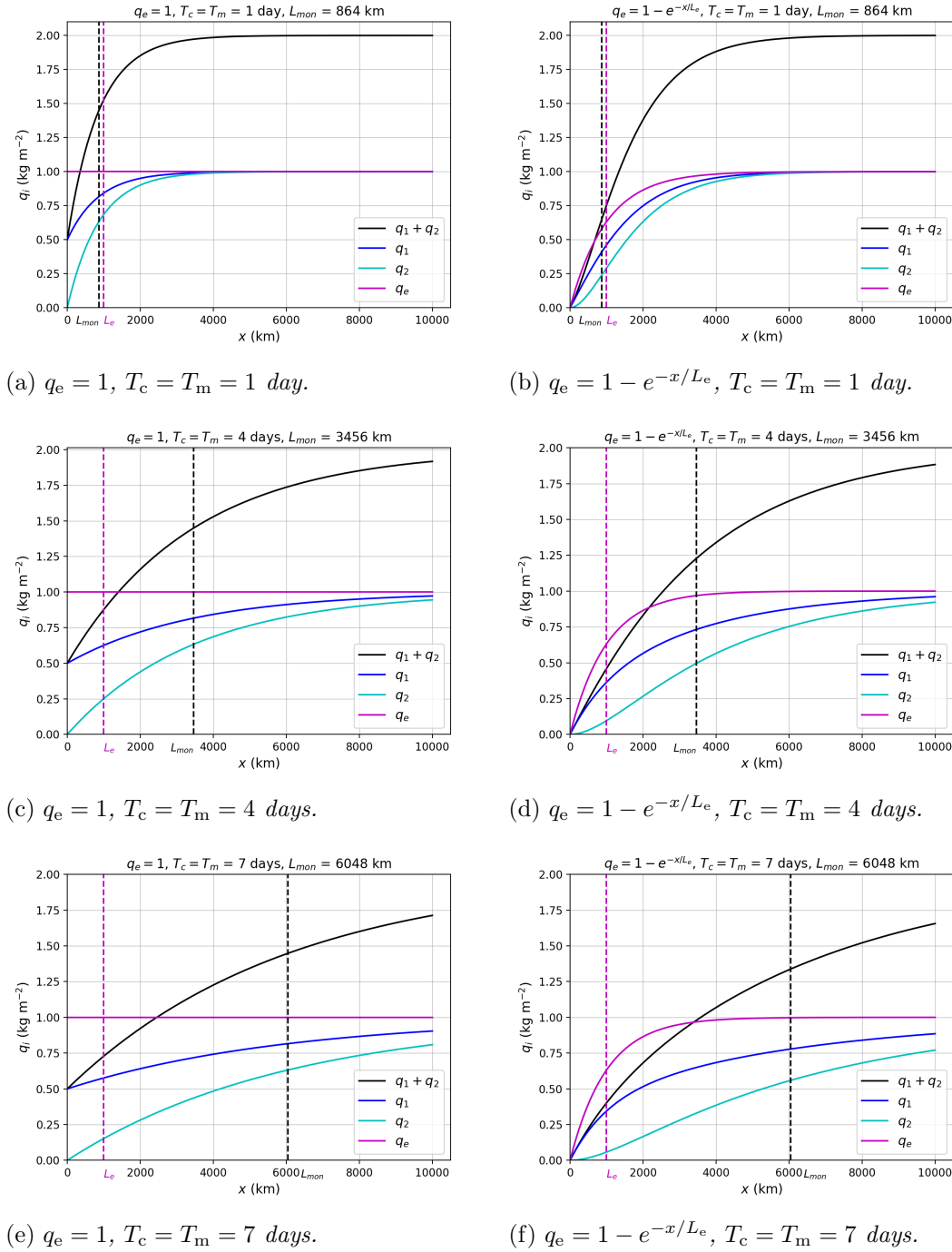
Figure 5.1: *Equilibrium plots, with* $T_c = T_m = 1$, 4, 7 *days and* $L_e = 1000$ *km.*

5.3.3   Variation of moisture over distance at equilibrium

In this section it is considered how the moisture in the upper (q_2) and lower (q_1) layers at equilibrium, against distance, x, varies with different timescales, T_c, T_m, and thus different monsoon length-scale, L_{mon}. Also shown for reference is the total moisture, $q_1 + q_2$, and the relaxation profile, q_e. Plots 5.1a, 5.1b are with $T_c = T_m = 1$ day, plots 5.1c, 5.1d are with $T_c = T_m = 4$ days, and plots 5.1e, 5.1f are with $T_c = T_m = 7$ days. The left column shows the case $q_e = 1$, the right column the case $q_e = 1 - e^{-x/L_e}$. A large domain is shown,

although the primary region of interest is approximately $0 \leq x \leq 3000$ km, representing the length of a transect from northwest to southeast India.

For all of the plots, an adjustment over distance is observed, from the value set by the boundary condition (minimum) to the limiting value as $x \to \infty$ (maximum). In the case $q_e = 1$, at $x = 0$, $q_2 = 0$ and $q_1 = 0.5$ (from Equations 5.11a, 5.11b, with $T_c = T_m$). Whereas in the case $q_e = 1 - e^{-x/L_e}$, at $x = 0$, the moisture content is zero - $q_2 = q_1 = 0$ (from Equations 5.12a, 5.12b, with $T_c = T_m$). The maximum value is 1 for both layers and both cases of q_e. Both cases of q_e look similar for $x > 2000$ km. Depending on the value of L_{mon}, and thus T_c and T_m, the distance to reach the maximum moisture content varies. When the monsoon length-scale is smaller and closer to the value of L_e (Figures 5.1a, 5.1b), the distance is about 5000 km. As the timescales are lengthened so that $L_{mon} \gg L_e$, the distance for the moisture contents to reach a constant value increases. This distance is larger than the domain size for Figures 5.1e and 5.1f.

5.3.4 Scaling of moisture with distance at equilibrium

Here, a scaling for the equilibrium plots in Subsection 5.3.3 is suggested, to investigate whether each of the lines can collapse to their limiting value at the same point. The x-axis is scaled by the monsoon length-scale L_{mon}, transforming some of the subplots from Figure 5.1 to Figure 5.2. Four monsoon length-scales are considered, relating to four combinations of T_c and T_m, in terms of days: $(T_c = 1, \ T_m = 1), (T_c = 1, \ T_m = 7), (T_c = 7, \ T_m = 1)$ and $(T_c = 7, \ T_m = 7)$. These pairs of T_c, T_m are denoted in the subplots as $L_{mon_{(1,1)}}$, $L_{mon_{(1,7)}}$, $L_{mon_{(7,1)}}$ and $L_{mon_{(7,7)}}$, respectively. The top row (Figure 5.2a, 5.2b) shows the total moisture, halved, the middle row (Figure 5.2c, 5.2d) shows the upper level moisture, q_2, and the bottom row (Figure 5.2e, 5.2f) shows the lower level moisture, q_1, all against x/L_{mon}. As before, the left column is for the case $q_e = 1$ and the right column is for the case $q_e = 1 - e^{-x/L_e}$.

Solutions for the upper layer moisture, with $q_e = 1$ (Figure 5.2c), will always collapse to the same curve when the x-axis is scaled by L_{mon}, regardless of the values taken for timescales T_c, T_m, and thus L_{mon}. This is evident from Equation 5.11a, where $q_2(x/L_{mon})$. For the case $q_e = 1 - e^{-x/L_e}$, only solutions with the same value of L_{mon} will collapse to the same curve. In Figure 5.2e, for the lower layer moisture with $q_e = 1$, it can be seen that the solutions follow the same curve when $T_c = T_m$. Again, this is evident from Equation 5.11b, where $q_1(x/L_{mon})$ in the case $T_c = T_m$. There is no universal behaviour for q_1 in the case $q_e = 1 - e^{-x/L_e}$. The total moisture follows the lower layer moisture. So for $q_e = 1$, solutions for the total moisture collapse onto the same curve only when $T_c = T_m$, and for $q_e = 1 - e^{-x/L_{mon}}$, the curves will not collapse regardless of whether timescales or monsoon length-scales are equal.

For $q_e = 1$, the lower layer and total moisture solutions simplify to $q_1 = 1 - e^{-x/L_{mon}}/2$ and $q_1 + q_2 = 2 - 3e^{-x/L_{mon}}/2$, when $T_c = T_m$, thus collapsing to the same curve. When $T_c > T_m$, the solutions for the lower layer and total moisture lie above the collapsed curve.

Conversely, when $T_c < T_m$, the solutions for the lower layer and total moisture lie below the collapsed curve. Another point to note is that the lower layer plots show the greatest variation with L_{mon}. In particular, there is a large spread in magnitude of q_1 for the case q_e, at small x/L_{mon} values (<0.5).
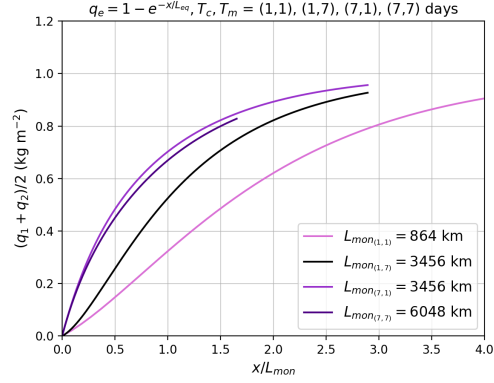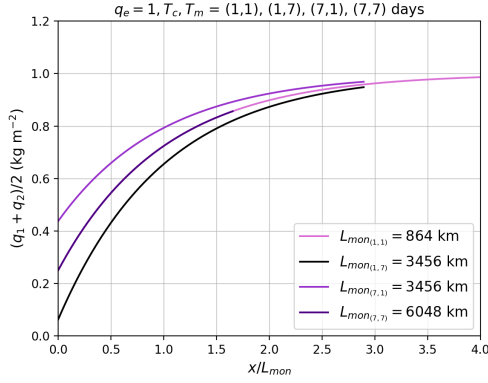
(a) $q_e = 1$, total moisture $(q_1 + q_2)/2$ against x. (b) $q_e = 1 - e^{-x/L_e}$, total moisture $(q_1 + q_2)/2$ against x.
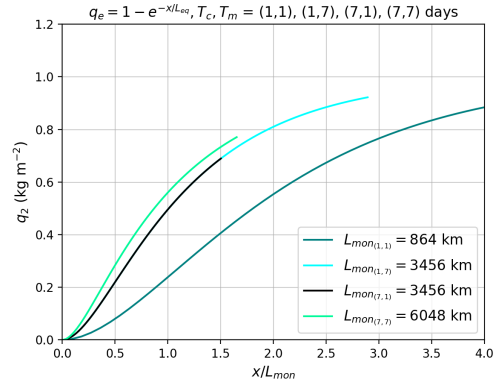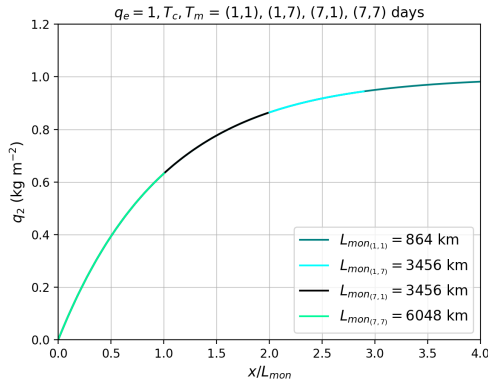
(c) $q_e = 1$, upper layer moisture q_2 against x. (d) $q_e = 1 - e^{-x/L_e}$, upper layer moisture q_2 against x.
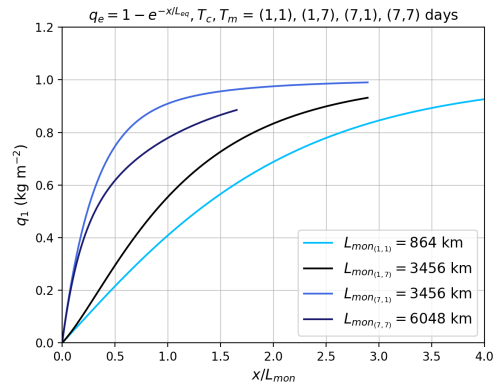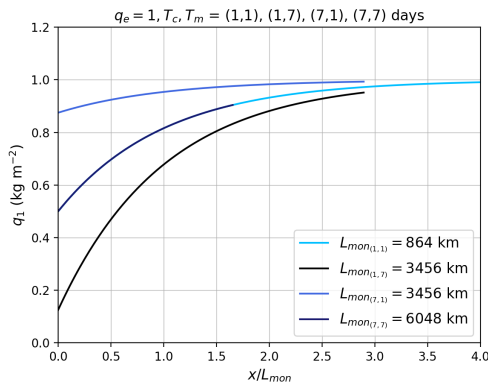
(e) $q_e = 1$, lower layer moisture q_1 against x. (f) $q_e = 1 - e^{-x/L_e}$, lower layer moisture q_1 against x.

Figure 5.2: *Equilibrium plots for $(T_c, \ T_m) = (1, 1), \ (1, 7), \ (7, 1)$ and $(7, 7)$ days. $L_e = 1000$ km. Sub-figures 5.2a, 5.2b show the total moisture (scaled by a factor of 1/2), 5.2c, 5.2d show the upper layer moisture and 5.2e, 5.2f show the lower layer moisture.*

In the case of $q_e = 1 - e^{-x/L_e}$, the lowest magnitudes of q_1, q_2 and $q_1 + q_2$ are given by the curve with the smallest monsoon length-scale, L_{mon}. Also, the curve for the case where $T_c > T_m$ lies above the inverse case where $T_c < T_m$, except for q_2 where they collapse onto the same curve.

The monsoon length-scale L_{mon} is the controlling length-scale in both cases of q_e. When $q_e = 1 - e^{-x/L_e}$, this becomes clear when $L_{mon} \gg L_e$. In other words, when the exponential case q_e looks likes the constant case ($q_e = 1$).

5.3.5 Sensitivity to timescale parameters at equilibrium

Having focussed on the lengthscales present in the equilibrium solutions, in this subsection the focus is now on the total moisture content of the layers, and how this depends upon T_c and T_m. Taking a large domain (so that $x_L \gg L_{mon}$) should be reflective of the limiting behaviour where $q_1 \to 1$, $q_2 \to 1$. Here, x_0 is generally taken as zero.

Case: $q_e = 1$

To consider the sensitivity of the system at equilibrium to timescale parameters T_c, T_m, Equations 5.11a–5.11c are taken and horizontally integrate over the domain $x_0 < x < x_L$. Dividing through by $x_L - x_0$, to take the average of the integral. The domain average of the convective flux F is also calculated.

$$\frac{1}{x_L - x_0} \int_{x_0}^{x_L} q_2 \ dx = \frac{1}{x_L - x_0} \int_{x_0}^{x_L} \left(1 - e^{-x/L_{mon}}\right) dx$$

$$= 1 + \frac{L_{mon}}{x_L - x_0} \left(e^{-x_L/L_{mon}} - e^{-x_0/L_{mon}}\right), \tag{5.15a}$$

$$\frac{1}{x_L - x_0} \int_{x_0}^{x_L} q_1 \ dx = \frac{1}{x_L - x_0} \int_{x_0}^{x_L} \left(1 - e^{-x/L_{mon}} \left(\frac{T_m}{T_c + T_m}\right)\right) dx$$

$$= 1 + \frac{u_2 T_m}{x_L - x_0} \left(e^{-x_L/L_{mon}} - e^{-x_0/L_{mon}}\right), \tag{5.15b}$$

$$\frac{1}{x_L - x_0} \int_{x_0}^{x_L} (q_1 + q_2) \ dx = \frac{1}{x_L - x_0} \int_{x_0}^{x_L} \left(2 - e^{-x/L_{mon}} \left(\frac{T_c + 2T_m}{T_c + T_m}\right)\right) dx$$

$$= 2 + \frac{u_2 (T_c + 2T_m)}{x_L - x_0} \left(e^{-x_L/L_{mon}} - e^{-x_0/L_{mon}}\right), \tag{5.15c}$$

$$\frac{1}{x_L - x_0} \int_{x_0}^{x_L} F \ dx = \frac{1}{x_L - x_0} \int_{x_0}^{x_L} \frac{1}{T_c} (q_1 - q_2) \ dx$$

$$= \frac{u_2}{x_L - x_0} \left(e^{-x_0/L_{mon}} - e^{-x_L/L_{mon}}\right). \tag{5.15d}$$

Note that Equation 5.15d shows that the convective flux F is positive since $x_0 < x_L$, meaning it acts vertically upwards, as assumed. When $x_0 = 0$ and $x_L \gg L_{mon}$, then

$e^{-x_L/L_{\mathrm{mon}}} \to 0$, and Equations 5.15b – 5.15c simplify:

$$\frac{1}{x_L} \int_0^{x_L} q_2 \, dx \quad \to \quad 1 - \frac{L_{\mathrm{mon}}}{x_L} \approx 1 \text{ (since } x_L \gg L_{\mathrm{mon}}\text{)}, \tag{5.16a}$$

$$\frac{1}{x_L} \int_0^{x_L} q_1 \, dx \quad \to \quad 1 - \frac{u_2 T_{\mathrm{m}}}{x_L} \approx 1 \text{ (since } x_L \gg L_{\mathrm{mon}} = u_2(T_{\mathrm{c}} + T_{\mathrm{m}}) > u_2 T_{\mathrm{m}}\text{)}, \tag{5.16b}$$

$$\frac{1}{x_L} \int_0^{x_L} (q_1 + q_2) \, dx \quad \to \quad 2 - \frac{u_2 \left(T_{\mathrm{c}} + 2T_{\mathrm{m}} \right)}{x_L} \approx 2, \tag{5.16c}$$

$$\frac{1}{x_L} \int_0^{x_L} F \, dx \quad \to \quad \frac{u_2}{x_L}. \tag{5.16d}$$

Case: $q_{\mathrm{e}} = 1 - e^{-x/L_{\mathrm{e}}}$

Now taking Equations 5.12a–5.12c and horizontally integrating over the domain $x_0 < x < x_L$, again dividing through by $x_L - x_0$ for the average.

$$\frac{1}{x_L - x_0} \int_{x_0}^{x_L} q_2 \, dx$$

$$= \frac{1}{x_L - x_0} \int_{x_0}^{x_L} \left(1 - e^{-x/L_{\mathrm{mon}}} \left(\frac{L_{\mathrm{mon}}}{L_{\mathrm{mon}} - L_{\mathrm{e}}} \right) + e^{-x/L_{\mathrm{e}}} \left(\frac{L_{\mathrm{e}}}{L_{\mathrm{mon}} - L_{\mathrm{e}}} \right) \right) dx$$

$$= 1 + \frac{(x_L - x_0)^{-1}}{L_{\mathrm{mon}} - L_{\mathrm{e}}} \left(L_{\mathrm{mon}}^2 \left(e^{-x_L/L_{\mathrm{mon}}} - e^{-x_0/L_{\mathrm{mon}}} \right) - L_{\mathrm{e}}^2 \left(e^{-x_L/L_{\mathrm{e}}} - e^{-x_0/L_{\mathrm{e}}} \right) \right), \tag{5.17a}$$

$$\frac{1}{x_L - x_0} \int_{x_0}^{x_L} q_1 \, dx$$

$$= \frac{1}{x_L - x_0} \int_{x_0}^{x_L} \left(1 - e^{-x/L_{\mathrm{mon}}} \left(\frac{u_2 T_{\mathrm{m}}}{L_{\mathrm{mon}} - L_{\mathrm{e}}} \right) - e^{-x/L_{\mathrm{e}}} \left(\frac{u_2 T_{\mathrm{c}} - L_{\mathrm{e}}}{L_{\mathrm{mon}} - L_{\mathrm{e}}} \right) \right) dx$$

$$= 1 + \frac{(x_L - x_0)^{-1}}{L_{\mathrm{mon}} - L_{\mathrm{e}}} \left[u_2 T_{\mathrm{m}} L_{\mathrm{mon}} \left(e^{-x_L/L_{\mathrm{mon}}} - e^{-x_0/L_{\mathrm{mon}}} \right) \right.$$

$$\left. + L_{\mathrm{e}} \left(u_2 T_{\mathrm{c}} - L_{\mathrm{e}} \right) \left(e^{-x_L/L_{\mathrm{e}}} - e^{-x_0/L_{\mathrm{e}}} \right) \right], \tag{5.17b}$$

$$\frac{1}{x_L - x_0} \int_{x_0}^{x_L} (q_1 + q_2) \, dx$$

$$= \frac{1}{x_L - x_0} \int_{x_0}^{x_L} \left(2 - e^{-x/L_{\mathrm{mon}}} \left(\frac{u_2 \left(T_{\mathrm{c}} + 2T_{\mathrm{m}} \right)}{L_{\mathrm{mon}} - L_{\mathrm{e}}} \right) - e^{-x/L_{\mathrm{e}}} \left(\frac{u_2 T_{\mathrm{c}} - 2L_{\mathrm{e}}}{L_{\mathrm{mon}} - L_{\mathrm{e}}} \right) \right) dx$$

$$= 2 + \frac{(x_L - x_0)^{-1}}{L_{\mathrm{mon}} - L_{\mathrm{e}}} \left[L_{\mathrm{mon}} \left(L_{\mathrm{mon}} + u_2 T_{\mathrm{m}} \right) \left(e^{-x_L/L_{\mathrm{mon}}} - e^{-x_0/L_{\mathrm{mon}}} \right) \right.$$

$$\left. + L_{\mathrm{e}} \left(u_2 T_{\mathrm{c}} - 2L_{\mathrm{e}} \right) \left(e^{-x_L/L_{\mathrm{e}}} - e^{-x_0/L_{\mathrm{e}}} \right) \right]. \tag{5.17c}$$

Plots & analysis

From Equations 5.15b – 5.15c (case $q_e = 1$) and Equations 5.17b – 5.17c (case $q_e = 1 - e^{-x/L_e}$), the sensitivity to the parameters T_c and T_m at equilibrium is plotted as contours. Note that the total moisture $(q_1 + q_2)$ is halved, in order to show on the same colour-scale and levels as the layer moisture, q_1, q_2. Firstly, for Figure 5.3, a large domain in x is taken, to show that $q_1 \to 1$, $q_2 \to 1$ and $(q_1 + q_2)/2 \to 1$ at small T_m, T_c, in agreement with the limiting behaviour expected. The range for both the timescales T_c and T_m is 0–6 weeks. Both cases of q_e look very similar, which is unsurprising given that the difference in the cases is around $x = 0$; integrating over the whole domain of x means that these details are somewhat obscured. The descriptions given of each subplot will be applicable to either case.

For the lower layer, q_1, the moisture content is greatest when $T_m < 1$ week, irrespective of the value of T_c. As the timescale T_m is increased towards 6 weeks, corresponding to a decreasing rate of moisture inflow, the amount of moisture in q_1 reduces. The timescale for convection, T_c, has little effect on the moisture content in the lower layer, except at longer timescales of 5+ weeks for both T_m and T_c, where the reduction in convective activity allows slightly more moisture to accumulate. The importance of T_m for the lower layer moisture is evident in Equation 5.16b. Here, there is no dependence on T_c for large domains $(x_L \gg L_{mon})$, as seen by the almost horizontal contours in the q_1 subplot, Figure 5.3.

In the upper layer, q_2, decreasing both timescales T_m and T_c, reflecting an increase in moisture inflow and convective activity, leads to more moisture, reaching a maximum of 1. A greater amount of moisture input to the lower layer means a more moist lower layer, increasing the gradient between the layers and thus the flux. This means that more moisture is transported to the upper layer, which in turn becomes more moist. A faster rate of convection (i.e. shorter timescale T_c) also allows more moisture to be transported from the lower to upper layer, leading to a greater value of q_2. The contours in the q_2 subplot, Figure 5.3 are at 45° from the horizontal, meaning that q_2 has a linear dependence on $T_c + T_m$. This can also be seen from Equation 5.16a, where $L_{mon} = u_2 (T_c + T_m)$.

The contours for the flux (F) subplot are similar to q_2. Looking at Equation 5.16d, given that $x_L \gg L_{mon}$, the flux only depends on the ratio of the upper level advection, u_2, to the size of the domain, x_L. The flux is greatest when the timescales T_m and T_c are smallest, i.e. when the rates of moisture inflow and convection are highest, as would be expected.

The total moisture, $q_1 + q_2$, scaled by 1/2, has contours at approximately 23°, reflecting Equation 5.16c, which shows a dependence on $2T_m$ compared with T_c. As T_m is decreased, thereby increasing the moisture inflow, the total moisture increases at a greater rate than with decreasing convective timescale, T_c. Generally, the system is more sensitive to the choice of replenishment timescale, T_m, than convective timescale, T_c.

Secondly, for Figure 5.4, a smaller domain $0 < x < 3000$ km is taken, representing the
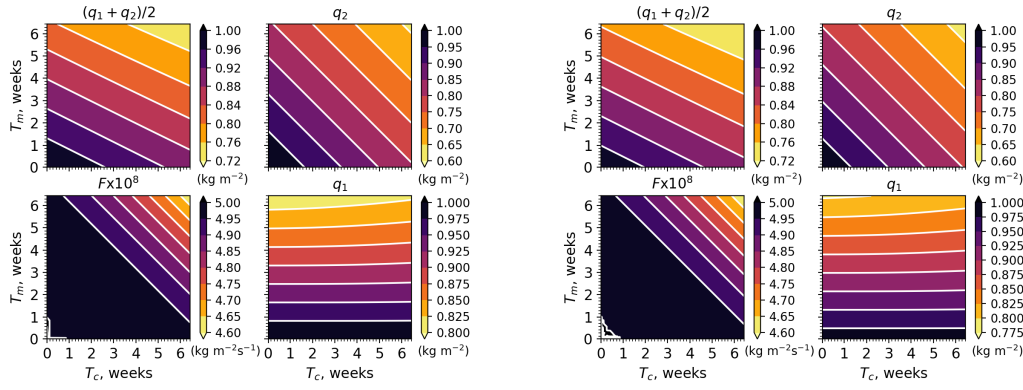
(a) $q_e = 1$ (b) $q_e = 1 - e^{-x/L_e}$

Figure 5.3: *Sensitivity of total moisture $q_1 + q_2$, flux F, upper layer moisture q_2 and lower layer moisture q_1 to varying convective and moisture replenishment timescales, T_c and T_m. Horizontally integrated over a large domain, $0 < x < 100\,000$ km, to show limiting behaviour. $u_2 = 5$ ms^{-1} and $L_e = 1000$ km. Threshold T_m^* denoted by dashed white line.*
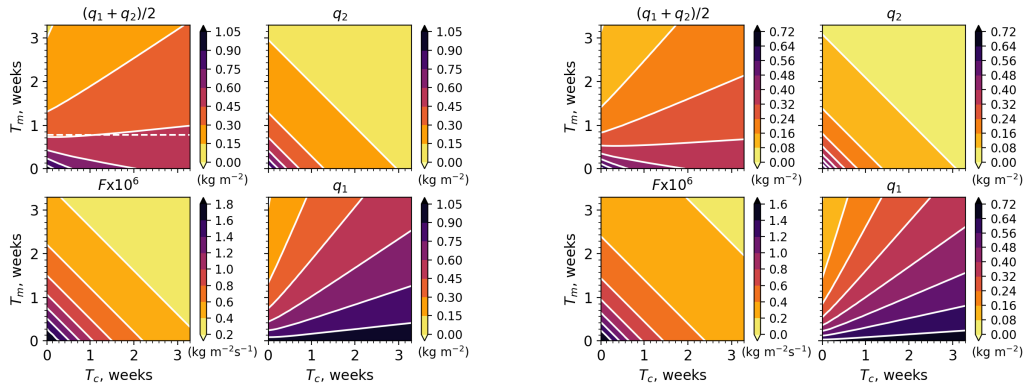
(a) $q_e = 1$ (b) $q_e = 1 - e^{-x/L_e}$

Figure 5.4: *Sensitivity of total moisture $q_1 + q_2$, flux F, upper layer moisture q_2 and lower layer moisture q_1 to varying convective and moisture replenishment timescales, T_c and T_m. Horizontally integrated over India, $0 < x < 3000$ km. $u_2 = 5$ ms^{-1} and $L_e = 1000$ km. Threshold T_m^* denoted by dashed white line.*

length of a transect over India. Note that there are large differences in the total moisture content as T_c and T_m vary, and these differences need to be understood. Also, the range of 0–6 weeks is taken to show the "big picture", and more realistic (shorter) timescales will be focused on due course. For this choice of domain size, it means that $x_L < L_{mon}$, except at small T_m, T_c (<3.5 days). Here, the range for both the timescales T_c and T_m is 0–3 weeks, as the behaviour at smaller timescales is of more interest. As before, both cases of q_e look very similar, differing only in magnitude. The subplots for q_2 and F follow the same pattern as for Figure 5.3, with both quantities increasing linearly with decreasing T_m and T_c.

The contours for the lower layer, q_1, are arranged in a radiating pattern. A longer
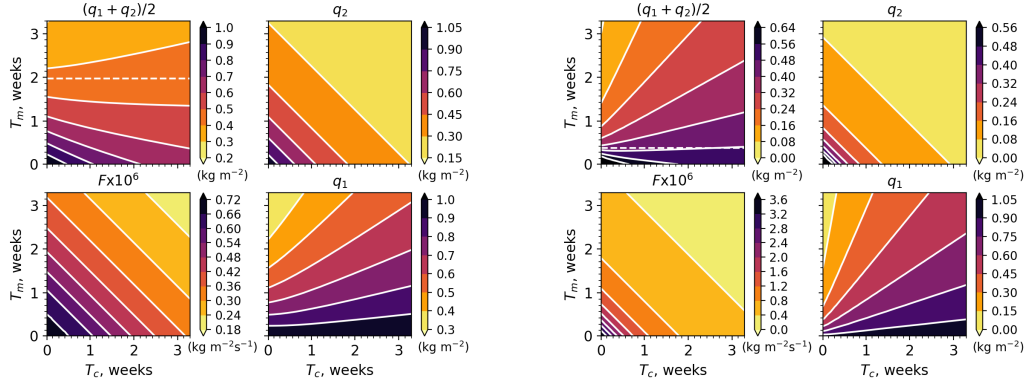
(a) $q_e = 1$, $u_2 = 2\ ms^{-1}$ (b) $q_e = 1$, $u_2 = 10\ ms^{-1}$

Figure 5.5: *Sensitivity of total moisture $q_1 + q_2$, flux F, upper layer moisture q_2 and lower layer moisture q_1 to varying convective and moisture replenishment timescales, T_c and T_m. Horizontally integrated over India, $0 < x < 3000$ km. For the case $q_e = 1$, $u_2 = 2\ ms^{-1}$ (left) and $u_2 = 10\ ms^{-1}$ (right).*

convective timescale, T_c, meaning a slower rate of moisture being transported to the upper layer, allows more moisture to accumulate in the lower layer. Contrastingly, a longer replenishment timescale, T_m, leads to a reduction in moisture in the lower layer as the rate of moisture inflow is reduced. For very small T_m, T_c (black segment in contour plot), the behaviour for $x_L \gg L_{mon}$, as in Figure 5.3, is recovered.

For the total moisture subplot, $(q_1+q_2)/2$, for approximately $T_m > 4$ days, the contours follow a similar pattern to the lower layer, q_1. Above this threshold, which is denoted T_m^* (dashed line), the total moisture decreases with decreasing timescale T_c, and increases with decreasing timescale T_m. Physically, this corresponds to moisture gain in the system when the rate of replenishment to the lower layer is higher, as would be expected. However, when the rate of convection is greater, more moisture is accumulated in the upper layer and thus more moisture can be advected from the upper layer out of the domain, explaining the reduction in total moisture. Below the threshold T_m^*, the contours change from increasing with T_c to decreasing with T_c. In this region, the total moisture increases with a higher rate of convection (i.e. smaller T_c), dominating over the upper-level advection. For small T_m and T_c (dark purple/black contour segments), the total moisture follows the same behaviour as in Figure 5.3.

T_m^* is interpreted as the threshold between two regimes. Below T_m^*, convection dominates over advection, with higher convective activity leading to moisture gain in the system. Above T_m^*, upper level advection dominates, with higher convective activity being linked with moisture loss. Shifts in regime in the model represents periods of increased/decreased moisture inflow to the Indian monsoon system. For example, a strengthening of the Somali Jet would increase the moisture inflow from the Arabian Sea (decreasing T_m), thereby shifting below T_m^* and being in a convection-dominant regime.

Figure 5.5 investigates how the system varies with upper level advection, u_2, for the

case $q_e = 1$. Both cases of q_e are similar enough that the results for $q_e = 1$ can be extended to the case $q_e = 1 - e^{-x/L_e}$. Most obviously, given that Figure 5.5 has the same domain as Figure 5.4, is how T_m^* scales with u_2. When the upper level advection is roughly halved (Figure 5.5a), the threshold T_m^* is approximately doubled, effectively increasing the area that the convection-dominant regime occupies. This is reversed in Figure 5.5b, with doubling u_2 giving a halved T_m^*. Increasing the upper level advection gives an increased area of advection-dominant regime, somewhat unsurprisingly. Empirically, it can be seen that $T_m^* \propto x_L/u_2$. In order for the T_m^* threshold to be visible on Figure 5.3, which takes a larger domain ($x_L = 100\,000$ km), the plot would need to be extended to $T_c,\ T_m \sim 33$ weeks.

Derivation of threshold T_m^*

To find the threshold T_m^* analytically, let $\bar{q}_t$ represent the averaged integral for total moisture in the case $q_e = 1$, Equation 5.15c. Note that, for simplicity, only the case $q_e = 1$ is considered. Next, an expression for the derivative $\partial \bar{q}_t / \partial T_c$ at the point $T_c = 0$ is found. Then $T_m = T_m^*$ where the expression $\dfrac{\partial \bar{q}_t}{\partial T_c}\bigg|_{T_c=0} = 0$.

$$\frac{\partial \bar{q}_t}{\partial T_c} = \frac{1}{x_L - x_0} \left[e^{-x_L/L_{\text{mon}}} \left(u_2 + \frac{x_L (T_c + 2T_m)}{(T_c + T_m)^2} \right) - e^{-x_0/L_{\text{mon}}} \left(u_2 + \frac{x_0 (T_c + 2T_m)}{(T_c + T_m)^2} \right) \right],$$

$$\frac{\partial \bar{q}_t}{\partial T_c}\bigg|_{T_c=0} = \frac{1}{x_L - x_0} \left[e^{-x_L/(u_2 T_m)} \left(u_2 + \frac{2x_L}{T_m} \right) - e^{-x_0/(u_2 T_m)} \left(u_2 + \frac{2x_0}{T_m} \right) \right],$$

$$0 = \frac{1}{x_L - x_0} \left[e^{-x_L/(u_2 T_m^*)} \left(u_2 + \frac{2x_L}{T_m^*} \right) - e^{-x_0/(u_2 T_m^*)} \left(u_2 + \frac{2x_0}{T_m^*} \right) \right],$$

$$0 = e^{-x_L/(u_2 T_m^*)} \left(1 + \frac{2x_L}{u_2 T_m^*} \right) - 1. \tag{5.18}$$

Here, $x_0 = 0$ is taken, resulting in an expression for T_m^* (Equation 5.18). It is suspected that T_m^* scales with x_L/u_2, so a new non-dimensional parameter ϕ is introduced (Equation 5.19), to simplify the expression for T_m^*. Thus, Equation 5.18 becomes Equation 5.20.

$$\phi = \frac{x_L}{u_2 T_m^*} \tag{5.19}$$

$$0 = e^{-\phi} (1 + 2\phi) - 1 \quad \Leftrightarrow \quad e^{-\phi} = \frac{1}{1 + 2\phi}. \tag{5.20}$$

The solution to Equation 5.20 can be shown graphically (Figure 5.6), where the intersection of $f(\phi) = e^{-\phi}$ and $f(\phi) = 1/(1 + 2\phi)$ gives the desired value of ϕ. As illustrated in Figure 5.6, it can be seen visually that Equation 5.20 only has a single real positive root $1/(1+2\phi)$. Initially, $1/(1+2\phi)$ decreases more quickly than $e^{-\phi}$ as ϕ increases from 0, but $e^{-\phi} \ll 1/(1+2\phi)$ when $\phi \gg 1$. This root is found numerically using the Newton-Raphson

iteration method, as detailed below:

$$\phi_{i+1} = \phi_i - \frac{f(\phi_i)}{f'(\phi_i)},$$

$$= \phi_i - \frac{\left(e^{-\phi_i}(1+2\phi_i)-1\right)}{e^{-\phi_i}(1-2\phi_i)},$$

$$= \frac{e^{\phi_i} - 2\phi_i^2 - \phi_i - 1}{1 - 2\phi_i}. \tag{5.21}$$
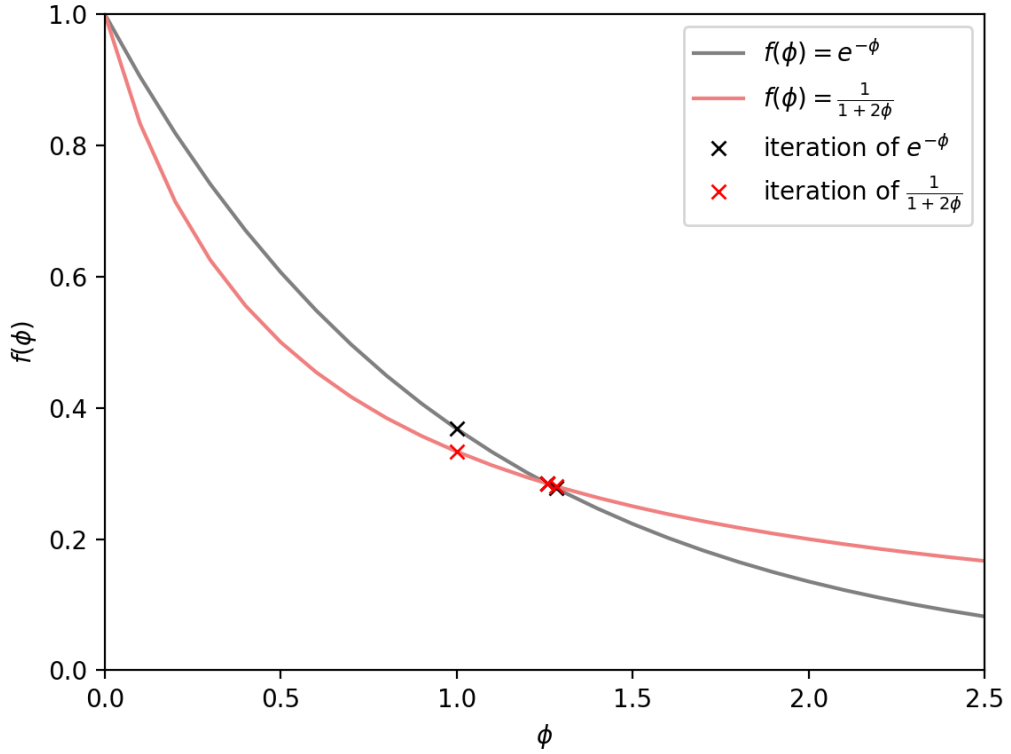
Figure 5.6: *Illustrating the single non-trivial root (i.e. $\phi \neq 0$) of Equation 5.20, plotting the left-hand side ($e^{-\phi}$) and the right-hand side ($1/(1+2\phi)$) as continuous curves. Convergence of the Newton-Raphson iteration scheme (overlaid crosses) is also shown, based on Equation 5.21 with a starting value of $\phi_i = 1$.*

From performing the Newton-Raphson iteration, with an initial guess of $\phi_i = 1$, the solution is returned as approximately 1.256. Now there is an exact expression for the threshold T_m^* (Equation 5.22), where the total moisture contours change from decreasing with T_c to increasing with T_c.

$$T_m^* = \frac{x_L}{u_2 \phi}, \quad \text{where} \quad \phi \simeq 1.256. \tag{5.22}$$

For the domain over India ($x_L = 3000$ km), given a value for the upper level advection, u_2, calculating T_m^*:

- for $u_2 = 2 \text{ ms}^{-1}$, $T_m^* \simeq 2$ weeks or 14 days,

- for $u_2 = 5$ ms^{-1}, $T_m^* \simeq 0.8$ weeks or 5.5 days,

- for $u_2 = 10$ ms^{-1}, $T_m^* \simeq 0.4$ weeks or 3 days.

5.3.6   Summary

Here it has been found that for $q_e = 1$, a length-scale $L_{mon} = u_2(T_c + T_m)$ emerges, over which the upper layer solution changes from dry ($q_2(0) = 0$) to moist ($q_2 = 1$). The same length-scale appears for the lower layer moisture q_1. When $T_m = 0$ (i.e. instantaneous adjustment in the lower layer, as in Chapter 4), the length-scale becomes $L_{mon} = u_2 T_c$, thus recovering the expression for L_{mon} in Chapter 4 — this theory generalises those results.

It has also been considered how the total moisture content over $0 < x < x_L$ depends upon T_c, T_m, and u_2. In particular, there is an interesting threshold value of T_m, denoted by T_m^*, which $\approx x_L/(1.256 u_2)$. Above this threshold the domain-integrated water increases as the convective timescale increases (i.e., as convection weakens). So there is one regime ($T_m < T_m^*$) in which weaker convection leads to less domain-integrated column water, and one regime ($T_m > T_m^*$) in which weaker convection leads to greater domain-integrated column water.

5.4   Time-dependent solutions

Although the time-dependent system of the dynamic lower layer model is generally solved numerically, alternative analytical methods can be applied to gain further insight. In this section, the configuration of the experiments undertaken with the dynamic lower layer model, in terms of varying the low-level moist inflow, upper layer advection and convection, is discussed. Then, using the methods in Subsection 5.2.1, the solutions valid for a small time after the system is initialised are presented. Using analytical techniques, expressions for the initial onset speed and the time taken for the system to adjust from an initial equilibrium (pre-onset) to a new equilibrium (post-onset) are derived. Finally, a strategy is given for calculating the onset speed and adjustment numerically.

5.4.1   Experiment configuration

The dynamic lower layer model is used to test the importance of several processes on the Indian monsoon onset. To do this, the model will be initialised in an equilibrium state, then one of the parameters representing a key process in terms of the monsoon onset will be varied. After a period of transition, a new equilibrium state will be reached with the varied parameter. The system is initialised from Equations 5.11a, 5.11b (for case $q_e = 1$) and Equations 5.12a, 5.12b (for case $q_e = 1 - e^{-x/L_e}$), in terms of parameters u_2, T_c, T_m, and q_e. These parameters represent the upper level wind speed, the timescale of convection, the timescale of low-level moisture replenishment and the equilibrium state in the absence of convection, respectively. Note that the combination of the first three

parameters determine the length-scale of the monsoon system, L_{mon}. Three experiments are designed by varying the parameters u_2, T_{c}, T_{m} in turn.

Firstly, the upper level wind speed is varied from u_2 to $\widetilde{u}_2$, which represents a strengthening or a weakening mid-level dry intrusion, depending on whether the upper level wind speed is increased or decreased. Secondly, the convective timescale, T_{c}, is changed to $\widetilde{T}_{\mathrm{c}}$, corresponding to a change in the amount of moisture transported from the lower to the upper atmosphere. At the time of monsoon onset, beginning in southeast India, the convective activity increases, leading to cloud formation. Thirdly, the timescale of moisture replenishment, T_{m}, becomes $\widetilde{T}_{\mathrm{m}}$. In terms of the monsoon, this represents an increase in the monsoon flux, i.e. an increase in the amount of moisture into the monsoon system from low-level flow, which occurs prior to monsoon onset. By considering each of the key processes individually, constituting three experiments, it should be evident which parameter in our model has the greatest impact on the monsoon onset. The effect is evaluated, analytically and numerically, in terms of onset speed and time to adjust from the initial equilibrium to a new equilibrium. The results of the three experiments are presented in Sections 5.5–5.7.

For the remainder of this section, an analytical approach is considered, based upon the small-time solutions of Subsection 5.2.1, to estimate both onset speed and the adjustment timescale. This is considered in general terms in Subsections 5.4.2–5.4.4, and more specifically in Sections 5.5–5.7, in terms of the individual experiments.

5.4.2 Small-time solutions

Key quantities of interest, such as the onset speed and the adjustment time, can be determined analytically. The results of this analysis can then be compared with the numerically calculated values. The state of the system in its initial equilibrium and its new equilibrium is known (by Section 5.3), and the methods of Section 5.2.1 are used to model q_2, q_1, after a small time.

The initial condition of equilibrium (i.e. with $\partial/\partial t = 0$) is used to determine q_{10}, q_{20} in the small-time solutions.

$$u_2 \frac{dq_{20}}{dx} = +\frac{1}{T_{\mathrm{c}}} \left(q_{10} - q_{20} \right), \tag{5.23a}$$

$$0 = -\frac{1}{T_{\mathrm{c}}} \left(q_{10} - q_{20} \right) - \frac{1}{T_{\mathrm{m}}} \left(q_{10} - q_{\mathrm{e}} \right). \tag{5.23b}$$

Taking the series representation of q_2, q_1, (Equations 5.6a, 5.6b), which begin at some equilibrium with $q_1 = q_{10}(x)$ and $q_2 = q_{20}(x)$, the series are rewritten in terms of the perturbed parameters $\widetilde{u}_2$, $\widetilde{T}_{\mathrm{c}}$, $\widetilde{T}_{\mathrm{m}}$, $\widetilde{L}_{\mathrm{mon}}$, $\widetilde{q}_{\mathrm{e}}$, that make up the new state for the system.

$$q_2 = q_{20} + t \left(\frac{1}{\widetilde{T}_{\mathrm{c}}} \left(q_{10} - q_{20} \right) - \widetilde{u}_2 q_{20}' \right) + \ldots \tag{5.24a}$$

$$q_1 = q_{10} + t \left(-\frac{1}{\widetilde{T}_{\mathrm{c}}} \left(q_{10} - q_{20} \right) - \frac{1}{\widetilde{T}_{\mathrm{m}}} \left(q_{10} - \widetilde{q}_{\mathrm{e}} \right) \right) + \ldots \tag{5.24b}$$

Case: $q_e = 1$

The solutions for case $q_e = 1$, following Equations 5.11a, 5.11b:

$$q_{20} = 1 - e^{-x/L_{mon}}, \tag{5.25a}$$

$$q_{10} = 1 - e^{-x/L_{mon}} \left(\frac{T_m}{T_c + T_m} \right). \tag{5.25b}$$

Simplifying some expressions that will be useful in formulating the series:

$$q'_{20} = \frac{e^{-x/L_{mon}}}{L_{mon}},$$

$$q_{10} - q_{20} = e^{-x/L_{mon}} \left(\frac{T_c}{T_c + T_m} \right),$$

$$q_{10} - \widetilde{q_e} = 1 - e^{-x/L_{mon}} \left(\frac{T_m}{T_c + T_m} \right) - \widetilde{q_e}.$$

Then the series for $q_e = 1$, up to $O(t^2)$, become:

$$q_2 = 1 - e^{-x/L_{mon}} + t \left(\frac{e^{-x/L_{mon}}}{T_c + T_m} \right) \left(\frac{T_c}{\widetilde{T_c}} - \frac{\widetilde{u_2}}{u_2} \right) + \frac{t^2}{2} \left[\frac{e^{-x/L_{mon}}}{T_c + T_m} \left(\frac{1}{\widetilde{T_c}} \left(\frac{T_m}{\widetilde{T_m}} - \frac{2T_c}{\widetilde{T_c}} \right) \right. \right.$$

$$\left. \left. + \frac{\widetilde{u_2}}{u_2 (T_c + T_m)} \left(\frac{2T_c + T_m}{\widetilde{T_c}} + \frac{\widetilde{u_2}}{u_2} \right) \right) + \frac{1}{\widetilde{T_c}\widetilde{T_m}} (\widetilde{q_e} - 1) \right] + \dots \tag{5.26a}$$

$$q_1 = 1 - e^{-x/L_{mon}} \left(\frac{T_m}{T_c + T_m} \right) + t \left[\left(\frac{e^{-x/L_{mon}}}{T_c + T_m} \right) \left(\frac{T_m}{\widetilde{T_m}} - \frac{T_c}{\widetilde{T_c}} \right) + \frac{1}{\widetilde{T_m}} (\widetilde{q_e} - 1) \right]$$

$$+ \frac{t^2}{2} \left[\frac{e^{-x/L_{mon}}}{T_c + T_m} \left(-\frac{T_m}{\widetilde{T_m}^2} + \frac{1}{\widetilde{T_c}} \left(\frac{T_c - T_m}{\widetilde{T_m}} + \frac{2T_c}{\widetilde{T_c}} - \frac{\widetilde{u_2}}{u_2} \right) \right) + \frac{\widetilde{T_c} + \widetilde{T_m}}{\widetilde{T_c}\widetilde{T_m}^2} (1 - \widetilde{q_e}) \right] + \dots \tag{5.26b}$$

$$q_1 + q_2 = 2 - e^{-x/L_{mon}} \left(\frac{T_c + 2T_m}{T_c + T_m} \right) + t \left[\left(\frac{e^{-x/L_{mon}}}{T_c + T_m} \right) \left(\frac{T_m}{\widetilde{T_m}} - \frac{\widetilde{u_2}}{u_2} \right) + \frac{1}{\widetilde{T_m}} (\widetilde{q_e} - 1) \right]$$

$$+ \frac{t^2}{2} \left[\frac{e^{-x/L_{mon}}}{T_c + T_m} \left(\frac{1}{\widetilde{T_m}} \left(\frac{T_c}{\widetilde{T_c}} - \frac{T_m}{\widetilde{T_m}} \right) + \frac{\widetilde{u_2}}{u_2 (T_c + T_m)} \left(\frac{T_c}{\widetilde{T_c}} + \frac{\widetilde{u_2}}{u_2} \right) \right) + \frac{1}{\widetilde{T_m}^2} (1 - \widetilde{q_e}) \right] + \dots \tag{5.26c}$$

Case: $q_e = 1 - e^{-x/L_e}$

And the solutions for case $q_e = 1 - e^{-x/L_e}$, following Equations 5.12a, 5.12b:

$$q_{20} = 1 - e^{-x/L_{mon}} \left(\frac{L_{mon}}{L_{mon} - L_e} \right) + e^{-x/L_e} \left(\frac{L_e}{L_{mon} - L_e} \right), \tag{5.27a}$$

$$q_{10} = 1 - e^{-x/L_{mon}} \left(\frac{u_2 T_m}{L_{mon} - L_e} \right) - e^{-x/L_e} \left(\frac{u_2 T_c - L_e}{L_{mon} - L_e} \right). \tag{5.27b}$$

Simplifying some expressions that will be useful in formulating the series:

$$q'_{20} = \left(e^{-x/L_{\text{mon}}} - e^{-x/L_{\text{e}}} \right) \left(L_{\text{mon}} - L_{\text{e}} \right)^{-1},$$

$$q_{10} - q_{20} = e^{-x/L_{\text{mon}}} \left(\frac{u_2 T_{\text{c}}}{L_{\text{mon}} - L_{\text{e}}} \right) - e^{-x/L_{\text{e}}} \left(\frac{u_2 T_{\text{c}}}{L_{\text{mon}} - L_{\text{e}}} \right),$$

$$q_{10} - \widetilde{q}_{\text{e}} = 1 - e^{-x/L_{\text{mon}}} \left(\frac{u_2 T_{\text{m}}}{L_{\text{mon}} - L_{\text{e}}} \right) - e^{-x/L_{\text{e}}} \left(\frac{u_2 T_{\text{c}} - L_{\text{e}}}{L_{\text{mon}} - L_{\text{e}}} \right) - \widetilde{q}_{\text{e}}.$$

The series for $q_{\text{e}} = 1 - e^{-x/L_{\text{e}}}$, up to $O(t)$, become:

$$
\begin{aligned}
q_2 \quad &= 1 - e^{-x/L_{\text{mon}}} \left(\frac{L_{\text{mon}}}{L_{\text{mon}} - L_{\text{e}}} \right) + e^{-x/L_{\text{e}}} \left(\frac{L_{\text{e}}}{L_{\text{mon}} - L_{\text{e}}} \right) \\
&\quad + t \left[\left(e^{-x/L_{\text{mon}}} - e^{-x/L_{\text{e}}} \right) \left(\frac{u_2}{L_{\text{mon}} - L_{\text{e}}} \right) \left(\frac{T_{\text{c}}}{\widetilde{T}_{\text{c}}} - \frac{\widetilde{u}_2}{u_2} \right) \right] + \dots
\end{aligned}
\tag{5.28a}
$$

$$
\begin{aligned}
q_1 \quad &= 1 - e^{-x/L_{\text{mon}}} \left(\frac{u_2 T_{\text{m}}}{L_{\text{mon}} - L_{\text{e}}} \right) - e^{-x/L_{\text{e}}} \left(\frac{u_2 T_{\text{c}} - L_{\text{e}}}{L_{\text{mon}} - L_{\text{e}}} \right) \\
&\quad + t \left[\left(\frac{u_2}{L_{\text{mon}} - L_{\text{e}}} \right) \left(e^{-x/L_{\text{mon}}} \left(\frac{T_{\text{m}}}{\widetilde{T}_{\text{m}}} - \frac{T_{\text{c}}}{\widetilde{T}_{\text{c}}} \right) - e^{-x/L_{\text{e}}} \left(\frac{T_{\text{c}} - L_{\text{e}}/2}{\widetilde{T}_{\text{m}}} - \frac{T_{\text{c}}}{\widetilde{T}_{\text{c}}} \right) \right) \right. \\
&\quad \left. + \frac{1}{\widetilde{T}_{\text{m}}} \left(\widetilde{q}_{\text{e}} - 1 \right) \right] + \dots
\end{aligned}
\tag{5.28b}
$$

$$
\begin{aligned}
q_1 + q_2 &= 2 - e^{-x/L_{\text{mon}}} \left(\frac{u_2 \left(T_{\text{c}} + 2 T_{\text{m}} \right)}{L_{\text{mon}} - L_{\text{e}}} \right) - e^{-x/L_{\text{e}}} \left(\frac{u_2 T_{\text{c}} - 2 L_{\text{e}}}{L_{\text{mon}} - L_{\text{e}}} \right) \\
&\quad + t \left[\left(\frac{u_2}{L_{\text{mon}} - L_{\text{e}}} \right) \left(e^{-x/L_{\text{mon}}} \left(\frac{T_{\text{m}}}{\widetilde{T}_{\text{m}}} - \frac{\widetilde{u}_2}{u_2} \right) - e^{-x/L_{\text{e}}} \left(\frac{T_{\text{c}} - L_{\text{e}}/2}{\widetilde{T}_{\text{m}}} - \frac{\widetilde{u}_2}{u_2} \right) \right) \right. \\
&\quad \left. + \frac{1}{\widetilde{T}_{\text{m}}} \left(\widetilde{q}_{\text{e}} - 1 \right) \right] + \dots
\end{aligned}
\tag{5.28c}
$$

5.4.3 Initial onset speed

Here, the method of determining the speed at which the monsoon onset "front" propagates across India in the model is outlined. Onset is declared once the total moisture, $q_1 + q_2$, reaches a particular threshold, say q_*, shown as a (black) contour of x and t (e.g. Figure 5.7).

Suppose there is some quantity $Q(x,t)$ with small-time representation $Q_0(x) + tQ_1(x) + \cdots$. The location at which $Q(x,t) = Q_*$ is tracked, where Q_* is some prescribed constant. The location is taken as $x = x_*$ when $t = 0$, so $Q_0(x_*) = Q_*$. The subsequent deviation of x from x_* at small time is tracked, by writing $x = x_* + \nu t$. Then:

$$Q_* = Q_0(x_* + \nu t) + t Q_1(x_* + \nu t) + O(t^2),$$

$$= Q_0(x_*) + \nu t Q'_0(x_*) + t Q_1(x_*) + O(t^2).$$

But, since $Q_* = Q_0(x_*)$, the term on the left hand side and the first term on the right cancel. Equating the remaining terms of $O(t)$ gives:

$$\nu = -Q_1(x_*)/Q_0'(x_*). \tag{5.29}$$

Here, $Q(x, t)$ could be taken as q_1, q_2, or indeed $q_1 + q_2$. The total moisture $q_1 + q_2$ is the main focus in this section due to its importance in defining monsoon onset, which is taken as a threshold of the total moisture. Equation 5.29 for the onset speed can then be applied to Equations 5.26c (when $q_e = 1$) and 5.28c (when $q_e = 1 - e^{-x/L_e}$).

Case: $q_e = 1$

From Equation 5.29, taking q_{*0} and q_{*1} as the first two terms in the $q_1 + q_2$ series expansion, an expression for the onset speed ν in the case $q_e = 1$ is written:

$$\nu = -\frac{u_2 (T_c + T_m)}{(T_c + 2T_m)} \left(\frac{T_m}{\widetilde{T}_m} - \frac{\widetilde{u}_2}{u_2} + \left(\frac{T_c + T_m}{\widetilde{T}_m} \right) (\widetilde{q}_e - 1) e^{x_*/L_{mon}} \right). \tag{5.30}$$

Note that the initial speed thus depends on the choice of x_*, or equivalently the value of the contour chosen.

Case: $q_e = 1 - e^{-x/L_e}$

From Equation 5.29, taking q_{*0} and q_{*1} as the first two terms in the $q_1 + q_2$ series expansion, an expression for the onset speed ν in the case $q_e = 1 - e^{-x/L_e}$ is written:

$$\nu = - \left[u_2 L_{mon} L_e \left(e^{-x_*/L_{mon}} \left(\frac{T_m}{\widetilde{T}_m} - \frac{\widetilde{u}_2}{u_2} \right) - e^{-x_*/L_e} \left(\frac{T_c - L_e/2}{\widetilde{T}_m} - \frac{\widetilde{u}_2}{u_2} \right) \right) \right.$$
$$\left. + \frac{L_{mon} L_e (L_{mon} - L_e)}{\widetilde{T}_m} (\widetilde{q}_e - 1) \right] \tag{5.31}$$
$$\times \left[\left(u_2 L_e (T_c + 2T_m) e^{-x_*/L_{mon}} + L_{mon} (u_2 T_c - 2L_e) e^{-x_*/L_e} \right)^{-1} \right].$$

If $L_e \to 0$, so $e^{-x_*/L_e} \to 0$, then:

$$\nu = - \left[u_2 L_{mon} L_e e^{-x_*/L_{mon}} \left(\frac{T_m}{\widetilde{T}_m} - \frac{\widetilde{u}_2}{u_2} \right) + \frac{L_{mon} L_e L_{mon}}{\widetilde{T}_m} (\widetilde{q}_e (x_*) - 1) \right]$$
$$\times \left[\frac{e^{x_*/L_{mon}}}{u_2 L_e (T_c + 2T_m)} \right]$$
$$= - \left[\frac{u_2 (T_c + T_m)}{(T_c + 2T_m)} \left(\frac{T_m}{\widetilde{T}_m} - \frac{\widetilde{u}_2}{u_2} \right) + \frac{u_2 (T_c + T_m)}{(T_c + T_m)} \left(\frac{T_c + T_m}{\widetilde{T}_m} \right) (\widetilde{q}_e - 1) e^{x_*/L_{mon}} \right].$$

Hence, the expression for the onset speed in the case $q_e = 1$ (Equation 5.30) is recovered, as expected.

5.4.4 Adjustment timescale

The adjustment time T_{adj} can be calculated by dividing the distance travelled, x_{adj}, by the onset speed, ν (Subsection 5.4.3), as per Equation 5.32. More formally, the same result can be derived by considering a location on the onset contour, x_*, then moving forwards/backwards along the contour by a distance of length $\pm L$. Thus, $x_* \pm L = x_* + \nu T$ can be written, with ν being the onset speed and T representing time. Letting $T = T_{\mathrm{adj}}$ and $L = x_{\mathrm{adj}}$, cancelling terms and rearranging, gives the required result.

$$T_{\mathrm{adj}} = \left| \frac{x_{\mathrm{adj}}}{\nu} \right|. \tag{5.32}$$

The distance travelled by the onset "front", x_{adj}, is the difference between the initial location of onset, x_*, and the location of onset at the new equilibrium, $\widetilde{x}_*$, following a change to one of the variables (Equation 5.33). Both locations, x_* and $\widetilde{x}_*$, can be determined from the equilibrium solutions in Section 5.3, as system is moving from an initial equilibrium state to another equilibrium state. The cases of q_{e} are considered separately to determine the adjustment distance, x_{adj}.

$$x_{\mathrm{adj}} = \widetilde{x}_* - x_*. \tag{5.33}$$

Case: $q_{\mathrm{e}} = 1$

Using the results of Section 5.3.1, the initial expression for the total moisture (scaled by $1/2$) is given by Equation 5.34. The total moisture (scaled by $1/2$) at the end of the experiment, having reached a new equilibrium, is given by Equation 5.35, where $\widetilde{q}_{\mathrm{e}}$ is a multiple of q_{e}.

$$\frac{q_1 + q_2}{2} = 1 - \frac{e^{-x/L_{\mathrm{mon}}}}{2} \left(\frac{T_{\mathrm{c}} + 2T_{\mathrm{m}}}{T_{\mathrm{c}} + T_{\mathrm{m}}} \right). \tag{5.34}$$

$$\frac{q_1 + q_2}{2} = \widetilde{q}_{\mathrm{e}} \left(1 - \frac{e^{-x/\widetilde{L}_{\mathrm{mon}}}}{2} \left(\frac{\widetilde{T}_{\mathrm{c}} + 2\widetilde{T}_{\mathrm{m}}}{\widetilde{T}_{\mathrm{c}} + \widetilde{T}_{\mathrm{m}}} \right) \right). \tag{5.35}$$

These equations can be written specifically for the onset contour, so that $q_* = (q_1 + q_2)/2$, $x_* + x$ and $\widetilde{x}_* + \widetilde{x}$. The threshold for onset is taken as $(q_1 + q_2)/2 = 0.5$, thus $q_* = 0.5$ and is constant throughout. On rearranging, expressions are derived for the initial (x_*) and the final $(\widetilde{x}_*)$ location of the onset contour.

$$x_* = -L_{\mathrm{mon}} \ln \left(\frac{T_{\mathrm{c}} + T_{\mathrm{m}}}{T_{\mathrm{c}} + 2T_{\mathrm{m}}} \right). \tag{5.36}$$

$$\widetilde{x}_* = -\widetilde{L}_{\mathrm{mon}} \ln \left[\left(2 - \frac{1}{\widetilde{q}_{\mathrm{e}}} \right) \left(\frac{\widetilde{T}_{\mathrm{c}} + \widetilde{T}_{\mathrm{m}}}{\widetilde{T}_{\mathrm{c}} + 2\widetilde{T}_{\mathrm{m}}} \right) \right]. \tag{5.37}$$

Using Equation 5.33, an expression for the adjustment distance is derived in the case of $q_{\mathrm{e}} = 1$.

$$x_{\mathrm{adj}} = -\widetilde{L}_{\mathrm{mon}} \ln \left[\left(2 - \frac{1}{\widetilde{q}_{\mathrm{e}}} \right) \left(\frac{\widetilde{T}_{\mathrm{c}} + \widetilde{T}_{\mathrm{m}}}{\widetilde{T}_{\mathrm{c}} + 2\widetilde{T}_{\mathrm{m}}} \right) \right] + L_{\mathrm{mon}} \ln \left(\frac{T_{\mathrm{c}} + T_{\mathrm{m}}}{T_{\mathrm{c}} + 2T_{\mathrm{m}}} \right). \tag{5.38}$$

Thus, Equation 5.32 can be expanded using Equations 5.30 and 5.38 for ν and x_{adj} respectively, giving an expression for the adjustment time, T_{adj}, in terms of initial and perturbed parameters.

$$T_{\mathrm{adj}} = \frac{\widetilde{T}_{\mathrm{m}}\left(T_{\mathrm{c}}+2T_{\mathrm{m}}\right)\left(\widetilde{L}_{\mathrm{mon}}\ln\left[\left(2-\frac{1}{\widetilde{q}_{\mathrm{e}}}\right)\left(\frac{\widetilde{T}_{\mathrm{c}}+\widetilde{T}_{\mathrm{m}}}{\widetilde{T}_{\mathrm{c}}+2\widetilde{T}_{\mathrm{m}}}\right)\right]-L_{\mathrm{mon}}\ln\left(\frac{T_{\mathrm{c}}+T_{\mathrm{m}}}{T_{\mathrm{c}}+2T_{\mathrm{m}}}\right)\right)}{\left(T_{\mathrm{c}}+T_{\mathrm{m}}\right)\left(u_2 T_{\mathrm{m}}-\widetilde{u}_2\widetilde{T}_{\mathrm{m}}+L_{\mathrm{mon}}\left(\widetilde{q}_{\mathrm{e}}-1\right)e^{x_*/L_{\mathrm{mon}}}\right)}. \tag{5.39}$$

The expression for the adjustment time is a key formula that will be used in the remainder of this section. Although it looks complicated in this form, various simplifications will be considered (i.e., changing only one parameter at a time), which will allow some insight to be gained.

Case: $q_{\mathrm{e}} = 1 - e^{-x/L_{\mathrm{e}}}$

In this case, the situation is more complex as there are two length-scales, L_{mon} and L_{e}. The analytic theory will be considered with the case $q_{\mathrm{e}} = 1$ only, but numerical results will be shown for both cases. Strong agreement between the analytical theory and the numerical results for the case $q_{\mathrm{e}} = 1$ would indicate that the theory could be extended to the case $q_{\mathrm{e}} = 1 - e^{-x/L_{\mathrm{e}}}$, but the simplicity of the method would be lost.

5.4.5   Numerical strategy

To solve Equations 5.11a, 5.11b, and 5.12a, 5.12b, numerically, a fourth-order accuracy Runge-Kutta scheme is used to step the quantities q_1 and q_2 in time. An equi-spaced finite difference grid of second-order accuracy (Fornberg, 1998) is used to approximate the first spatial derivative $\partial/\partial x$. The grid in x has 128 points and the code is run for 5000 time-steps with an interval of 500 seconds.

The results of each experiment will be displayed as filled contour plots of moisture (example style in Figure 5.7), with respect to distance and time. Subplots are used to show the evolution of moisture in the lower layer, q_1, the flux F, the upper layer moisture, q_2, and the total column moisture, $q_1 + q_2$. The latter is halved, so that all subplots can be shown with the same levels and colour-scale. Distance is shown on the x-axis, which runs from northeastern Iran to the Indian Ocean south of Indonesia, over about $10\,000$ km. The region of interest, India, lies approximately in the range $0 < x < 3000$. The y-axis depicts time. A sufficient period of time is needed to ensure that the system reaches its new equilibrium. Here, 0–4 weeks is deemed sufficient. The monsoon length-scale, L_{mon}, for each state of equilibrium will be highlighted. The Indian monsoon usually takes six weeks to progress over all of India, so it is expected that our model adjusts faster than the real-world system.

The onset of the monsoon is defined as a contour of the adjusted total moisture $(q_1 + q_2)/2$, which will be shown as a thick black contour on the relevant figures in Sections 5.5–5.7 (as shown in Figure 5.7), at a specified threshold value of 0.5 (dimensional units of kg m^{-2}). The total moisture is a more relevant quantity for determining onset than
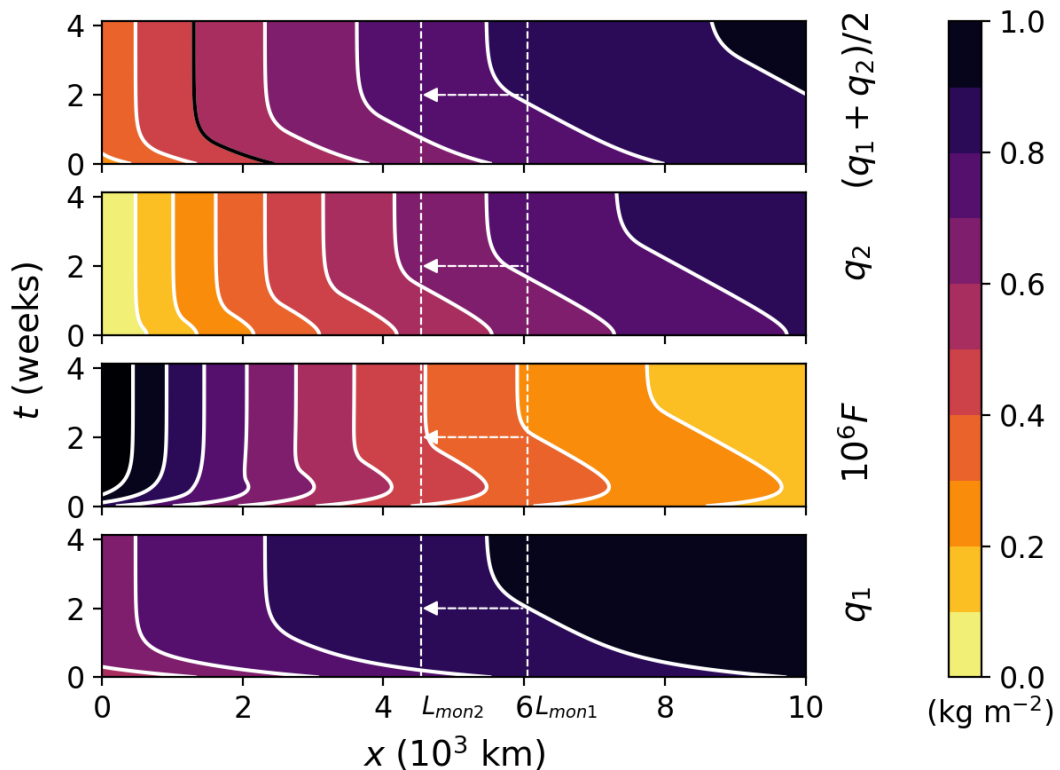
Figure 5.7: *Example figure style for the experiment results, derived numerically.*

solely the upper level moisture. Although this is an arbitrary choice, it is justified because it is the direction of propagation and the shape of the onset front that is key. Using an alternative value would move the position of the contour spatially, but it would not alter the shape and direction of travel, which is the main concerned.

Empirically, it seems that the onset speed, ν, i.e. the average speed of progression between the initial and the new equilibrium, remains approximately constant across contours, for a given set of variables. The distance and time of adjustment, x_{adj} and T_{adj}, between the states of equilibrium increase proportionally when contours towards the southeast, at higher x values, are considered.

Determination of the adjustment distance, x_{adj}, is equivalent numerically and analytically, as the system is initialised at equilibrium (as per the equations in Section 5.3), and run until a new equilibrium state is reached. So, in the case $q_{\text{e}} = 1$, x_{adj} is simply Equation 5.38. Calculating T_{adj} numerically is more complicated. A test based on the area under the total moisture contours is conceived, with T_{adj} determined from where this integrated quantity drops below a defined threshold. Equation 5.40 defines the integral and threshold. The threshold level is taken as 0.1, i.e. at 90%. Here, $q_{\text{start}}(x)$ and $q_{\text{end}}(x)$ refer to the total moisture at the initial and final equilibrium states, known analytically, whilst $q(x, t)$ is the time-evolving total moisture, derived numerically. The integral is designed to equal 1 initially (i.e. when $t = 0$), then decrease over time, tending to zero as $t \to \infty$.

The limits of integration are derived from the location of the onset contour at its initial

equilibrium, x_*, and at its new equilibrium, $\widetilde{x}_*$. Then the area to be integrated is widened by a margin of $\lambda = 50$ km. This takes into account the varying monsoon length-scales for each case, impacting the location of the onset, whilst maintaining a sufficient area to ensure robustness of results.

Another method based on the location of the onset contour (x_*) was also tested, using the expression $(x_* - x_{*\mathrm{end}})/(x_{*\mathrm{start}} - x_{*\mathrm{end}})$. However, using the location of a single contour was deemed more sensitive and less robust than the moisture-based integral method.

$$\frac{1}{x_L - x_0} \int_{x_0}^{x_L} \left| \frac{q(x,t) - q_{\mathrm{final}}(x)}{q_{\mathrm{initial}}(x) - q_{\mathrm{final}}(x)} \right| \, dx \;\; < \;\; 0.1, \quad \begin{array}{l} \text{where for } x_* > \widetilde{x}_*, \quad \left\{ \begin{array}{l} x_0 = x_* + \lambda, \\[1em] x_L = \widetilde{x}_* - \lambda, \end{array} \right. \\[2em] \text{and for } x_* < \widetilde{x}_*, \quad \left\{ \begin{array}{l} x_0 = x_* - \lambda, \\[1em] x_L = \widetilde{x}_* + \lambda. \end{array} \right. \end{array}$$

$$(5.40)$$

Once the adjustment time has been determined numerically, given that the adjustment distance is already known, the average speed of the onset "front" can be calculated, using speed = distance/time. Note that a negative value of onset speed is expected, indicating a direction towards negative x, reflecting the real-world onset travelling from southeast to northwest India.

5.5   Experiment: increasing the rate of moisture inflow

At pre-onset (early May), the low-level southwesterly winds increase in speed and depth, bringing an influx of moisture to southeast India, triggering monsoon onset (June). In our model, the effect of increasing the monsoon flux and the depth of monsoon flow can be tested separately, gauging the response of the monsoon onset. The monsoon flux is determined by the rate of replenishment, occurring on timescale T_{m}. Decreasing T_{m} means a greater amount of moisture inflow (higher monsoon flux), from more moist low-level flow and/or from increased surface evaporation. The importance of lower tropospheric humidity, which dominates total column water vapour (Holloway and Neelin, 2009, 2010), in convective onset (Schiro and Neelin, 2019) has been noted in Chapter 3.

Here, several different options for decreasing the timescale of replenishment are investigated. All other quantities such as upper level advection, u_2, are kept constant once the system has been initialised, with only the timescale of replenishment, T_{m}, being varied to $\widetilde{T}_{\mathrm{m}}$. The configurations for both cases of q_{e} are summarised in Table 5.1. Firstly, initialising with convective (T_{c}) and replenishment timescales (T_{m}) of 7 days, then halve the replenishment timescale to $\widetilde{T}_{\mathrm{m}} = 3.5$ days. This effectively doubles the moisture inflow to the system, which would be expected to trigger monsoon onset. The choice of 7 days is at the higher end of the range given in Subsection 3.3.1. Next, timescales at the lower end of

the range are considered, initialising with $T_\mathrm{c} = T_\mathrm{m} = 2$ days, and reducing the replenishment timescale to $\widetilde{T}_\mathrm{m} = 1$ day. Finally, an asymmetric configuration is investigated, with $T_\mathrm{c} = 1$ day and $T_\mathrm{m} = 7$ days initially, then, as before, halving the replenishment timescale to $\widetilde{T}_\mathrm{m} = 3.5$ days. If unequal values for the convective and replenishment timescales are to be considered, then it could be argued that the convective timescale is shorter than the replenishment timescale. It is dependent on the definition and/or measurement of either timescale. For example, in our asymmetric case, the replenishment timescale is taken to reflect changes to the Somali Jet, which brings a large moisture influx over the Arabian Sea. Variations in such a robust air current may occur over timescales of a week or more. In contrast, the convective timescale is chosen to represent shorter-lived events, up to day, such as formation of convective clouds.

Table 5.1: *Configuration of parameters for varying T_m experiment.*

T_c (days)	T_m (days)	$\widetilde{T}_\mathrm{m}$ (days)	u_2 (ms^{-1})
7	7	3.5	5
2	2	1	5
1	7	3.5	5

5.5.1   Analytical prediction

For this experiment, the timescale of the monsoon flux is varied T_m to $\widetilde{T}_\mathrm{m}$, keeping the timescale for the rate of convection, the upper level advection, and q_e, constant throughout. Calculating the speed of onset ν from Equation 5.30, with $q_\mathrm{e} = 1$, $\widetilde{q}_\mathrm{e} = q_\mathrm{e} = 1$, $\widetilde{T}_\mathrm{c} = T_\mathrm{c}$ and $\widetilde{u}_2 = u_2$:

$$\nu = -\frac{u_2 \left(T_\mathrm{c} + T_\mathrm{m} \right)}{\left(T_\mathrm{c} + 2T_\mathrm{m} \right)} \left(\frac{T_\mathrm{m}}{\widetilde{T}_\mathrm{m}} - 1 \right), \quad \text{for } \widetilde{T}_\mathrm{m} \neq T_\mathrm{m}. \tag{5.41}$$

If $\widetilde{T}_\mathrm{m} < T_\mathrm{m}$, as in these experiments, then $\nu < 0$, corresponding to contours moving to the left (i.e., towards northwest India), as expected. A constraint of $\widetilde{T}_\mathrm{m} \neq T_\mathrm{m}$ is explicitly stated, otherwise the onset speed, and thus x_adj and T_adj, would vanish. The point of these experiments is to vary one of the parameters, otherwise the system remains in its initial equilibrium, so it would be counter-intuitive to set $\widetilde{T}_\mathrm{m}$ to T_m. The distance travelled by contours from an initial to a new equilibrium, x_adj, from Equation 5.38, is:

$$x_\mathrm{adj} = -u_2 \left(T_\mathrm{c} + \widetilde{T}_\mathrm{m} \right) \ln \left(\frac{T_\mathrm{c} + \widetilde{T}_\mathrm{m}}{T_\mathrm{c} + 2\widetilde{T}_\mathrm{m}} \right) + u_2 \left(T_\mathrm{c} + T_\mathrm{m} \right) \ln \left(\frac{T_\mathrm{c} + T_\mathrm{m}}{T_\mathrm{c} + 2T_\mathrm{m}} \right). \tag{5.42}$$

Similarly, the adjustment time, T_adj, by Equation 5.39, is:

$$T_\mathrm{adj} = \widetilde{T}_\mathrm{m} \left(\frac{T_\mathrm{c} + 2T_\mathrm{m}}{T_\mathrm{m} - \widetilde{T}_\mathrm{m}} \right) \left[\left(\frac{T_\mathrm{c} + \widetilde{T}_\mathrm{m}}{T_\mathrm{c} + T_\mathrm{m}} \right) \ln \left(\frac{T_\mathrm{c} + \widetilde{T}_\mathrm{m}}{T_\mathrm{c} + 2\widetilde{T}_\mathrm{m}} \right) - \ln \left(\frac{T_\mathrm{c} + T_\mathrm{m}}{T_\mathrm{c} + 2T_\mathrm{m}} \right) \right]. \tag{5.43}$$

Note that this adjustment time is independent of the upper level wind speed, u_2. For particular cases, Equation 5.43 can be further simplified. For instance, if an asymmetric case where $T_\mathrm{c} \ll T_\mathrm{m}$ is considered, then:

$$T_\mathrm{adj} = 2\widetilde{T}_\mathrm{m} \ln 2 \simeq 1.4 \, \widetilde{T}_\mathrm{m}, \quad \text{for } T_\mathrm{c} \ll T_\mathrm{m} \text{ and } T_\mathrm{c} \ll \widetilde{T}_\mathrm{m}. \tag{5.44}$$

5.5.2   Numerical analysis

Solving the system with parameters as per Table 5.1, for cases $q_e = 1$ and $q_e = 1 - e^{-x/L_e}$, gives rise to Figure 5.8. Mostly importantly, each panel in Figure 5.8 shows a monsoon onset, defined on a moisture threshold of $(q_1 + q_2)/2 = 0.5$, which travels from southeast to northwest (i.e. in decreasing x direction) India, against a northwesterly wind of 5 ms^{-1} in the upper layer.

The lower layer moisture, q_1, behaves similarly for all cases, with increasing moisture content over time until the new equilibrium is reached. This is to be expected, given that the parameter being varied, T_m, represents the moisture flow or monsoon flux into the system, which is being increased. The lower layer moisture is greatest towards southeast India ($x = 1$), reflecting the real-world monsoon system. For the cases of $q_e = 1 - e^{-x/L_e}$, the moisture content approaches zero towards the $x = 0$ boundary, following the equilibrium solutions. The adjustment time and distance are both smaller at low x, and larger at high x, increasing proportionally so that the onset speed remains constant. For the cases of $q_e = 1$, the lower layer moisture contours travel further to reach the new equilibrium, compared with the cases of $q_e = 1 - e^{-x/L_e}$. When the initial replenishment timescale, T_m, is shorter (Figures 5.8c, 5.8d), the lower moisture adjusts faster and over a shorter distance.

The flux, F, for cases $q_e = 1$, increases rapidly at first, responding to the sudden variation of T_m, then decreases over time as a new steady-state is reached, and the difference in moisture content between the layers remains constant. This pattern is easier to see in Figure 5.8a, as the initial increase is very fast in Figures 5.8c, 5.8e. The flux is greatest towards small x values, where $q_1 - q_2$ is greatest, due to the lateral boundary condition on the upper layer ($q_2 = 0$ at $x = 0$). For the cases where $q_e = 1 - e^{-x/L_e}$, a flux maximum located around $x = 2000$ km is observed. This feature is an indirect result of the lateral boundary condition on the upper layer and the equilibrium solutions, as both the lower and upper layers are completely dry at $x = 0$. The flux maximum could be interpreted as being associated with increased cloud activity ahead of the monsoon onset "front". To the right of the maximum, the flux contours follow the same pattern as the $q_e = 1$ cases, with an initial rapid increase and then decreasing to the new equilibrium value. To the left, the flux decreases towards zero.

The upper layer moisture evolution, q_2, looks approximately like the lower layer, moistening over time to reach the new equilibrium state and increasing in moisture content with increasing x. Close to $x = 0$, the upper layer is kept dry by the boundary constraint, representing the dry mid-upper level flow from the northwest. For Figures 5.8a, 5.8b, the upper layer is significantly less moist than the lower layer, due to the longer convective timescale ($T_c = 7$ days), meaning that less moisture is transported from the lower to the upper layer. Note that there is also advection in the upper layer, acting to remove moisture out of the domain at the southeastern edge.

The total moisture, $(q_1 + q_2)/2$, follows the lower and upper layer moisture, increasing

(a) $q_e = 1$, *initialising with* $T_c = 7$ *&*
$T_m = 7$ *days, then reducing to* $\widetilde{T}_m = 3.5$ *days.*

(b) $q_e = 1 - e^{-x/L_e}$, *initialising with* $T_c = 7$
& $T_m = 7$ *days, then reducing to* $\widetilde{T}_m = 3.5$ *days.*

(c) $q_e = 1$, *initialising with* $T_c = 2$ *&*
$T_m = 2$ *days, then reducing to* $\widetilde{T}_m = 1$ *day.*

(d) $q_e = 1 - e^{-x/L_e}$, *initialising with* $T_c = 2$
& $T_m = 2$ *days, then reducing to* $\widetilde{T}_m = 1$ *day.*

(e) $q_e = 1$, *initialising with* $T_c = 1$ *&*
$T_m = 7$ *days, then reducing to* $\widetilde{T}_m = 3.5$ *days.*

(f) $q_e = 1 - e^{-x/L_e}$, *initialising with* $T_c = 1$
& $T_m = 7$ *days, then reducing to* $\widetilde{T}_m = 3.5$ *days.*

Figure 5.8: *Doubling moisture inflow by reducing the relaxation timescale from* T_m *to* $\widetilde{T}_m$.
$u_2 = 5\ ms^{-1}$ *and* $L_e = 1000\ km$.

with t and x. The monsoon length-scales, L_{mon_1} and L_{mon_2}, illustrate the distance that the contours travel to move from one equilibrium to a new equilibrium. The black contour, delineating monsoon onset, begins in the range $x = 2000$ to $x = 3000$ km for Figures 5.8a, 5.8b, 5.8e, 5.8f, which is approximately southeast India. For these parameter choices, the adjustment time between equilibria, representing the time taken for the onset to progress

over India, is approximately a week. This is considerably faster than the observed monsoon onset, which takes about 6 weeks to progress over India. Additionally, the onset in the model travels around 1000 km, compared to 3000 km (distance over India). For Figures 5.8c, 5.8d, the onset contour starts at $x = 1000$ to $x = 2000$ km, which is further northwest than the observed monsoon onset. The monsoon length-scales are also shorter and closer together here, when T_c and T_m are of order 1–2 days. The adjustment time (2-3 days) and distance (<500 km) for $T_c = T_m = 2$ days is much smaller than the other cases or the observed monsoon.

(a) *Case $q_e = 1$.*

(b) *Case $q_e = 1 - e^{-x/L_e}$.*
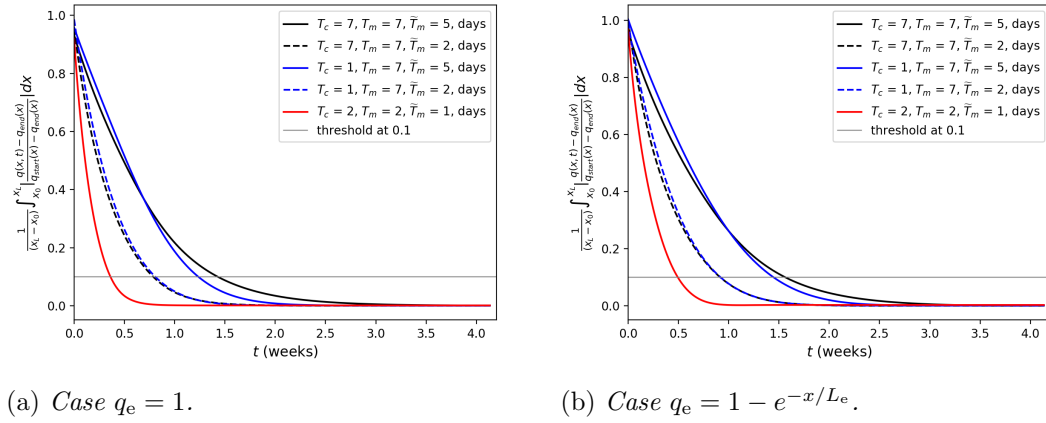
Figure 5.9: *Convergence of Equation 5.40 against time, t, for varying T_m to $\widetilde{T}_m$. $u_2 = 5$ ms^{-1} and $L_e = 1000$ km.*

To quantify monsoon onset, the test described in Subsection 5.4.5 is applied to determine the adjustment time. Figure 5.9 shows the convergence of Equation 5.40 for each case of q_e, against the time in weeks. The time for the system to adjust to the new equilibrium is the point at which the curves cross the threshold line of 0.1. The cases where T_c and T_m are longer, of order 7 days, take longer to converge and thus give longer adjustment times, irrespective of $\widetilde{T}_m$. The quickest to converge is $T_c = T_m = 2$ days.

5.5.3   Comparison

Figures 5.10 and 5.11 show the results of applying the analytical theory and using numerical techniques to determine the adjustment time, T_{adj}, and the onset speed, ν, against $\widetilde{T}_m$. Note that only numerical results are shown for the case $q_e = 1 - e^{-x/L_e}$.

Firstly, considering the adjustment time, it can be seen from both panels in Figure 5.10 that T_{adj} is (approximately) linearly related to $\widetilde{T}_m$. Thus, the scaling is performing reasonably well. The difference of a (constant) multiplicative factor is trivial, as the gradient and shape are the key aspects to represent. Presumably, much closer agreement could be achieved by changing the critical tolerance in the numerics, from 10% to something else. The greater the increase in moisture inflow, i.e. the smaller $\widetilde{T}_m$, the faster the adjustment time. By inspection, the gradient of the asymmetric case, $T_c = 1$, $T_m = 7$, agrees with Equation 5.44. The adjustment times for each of the parameter combinations are all below

2 weeks, meaning that the system adapts unrealistically fast compared to the observed monsoon. The analytical and numerical results are similar in that they have roughly the same gradient, but there is a discrepancy of 1–2 days between them.

(a) *Case $q_e = 1$.*

(b) *Case $q_e = 1 - e^{-x/L_e}$.*
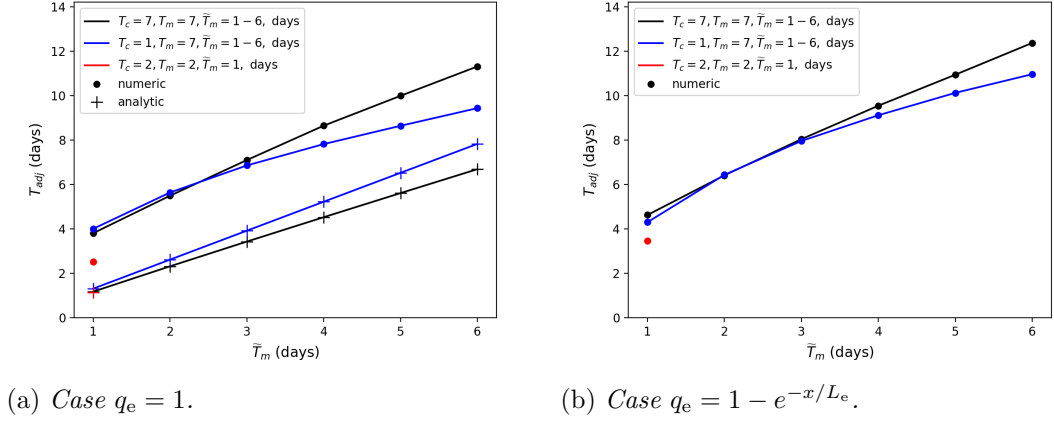
Figure 5.10: *Adjustment time, T_{adj}, against $\widetilde{T}_{\mathrm{m}}$, for analytical and numerical results. $u_2 = 5~ms^{-1}$ and $L_e = 1000~km$.*

(a) *Case $q_e = 1$.*

(b) *Case $q_e = 1 - e^{-x/L_e}$.*
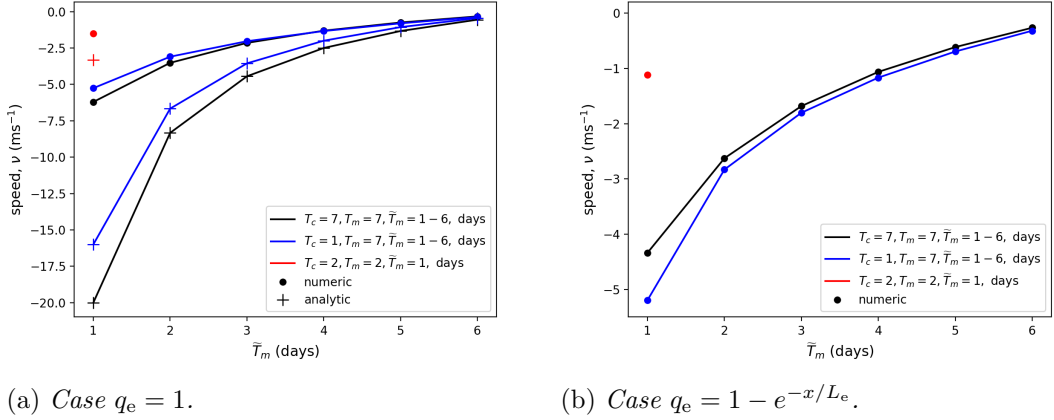
Figure 5.11: *Onset speed, ν, against $\widetilde{T}_{\mathrm{m}}$, for analytical and numerical results. $u_2 = 5~ms^{-1}$ and $L_e = 1000~km$.*

Secondly, looking at Figure 5.11, the onset speed is close to zero when $\widetilde{T}_{\mathrm{m}} \to T_{\mathrm{m}}$, and increases when $\widetilde{T}_{\mathrm{m}}$ decreases. Note that the negative value of onset speed is indicating the direction, from southeast to northwest India (i.e. decreasing x direction). The rate of increase in speed becomes greater towards $\widetilde{T}_{\mathrm{m}} = 1$ day. This is particularly evident in the analytical theory. Considering the analytical expression for onset speed, Equation 5.41, it can be seen that $\nu \to 0$ as $\widetilde{T}_{\mathrm{m}} \to T_{\mathrm{m}}$, and $\nu \to -\infty$ as $\widetilde{T}_{\mathrm{m}} \to 0$. The numerical results agree more strongly with the analytical results at higher values of $\widetilde{T}_{\mathrm{m}}$, but diverge towards $\widetilde{T} = 1$. In terms of the real-world monsoon, speeds of <5 ms^{-1} are more rational, indicating that timescales of $T_{\mathrm{m}} = 7$ days and $\widetilde{T}_{\mathrm{m}} = 3 - 4$ days are more representative.

It is concluded that the analytical expressions for front speed ν (Equation 5.41) and adjustment timescale T_{adj} (Equation 5.43) are useful predictors of the actual behaviour.

A key point is that, for this experiment, the adjustment timescale is independent of u_2: the contour speed and adjustment length are both proportional to u_2, but this dependence cancels out when calculating the adjustment timescale.

5.6   Experiment: varying upper level advection

Here, the role that the dry intrusion from northwest India plays in moderating the onset of the monsoon is investigated. Parker et al. (2016) and Krishnamurti et al. (2010) emphasise that these dry intrusions may slow progress of monsoon onset, leading to monsoon breaks and potentially drought. Conversely, a weakening dry intrusion would allow the monsoon onset to propagate to the northwest at a greater speed. Using our model, the effect a dry intrusion has on the monsoon onset can be tested by varying the upper level advection, u_2, to $\widetilde{u}_2$. Table 5.2 summarises the parameter configurations that will be investigated. Firstly, the system will be initialised with $T_c = T_m = 7$ days and $u_2 = 5$ ms^{-1}, then the strength of the upper level advection will be increased to $\widetilde{u}_2 = 7.5$ ms^{-1}, indicating a strengthening dry intrusion. The second configuration is similar, but the upper level advection is halved. Finally, a reduction of the upper level wind speed is considered, in an asymmetric case, with $T_c = 1$ day and $T_m = 7$ days.

Table 5.2: *Configuration of parameters for varying u_2 experiment.*

T_c (days)	T_m (days)	u_2 (ms^{-1})	$\widetilde{u}_2$ (ms^{-1})
7	7	5	7.5
7	7	5	2.5
1	7	5	2.5

5.6.1   Analytical prediction

Here, the strength of the upper level advection is varied, changing only the wind speed, u_2, to $\widetilde{u}_2$. The speed of onset ν with varying u_2 is determined from Equation 5.30, with $q_e = 1$:

$$\nu = \frac{(T_c + T_m)}{(T_c + 2T_m)} \left(\widetilde{u}_2 - u_2\right), \text{ for } \widetilde{u}_2 \neq u_2. \tag{5.45}$$

The distance travelled by contours from an initial to a new equilibrium, x_{adj}, from Equation 5.38, with $q_e = 1$:

$$x_{\text{adj}} = \left(\widetilde{u}_2 - u_2\right)(T_c + T_m) \ln\left(\frac{T_c + 2T_m}{T_c + T_m}\right). \tag{5.46}$$

Thus, the adjustment time, from Equation 5.39, is given by:

$$T_{\text{adj}} = (T_c + 2T_m) \ln\left(\frac{T_c + 2T_m}{T_c + T_m}\right). \tag{5.47}$$

Note that this adjustment time, for varying u_2, is in fact independent of u_2 itself. For this experiment, T_{adj} depends only on the combination of the replenishment and convective timescales. Also, if the timescales of convection and replenishment are of a similar

magnitude, then:

$$T_{\text{adj}} = 3 \ln\left(\frac{3}{2}\right) \simeq 1.2 \, T_{\text{m}}, \text{ for } T_{\text{c}} \sim T_{\text{m}}. \tag{5.48}$$

5.6.2 Numerical analysis

Here the system is solved with parameters as per Table 5.2, for cases $q_{\text{e}} = 1$ and $q_{\text{e}} = 1 - e^{-x/L_{\text{e}}}$. Figure 5.12 shows the results. A forwards (southeast to northwest) propagating onset is shown by the black contour when the upper level advection is decreased, e.g. in Figures 5.12c–5.12f. However, when the upper level advection is increased, e.g. in Figures 5.12a–5.12b, an onset travelling in the reverse direction is observed. This highlights the role that dry intrusions can play in halting the progress of the Indian monsoon, potentially leading to monsoon breaks.

Considering Figures 5.12a–5.12b, it can be seen that the lower and upper moisture, and hence the total moisture, decreases over time until a new equilibrium state is reached. It is particularly evident in q_2. This is not surprising, as the strong upper level advection acts to remove moisture at the southeastern edge of the domain. There is also movement of moisture from northwest to southeast (increasing x direction) in both layers, reflecting the direction of travel of the onset "front". As discussed previously, there is a flux maximum for the case $q_{\text{e}} = 1 - e^{-x/L_{\text{e}}}$, which is evident from the equilibrium solutions, as $q_1 = q_2 = 0$ and thus $F = 0$ at the lateral boundary, $x = 0$. For the case $q_{\text{e}} = 1$ and to the right of the maximum in case $q_{\text{e}} = 1 - e^{-x/L_{\text{e}}}$, the flux increases at a reasonably fast rate initially. This is in response to the reduction of moisture in the upper layer as advection strengthens. Then, the flux decreases more gradually to its steady-state value. For the total moisture subplot, a reverse onset is observed, with the total moisture decreasing, as upper level advection is dominant over the timescale of moisture inflow or convection. The monsoon length-scale, L_{mon}, increases.

For the cases with a southeast to northwest propagating onset, Figures 5.12c–5.12f, the lower, upper and total moisture contents all increase at a similar rate over time. The moisture content in the upper and lower layers is comparable in each panel of Figure 5.12. Weakening of the upper level winds allows moisture to accumulate in the layers. The adjustment time and distance, based on the black contour, from the initial to the new equilibrium are similar for these cases, taking 1–2 weeks to progress about 1000 km. Moreover, the adjustment time and distance for Figures 5.12a–5.12b seems comparable to Figures 5.12c–5.12d, albeit in the opposing direction. The system adjusts faster and the onset travels a shorter distance than the observed monsoon.

The upper level moisture, q_2, is very low at the northwest limit, due to the boundary condition. For the $q_{\text{e}} = 1 - e^{-x/L_{\text{e}}}$ case, q_1, and thus the flux, are also zero at $x = 0$. Whereas for $q_{\text{e}} = 1$, when $T_{\text{c}} = T_{\text{m}} = 7$ days, the low level moisture is fairly high at low x. For these Figures 5.12c–5.12f, the flux for $x > 3000$ km decreases over time. At lower x values, the contours for the flux decrease below the new equilibrium value, then increase slightly.
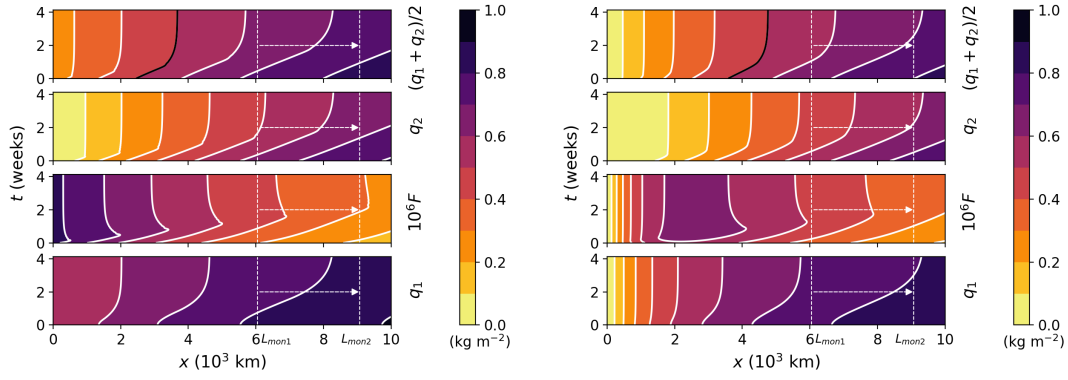
(a) $q_e = 1$, with $T_c = T_m = 7$ days $\&$ $u_2 = 5$ ms^{-1}, then increase to $\widetilde{u}_2 = 7.5$ ms^{-1}.

(b) $q_e = 1 - e^{-x/L_e}$, with $T_c = T_m = 7$ days $\&$ $u_2 = 5$ ms^{-1}, then increase to $\widetilde{u}_2 = 7.5$ ms^{-1}.
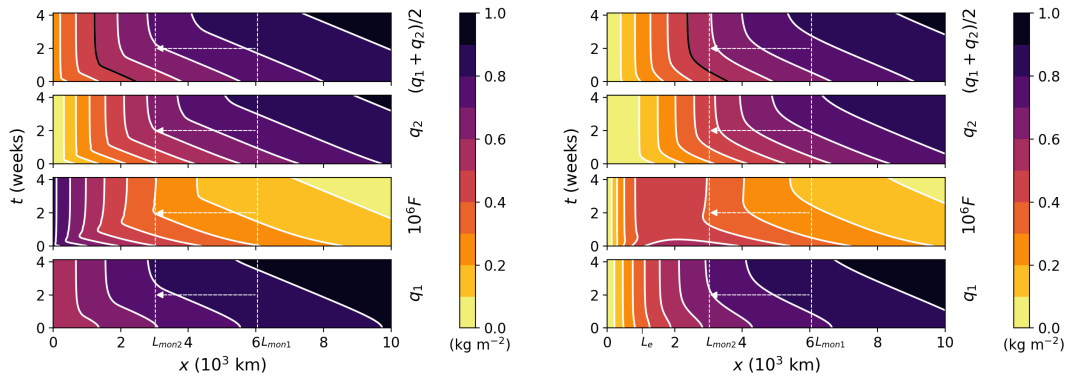
(c) $q_e = 1$, with $T_c = T_m = 7$ days $\&$ $u_2 = 5$ ms^{-1}, then decrease to $\widetilde{u}_2 = 2.5$ ms^{-1}.

(d) $q_e = 1 - e^{-x/L_e}$, with $T_c = T_m = 7$ days $\&$ $u_2 = 5$ ms^{-1}, then decrease to $\widetilde{u}_2 = 2.5$ ms^{-1}.
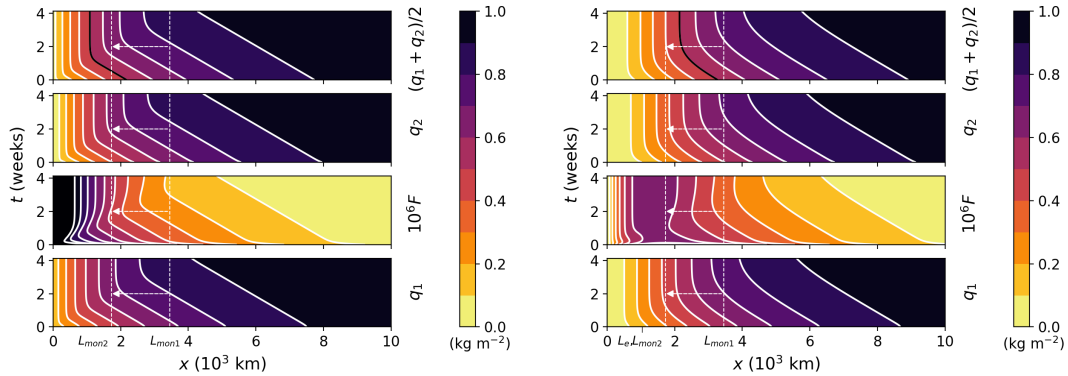
(e) $q_e = 1$, with $T_c = 1$, $T_m = 7$ days $\&$ $u_2 = 5$ ms^{-1}, then decrease to $\widetilde{u}_2 = 2.5$ ms^{-1}.

(f) $q_e = 1 - e^{-x/L_e}$, with $T_c = 1$, $T_m = 7$ days $\&$ $u_2 = 5$ ms^{-1}, then decrease to $\widetilde{u}_2 = 2.5$ ms^{-1}.

Figure 5.12:   *Investigating a strengthening/weakening dry intrusion by increasing/decreasing the upper level wind speed from u_2 to $\widetilde{u}_2$. $u_2 = 5$ ms^{-1} and $L_e = 1000$ km.*

Applying the convergence test (Subsection 5.4.5), with the threshold at 0.1, the adjustment time and onset speed can be determined. The results of this test are shown in Figure 5.13. Note that several other combination of parameters have been included, compared with Table 5.2. The shortest adjustment times and fastest convergence are seen

with $T_c = T_m = 2$ days. However, the choice of $\widetilde{u}_2$ has a significant impact here, with $\widetilde{u}_2 = 10$ ms^{-1} converging much faster than $\widetilde{u}_2 = 2$ ms^{-1}.

(a) *Case $q_e = 1$.*   (b) *Case $q_e = 1 - e^{-x/L_e}$.*
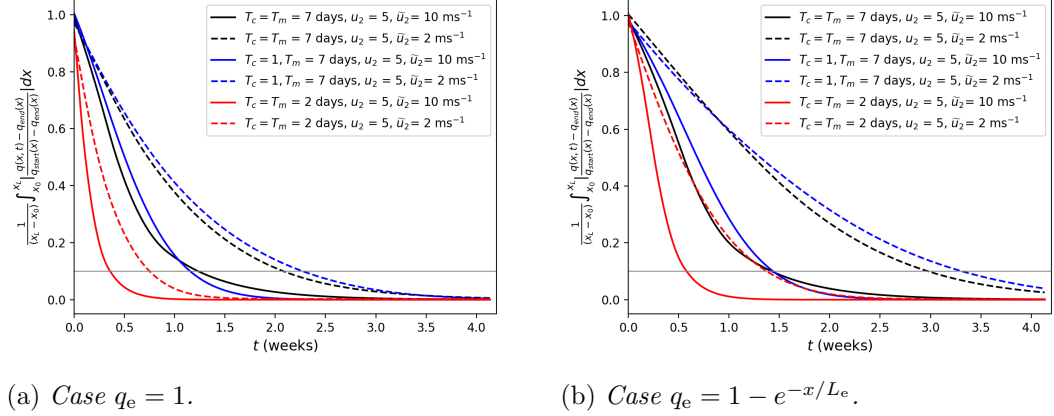
Figure 5.13: *Convergence of Equation 5.40 against time, t, for varying u_2 to $\widetilde{u}_2$. $u_2 = 5$ ms^{-1} and $L_e = 1000$ km.*

(a) *Case $q_e = 1$.*   (b) *Case $q_e = 1 - e^{-x/L_e}$.*
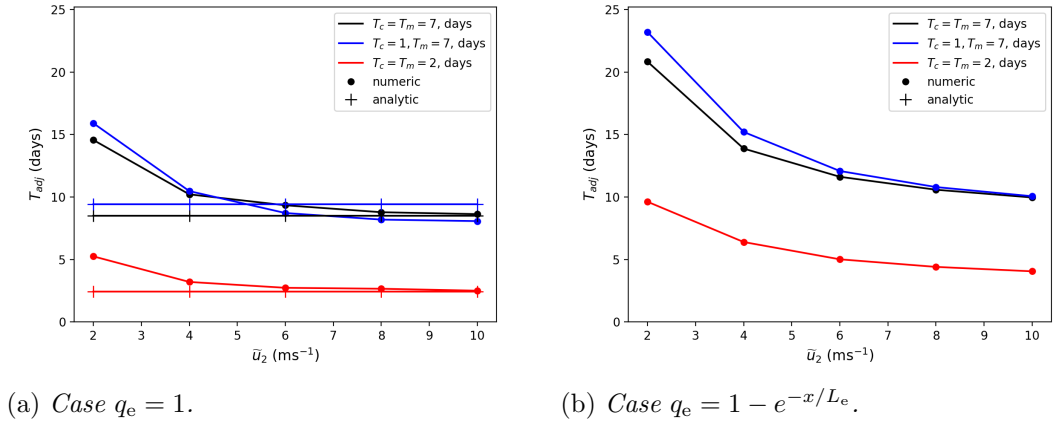
Figure 5.14: *Adjustment time, T_{adj}, against $\widetilde{u}_2$, for analytical and numerical results. $u_2 = 5$ ms^{-1} and $L_e = 1000$ km. Note no analytical results available for case $q_e = 1 - e^{-x/L_e}$.*

5.6.3   Comparison

Figures 5.14 and 5.15 show the results of applying the analytical theory and using numerical techniques to determine the adjustment time, T_{adj}, and the onset speed, ν, against $\widetilde{u}_2$. Note that only numerical results are shown for the case $q_e = 1 - e^{-x/L_e}$.

Looking at Figure 5.14 for the adjustment time against $\widetilde{u}_2$, the analytical theory gives a linear result, as the expression for T_{adj} is not dependent on either the initial (u_2) or the varied ($\widetilde{u}_2$) upper level wind speed. For $\widetilde{u}_2 > 4$ ms^{-1} in case $q_e = 1$, the numerical results match closely, although are not linear. In Figure 5.14b, the numerical results are more evidently non-linear. Towards lower $\widetilde{u}_2$, the numerical results give increasingly larger T_{adj}.

In terms of onset speed (Figure 5.15), the numerical and analytical results are in close
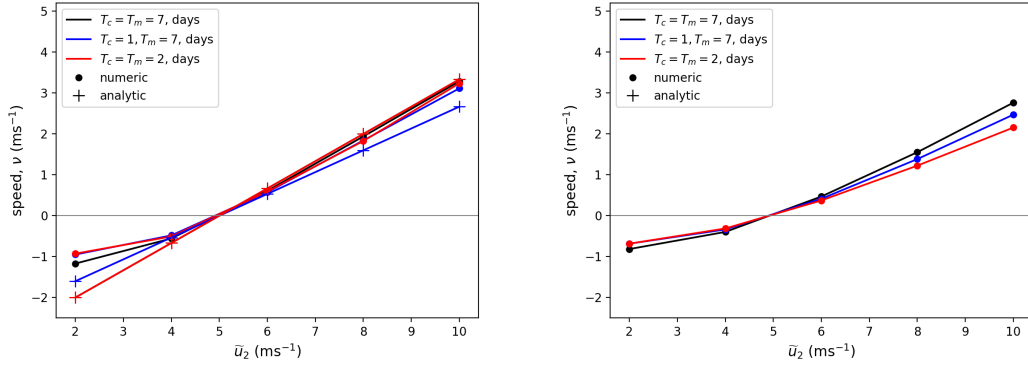
(a) *Case $q_{\mathrm{e}} = 1$.*

(b) *Case $q_{\mathrm{e}} = 1 - e^{-x/L_{\mathrm{e}}}$.*

Figure 5.15: *Onset speed, ν, against $\widetilde{u}_2$, for analytical and numerical results. $u_2 = 5\ ms^{-1}$ and $L_{\mathrm{e}} = 1000\ km$. Note no analytical results available for case $q_{\mathrm{e}} = 1 - e^{-x/L_{\mathrm{e}}}$.*

agreement. As the initial speed, u_2, is increased, the onset "front" propagates faster, and in a southeasterly direction (i.e. reverse onset). Conversely, when u_2 is decreased, the onset travels towards the northwest at greater speed.

It is concluded that the analytical expressions for front speed ν (Equation 5.45) and adjustment timescale T_{adj} (Equation 5.47) are useful predictors of the actual behaviour. In particular, the adjustment timescale is more sensitive to T_{m} than T_{c}, due to the factor of 2 in front of the former.

5.7   Experiment: increasing the rate of convection

In this experiment, the intensity of convection from the lower to the upper layer is varied through T_{c}. Decreasing the timescale T_{c} means greater convective activity, linked to cloud growth at the onset of the monsoon. An upper level wind speed of $u_2 = 5$ ms^{-1} is maintained throughout. Referring to Table 5.3, the first combination to be investigated is $T_{\mathrm{c}} = T_{\mathrm{m}} = 7$, $\widetilde{T}_{\mathrm{c}} = 3.5$, days. By halving the convective timescale, the amount of convective events is doubled, meaning a higher rate of moisture transport from the lower to the upper layer. The second combination is similar, but initialising at shorter timescales, $T_{\mathrm{c}} = T_{\mathrm{m}} = 2$ days. Thirdly, an asymmetric case with $T_{\mathrm{c}} \gg T_{\mathrm{m}}$ is taken, considering the inverse of the case in the previous section where the moisture inflow was being varied. Here, T_{m} is interpreted as representing moisture input on a diurnal timescale (such as evaporation), whilst T_{c} is the timescale of longer convective events. Example of these would be clusters of clouds, storms and monsoon depressions.

Table 5.3: *Configuration of parameters for varying T_c experiment.*

T_c (days)	$\widetilde{T}_c$ (days)	T_m (days)	u_2 (ms^{-1})
7	3.5	7	5
2	1	2	5
7	3.5	1	5

5.7.1 Analytical prediction

In this experiment, varying T_c, the analytic theory from Subsection 5.4.3 requires modification. Here, $\widetilde{T}_m = T_m$, $\widetilde{u}_2 = u_2$ and $\widetilde{q}_e = q_e$. In this instance, the term q_{*1}, representing the $q_1 + q_2$ series term of order t, is zero. The onset speed is then also zero. Thus, the next order in the series needs to be considered, $O(t^2)$, for q_1 and q_2, using Equations 5.26a-5.26c.

Similarly to Subsection 5.4.3, a quantity $Q(x,t)$ is expanded as a series for a small time t, setting $x = x_* + at^2 + \ldots$, $Q\left(x_* + at^2 + O(t^3), t\right) = Q_*$, and noting that $Q_{*1} = 0$. The parameter a is interpreted as acceleration.

$$Q_* = Q_{*0}\left(x_* + at^2 + \ldots\right) + t\cancel{Q_{*1}\left(x_* + at^2 + \ldots\right)} + t^2 Q_{*2}\left(x_* + at^2 + \ldots\right) + \ldots$$

$$= Q_{*0}(x_*) + t^2\left(a Q'_{*0}(x_*) + Q_{*2}(x_*)\right) + \ldots$$

Letting $Q(x_*) = q_*$ and neglecting higher order terms, Equation 5.49 gives the expression for a, which is analogous to Equation 5.29.

$$a = -\frac{q_{*2}(x_*)}{q'_{*0}(x_*)}. \tag{5.49}$$

Following Subsection 5.4.4, a point on the onset contour x_* can be considered, which moves a distance $\pm L$. Then, $x_* \pm L = x_* + aT^2$, where a is acceleration and T is time. As previously, $L = x_{\text{adj}}$ and $T = T_{\text{adj}}$, giving:

$$T_{\text{adj}} = \left|\sqrt{\frac{x_{\text{adj}}}{a}}\right|. \tag{5.50}$$

For the case $q_e = 1$, the expression for a is given by Equation 5.51. The exponential case of q_e is neglected, for simplicity.

$$a = \frac{1}{T_c + 2T_m - 2\left(T_c + T_m\right)e^{x/L_{\text{mon}}}}\left(\frac{1}{T_m}\left(\frac{T_c}{\widetilde{T}_c} - 1\right) + \frac{1}{T_c + T_m}\left(\frac{T_c}{\widetilde{T}_c} + 1\right)\right). \tag{5.51}$$

The distance travelled by contours from an initial to a new equilibrium, x_{adj}, from Equation 5.38, is:

$$x_{\text{adj}} = -u_2\left(\widetilde{T}_c + T_m\right)\ln\left(\frac{\widetilde{T}_c + T_m}{\widetilde{T}_c + 2T_m}\right) + u_2\left(T_c + T_m\right)\ln\left(\frac{T_c + T_m}{T_c + 2T_m}\right). \tag{5.52}$$

The adjustment timescale T_{adj} can then be calculated from Equations 5.50–5.52, but the final result is not included here. It is difficult to make a corresponding simple analysis

for onset speed and adjustment timescale because $Q'(x_*) = 0$. Changing the rate of convection is a distinct and unusual case, compared to varying advection or low-level inflow. Although it is possible to make a calculation by considering $O(t^2)$, it is not presented here. Thus, the analysis for the case of increasing convection is restricted to the numerical results presented in the following section.

5.7.2   Numerical analysis

Using the combination of parameters in Table 5.3, the system is solved for cases $q_e = 1$ and $q_e = 1 - e^{-x/L_e}$. Results are shown in Figure 5.16. It is immediately evident from Figure 5.16 that the scenario with increasing convection is different to the previous two experiments with low-level moist inflow and upper-level advection.

For these experiments, when decreasing u_2 or decreasing T_m, all contours (in both q_1 and q_2) move smoothly to the northwest. But when T_c is reduced, although the q_2 contours move northwestwards, the q_1 move southeastwards initially. At small times these effects offset in the total column water $q_1 + q_2$, which is why the changes in that are $O(t^2)$. This is a subtle and interesting effect.

For all cases, there is an initial sharp drop in the lower layer moisture, as it is transported to the upper layer, because of the sudden increase in the rate of convection. Then, there is a gradual increase in low level moisture as the system stabilises at a new equilibrium. The immediate decline of q_1 is easier to see at higher x, where the contours are more spaced further apart. Figures 5.16c–5.16d respond similarly to Figures 5.16e–5.16f, although due to the shorter timescales, T_c and T_m, the system adjusts much more quickly. Thus, the adjustment times and distances are reduced. The cases where the moisture inflow is greater (Figures 5.16c-5.16f), i.e. where T_m is smaller, have more moisture in the lower layer compared to Figures 5.16a–5.16b. The lower layer is dry at $x = 0$ in the $q_e = 1 - e^{-x/L_e}$ cases, creating a strong moisture gradient over $0 < x < 3000$ km, which represents the distance over India.

The flux, for Figures 5.16a–5.16b, is strongest initially, when the rate of convection is doubled. Then there is a rapid decrease to some minimum level, as the lower layer moisture is depleted, before a slight increase to reach an equilibrium state where the moisture inflow, rate of transport between layers and the rate of advection are in balance. For $x > 8000$ km, the flux has not necessarily attained a steady-state. In Figures 5.16c–5.16f, the flux decreases at a steady rate until a new equilibrium is reached.

For cases with $q_e = 1$, the flux is greatest towards the northwest and weakest towards the southeast. With $q_e = 1 - e^{-x/L_e}$, there is a flux maximum centered on $x = 2000$ km, which arises from the flux being zero at the lateral boundary.

The upper layer moisture, for Figures 5.16a–5.16b, initially increases, as more moisture is being transported via increased convective activity, then the moisture slightly decreases to its constant value at equilibrium. For Figures 5.16c-5.16f, q_2 increases over time until equilibrium is reached. The amount of moisture in the upper layer is similar to the lower

(a) $q_e = 1$, *initialising with* $T_c = 7$ & $T_m = 7$ *days, then reducing to* $\widetilde{T}_c = 3.5$ *days.*

(b) $q_e = 1 - e^{-x/L_e}$, *initialising with* $T_c = 7$ & $T_m = 7$ *days, then reducing to* $\widetilde{T}_c = 3.5$ *days.*

(c) $q_e = 1$, *initialising with* $T_c = 2$ & $T_m = 2$ *days, then reducing to* $\widetilde{T}_c = 1$ *day.*

(d) $q_e = 1 - e^{-x/L_e}$, *initialising with* $T_c = 2$ & $T_m = 2$ *days, then reducing to* $\widetilde{T}_c = 1$ *day.*

(e) $q_e = 1$, *initialising with* $T_c = 7$ & $T_m = 1$ *days, then reducing to* $\widetilde{T}_c = 3.5$ *days.*

(f) $q_e = 1 - e^{-x/L_e}$, *initialising with* $T_c = 7$ & $T_m = 1$ *days, then reducing to* $\widetilde{T}_c = 3.5$ *days.*

Figure 5.16: *Doubling the convective activity by reducing the convection timescale from* T_c *to* $\widetilde{T}_c$. $u_2 = 5$ *ms*$^{-1}$ *and* $L_e = 1000$ *km.*

layer for all cases, with the rate of convection balancing the moisture inflow, relative to upper level advection. There is a much sharper transition to the new equilibrium for Figures 5.16c and 5.16e.

The total moisture is dominated by the upper layer moisture in each case. Also, the adjustment times are faster than with the varying T_m experiments. The onset contours

(in black) are nearly vertical, indicating very little travel across India. The rapidity of onset is correlated with the abrupt switch-on of greater convective activity. In terms of the real-world monsoon, this could indicate that sudden convective events trigger an onset, but also delay its progression to the northwest, consistent with (Volonté et al., 2019).

5.8   Conclusions

At this stage there is a time-evolving, spatially one-dimensional, two layer model which represents the evolution of moisture over lower and upper layers of the troposphere. Moisture inflow to the lower layer is provided via a relaxation term to a prescribed profile q_e on a timescale T_m. Between the layers there is a down-gradient flux, parameterising deep convection in terms of $q_1 - q_2$, on a timescale T_c. Further research regarding the form of the flux function could to be undertaken. The system is initialised at equilibrium with parameters T_m, T_c, u_2 and q_e, from steady-state solutions which can be determined analytically. The initial system is associated with a monsoon length-scale L_{mon1}. Three experiments are undertaken which vary parameters $T_m \to \widetilde{T}_m$, $T_c \to \widetilde{T}_c$ and $u_2 \to \widetilde{u}_2$, independently. An additional experiment where q_e is adjusted to $\widetilde{q}_e$, effectively meaning an increase in the depth of monsoon flow, could be considered for future work. The system transitions from its initial equilibrium (pre-onset) to a new equilibrium (post-onset), with the monsoon length-scale L_{mon1} becoming L_{mon2}, where $L_{mon2} < L_{mon1}$, representing the monsoon onset (defined as a threshold of total column moisture) progression from southeast to northwest India. The theory presented in this chapter generalises the results of those in Chapter 4.

It is found that the controlling length-scale is L_{mon}, rather than L_e, the monsoon length-scale in the absence of equilibrium which is associated with the choice of lower layer profile $q_e = 1 - e^{-x/L_e}$. For the case $q_e = 1$, equilibrium solutions for q_2 all scale by x/L_{mon}. So do q_1 and $q_1 + q_2$ when $T_c = T_m$. However, in the case $q_e = 1 - e^{-x/L_e}$, the only universal behaviour in terms of scaling is for q_2 when $L_{mon_i} = L_{mon_j}$. Limiting behaviour ($q_1 \to 1$, $q_2 \to 1$) can be inferred when $x_L \gg L_{mon}$. It can also be seen that the system is more sensitive to choice of T_m than T_c, due a factor of 2 that appears in front of the former. In terms of the sensitivity to T_m and T_c, a point of contour turnover (T_m^*) can be derived, which represents the transition between a convective-dominant to an (upper layer) advection-dominant regime.

A combination of alternative analytical methods including small-time solutions, scaling arguments and numerical solutions, allow the nature of the onset transition to be quantified in terms of an onset speed ν and an adjustment timescale T_{adj}. The calculated onset speeds are generally < 5 ms^{-1}, comparable to observed speeds. The adjustment timescale of the model is faster than the observed monsoon, on the order of 1–2 weeks compared with 6 weeks, and does not tend to progress over the full length of India, approximately 3000 km. It is noted for the experiments varying low-level inflow and upper level advection, T_{adj} does not depend on the initial upper level wind speed, u_2. The theory using scaling

arguments agrees well with numerical results for the inflow and advection experiments. For the convection experiment, the situation is more complex, showing non-linear behaviour, as lower layer moisture contours move southeastwards initially, before reversing direction and travelling to the northwest.

Chapter 6

Simulating Indian monsoon onset with the WRF model

6.1 Introduction & aims

In this chapter, the methodology of running a numerical weather prediction model over the Indian region is described, followed by analysis of results and evaluation of the model's performance. The Weather Research and Forecasting (WRF) model is selected, due to its open source nature giving universal accessibility, and also the ease and flexibility of use. Section 6.2 is a description of the model, with the results of the simulation presented in Section 6.3. The aim is to demonstrate that the WRF model can simulate the Indian monsoon onset and progression for the year 2016, to a reasonable degree of accuracy, compared with reanalysis datasets and observations. Then, the output from the WRF model can be compared with the results of the two-layer model discussed in Chapter 5.

6.2 Model description

The WRF model was developed in the late 1990s by a collaboration of the National Center for Atmospheric Research (NCAR), the National Oceanic and Atmospheric Administration (NOAA) (represented by the National Centers for Environmental Prediction (NCEP) and the NOAA Earth System Research Laboratory (ESRL)), the United States Air Force, the Naval Research Laboratory, the University of Oklahoma, and the Federal Aviation Administration. The atmospheric modelling system is used for both research and numerical weather prediction, including operationally by the India Meteorological Department. A more detailed history regarding the use of the WRF model and its development is given by Powers et al. (2017). Here, the Advanced Research WRF (ARW) Version 4.0 configuration is used. The model is split into a central dynamical core (the ARW solver) which solves a system of equations, and numerous physics schemes which represent different meteorological processes such as cloud microphysics, planetary boundary layer development and land-surface interactions. These physics schemes are necessary for simulations over

about 4 km horizontal grid resolution, and sometimes required for 1.5–4 km grid resolution, where processes must be parameterised, rather than explicitly resolved, due to limits of computation.

6.2.1 ARW solver

The ARW model features a dynamical core which solves the set of compressible, non-hydrostatic Euler equations. The equations (see Shamrock et al. (2019)) are written in flux-form, to allow for conservation of dry air mass and scalar mass. A key feature of Version 4.0 is the modification of the vertical coordinate to a hybrid sigma-pressure coordinate. Towards the surface, the vertical coordinate is terrain-following, in line with the traditional sigma coordinate (η). To reduce the influence of the terrain on coordinate surfaces more rapidly, the vertical coordinate follows the hydrostatic pressure coordinate at greater heights above the surface. A third order polynomial is used to describe the transition from sigma to pressure coordinates.

The ARW model solves the governing equations using a time-split integration scheme, which follows a third order Runge-Kutta scheme, but splits acoustic modes where smaller time steps are desirable. Spatially, Arakawa C-grid staggering is used in the discretisation, meaning that normal velocities are half a grid length from the thermodynamic variables, which are computed at grid-centres (mass points). The model takes into account full Coriolis and curvature terms. A Mercator projection is used, which minimises distortion near the equator. This is appropriate given that the region of interest, India, lies within 0–30°N.

The ARW model is run for real-data cases (as opposed to an idealised configuration), using three-dimensional meteorological data to initialise and set the lateral boundary conditions. These boundary conditions are constructed as a relaxation towards the specified values from the data provided; this is also referred to as nudged boundary condition. The atmospheric dataset used in these simulations is NCEP GDAS/FNL 0.25 Degree Global Tropospheric Analyses and Forecast Grids (National Centers for Environmental Prediction et al., 2015). The WRF Preprocessing System (WPS) is used to convert the input GRIB data to an intermediate binary format and to interpolate the data onto the projected domain. Certain fields such as land-use category and vegetation fraction are derived from a terrestrial dataset using NASA's MODerate resolution Imaging Spectroradiometer (MODIS) (National Center for Atmospheric Research, 2020), where quantities vary monthly–seasonally. Further information regarding the datasets used to run the ARW model is given in subsection 6.2.3.

Parameters that are not region-specific are left as the default value or are set as the option appropriate for real-data cases, as recommended by Wang et al. (2019) and University Corporation for Atmospheric Research (2020). For example, the turbulence and mixing option is set to evaluate second-order diffusion terms on coordinate surfaces, with no sixth-order numerical diffusion or gravity wave drag. The eddy coefficient option is

set as Horizontal Smagorinsky first order closure. Upper level w-Rayleigh damping is applied with damping coefficient inverse timescale of 0.2 s^{-1}. Certain processes, such as the vertical diffusion, are defined within the physics schemes.

6.2.2 Physics schemes

The physics options in the ARW model configuration are set by the use of a physics suite, "tropical". This consists of a combination of schemes that have been well tested and shown good results in previous versions. Table 6.1 gives a summary of the physics schemes selected as part of the tropical suite.

Table 6.1: *Combination of physics scheme options for the tropical suite in ARW model.*

Physics scheme type	Name of scheme	Reference
Longwave radiation	RRTMG	Iacono et al. (2008)
Shortwave radiation	RRTMG shortwave	Iacono et al. (2008)
Microphysics	WSM6	Hong and Lim (2006)
Cumulus parameterisation	New Tiedtke	Zhang et al. (2011)
Planetary boundary layer	Yonsei University	Hong et al. (2006)
Surface layer	MM5 similarity (old)	see text for full list
Land-atmosphere interface	Noah Land Surface Model	Tewari et al. (2004)

The Rapid Radiative Transfer Model for General Circulation Models (RRTMG) scheme is used for longwave and shortwave radiation (Iacono et al., 2008). This is a one-dimensional scheme which uses the Monte Carlo Independent Column Approximation method of random cloud overlap. The radiation scheme computes the clear-sky and cloudy upward and downward radiation fluxes, taking into account annual and diurnal solar cycles, and interacting with the surface scheme. Figure 6.1 summarises the key information exchanged between physics schemes, as a result of the parameterisations.

For the parameterisation of the cloud microphysics, the WRF Single-Moment 6-class (WSM6) scheme is used (Hong and Lim, 2006), which follows a traditional bulk method. The performance of this scheme has been well studied and evaluated (e.g. Otkin and Greenwald (2008); Medina et al. (2010)). The simulations will be run at medium resolution, i.e. 10–40 km horizontal grid size. The WSM6 scheme is deemed sufficient for the purposes of this chapter, as it is appropriate for use in low to high resolution simulations, including at cloud-resolving scales, i.e. <10 km (Hong and Lim, 2006). Single-moment schemes have a single prediction equation for mass for each quantity. There are six quantities, namely, water vapour, cloud water, cloud ice, snow, rain and graupel. The distribution of particle sizes is computed from fixed parameters. The microphysics scheme passes information relating to cloud effects, such as particle sizes of ice, snow and cloud water, to the radiation scheme (Figure 6.1). Additionally, the microphysics scheme interacts with the surface scheme, relating the amount of precipitation from sub-grid scale processes.

The new Tiedtke scheme (Zhang et al., 2011) is used as the cumulus parameterisation

scheme. It is a mass-flux type scheme which includes treatment of shallow convection, turbulence entrainment/detrainment and momentum transport. The surface air conveyed to the tops of clouds by updrafts is entirely compensated for by environmental subsidence, so that the net mass flux remains zero. The parameterisations represent the effects of sub-grid scale convective and shallow clouds on the large-scale vertical profiles of heat, moisture and momentum. As per Figure 6.1, the cumulus parameterisation scheme passes information on cloud detrainment to the microphysics scheme, the amount of convective clouds to the radiation scheme and the accumulation of convective-derived precipitation to the surface layer scheme. Modifications from the original Tiedtke scheme include a convective available potential energy (CAPE) closure for deep convection, as opposed to a moisture convergence closure, a dependence on environmental moisture for entrainment in deep convection and changing the convective adjustment timescale from a constant to a function of the vertical velocity averaged in the updraft and cloud depth (Shamrock et al., 2019). In the following chapter, comparisons will be drawn between the convective adjustment timescale in the WRF model and in the idealised two-layer model. These modifications have been shown to improve simulations of tropical storm systems and diurnal precipitation over land in the Tropics (e.g. Zhang et al. (2011); Zhang and Wang (2017); Gbode et al. (2019); Sun and Bi (2019)).

The surface layer scheme acts as an in interface between the land-surface and planetary boundary layer schemes, calculating heat, moisture and momentum exchange coefficients and friction velocities. This enables the sensible and latent heat fluxes at the surface, and the surface stress, to be determined by the land-surface and planetary boundary layer schemes, respectively. In the WRF model set-up, an MM5 similarity theory scheme is used, which is derived from the scheme used in the Fifth-Generation Penn State/NCAR Mesoscale Model (referred to as MM5). The scheme uses Monin-Obukhov similarity theory (Monin and Obukhov, 1954), an empirical theory based on local first-order turbulence closure, to calculate vertical profiles of the non-dimensionalised mean flow and temperature near the surface. The surface layer, approximately the lowest 10% of the planetary boundary layer, lies between the land surface boundary and the lowest vertical model level. The vertical profiles are derived from the standard logarithmic wind profile, which describes mean flow as a function of height under neutral conditions, with empirical corrections to account for stable/unstable conditions. These corrections are universal functions of a non-dimensional stability parameter, such as the gradient Richardson number or vertical height divided by the Obukhov length. Then, the transfer (or exchange) universal coefficients for heat, moisture and momentum can be deduced, as detailed in Paulson (1970); Dyer and Hicks (1970), and Webb (1970). Following Zhang and Anthes (1982), there are corrections for four stability regimes: stable, mechanically induced turbulence, unstable through forced convection and unstable through free convection. An extension to the Monin-Obukhov theory is used in the MM5 scheme, accounting for free convection over land and sea surfaces, which involves parameterising free convection as a special case of

forced convection, and the inclusion of a term representing the near surface wind induced by large eddies (Beljaars, 1994). A length-scale of the roughness of the surface is taken into account, which is particularly important over complex, urban or forested terrain. To relate the surface roughness length-scale to the friction velocity over water, a Charnock relation is used (Charnock, 1955).

The Yonsei University scheme (Hong et al., 2006) is selected for the planetary boundary layer, which is linked to the choice of the surface layer scheme. The planetary boundary layer scheme determines the vertical sub-grid scale fluxes due to eddy transports of heat, moisture and momentum. Then, the tendencies of these quantities can be calculated in the whole atmospheric column. The surface fluxes from the surface and land-surface schemes are incorporated with the boundary layer eddy fluxes, distributed by a parameterisation of turbulence, which allows for growth of the planetary boundary layer via entrainment. The Yonsei University scheme is a diagnostic non-local K scheme, using counter-gradient terms for the fluxes due to large-scale wind and potential temperature gradients. The "K" refers to an eddy diffusivity coefficient, which is constrained to a fixed parabolic profile over the depth of the planetary boundary layer. This type of non-local scheme was first proposed by Troen and Mahrt (1986), with subsequent improvements being made by Hong and Pan (1996); Noh et al. (2003); Hong et al. (2006). Non-local schemes have been shown to give a more realistic representation of large eddy fluxes within the planetary boundary layer, particularly under unstable conditions, and to predict the precipitation field more accurately (see Hong and Pan (1996), Basu et al. (2002)). The most important modification has been the addition of an asymptotic entrainment flux term at the inversion layer, where the entrainment is proportional to the surface buoyancy flux, allowing explicit treatment of the entrainment layer of the top of the planetary boundary layer. This has been supported by large eddy simulation studies (Noh et al., 2003), and means that the growth of the planetary boundary layer can be predicted directly.

Another improvement is defining the top of the planetary boundary layer at the maximum entrainment layer, as opposed to the layer where the diffusivity becomes zero. This is done by using a critical bulk Richardson number of zero, meaning that the top of the planetary boundary layer is effectively dependent on the buoyancy profile (Shamrock et al., 2019). In the free atmosphere above the planetary boundary layer, a local K scheme is applied, where diffusivity coefficients are parameterised as functions of the Richardson number and observations are used to inform the turbulent mixing length and stability formula.

The Unified Noah Land-Surface Model (Tewari et al., 2004) is used in the surface physics scheme to provide information about the amount of vegetation, land-use category, soil properties, sea ice and snow cover. Combined with the surface layer scheme, variables such as surface emissivity and albedo can then be passed back to the radiation scheme. The Unified Noah Land-Surface Model also calculates the surface fluxes, using the exchange coefficients from the surface layer scheme. The surface fluxes are input to the planetary

boundary layer scheme and variables are updated each time cycle. The model has four soil layers and predicts soil moisture and soil temperature in each layer. It includes root zone, evapotranspiration, soil drainage, monthly vegetation fraction, vegetation category and soil texture (Shamrock et al., 2019). Canopy moisture (not temperature) is considered. Additionally, the model predicts snow cover and compensates for fractional snow cover effects. Note that soil temperature, soil moisture and water equivalent snow depth are derived from the atmospheric dataset (Subsection 6.2.3), whilst the albedo, green vegetation fraction and land-use category are derived from the terrestrial dataset (Subsection 6.2.3).

Sea surface temperatures (from the atmospheric dataset) are kept fixed. Oceanic phenomena such as El Niño or the Indian Ocean Dipole vary slowly (i.e. on timescales of months–years) relative to the onset and progression of the Indian monsoon (timescales of days–weeks). For longer simulations over multiple years, e.g. for climate research, it is recommended to update sea surface temperatures or couple to an ocean model.
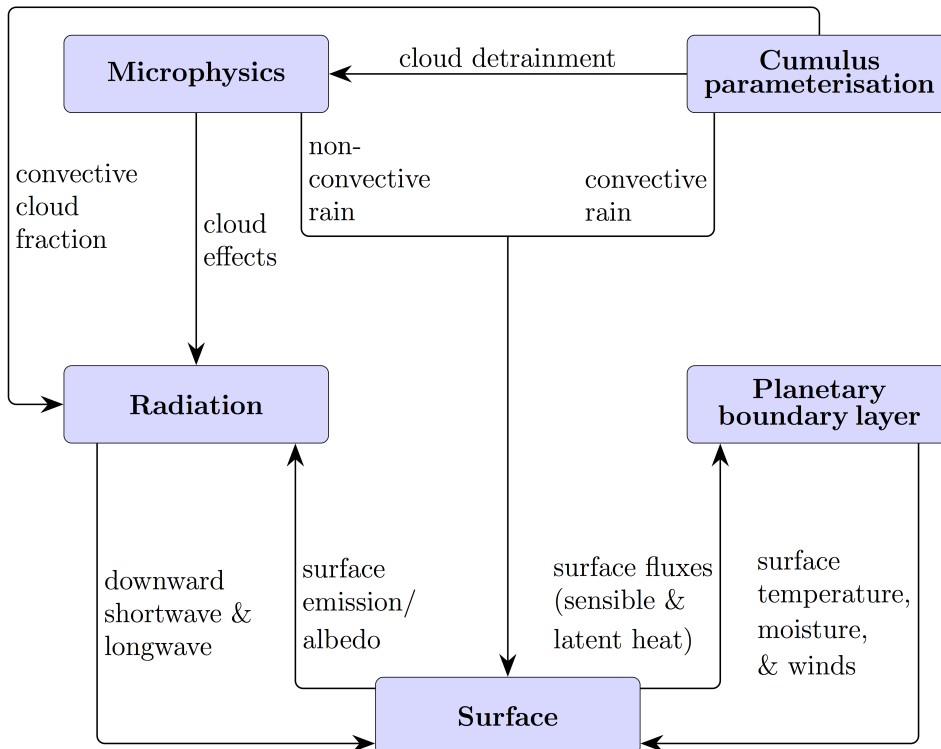
Figure 6.1: *Summary of the interactions between physics schemes parameterisations. Adapted from Dudhia (2019).*

6.2.3   Datasets

In order to run the WRF model for a real-data case, there is a need to provide information on terrestrial and atmospheric fields, to initialise the model and set boundary conditions. Slowly-varying parameters such as albedo, green vegetation fraction and land-use category are taken from the terrestrial dataset (which is included as part of the WRF model pack-

age). Key meteorological fields such as temperature, relative humidity and wind speed, which vary in time, are specified from the atmospheric dataset.

Atmospheric dataset

The atmospheric data used in these simulations is provided by NCEP (National Centers for Environmental Prediction et al., 2015), reference number ds083.3. It gives operational global tropospheric analysis and forecast data on a 0.25° by 0.25° horizontal grid, updated on a 6-hourly basis. The temporal range of data is from July 2015 to March 2020. Three-dimensional and surface fields of temperature, relative humidity, geopotential height, pressure, and the horizontal components of wind speed, are included. As part of the initial processing (WPS), two-dimensional time-dependent fields such as surface/sea-level pressure, layers of soil temperature and soil moisture, snow depth, skin temperature, sea surface temperature, and a sea ice flag (Shamrock et al., 2019) are incorporated. The dataset has 32 vertical pressure levels and 4 soil levels. Both observational and model data are used create the NCEP GDAS/FNL dataset. The former is derived from the Global Data Assimilation System (GDAS), which collates observations from the Global Telecommunications System, amongst others. The model data is taken from the operational Global Forecast System (GFS), but the final (FNL) analysis is delayed by about an hour so that more observational data can be incorporated. The atmospheric dataset described here will also be used to validate model performance.

Terrestrial dataset

The terrestrial dataset is given by National Center for Atmospheric Research (2020), which is derived from MODIS satellite products. A more detailed description of the MODIS global land cover product is given by Friedl et al. (2002). Here there are 21 land-use categories, including lakes, which can be viewed within Wang et al. (2019). The pre-processed two-dimensional fields include albedo, Coriolis parameters, terrain elevation, vegetation/land-use type, land/water mask, map factors, soil texture category, vegetation greenness fraction, annual mean temperature, and latitude/longitude (Shamrock et al., 2019). These fields are essentially static, with parameters either not varying in time or varying slowly (monthly–seasonally) in comparison to the processes of interest in the simulation.

6.2.4 Experiment configuration

The details of the simulation parameters and setup are summarised in Table 6.2. The domain is centred over India, with the midpoint at 75°E, 15 °N. It extends approximately 22.5° outwards to the north, south, east and west, forming a box (illustrated by the white box in Figure 6.2). The domain is sufficiently large such that it includes the main area of interest, namely the Indian land mass, and also large-scale features such as the Himalayas, Arabian Sea and the Bay of Bengal, which have a significant impact on the formation and

progression of the Indian monsoon. A resolution of 20 x 20 km is chosen for the horizontal grid spacing, as the predominant interest is in larger scale features and thus the accuracy or the increased computational cost of explicitly representing cloud-related processes is not needed. Generally, a higher resolution of <4 km is necessary for large-eddy type simulations, whereas a coarser resolution of >30 km is used for global models.
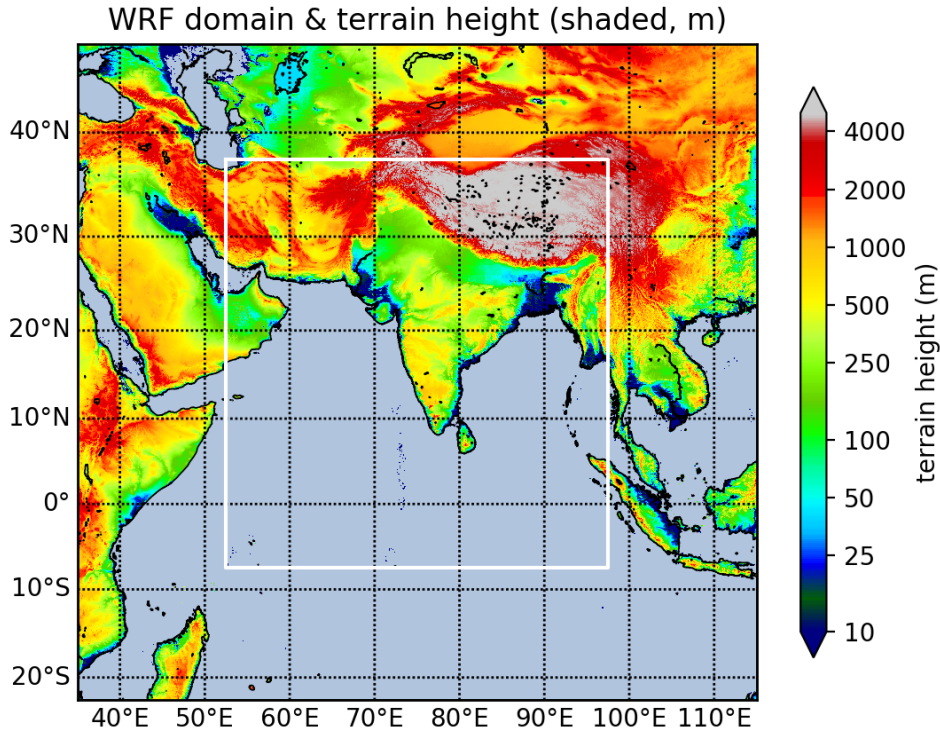
Figure 6.2: *Domain size used in the WRF model simulations (white box). The elevation (m) of the land is shown in shaded colours, with oceanic regions masked in light blue. Topographical data taken from The GLOBE Task Team et al. (1999).*

Table 6.2: *Configuration of domain and time parameters for WRF simulation.*

Option	Selection
Domain centre	75°E, 15 °N
Longitude bounds	52.5 to 97.5°E
Latitude bounds	-7.5 to 37.5°N
Start time/date	00Z 15th May 2016
End time/date	00Z 1st August 2016
Simulation length	11 weeks
Input data for B.C.	6-hourly
Model output	6-hourly
Time-step	60 seconds
dx, dy	20 km, 20 km

The simulation begins on the 15th May 2016, running for about 11 weeks to the 1st August 2016. The dataset used to set the boundary conditions (see Subsection 6.2.3 for a description) is 6-hourly, the same as the model output. This means the WRF model is strongly nudged at the boundaries, and that the model will be similar to the reanalysis data towards the edge of the domain. However, the domain is big enough that quantities will evolve differently in the interior of India if aspects such as the shallow and/or deep convection are switched off. A slighter smaller time-step of 60 seconds is chosen to maintain stability, which is of order $3 \times dx$, as recommended by Dearden (2018), than a time-step of order $6 \times dx$, as suggested in Wang et al. (2019). The combination of physics schemes for this simulation are given in 6.1, with a discussion in Subsection 6.2.2.

Analysis nudging

One aspect that has been investigated is nudging at grid-points, in other words a relaxation on a specified timescale, to the reanalysis dataset. A strongly nudged (i.e. relaxation on a shorter timescale) simulation closely follows the reanalysis dataset, which is used as an observational reference for the evaluation of the simulations. Thus, the nudged run can be compared to the un-nudged (free) run to validate model performance. The simulation needs to be sufficiently accurate that it reproduces the monsoon onset and large-scale features, but smaller scale deviations are acceptable. This is because the WRF model is being primarily used as a tool in further investigation and comparison to an idealised model, rather than being concerned with producing a perfect simulation of the 2016 monsoon onset or model development.

The 11 week simulation has been performed as a free run and as a nudged run. It is concluded that the free run is similar enough to the nudged run, i.e. close enough to the analysis, so that it is suitable for further analysis with respect to the two-layer model, presented in Chapter 7. In particular, it is desirable to undertake moisture budget calculations with a free model run, as nudging introduces virtual source and sink terms, which are difficult to determine. The results of the nudged run are not presented here to avoid excessive repetition.

6.3   11 week simulation

The 11 week simulation with the WRF model is considered in terms of monsoon stages. These are categorised as first onset, around 1st June, when monsoon onset is officially declared in the southeastern state of Kerala, mid-onset (mid-June), where the monsoon onset has progressed northwestwards over about half of India, and full monsoon, usually by mid-July, with the monsoon covering the entire country. The atmospheric reanalysis dataset (described in Subsection 6.2.3) is used to validate model performance, specifically for the year 2016, along with some results from the INCOMPASS field campaign.

Figure 6.3 (top) shows the plot format for a variable of interest - precipitation in this

case, which consists of six panels representing snapshots of the monsoon conditions on key dates. The dates presented are 16th May (pre-onset), 31st May (first onset), 15th June (mid-onset), 30th June (late onset), 16th July (full monsoon), 31st July (full monsoon). Precipitation is a daily accumulated value, but a daily average is taken for other variables.

Vertical cross-sections of the atmosphere at different monsoon stages are also examined. Quantities such as water vapour mixing ratio and relative humidity are contour plotted with distance along a transect on the x-axis and height in pressure levels on the y-axis. The locations of transects, along which the vertical cross-section are taken, are shown in Figure 6.8. They all begin in northwest India and traverse the country in a southerly/southeasterly direction. Transect 1 is the key transect to be considered with regards to observing the monsoon onset and its progression, as in Parker et al. (2016). It begins in Kandahar, Afghanistan and traverses to Visakhapatnam on India's eastern coast, passing close the cities of Jodhpur and Nagpur. Transects 2–4 are used to show the movement of air masses in a Lagrangian sense from offshore to onshore along the west coast (Subsection 6.3.5).

6.3.1   2016 monsoon onset & progression

The reference year 2016 is chosen because a field campaign, Interaction of Convective Organisation with Monsoon Precipitation, Atmosphere, Surface and Sea (INCOMPASS), was conducted over May–August of that year. The author participated in the field campaign and thus is more familiar with the events during the 2016 summer monsoon. The field campaign involved collecting data from research flights, flux towers and launching radiosondes. Further information regarding the INCOMPASS campaign is given by Turner et al. (2019); Jayakumar et al. (2019); Martin et al. (2019) and Fletcher et al. (2018).

A notable feature of the 2016 monsoon was a late onset date of 8th June at Kerala, compared with the normal date of 1st June. Despite a delayed start, the monsoon progressed rapidly in the last two weeks of June, reaching the northwest earlier than usual. Another event occurring in late June was a monsoon depression, originating in the Bay of Bengal and reaching the east coast of India at the start of July. The depression continued to propagate inland towards northwest India over the next few days (described further in Martin et al. (2019)). The India Meteorological Department (2016) note another depression over the north of the Arabian Sea at the end of June, although this dissipates reasonably quickly.

Martin et al. (2019) notes that the Madden-Julian Oscillation was in a convectively active phase over the Indian Ocean during May, and that this contributed to the formation of the monsoon depression over the Bay of Bengal. There was a very strong El Niño event for 2015–2016, which is often linked with a weaker Indian monsoon and correspondingly reduced precipitation. By July 2016, a strong negative Indian Ocean Dipole had developed, somewhat offsetting the El Niño effect and contributing to the transition to a weak La Niña phase towards the end of 2016 (Lim and Hendon, 2017; Lu et al., 2018).
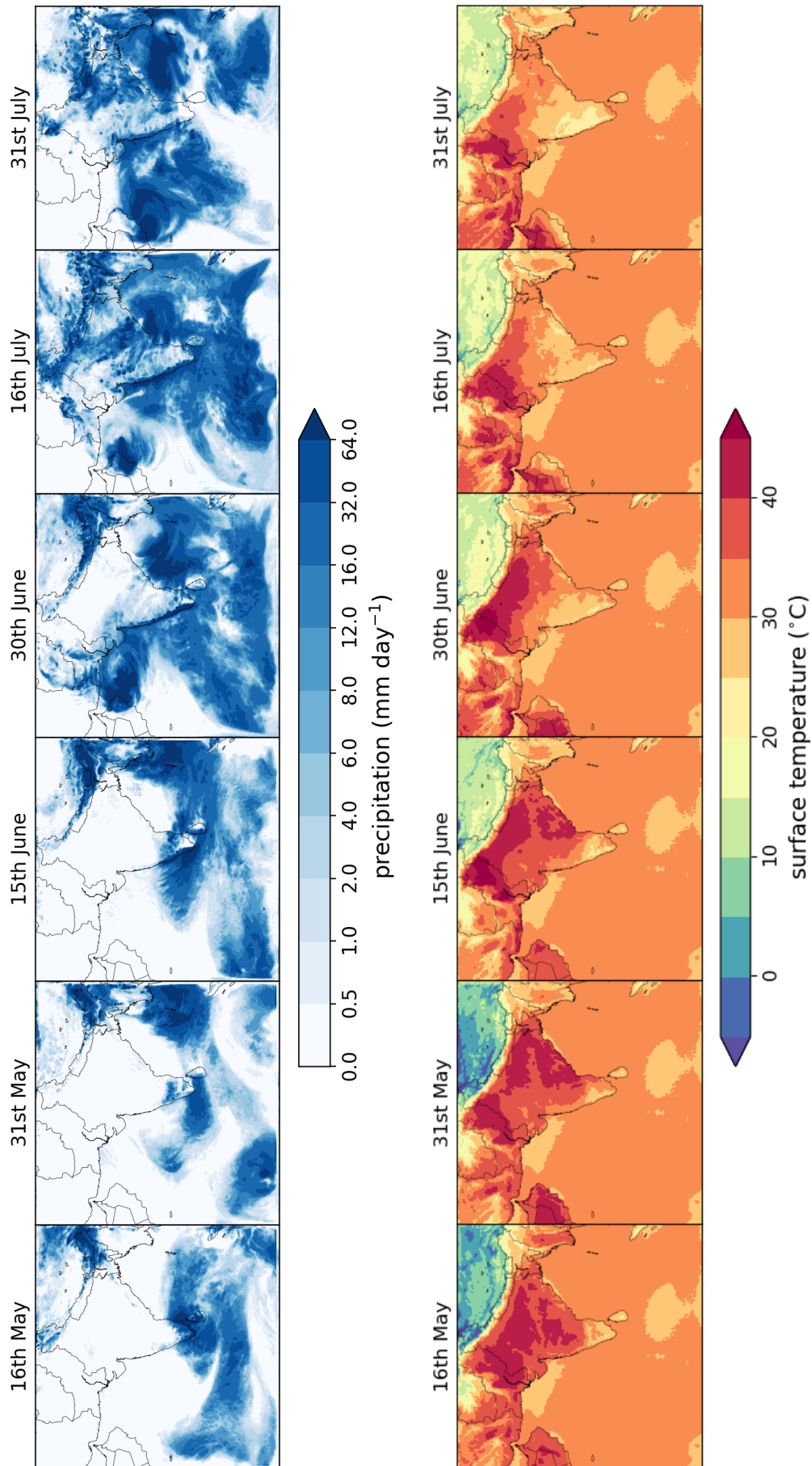
Figure 6.3: *Daily accumulated precipitation (mm day^{-1}, top) and surface temperature (°C, bottom) for various dates from the 11 week simulation with the WRF model.*
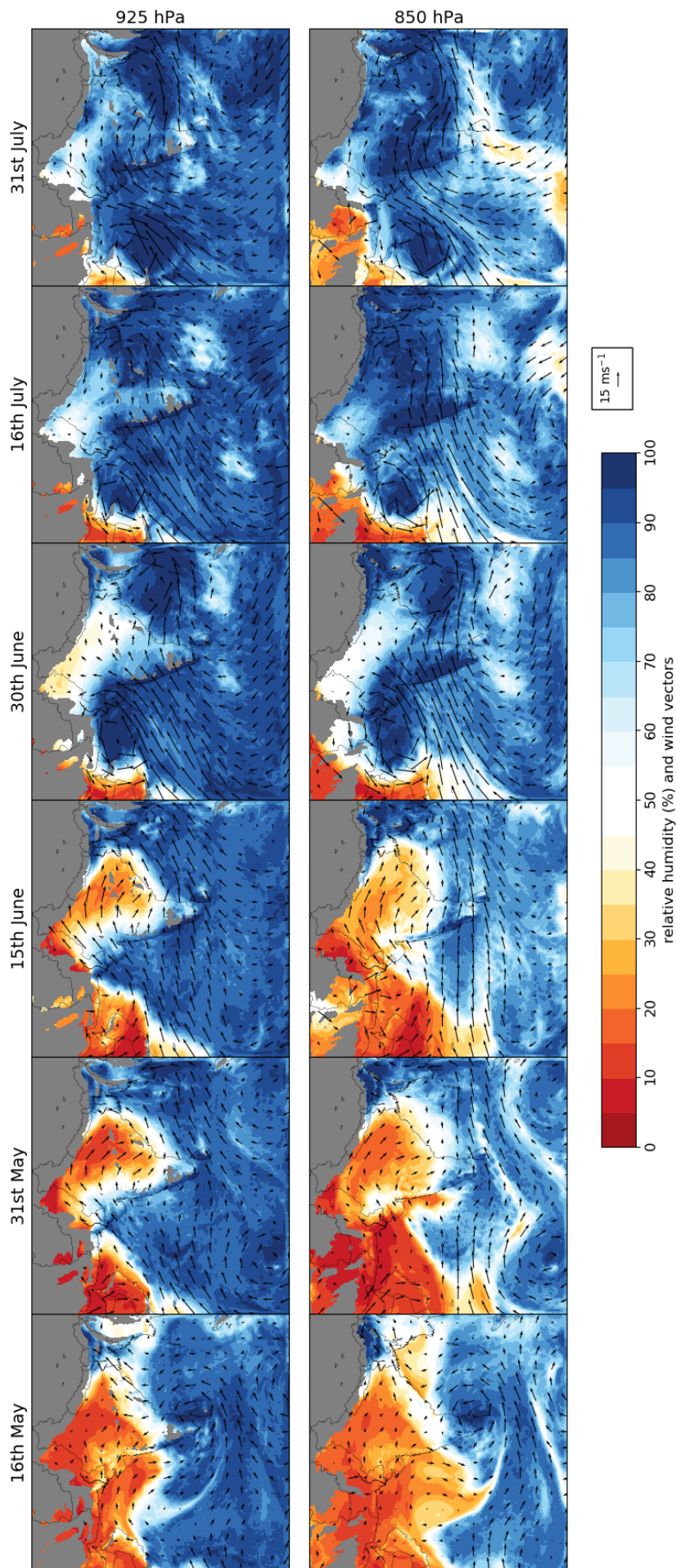
Figure 6.4: *Relative humidity (shading, %) and wind (vectors, ms^{-1}) at 925 (top) & 850 (bottom) hPa levels, from the 11 week simulation with the WRF model.*
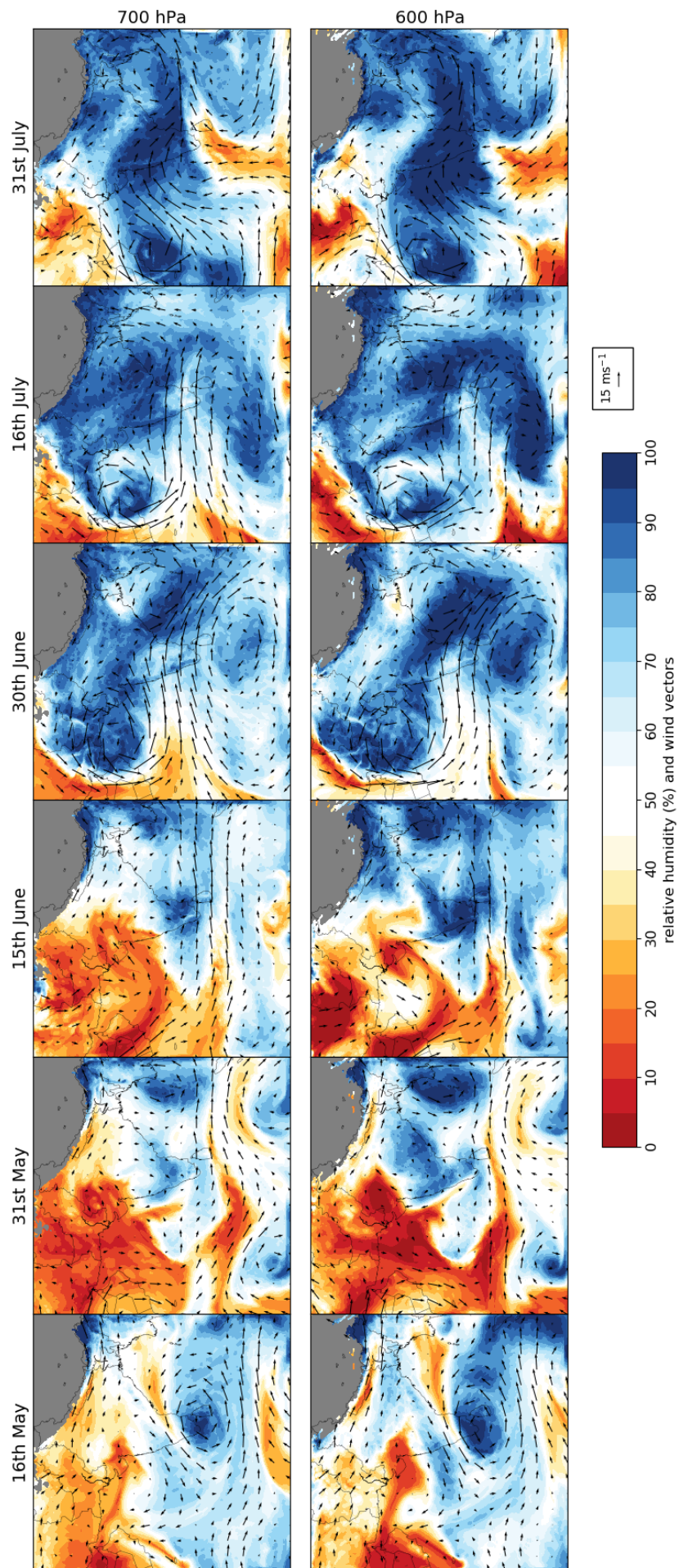
Figure 6.5: *Relative humidity (shading, %) and wind (vectors, ms⁻¹) at 700 (top) & 600 (bottom) hPa levels, from the 11 week simulation with the WRF model.*
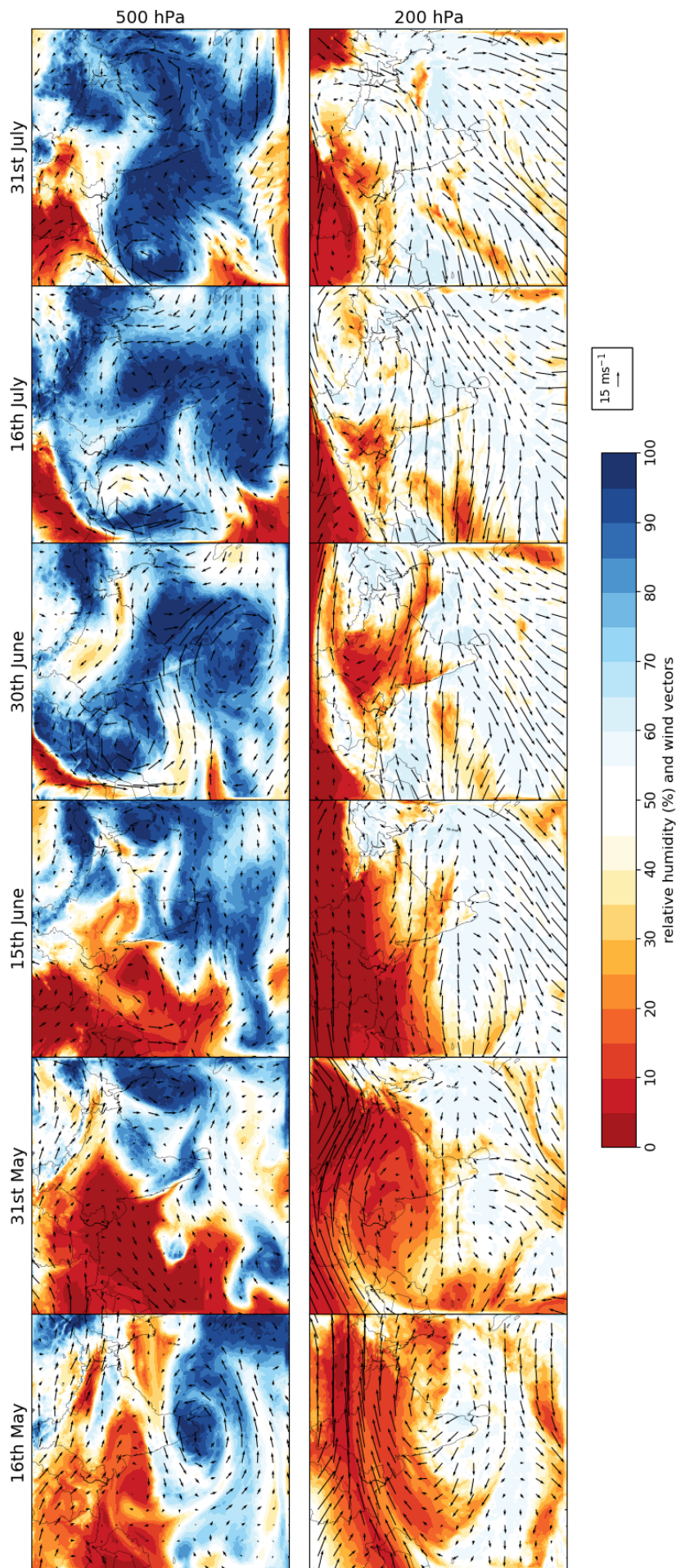
Figure 6.6:   *Relative humidity (shading, %) and wind (vectors, ms^{-1}) at 500 (top) & 200 (bottom) hPa levels, from the 11 week simulation with the WRF model.*

6.3.2 At first onset

The beginning of the Indian monsoon is marked by a disparity in land and sea temperatures, which contribute to changes in the large-scale circulation. Figure 6.3 (bottom) shows the average surface temperature for six days across the monsoon period. The sea surface temperature is kept constant here, as it varies slowly relative to the simulation length of 11 weeks. In the first two panels (16th and 31st May), a 5–10°C difference between the land and sea surface temperature can be seen. The Himalayas are marked by a sharp temperature gradient to the northwest of the panel, which is also apparent in Figure 6.10 (top).

The majority of the Indian landmass near the surface is dry, with a relative humidity of less than 30%, particularly where it joins the Eurasian continent (Figure 6.4). Looking at the 925 & 850 hPa level wind vectors in Figure 6.4, the southwesterly monsoon flow does not fully develop until mid–late June, which is consistent with the observed late onset date in Kerala (8th June) for 2016 (India Meteorological Department, 2016). A mid-level (around 600 hPa) dry intrusion from the northwest persists from May to the start of June (Figure 6.5), in agreement with observations from the INCOMPASS field campaign (Fletcher et al., 2018). At the 200 hPa level, shown in Figure 6.6, the Subtropical Jet (i.e. high level westerly wind) can be seen across northern India for 16th May. As time progresses towards the end of May/start of June, the Subtropical Jet weakens and moves northwards, out of the domain.

Figure 6.9 shows the geopotential height for the 850 and 500 hPa pressure levels. The formation of the monsoon trough, an area of low pressure over north India, can be seen for the dates in May, prior to onset. The monsoon trough extends in the vertical from the surface to mid-levels. There is a reasonable amount of precipitation over the oceans during May, but little over the Indian landmass, indicating a late onset. The normal onset date of 31st May shows little rainfall and there is no clear progression of the monsoon onset between 31st May and 15th June. Certain localised regions, like the southern tip of India and towards the northeastern states, do receive some rainfall during May. However, these pockets of rain are sparse compared with the widespread rainfall by mid-July during the full monsoon. The soil moisture correlates with the location of precipitation prior to onset and at first onset, with the southern peninsula and north eastern states becoming more wet throughout May. The soil temperature corresponds with the surface temperature, showing a north–south temperature gradient with north being warmer than the south. The Tibetan Plateau remains cool compared to the rest of India.

Figure 6.7 shows the vertical profile of relative humidity at Nagpur, a city in central India. The time along the x-axis is given in days relative to onset, which is taken as 18th June at Nagpur. At onset, a small moist layer at around 600 hPa suddenly deepens, extending from the surface to around 400 hPa. The lifting condensation level (dashed line) descends at onset, and remains low throughout the rest of the simulation. This pattern is consistent with Parker et al. (2016) and Menon et al. (2018), and lends to support to

the theory that cumulus and congestus clouds act to moisten the upper troposphere from below, allowing the monsoon onset to progress over India.

Considering the vertical cross-sections of water vapour mixing ratio and relative humidity (Figure 6.11) along transect 1, it can be seen that the whole atmospheric column over northwest India is dry in mid-May. To the southeast, a small moist plume extends from the surface to around 600 hPa. By 31st May, a moist wedge centred on 600 hPa is evident in relative humidity field, indicating a cloud layer. Figure 6.12 shows the vertical structure of the winds along transect 1. Here the westerly Subtropical Jet, located between 300 and 100 hPa, can be seen retreating throughout May as it moves to the north of India. The Tropical Easterly Jet develops during the monsoon period, just visible at first onset at the southeastern end of transect 1 and above 200 hPa. At mid-levels, over central India, the winds along transect 1 are relatively weak.
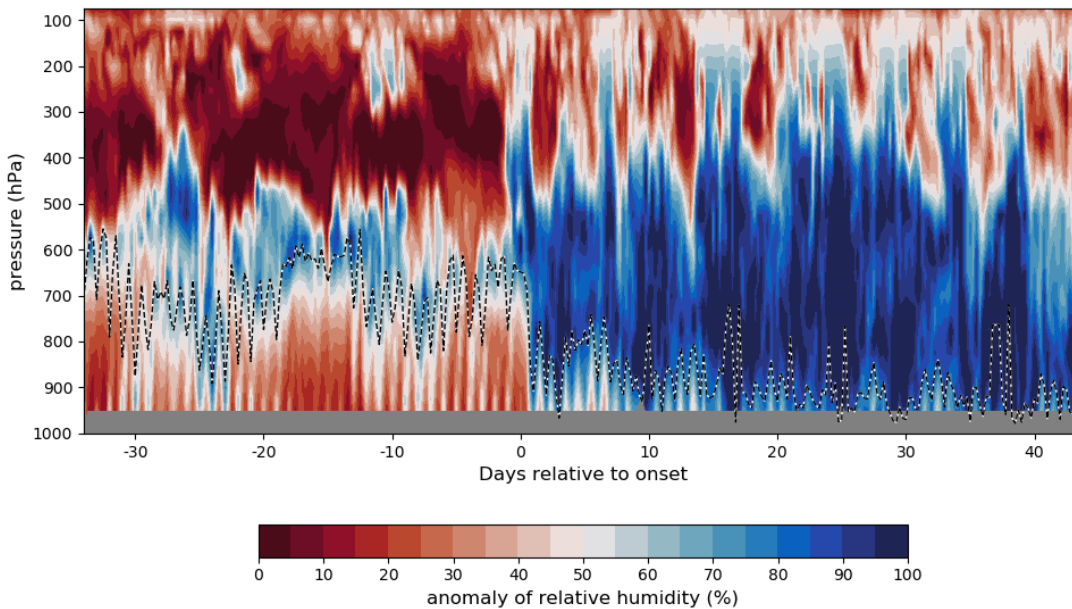
Figure 6.7: *Time-pressure section of relative humidity for Nagpur, Central India, from 11 week simulation with the WRF model. Lifting condensation level over-plotted (dashed line). Onset date for Nagpur in 2016 is taken as 18th June.*

6.3.3 Mid-onset

After the monsoon has first onset in Kerala, there is an increase of rainfall over the oceans and the southern peninsula, as shown by the 15th June panel in 6.3 (top). There is a marked change between mid and late June, predominantly over the oceans and mountains. The monsoon progresses more rapidly between 15th & 30th June, compared with 31st May & 15th June. The monsoon onset "front" can be visually determined from the spatial pattern of the rainfall, as per the isochrones in Figure 1.1. This is particularly evident over the Bay of Bengal, where the region of precipitation advances between 15th and 30th June. The India Meteorological Department (2016) reported that the rainfall in June 2016 was below average.

By mid June, the Tibetan Plateau shows a 5–10 °C increase in surface temperature, whilst the west coast cools slightly (Figure 6.3, bottom). An area beginning in the northwest and extending into central India remains very warm, around 40°C, throughout June. The air mass over this region is also warm and dry, extending in the vertical to 500 hPa. This dry intrusion is evident in Figures 6.4–6.6 for 15th June, but by 30th June, it has weakened dramatically and is barely seen at low levels (925–850 hPa). Strong northwesterly winds to the northwest of the domain follow a similar pattern, persisting through May to mid June, then almost disappearing by the end of June as the monsoon progression dominates. Indeed, on 30th June at the 500 hPa, the northwesterly winds have reversed direction, becoming southeasterly. The monsoonal flow, a low-level southwesterly current that becomes more westerly as it reaches India's west coast, is fully developed by mid-June. At high levels (Figure 6.6, bottom), the Subtropical Jet moves north, out of the domain, by the end of June. The Tropical Easterly Jet, centred on approximately 20°N, develops as the monsoon first onsets and is fully established by mid-June.

The monsoon trough is highlighted in Figure 6.9 (top) for the 15th June. Throughout June and into July, it gradually weakens at mid levels, with Figure 6.9 (bottom) showing that the 500 hPa level is at a higher altitude over northern India at the end of June. A low pressure system is established at the end of June, with characteristic features such as cyclonic circulation, reduced geopotential height and precipitation, clearly seen in Figures 6.3–6.9.

As previously noted, the land surface temperature is related to the soil temperature. The latter showing warming of the Tibetan Plateau and cooling of the southern peninsula during the onset period can be seen in Figure 6.10 (top). The soil moisture (Figure 6.10, bottom) is perhaps the best indicator of progression of the monsoon onset in the figures presented. The increase in the area covered by the monsoon is small between 31st May & 15th June, but greater between 15th June & 30th July. The significant increase in soil moisture by the end of June is representative of increased precipitation. Figure 6.3 (top) does not quite reflect this over land, but this is likely due to presenting a snapshot of daily data. Soil moisture varies over a longer timescale than precipitation, and thus is less sensitive to the specific monsoon date selected.

In the vertical cross-sections along transect 1, the most striking changes occur in the interim between mid and late June. The water vapour mixing ratio shows the progression of a moist shallow layer to the northwest throughout May and early June. This is shown by the blue filled contours in Figure 6.11 (top) between the surface and 900 hPa. By 30th June, the moist layer extends horizontally across the whole transect, has deepened to around 700 hPa and moistened. A clear vertical gradient in water vapour mixing ratio is observed, with lower values at higher levels. The relative humidity (Figure 6.11, bottom) shows the rapid moistening of the troposphere, from 15th–30th June, as the monsoon onset progresses. A dryer air mass of low relative humidity lies over the moist layer, with the 450 hPa level roughly separating them. The formation of clouds is indicated by the regions of saturated air. At 30th June, the relative humidity approaches 100% at localised areas in the southeast.

The Tropical Easterly Jet becomes more visible throughout June at high levels in Figure 6.12, shown by the green colours at high levels. The circulation alters significantly between mid and late June, as monsoon onset progresses over India. From northwest to central India at 30th June, the low–mid level winds along transect 1 become fairly strong southeasterly winds. Towards the end of the transect at around 2000 km, there is positive (red) region at low levels, indicating northwesterly winds. This represents part of the monsoon flow, which is southwesterly over the Arabian Sea, westerly over the southern peninsula of India, and northwesterly from India's east coast to the Bay of Bengal.
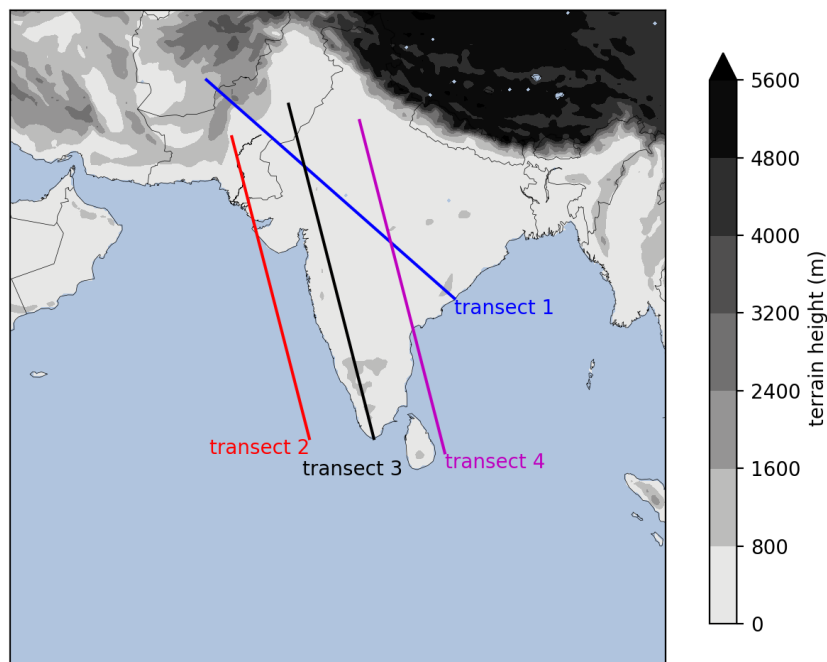
Figure 6.8: *Transect locations for cross-sections and further analysis.*
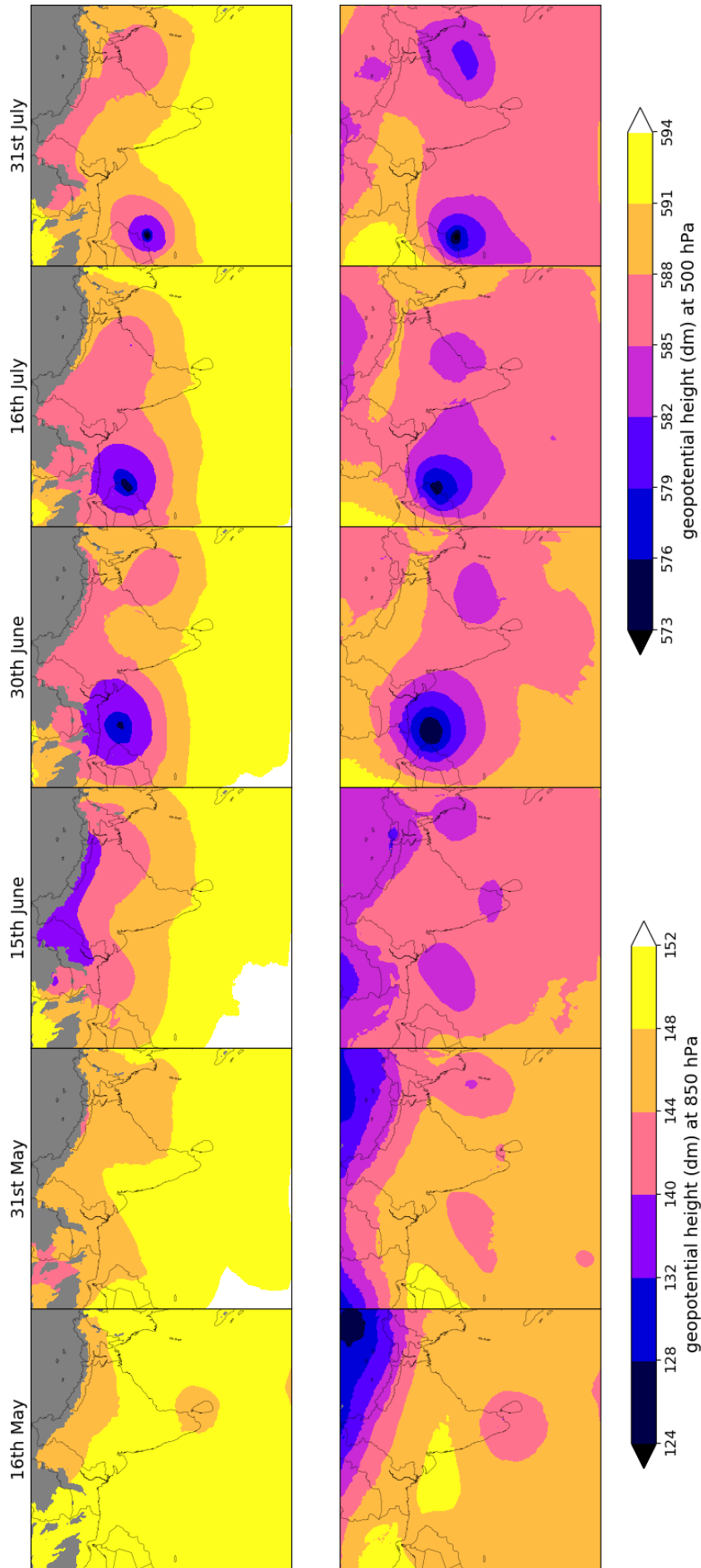
Figure 6.9: *Geopotential height (dm) at 850 (top) & 500 (bottom) hPa levels for various dates from the 11 week simulation with the WRF model.*
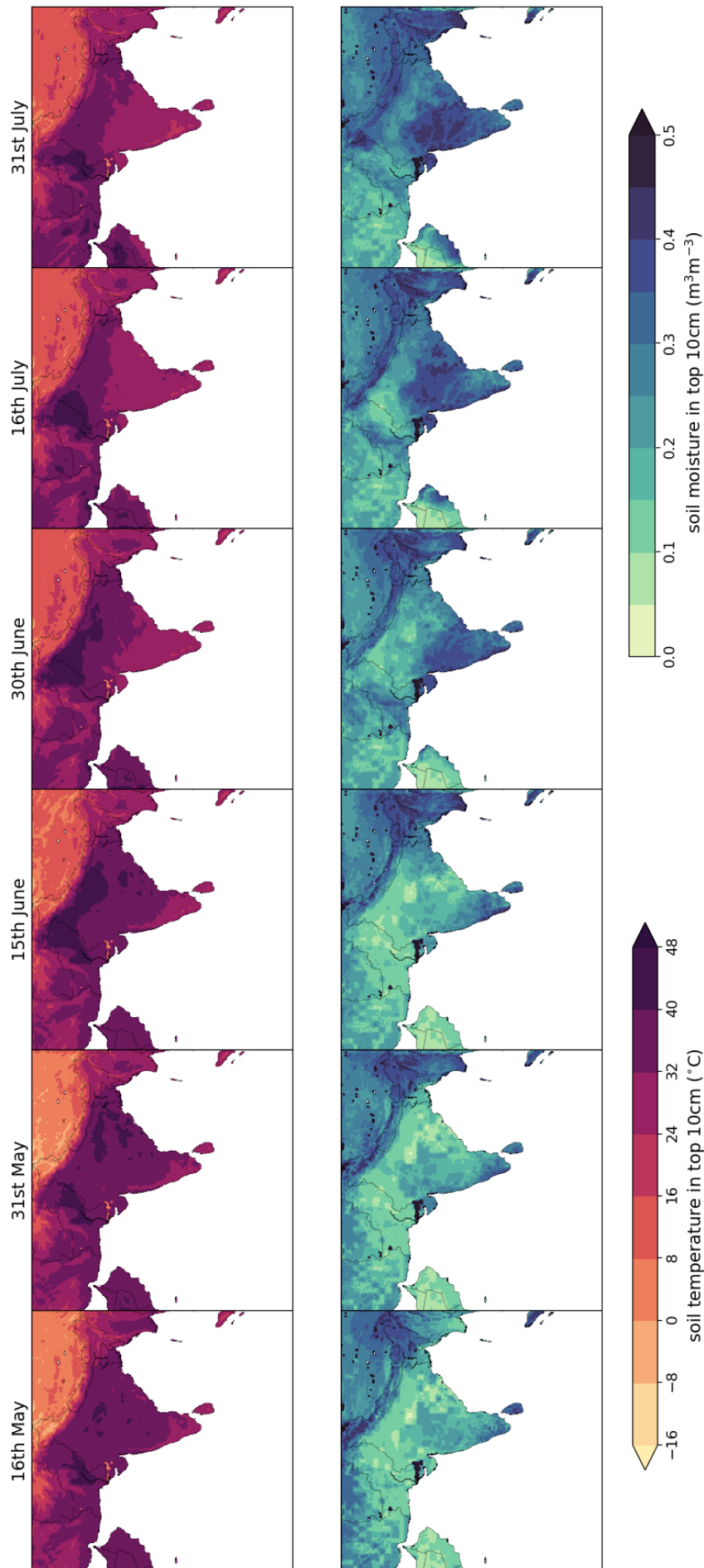
Figure 6.10: *Soil temperature (top, °C) and soil moisture (bottom, m^3m^{-3}) in the top 10cm for various dates from the 11 week simulation with the WRF model.*

6.3.4 Full monsoon

The monsoon onset progresses to the northwestern border of India by mid July, transitioning into the full monsoon phase which lasts until September. Precipitation is greatest over India during July, as seen in Figure 6.3 (top), especially compared to May and to a lesser extent, June. The presence of deep clouds is indicated by the location and intensity of rainfall. Central India receives both widespread (likely stratiform) and more localised, intense bursts (from deep convection) of rainfall in July. In contrast, the Thar desert to the northwest receives little even during the full monsoon. The simulation is consistent with observations for the year 2016, from which it is known that the monsoon onset progressed at a faster rate during the first two weeks of July than in the two weeks after first onset (8th June). Furthermore, India Meteorological Department (2016) state that the rainfall for July 2016 was above average.

By July, the region extending from northwest India of very warm land surface temperature has reduced in size (Figure 6.3, bottom). This corresponds with the retreating of the dry intrusion as the monsoon progresses to the northwest. Over the southern peninsula, particularly close to the west coast, and into part of central India, the surface temperature becomes several degrees cooler.

There is less of a significant change in the large-scale circulation and relative humidity from the end of June to the end of July, compared with mid–late June. As noted above, the air mass to the northwest becomes less dry, increasing from about 20% relative humidity at mid June to 50% by mid July (Figures 6.4–6.5). The predominant winds at low levels are southwesterly, becoming more westerly as they pass over south India. For 15th July, there is also some moist inflow at low levels from the Bay of Bengal to northeast India. At the 700 and 600 hPa levels, some plumes of dry air can be seen at the northwest and southwest corners of the domain for July, advected from the African and Eurasian continents. In Figure 6.6 (top), the plume from the northwest spans up to 500 hPa, becoming more dry with increasing height. There is a strengthening of the dry intrusion between 16th and 31st July at mid levels, extending further into central India, opposing the direction of monsoon propagation and possibly indicating a break phase. The key features of the horizontal wind field at high levels (Figure 6.6, top) remain largely unchanged from the end of June through to July, with the westerly Subtropical Jet to the north of the domain and the Tropical Easterly Jet visible over India.

The low pressure system noted at mid onset (30th June panels) remains over the Arabian Sea throughout July, weakening slightly and moving a little southwestwards. It extends from the surface to around 500 hPa, and is most evident in Figure 6.9. The relative humidity and horizontal wind field also show the system, with a strong anticlockwise circulation around the area of low pressure which is more moist than the surrounding air. The low pressure system is associated with a high amount of rainfall, especially on 31st July (Figure 6.3, top).

Looking at Figure 6.10, the soil temperature cools over most of India between mid

June and mid July, particularly along the Western Ghats, which receive a large amount of precipitation. Although the distribution of the surface temperature and the soil temperature is similar, the surface temperature is more sensitive and varies over a greater range. The soil moisture continues to increase over the land throughout the simulation. The difference between 16th May and 31st July in the soil moisture field really highlights the phase shift that occurs over India as the monsoon arrives, bringing moist airflow and prevalent rainfall.

In Figure 6.11 (top), there is little difference between 30th June and 16th July, although the water vapour mixing ratio is higher close to the surface and up to about 800 hPa. By the end of July, there is a reduction in water vapour mixing ratio near the mountains to the northwest of transect 1, associated with the resurgence of the dry intrusion. The relative humidity field in Figure 6.11 (bottom) also shows the reappearance of a dry air mass in the northwest at 31st July. The moist layer associated with the monsoon retreats slightly to the southeast, as the northwesterly dry intrusion prevails at mid levels. There is a greater region of saturated air visible at mid July than at the end of June, extending from the surface to 500 hPa, ranging about 500 km horizontally, which implies increased cloud development. The vertical extent of saturated air is somewhat reduced by 31st July, but increased in the horizontal direction, reaching over a distance of approximately 1000 km.

At high levels of 300 hPa and above, the Tropical Easterly Jet is clearly shown by the dark green areas for 16th and 31st July in Figure 6.12. Over July, the low–mid level southeasterly winds (green) at 0–1000 km weaken, partially reversing direction near the mountains at about 200 km by 31st July. Again, this indicates a strengthening of the northwesterly dry intrusion towards the end of July. To the far end of transect 1 near 2000 km, northwesterly winds, denoted by the red filled contours, persist at low levels. Between mid and late July, these northwesterly winds extend horizontally, stretching between 1000 and 2000 km.
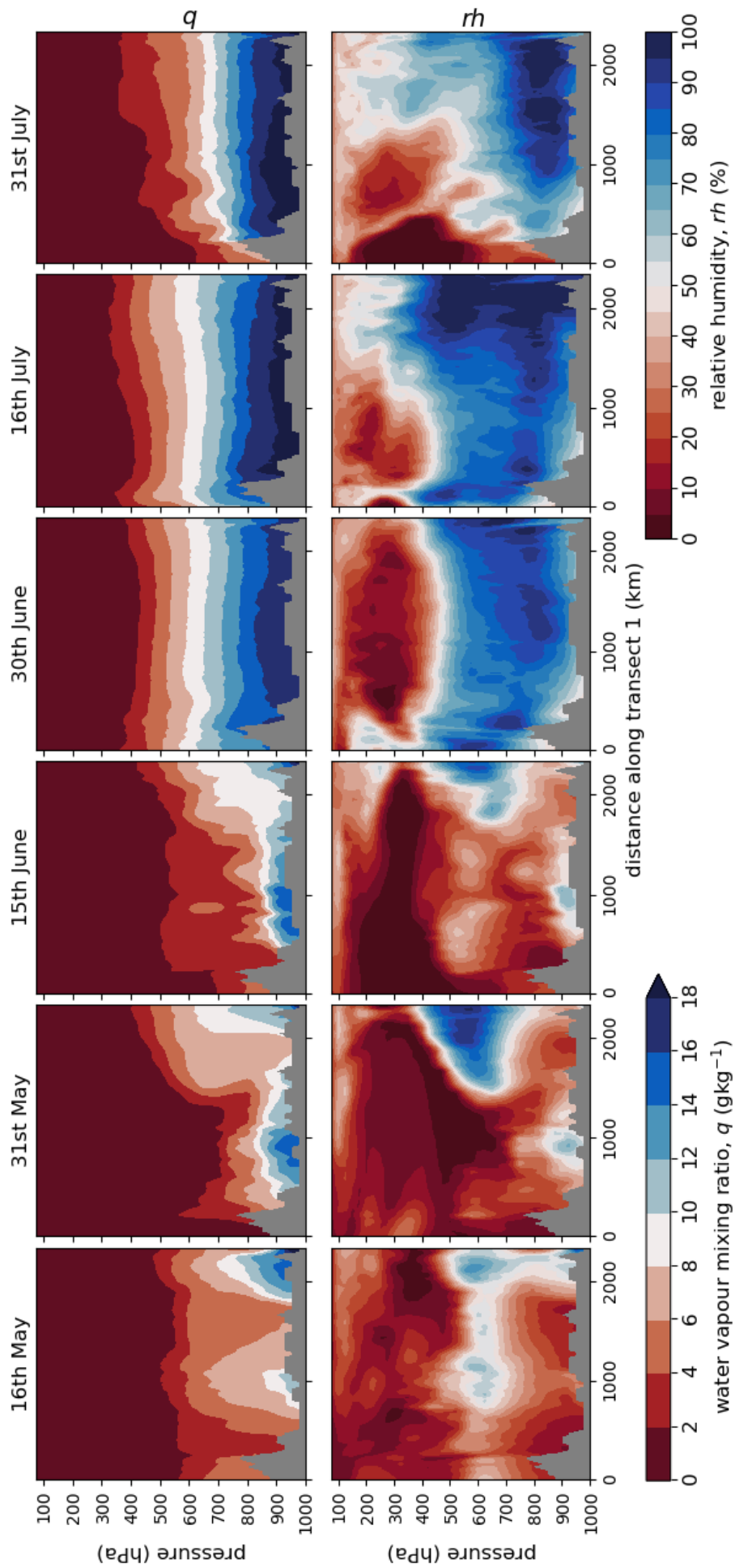
Figure 6.11: *Water vapour mixing ratio (gkg^{-1}, top row) & relative humidity (%, bottom row) along transect 1 for various dates from the 11 week simulation with the WRF model.*
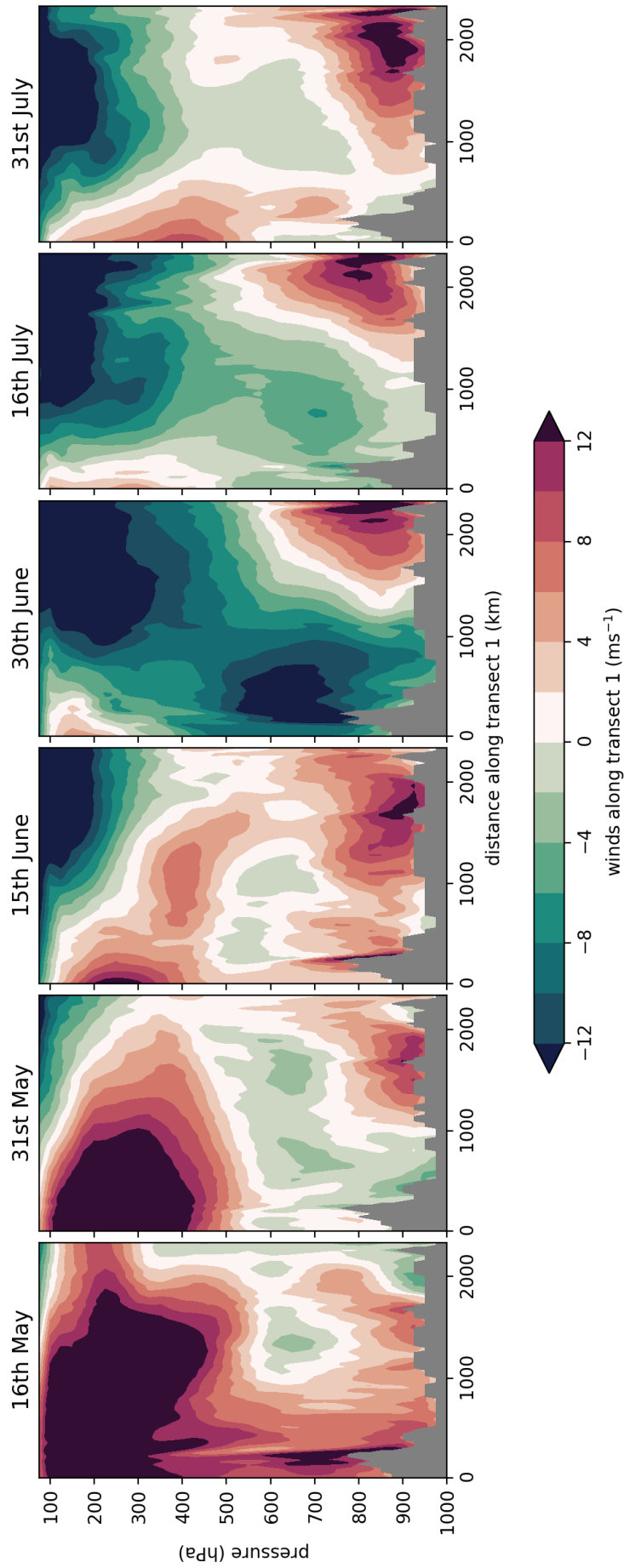
Figure 6.12: *Horizontal winds (ms^{-1}) along transect 1 for various dates from the 11 week simulation with the WRF model.*
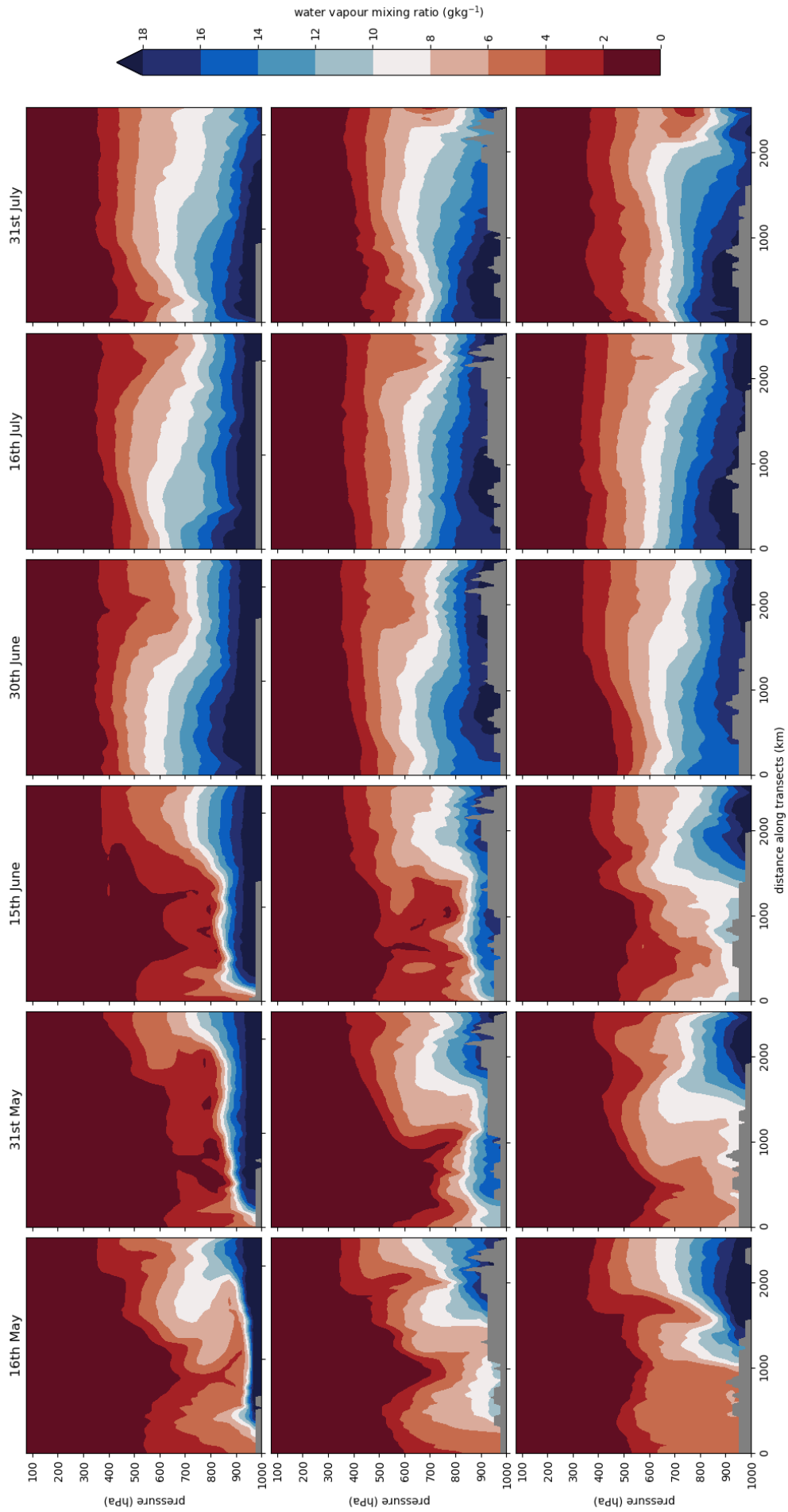
Figure 6.13: *Water vapour mixing ratio (gkg^{-1}) along transects 2 (top), 3 (middle) and 4 (bottom) for various dates from the 11 week simulation with the WRF model.*
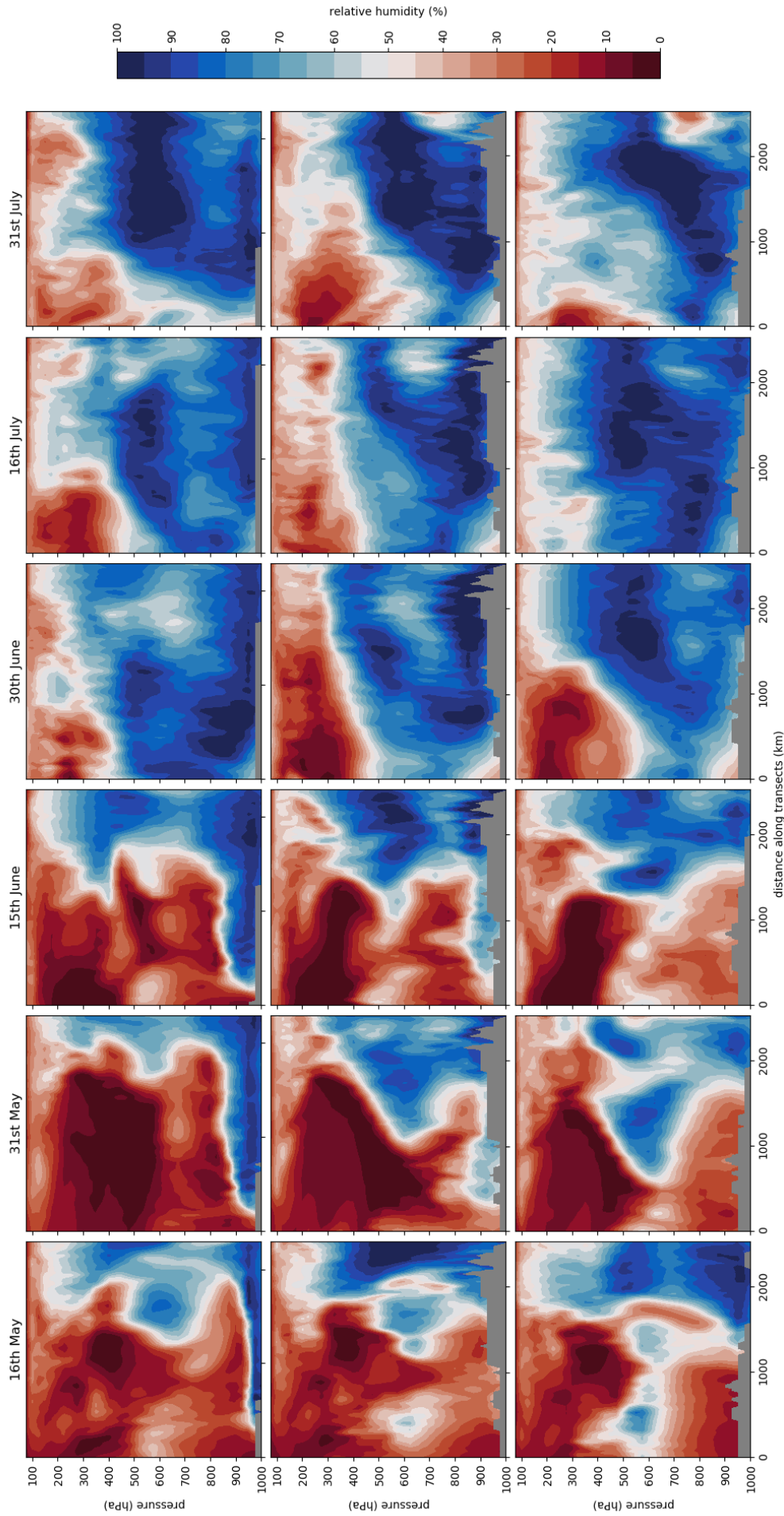
Figure 6.14: *Relative humidity (%) along transects 2 (top), 3 (middle) and 4 (bottom) for various dates from the 11 week simulation with the WRF model.*
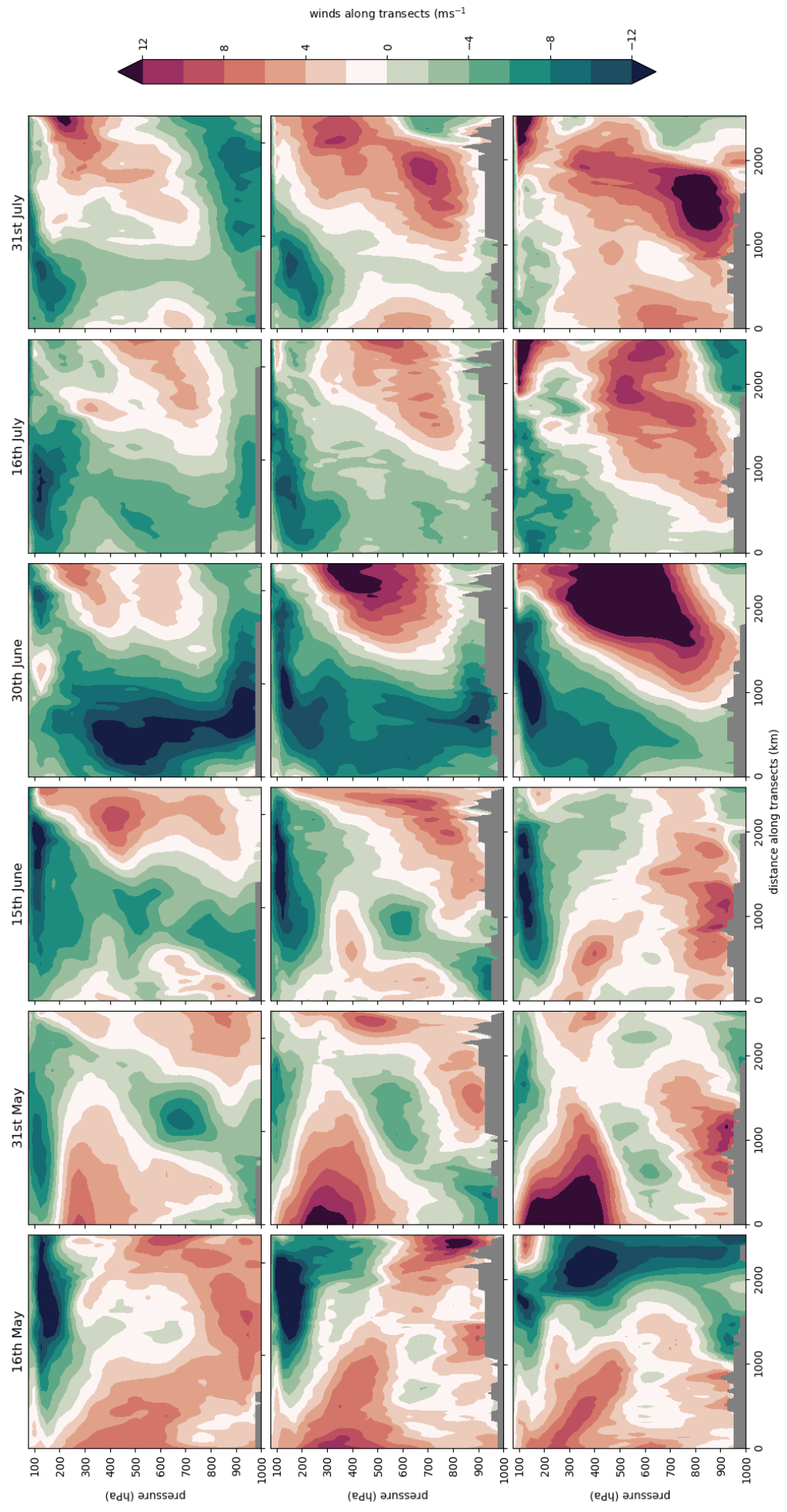
Figure 6.15: *Horizontal winds (ms⁻¹) along transects 2 (top), 3 (middle) and 4 (bottom) for various dates from the 11 week simulation with the WRF model.*

6.3.5   Lagrangian view

The Lagrangian movement of air masses from the Arabian Sea over India is considered, by examining vertical cross-sections of moisture and horizontal wind fields along Transects 2, 3, and 4 (shown in Figure 6.8). All transects are considered in a northwest to southeast direction. Transect 2 is mostly located offshore in the Arabian Sea, following India's western coast. Transect 3 begins in Multan, Pakistan, and ends in Kanyakumari, at the southernmost tip of India. It also follows India's west coast, but from the onshore side. Transect 4 is further to the east, passing through central India to the Bay of Bengal off the eastern coast. Transects 2–4 are approximately parallel to each other. The main monsoonal flow, consisting of moist southwesterly winds at low levels, travels from the south end of transect 2 to transect 4.

Looking first at the water vapour mixing ratio (Figure 6.13), there are high values seen at low levels in transect 2 during May, due to oceanic fluxes. In comparison, transects 3 and 4, which are mostly over land, have a lower water vapour mixing ratio near the surface. There is some increase in the depth of the moist layer at first onset, but the greatest difference is observed during the transition from 15th to 30th June, where there is a sudden jump in the vertical height of the moist layer. The advance of the monsoon onset is more clearly seen over the land surface than over the oceans. For example, in transects 3 and 4, similarly to transect 1, a region of high water vapour mixing ratio close to the surface is present in the southeast on 16th May. By late June, the moist region extends horizontally from southeast to northwest India.

In the relative humidity field (Figure 6.13), as in the water vapour mixing ratio, a thin layer of moist air is present over the ocean surface for transect 2 in mid May. Opposing the progression and growth of this moist layer is a warm, dry air mass to the northwest, referred to as a dry intrusion. The dry intrusion is at low–mid levels in all transects, and diminishes throughout June. Transect 3 shows the moist surface layer from 31st May, but to a lesser extent than for transect 2. In contrast, the air close to the surface to the northwest of transect 4 remains dry until the end of June. This can be explained by looking at the normal progression of the monsoon onset in Figure 1.1. Following the 10th June isochrone inland from the west coast, the isochrone retreats towards the southeast. Continuing along the isochrone, it then advances to the north towards the Himalayas. Thus, the monsoon onset progresses to the northwest at a faster rate along the west coast in June, than across central India.

The greatest shift in relative humidity occurs between mid June and the end of June, with a significant increases observed across all transects from the surface to about 500 hPa. Regions of saturated air are seen at 30th June and 16th July at low levels in transect 3 and at mid levels in transect 4. By 31st July, areas of 100% humidity are present in all transects towards the southeastern end, centred around 600 hPa. These areas indicate where clouds may form.

Figure 6.15 shows the winds along transects 2–4, with north-northwesterly winds being

positive (red) and south-southeasterly winds being negative (green). Transects 2–4 begin further south than transect 1, meaning that the Subtropical Jet is not well captured as it moves northwards during the monsoon period. The Tropical Easterly Jet is also poorly captured, because it moves in a direction almost perpendicular to transects 2–4. As noted previously, a significant change in circulation occurs during the last two weeks of June. At around 500 km in transect 2, strong south-southeasterly winds feature on 30th June, as in transect 1. The other transects (3, 4) show much weaker south-southeasterly winds at 500 km, but comparatively stronger winds in the opposite direction (red filled contours) at the south end. These north-northwesterly winds at low–mid levels, present to some extent in all transects, reduce in magnitude from 30th June–31st July.

6.3.6 Evaluation of model performance

The performance of the WRF model in simulating the Indian monsoon for the 2016 season is evaluated against observational and reanalysis data. In terms of forecasting, the key variable to represent accurately is the precipitation. A merged dataset (referred to as NMSG) dervied from rain gauge and the TRMM satellite measurements, described in Mitra et al. (2009, 2013), is used as a benchmark for the output precipitation field from the WRF model. Figure 6.16 shows the daily accumulated precipitation, averaged over June and July for the WRF model (top row) and the merged NMSG data (middle row). The anomaly, i.e. the WRF model output minus the regridded NMSG data, is plotted on the bottom row. In general, the WRF model produces too much rainfall over the oceans, particularly during July. Rainfall associated with the low pressure system in the Arabian Sea, noted in Subsections 6.3.3–6.3.4, appears to be anomalous compared with the NMSG dataset. Over northwest India and into central India, the WRF model slightly underestimates the precipitation. In contrast, the precipitation is overestimated by around 32 mm day^{-1} offshore of the Western Ghats. The WRF model also produces more precipitation than is observed along the Himalayan mountain range, especially to the east. Overall, the WRF model does a reasonable job of reproducing the observed precipitation field over India, despite some localised regions of exaggerated intensity.

Next, the relative humidity and winds at low and mid levels are considered against two reanalysis datasets, ERA5 (Copernicus Climate Change Service, 2017) and NCEP GDAS/FNL (National Centers for Environmental Prediction et al., 2015). Note that the latter is used to set the lateral boundary conditions in the WRF model simulations (Subsection 6.2.3). Figures 6.17 and 6.18 show the differences between the WRF model and the two reanalysis datasets for June and July, at the 850 and 500 hPa levels. At low levels (Figure 6.17, top row), the WRF model shows a dry bias over northwest–central India for June and July against ERA5 data. When compared to NCEP GDAS/FNL data, there is only a slight dry bias observed over central India in June. In July, the anomaly with NCEP GDAS/FNL data shows a significant wet bias over northwest India and to the north over the Arabian Sea (Figure 6.17, middle row). The northwesterly dry intrusion

is a much more prominent feature during July in the NCEP GDAS/FNL dataset than in the ERA5 dataset (Figure 6.17, bottom row). Surprisingly, the WRF model simulation follows the ERA5 dataset in this respect, despite the lateral boundaries being set by NCEP GDAS/FNL data.
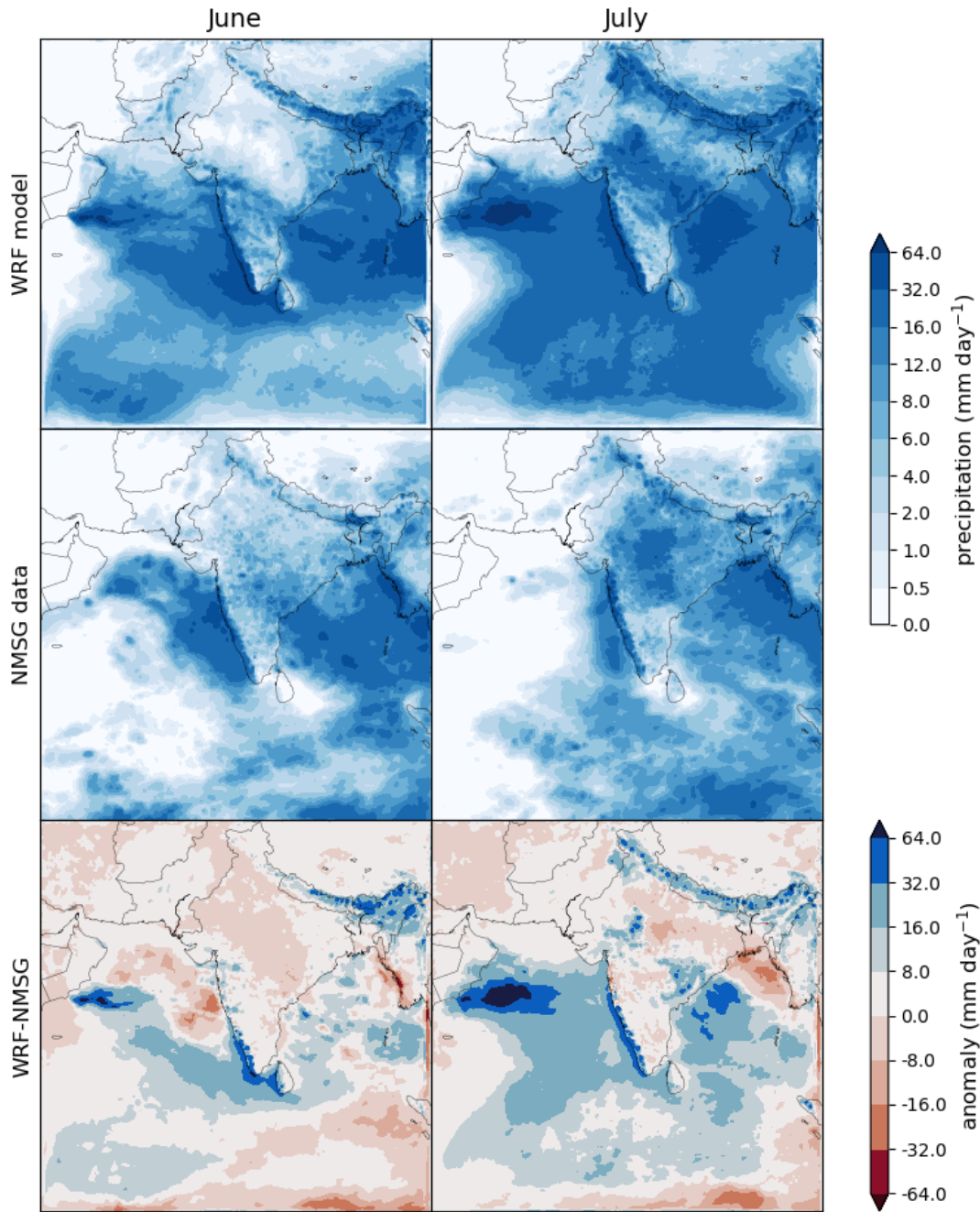
Figure 6.16: *Monthly averaged daily accumulated precipitation (mm day^{-1}) for June & July 2016. The top row shows data from the WRF model simulation and the middle row shows merged rain gauge/TRMM satellite data (Mitra et al., 2009, 2013). The bottom row shows the anomaly between model and observed data.*
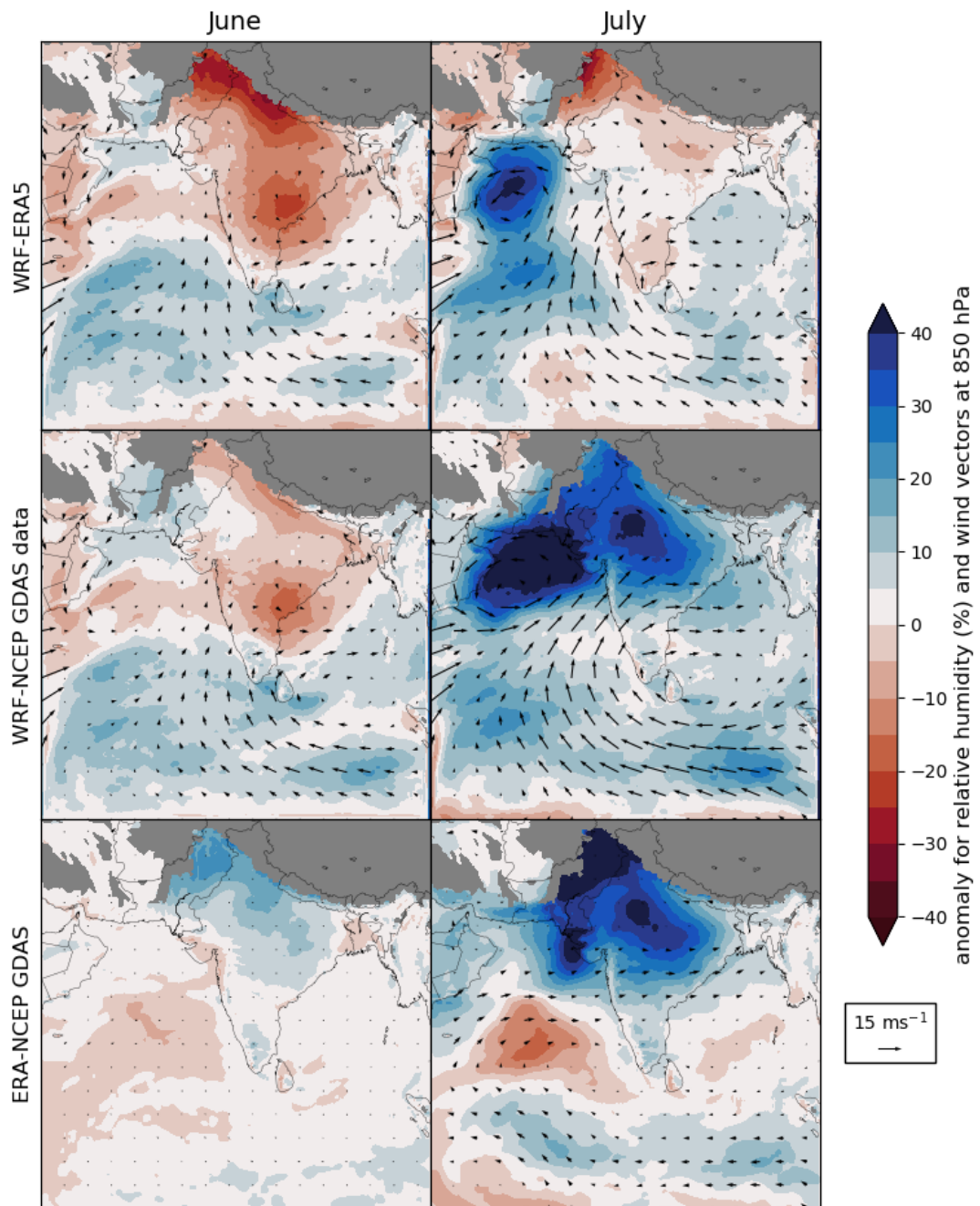
Figure 6.17: *Anomaly of monthly averaged relative humidity (%) and wind vectors (ms^{-1}) at 850 hPa for June & July 2016 between the WRF model & ERA5 reanalysis data (top row), the WRF model & NCEP GDAS/FNL reanalysis data (middle row) and ERA5 & NCEP GDAS/FNL reanalysis data (bottom row).*
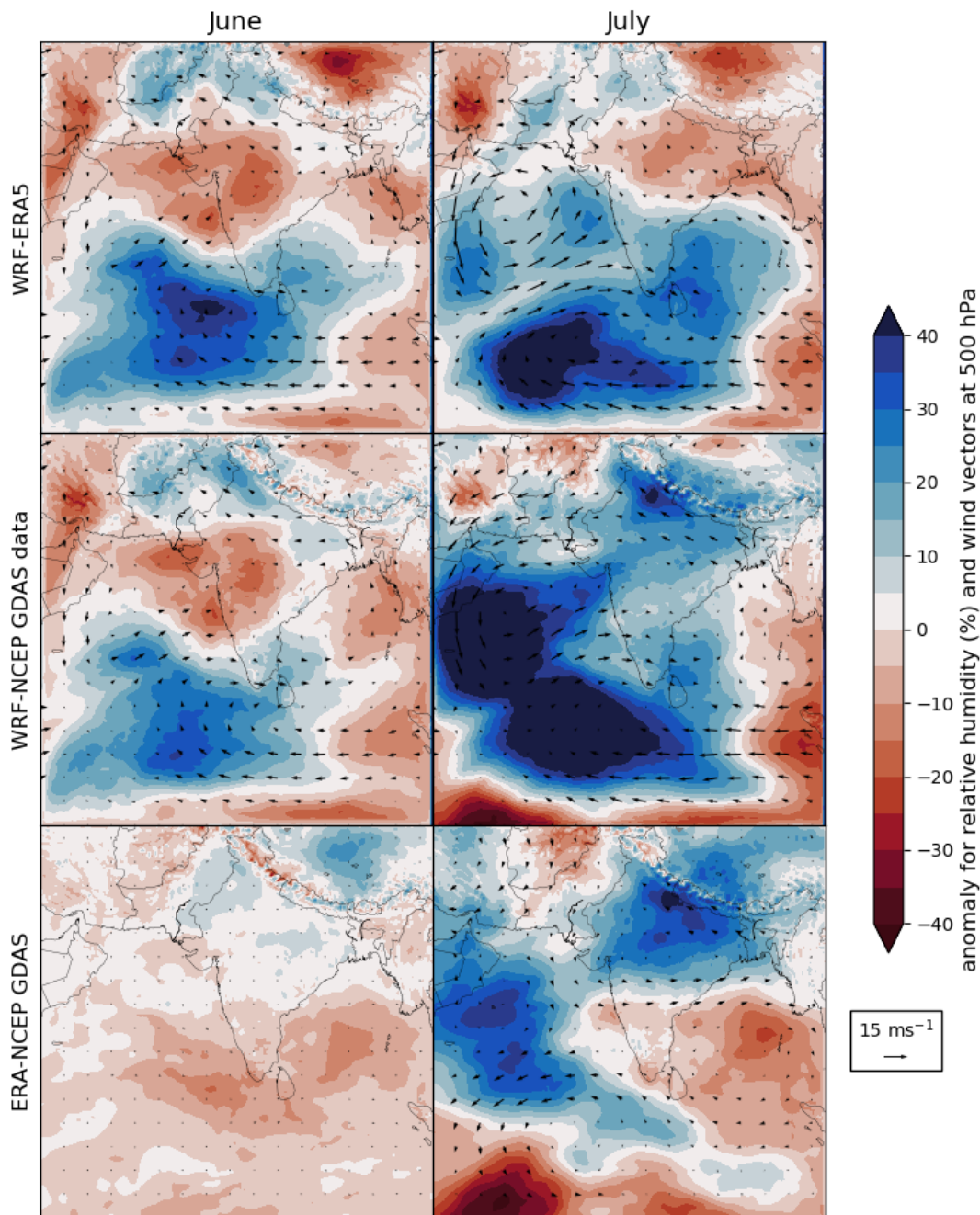
Figure 6.18: *Anomaly of monthly averaged relative humidity (%) and wind vectors (ms^{-1}) at 500 hPa for June & July 2016 between the WRF model & ERA5 reanalysis data (top row), the WRF model & NCEP GDAS/FNL reanalysis data (middle row) and ERA5 & NCEP GDAS/FNL reanalysis data (bottom row).*

Over the oceans to the south of India at 850 hPa, the WRF model has 5–10% higher relative humidity for June and July compared with the reanalysis datasets (Figure 6.17). All the subplots at 850 hPa show that the WRF model overestimates the monsoonal flow which becomes nearly westerly when passing over India's southern peninsula. A region of cyclonic winds located over the Arabian Sea, linked with the presence of a low pressure system, is shown for July at both 850 and 500 hPa. This implies that the system is an erroneous construct of the WRF model, as it does not appear in either of the reanalysis datasets.

The horizontal wind field at 850 hPa is almost identical in ERA5 and NCEP GDAS/FNL datasets for June, but a slightly stronger monsoonal flow is seen in July for ERA5 data compared to NCEP GDAS/FNL data. A monsoon depression is observed over the Arabian Sea at the end of June (India Meteorological Department, 2016), although it is not as strong or as persistent as the WRF model simulation shows. The other monsoon depression observed during the period of interest, forming over the Bay of Bengal at the start of July, is not reproduced by the WRF model.

The relative humidity anomaly between the WRF model and the reanalysis datasets is amplified at the 500 hPa level (Figure 6.18), with stronger biases that span greater areas. For June, the anomaly plots with ERA5 and NCEP GDAS/FNL data are fairly similar. A dry bias is seen over the north of the Arabian Sea to central India, which is offset by a wet bias to the south. For July, the difference in relative humidity between the WRF model simulation and ERA5 data is comparable to June, although the wet bias to the southeast becomes more moist. Against the NCEP GDAS/FNL dataset in July, the WRF model has a higher relative humidity over the entirety of India. Furthermore, there is a wet bias over the ocean to the east and southeast, which extends over a much larger region than in the ERA5 dataset. As at 850 hPa, the two reanalysis datasets are in reasonable agreement with regards to the relative humidity and horizontal wind field for June. For July, there are slight differences in the horizontal winds field at 500 hPa between ERA5 and NCEP GDAS/FNL datasets (Figure 6.18, bottom row), but it is difficult to quantify them at the scale shown. The WRF model produces stronger easterly winds at mid levels in June and July to the southeast of the domain, compared to either of the reanalysis datasets.

The differences in moisture over a vertical cross-section taken along transect 1 are investigated between the WRF model, ERA5 and NCEP GDAS/FNL reanalysis data. Figures 6.19 and 6.20 show the anomaly of water vapour mixing ratio and relative humidity, respectively. The six panels represent dates spanning the first onset, mid-onset and full monsoon phases. Up to mid June, the WRF model exhibits a dry bias at lower levels, centred on 800 hPa, compared with both reanalysis datasets (6.19, top & middle rows). It is more evident at 1000–2000 km along the transect. From 30th June to 16th July, the area at the northwestern end of the transect shows significantly higher values of water vapour mixing ratio from low–mid levels for the WRF model in relation to the reanalysis datasets. By 31st July, these differences to the northwest have dissipated, and instead a

slight dry bias at mid levels is the key feature. There are some differences at low levels between ERA5 and NCEP GDAS/FNL data (6.19, bottom row), mainly focused near the mountain/hill ranges.

The relative humidity field (Figure 6.20) shows differences in the vertical more starkly than the water vapour mixing ratio. There is a similar dry bias at low levels from the end of May to mid June. Additionally, the WRF model simulation has a lower relative humidity at high levels of over 200 hPa for May to mid June, compared to the reanalysis datasets (Figure 6.20, top & middle rows). After onset, from 30th June to 16th July, a layer of dry air relative to ERA5 and NCEP GDAS/FNL data can be seen from 400 hPa upwards, extending along the length of the transect. By July 31st, this dry layer has retreated slightly from the northwestern end of the transect, but deepened to 600–700 hPa. The wet bias over the mountains to the northwest, as observed in the water vapour mixing ratio field, is also seen in the relative humidity at the end of June and mid July, although it has a greater vertical extent.

Between the ERA5 and NCEP GDAS/FNL datasets (Figure 6.20, bottom row), there are various differences in relative humidity, but clear patterns are hard to detect. For 30th June, there are vertical plumes of lower relative humidity that stretch from around 800 hPa to the top of the atmosphere for ERA5 data compared with NCEP GDAS/FNL data. Also, there is a wet bias at low levels at the northwestern edge of the transect for June–July. This is consistent with Figure 6.17, where the northwesterly intrusion is more dry in the NCEP GDAS/FNL dataset than the ERA5 dataset. From Figure 6.21, it can be seen that there is more moisture present at around 500 hPa prior to onset in the WRF model compared to the reanalysis datasets, possibly indicating an abundance of mid-level clouds. After onset at Nagpur, the WRF model appears slightly more moist at low–mid levels and dryer at high levels than ERA5 or NCEP GDAS/FNL data. There are some differences in the vertical pattern of relative humidity between ERA5 and NCEP GDAS/FNL data, but they agree on the timing of onset.

The WRF model simulation is qualitatively consistent with observations from the INCOMPASS field campaign and the corresponding Met Office Unified Model runs, as described in papers by Fletcher et al. (2018); Turner et al. (2019); Volonté et al. (2019). In particular, the timing of the monsoon transition between mid and late June, incorporating dramatic changes across many atmospheric variables, is in agreement across models and observations for 2016 season.
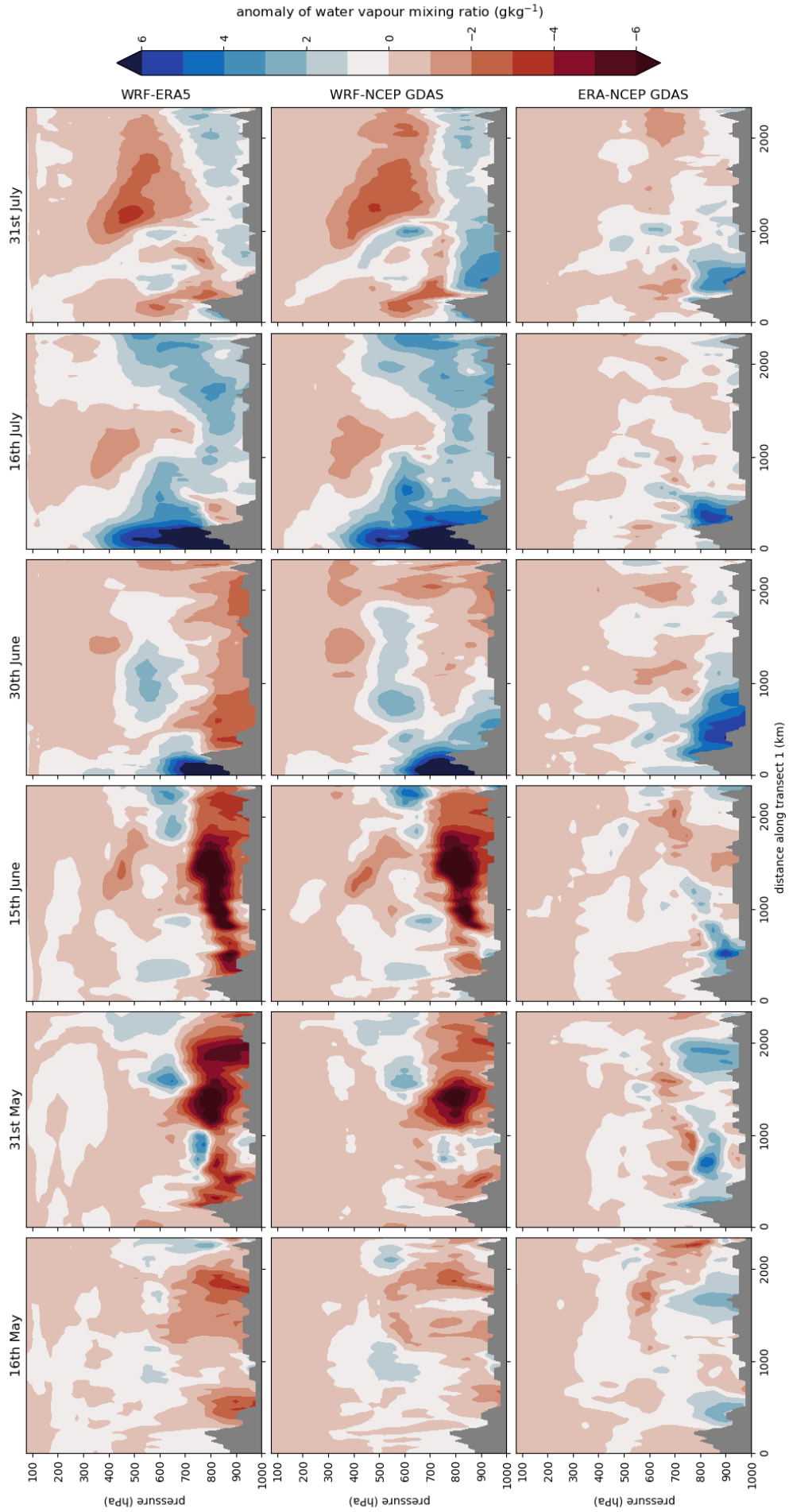
Figure 6.19: *Anomaly of water vapour mixing ratio (gkg^{-1}) along transect 1 for various dates during the 2016 monsoon between the WRF model & ERA5 reanalysis data (top row), the WRF model & NCEP GDAS/FNL reanalysis data (middle row) and ERA5 & NCEP GDAS/FNL reanalysis data (bottom row).*
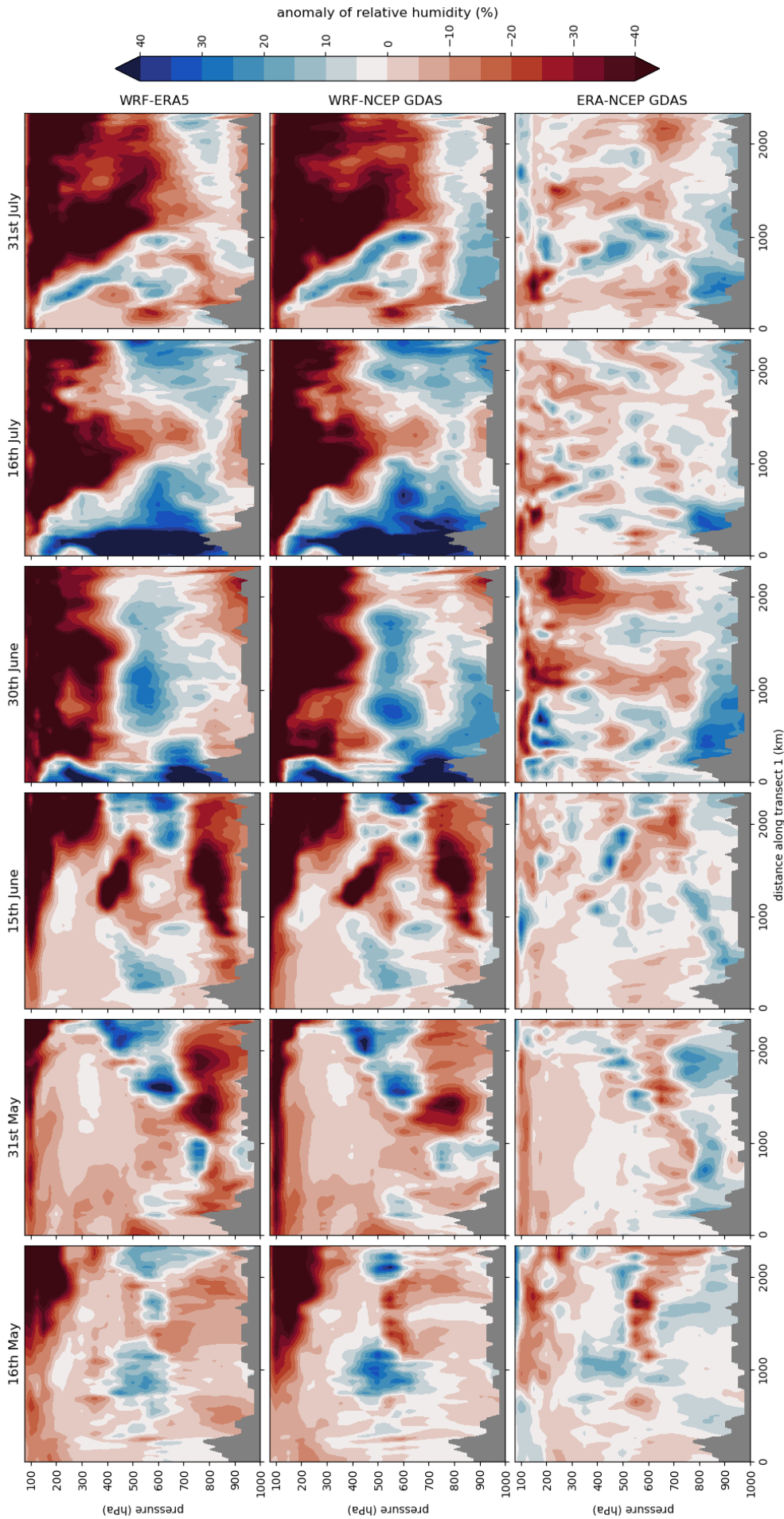
Figure 6.20: *Anomaly of relative humidity (%) along transect 1 for various dates during the 2016 monsoon between the WRF model & ERA5 reanalysis data (top row), the WRF model & NCEP GDAS/FNL reanalysis data (middle row) and ERA5 & NCEP GDAS/FNL reanalysis data (bottom row).*
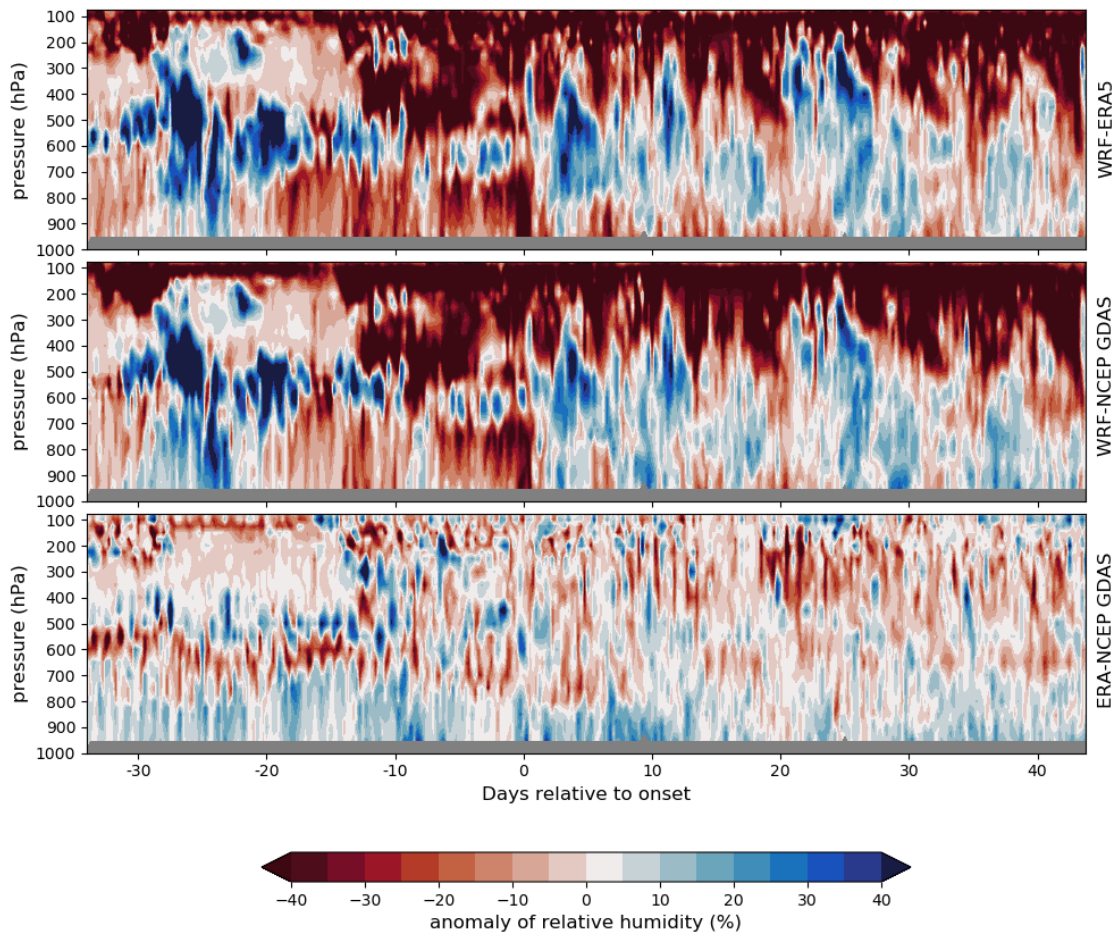
Figure 6.21: *Time-pressure section of relative humidity anomaly for Nagpur, Central India between the WRF model & ERA5 reanalysis data (top row), the WRF model & NCEP GDAS/FNL reanalysis data (middle row) and ERA5 & NCEP GDAS/FNL reanalysis data (bottom row). Lifting condensation level overplotted (dashed line). Onset date for Nagpur in 2016 is taken as 18th June.*

6.4 Concluding remarks

The 2016 monsoon season was characterised by a late onset over Kerala, a subsequently more rapid progression over India than normal, and the formation of a monsoon depression in the Bay of Bengal at the end of June. The WRF model has been used to simulate the Indian monsoon onset and progression for the 2016 season. The atmospheric dynamics have been presented and described in reasonable depth. The results have been validated against observations from the INCOMPASS field campaign and reanalysis datasets. The WRF model reproduces the timing of the transitions between pre-onset, mid-onset and the full monsoon, despite variations in the moisture and horizontal wind field over the interior of India. In particular, the late onset at Kerala and the moistening of the troposphere which enables rapid advancement during mid–late June, are well-captured. The differences

between the WRF model and reanalysis datasets are smaller than the changes associated with monsoon onset transitions, which this thesis aims to quantify. Note that there remains challenges regarding the accuracy and uncertainty of reanalysis datasets and field campaign observations (Collins et al., 2013). The formation of monsoon depressions and how well models reproduce their effects, is not one of the key research objectives. Thus, the failure of the WRF model to simulate the depression over the Bay of Bengal is not seen as significant in terms of this thesis. It is concluded that the WRF model simulation is sufficiently accurate to be used in further analysis and comparison to the dynamic lower layer model presented in Chapter 5.

Chapter 7

Comparing the two-layer moisture model with the WRF model

7.1 Introduction

The aims of this chapter are to explore the moisture budget of the Indian monsoon onset in a realistic numerical model simulation (Chapter 6), using the framework provided by the dynamic lower layer model (Chapter 5) to test hypotheses concerning the sensitivity of the onset to certain controlling processes. In particular, the evolution of integrated moisture content, low level moisture flux and upper level advection and their effect on the onset of the monsoon are examined in the WRF model simulation, in Sections 7.2–7.3. This enables testing of the theory behind the dynamic lower layer model and improves understanding regarding the dynamics in the real-world monsoon.

One of the key aspects to be evaluated is the convective timescale. In the dynamic lower layer model, values for this parameter were assumed. By conducting a moisture budget analysis over two vertical layers in the atmosphere in the WRF model simulation (derivation in Section 7.4, application in Section 7.5), a vertical convective flux between the layers can be diagnosed. Correlating the convective flux with the difference in integrated moisture content over the layers can inform a convective timescale for the WRF model (Section 7.6). It is difficult to quantify or measure such parameters in the real world, but knowledge of the timescales that processes act on can help to understand the Indian monsoon system.

The sensitivity of the convective timescale in the WRF model is also explored by switching off shallow and deep convection in turn, and the effect on the onset and progression of the monsoon is examined in Section 7.7. This should enable recommendations to be made regarding convective parameterisation schemes in models, and highlight the effect on the onset of the Indian monsoon.

7.2   Comparing column integrated moisture content

The key variable of interest in the dynamic lower model is the integrated moisture content, q. The WRF model is more complex than the dynamic lower layer model as it involves micro-physical processes of rain, snow and graupel as well as water vapour, although water vapour is usually several orders of magnitude greater than the other terms. Here, the integrated water vapour mixing ratio is taken as the corresponding variable in the WRF model. Another difference is that in the idealised model, layer heights are equal so that integrated quantities and mixing ratios are equivalent, but this is not the case in the WRF model. It is also not clear how to define and split the layers in the WRF model. The method adopted is to vertically interpolate variables from model to pressure levels, then separate the layers at a particular pressure level. Splitting the layers by pressure, which is effectively mass, was the assumption at the start of the derivation of the two-layer model. Pressure levels corresponding to the observed top of the monsoon layer, and the known typical top of shallow convection, are options for splitting the layers. The following tests will determine the best choice.
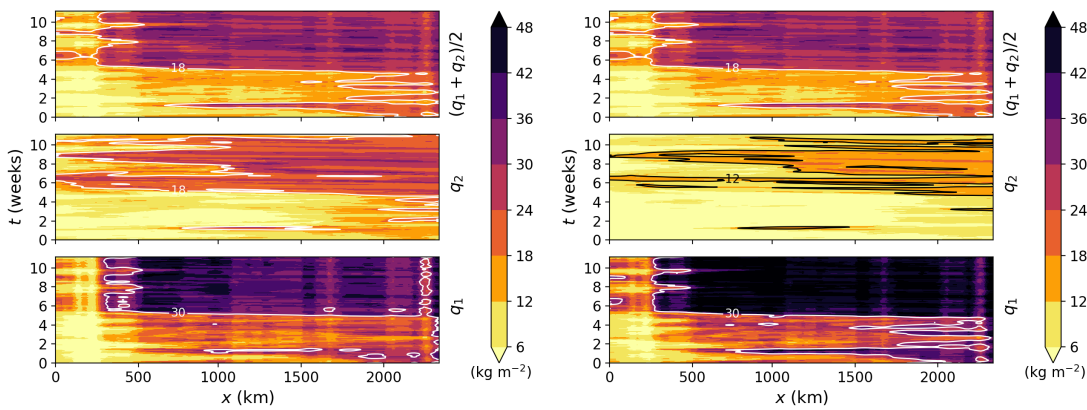
(a) *Transect 1, split at 700 hPa.*   (b) *Transect 1, split at 600 hPa.*

Figure 7.1: *Evolution of column integrated water vapour mixing ratio (kg m^{-2}) over two vertical layers, along transect 1, from the WRF model simulation.*

Figure 7.1 shows the integrated water vapour mixing ratio along transect 1 over time from the WRF model simulation for the lower, upper and combined layers. Distance along the transect from northwest to southeast is shown in km on the x-axis. The y-axis shows the time in weeks from the start of the simulation, with week 0 commencing on the 15th May. The lower layer is taken from the surface level (1000 hPa) to 700 hPa in Figure 7.1a, and from 1000 hPa to 600 hPa in Figure 7.1b. The upper layer moisture is integrated from the level split to 50 hPa. Note that 700 hPa, 600 hPa and 500 hPa have been considered as levels at which to separate the layers, although the results of 500 hPa are not presented to avoid repetition. Figure 7.2 is similar to Figure 7.1, but the sections are along transects 2–4. The location of the transects, which are all viewed in a direction from northwest to southeast, is shown in Figure 6.8 in Chapter 6. The white (or black for q_2 at 600 hPa)

contour line highlights the transition to onset, based on the increase in layer moisture content.

For the lower layer moisture in Figure 7.1 (labelled as q_1), there is a sudden jump between 4 and 6 weeks into the simulation, indicating monsoon onset. The increase is more striking in 7.1b than 7.1a, as would be expected with including a greater vertical extent in the lower layer. The upper layer moisture, q_2, also shows a significant increase around the time of onset. However, the increase for the upper layer is much smaller than for the lower layer, especially when the layers are split at 600 or 500 hPa. In weeks 0–4, prior to onset, the lower layer is more moist than the upper layer for the same period. Post-onset, the lower layer moisture content is slightly less than double the upper layer moisture content when split at 700 hPa, and more than double when split at 600 hPa. A gradient of increasing moisture from northwest to southeast is expected. This is evident in the upper layer, but difficult to see in the lower layer. The total moisture $(q_1 + q_2)$, scaled by $1/2$ to show on the same axes as q_1, q_2, is dominated by the evolution of the lower layer moisture, particularly when the lower layer extends over a greater vertical height. The moistening of the lower layer, signalling a transition from pre-onset to monsoonal conditions, occurs first towards the southeast (at approximately 2400 km). It is difficult to see the progression from southeast to northwest (i.e. from right to left) at this timescale. A plot focused around weeks 4–8 would be more clear, and more appropriate to compare to the experiments with the idealised model, which transition from one equilibrium to another in under 4 weeks. This is presented and discussed later in the section (Figure 7.3). The monsoon onset advances to the northwest to about 300 km. Further to the northwest (i.e. within $0 < x < 300$ km) is a desert region, that is beyond the limit of the Indian monsoon.

Considering the integrated water vapour mixing ratio along transect 2 (Figure 7.2a, 7.2b), a high amount of moisture is seen in the lower layer from the start of the simulation at 1500–2000 km, compared to transect 1. This is probably due to the southern end of transect 2 being located over the ocean, where surface moisture fluxes are greater than over land. The monsoon onset "front", approximately indicated by the white contour line, can be seen to progress from 1500 to 750 km, moving towards the northwest. This is also observed in the total moisture subplot. The upper layer moisture along transect 3 evolves similarly to transect 1, noting that there is less moisture in the upper layer (and correspondingly more in the lower layer) as the level at which the layers are separated is increased.

(a) *Transect 2, split at 700 hPa.*

(b) *Transect 2, split at 600 hPa.*

(c) *Transect 3, split at 700 hPa.*

(d) *Transect 3, split at 600 hPa.*

(e) *Transect 4, split at 700 hPa.*

(f) *Transect 4, split at 600 hPa.*
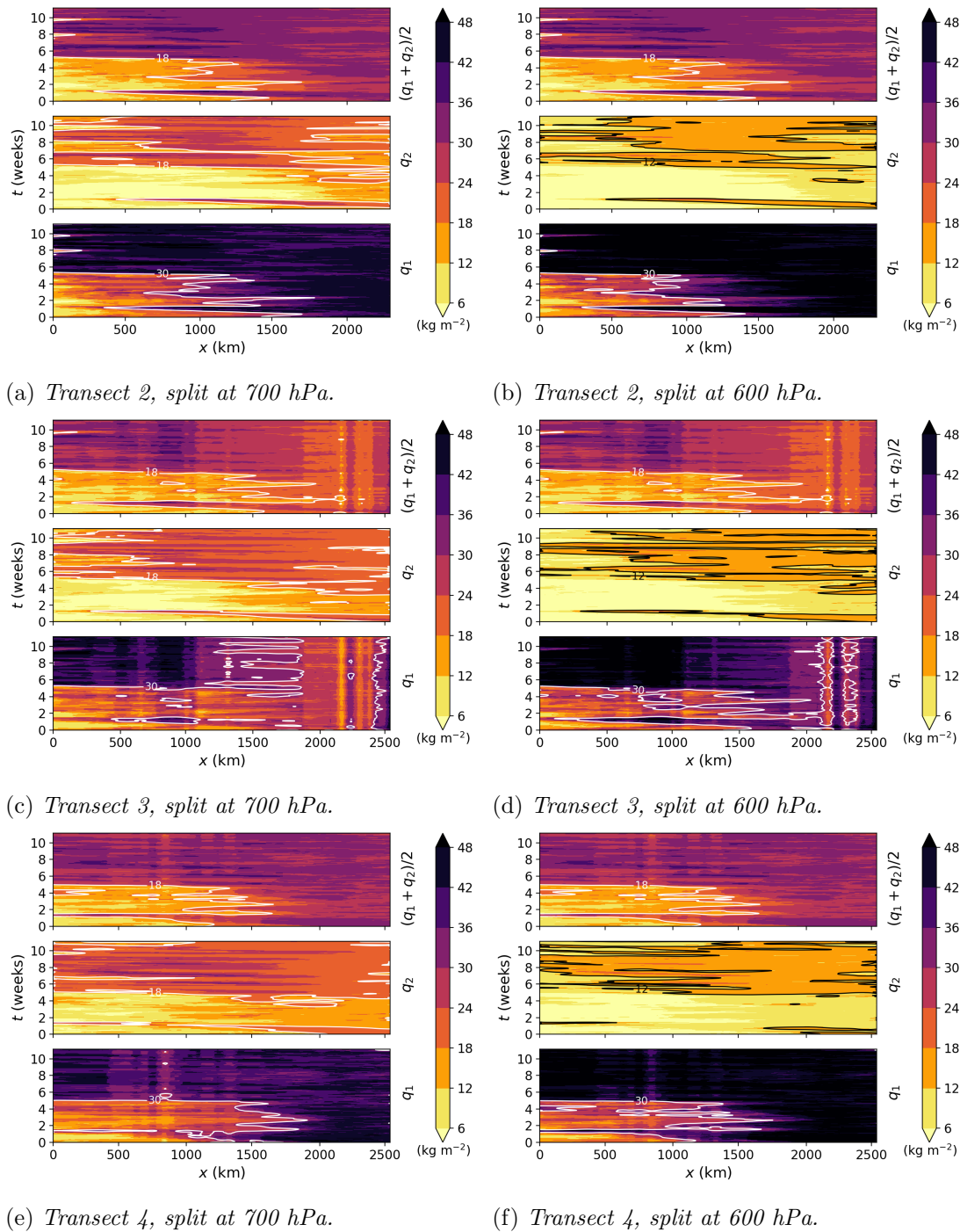
Figure 7.2: *Evolution of column integrated water vapour mixing ratio (kg m^{-2}) over two vertical layers, along transects 2 (top), 3 (middle) and 4 (bottom), from the WRF model simulation.*

The monsoon onset progresses along the whole length of transects 2–4, which begin further south than transect 1. At the southwest end of transect 3, between 2000 and 2500 km, the low level moisture field is disrupted by the presence of mountains, which are part of the south Western Ghats range. The moisture evolution along transect 4 is comparable to transect 2.

Having investigated the differences between splitting the atmosphere into two layers at 700, 600 and 500 hPa, the most appropriate choice is 700 hPa because it shows a

clear increase of moisture in both layers from the time of monsoon onset. This is most comparable to the dynamic lower layer model. Also, it means that cloud processes leading to rainfall would be contained solely within the upper layer (i.e. above 700 hPa), which simplifies further analysis regarding moisture budgets. It would also be consistent with the assumptions made in the derivation of full two-layer model in Chapter 3, where the precipitation is removed from the upper layer (Equations 3.1a–3.1c).
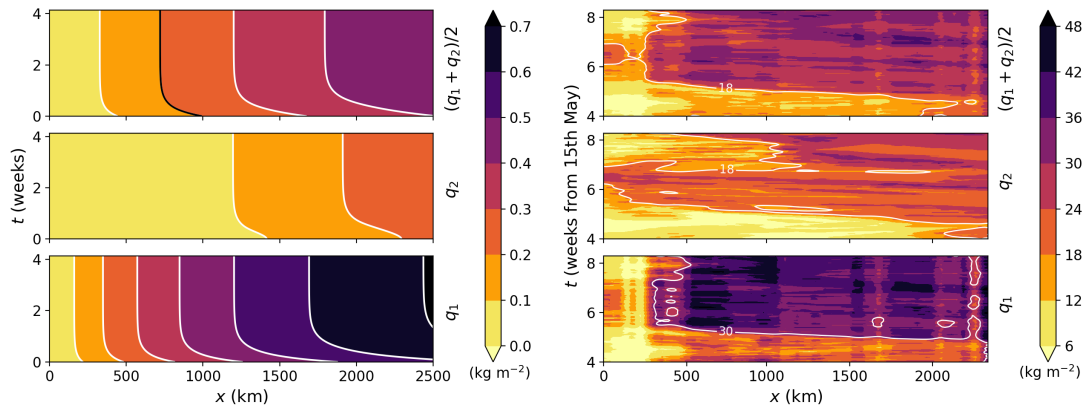
(a) *Dynamic lower layer, increasing moist in-flow.* (b) *WRF, along transect 1, separating at 700 hPa.*

Figure 7.3: *Evolution of column integrated water vapour mixing ratio (kg m^{-2}) over two vertical layers for the dynamic lower layer model and the WRF model.*

Figure 7.3 shows the evolution of moisture along a transect from northwest to southeast India around the time of onset. Figure 7.3a is produced from an experiment with the dynamic lower layer model where the monsoon flux is suddenly increased, initiating monsoon onset. Figure 7.3b is from the WRF model simulation, where the layers have been defined in terms of pressure levels, with the lower layer extending from 1000–700 hPa and the upper layer from 700–50 hPa. Both plots are shown on the same timescale (y-axis) and approximately the same length-scale (x-axis). The monsoon onset in the dynamic lower layer model, illustrated by the black contour in the total moisture subplot, progresses $\sim$250 km in less than a week. By comparison, the white contour in the total moisture plot for the WRF model travels $\sim$1600 km in about a week. The upper layer moisture content is qualitatively similar between the models. The middle subplots show more moisture in the southeast than the northwest, a slower rate of moistening than for the lower layer, and less moisture overall than in the lower layer. For the lower layer moisture content, the dynamic lower layer model shows a strong moisture gradient from northwest–southeast, which is less obvious in the WRF model. This is possibly due to simplification of processes in the dynamic lower layer model, leading to more linear effects. Additionally, the values of integrated moisture content (kg m^{-2}) differ by a factor of about 50. Even if the dp/g factor used in the integration of water vapour for the WRF model was not taken into account, they would still differ by a factor of about 30. In summary, the timing of monsoon onset is comparable between the two models, despite the differences in

progression distance and moisture values.

7.3   Comparing horizontal advection

Another aspect that can be compared between the dynamic lower layer model and the
WRF model is the horizontal wind field. In Chapter 3, the horizontal wind in the lower
layer is defined only in the direction perpendicular to the transect - $(u_1, v_1) = v_1$, i.e. to
the northeast. The upper layer wind is also assumed to be in a single direction, along
the transect, $(u_2, v_2) = u_2$. A positive value for the flow in the upper layer indicates a
northwesterly wind. Chapter 5 simplifies the wind field further, retaining the upper layer
winds along the transect (u_2), but incorporating the lower layer wind into a new term
representing the rate of moisture advected into the system at low levels.
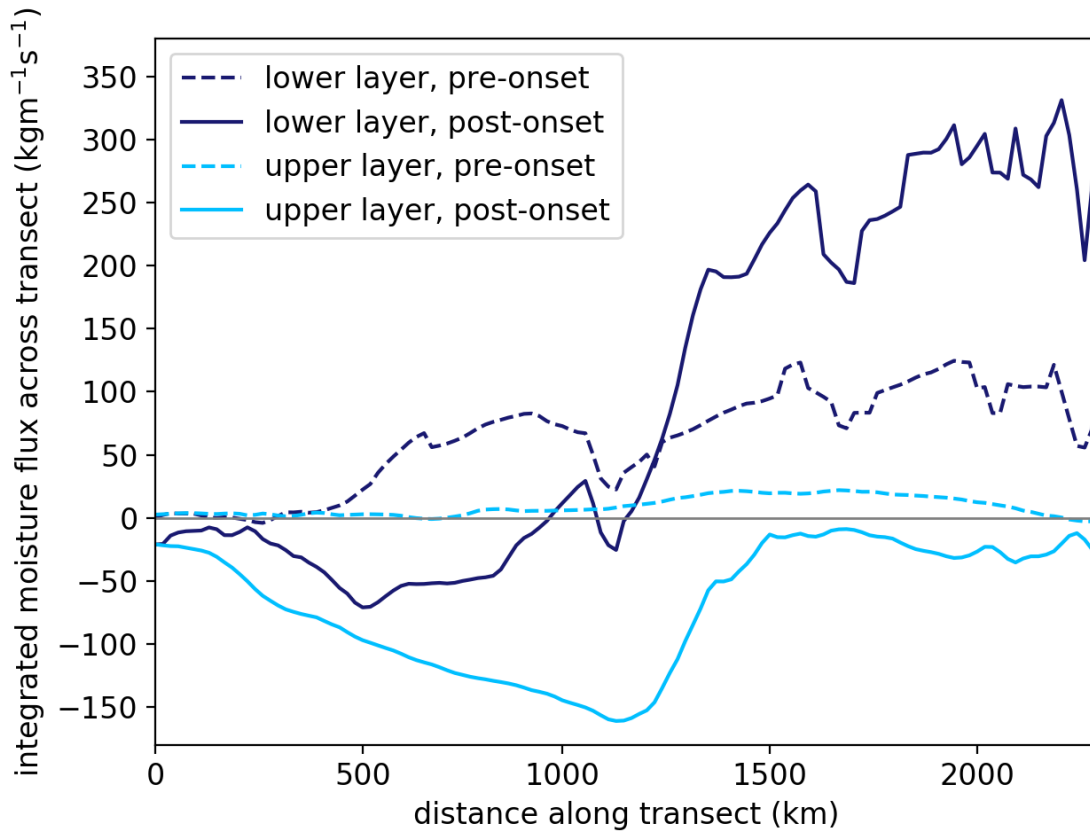
Figure 7.4: *Integrated moisture flux over lower and upper layers that are split at 700 hPa.
Taken along transect 1 using data the from the 11 week simulation with the WRF model.*

The (integrated) moisture flux at low levels and horizontal wind field along a northwest–
southeast transect can be determined from the WRF model simulation. The former is
shown in Figure 7.4, where the moisture flux across transect 1 (see Figure 6.8 for loca-
tion) has been integrated over two vertical layers in the atmosphere. The dashed lines
represent pre-onset conditions, which is calculated from averaging over the last 2 weeks in
May. Post-onset (solid lines) refers to data being averaged over the first 2 weeks of July.
Although the integrated moisture flux for the upper layer (light blue lines) is shown, it

is the integrated moisture flux for the lower layer (dark blue lines) that is of interest for comparison with the dynamic lower layer model. From pre-onset to post-onset, there is a sudden large increase of integrated moisture flux for the lower layer towards the southeast of the transect. Between about 1200 and 2300 km, the integrated moisture flux for the lower layer more than doubles over the 6 week interval. This result provides further justification to the basis of the idealised model experiment presented previously in Chapter 5, Section 5.5. There, the monsoon flux is increased by halving the timescale of moist inflow, which triggers a monsoon onset. It is encouraging that both models show that there is an abrupt rise in the moisture flux at low levels prior to onset, particularly towards southeast India. The increase in magnitude of the upper layer moisture flux after onset, and the change of direction (becoming more negative), is associated with the development of the Tropical Easterly Jet over central India.
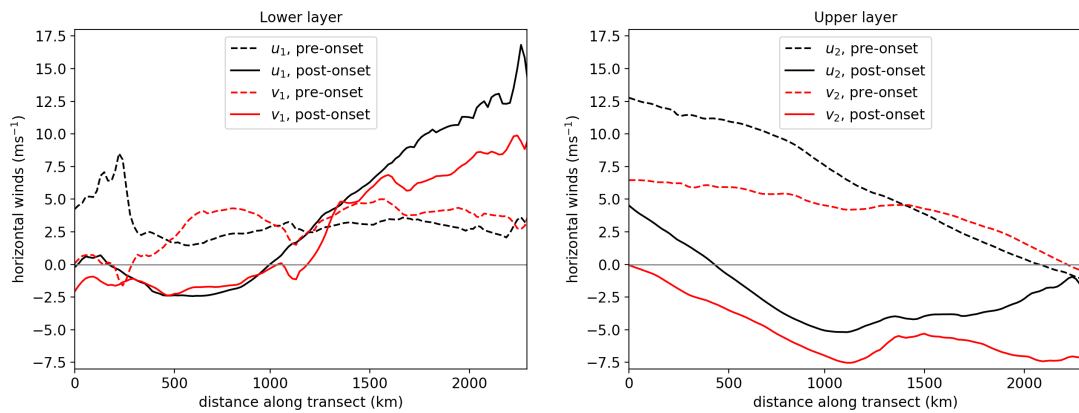
(a) *Lower layer.*   (b) *Upper layer.*

Figure 7.5: *Horizontal winds along (u, black lines) and perpendicular to (v, red lines) transect 1, averaged over lower and upper layers that are split at 700 hPa. Data the from the 11 week simulation with the WRF model.*

It is evident from Figure 7.5 that the lower layer winds to the southeast of the transect constitute a significant portion of the increase of the integrated moisture flux. However, the post-onset low level winds show a nearly linear increase between 1000 and 2000 km, particularly along the transect (i.e. for u_1). Prior to onset, the averaged lower layer winds are reasonably small (< 5 ms^{-1}) and positive, indicating northwesterly winds along the transect and southwesterly winds perpendicular to the transect. Post-onset over 0–1000 km, the low level winds become weak south-easterlies along transect 1 and weak north-westerlies perpendicular to transect 1. Then, from 1000 km onward, increasingly strong north-westerlies along and south-westerlies across the transect are seen. This is consistent with the observed strengthening of the low level southwesterly monsoon flow, which brings an influx of moisture from the Arabian Sea.

In the upper layer, the averaged pre-onset winds along (u_2) and perpendicular to (v_2) transect 1 show a gradual weakening over the length of the transect. Post-onset, the upper layer winds reverse direction. In terms of comparison with the dynamic lower layer model,

the key aspect to consider is the change of upper layer winds along a northwest–southeast transect at around the time of onset (i.e. u_2). At 0–500 km, the upper layer winds along the transect go from strong north-westerlies (~ 12 ms^{-1}) to weak north-westerlies (~ 2.5 ms^{-1}) once the monsoon has onset. This is coincident with a weakening dry intrusion over northwest India. Referring back to Chapter 5, the experiments with the dynamic lower model in Section 5.6 concern the effect of varying the upper level advection (u_2) on monsoon onset. Figure 7.5b validates the values chosen for u_2 in the dynamic lower layer model experiments. It also supports the result that halving the northwesterly upper level winds allows the monsoon onset to progress to the northwest.

7.4   Moisture budget derivation

A moisture budget analysis is undertaken in order to calculate a vertical convective flux between two layers of the troposphere for the WRF model. The moisture budget in each layer is considered, with the residual between the layers taken as the convective flux. Then, further investigation can be undertaken with the convective fluxes from the dynamic lower layer model and the WRF model. In this section the equations for the moisture budget are derived, then the results of applying the analysis are shown and discussed in Section 7.5.

Although deriving an expression for the moisture budget is reasonably common (for example, Yanai et al. (1973); Zangvil et al. (2001); Banacos and Schultz (2004); Seager and Henderson (2013)), there is no single difinitive method detailed in the literature. Often it is unclear where assumptions have been made or when certain terms can be neglected. Here, a comprehensive method for determining the moisture budget over a column of the atmosphere is outlined, highlighting the assumptions made and where terms have been approximated.

The moisture budget equation is derived in pressure coordinates (x, y, p), with horizontal variables being defined on surfaces of constant pressure. This introduces some error when applying to the WRF model output, as variables are interpolated from model levels to pressure levels. However, it is a necessary step when considering the moisture budget over layers representing the upper and lower troposphere, as the separation between the layers is defined as the 700 hPa pressure level (as per Sections 7.2 and 7.3).

$$Q(t) = \frac{1}{g} \iiint_V q \; dx \; dy \; dp. \tag{7.1}$$

The total mass of water, $Q(t)$, in a fixed volume (V) is defined in Equation 7.1, where t is time, g is the acceleration of mass due to gravity (taken as 9.80665 ms^{-2}) and q is the water vapour mixing ratio (kg kg^{-1}). In the vertical coordinate, height and pressure are related by Equation 7.2, where z represents the geometric height (m), ρ is the density of water vapour (kg m^{-3}), p_{top} is the pressure at the top of the atmosphere and p_{sfc} is the

pressure at the surface.

$$\int_0^z \rho q \; dz = \frac{1}{g} \int_{p_{\text{top}}}^{p_{\text{sfc}}} q \; dp. \tag{7.2}$$

Here, it is the the change of moisture over time for a fixed volume that is of interest. Taking the derivative with respect to time, Equation 7.1 becomes Equation 7.3. Note that the partial time derivative, $\partial/\partial t$, can be moved inside the integrals because the volume is spatially fixed and does not depend on time. The conservation and balance of the mass of water vapour will be used to derive an expression for the term $\partial q/\partial t$, at the right hand side of Equation 7.3.

$$\frac{dQ}{dt} = \frac{1}{g}\frac{\partial}{\partial t} \iiint_V q \; dx \; dy \; dp = \frac{1}{g} \iiint_V \frac{\partial q}{\partial t} \; dx \; dy \; dp. \tag{7.3}$$

7.4.1 Mass balance of water vapour

The material conservation of water vapour in pressure coordinates (x, y, p) for a parcel of air is given by Equation 7.4, where the change in water vapour mixing ratio, q, over time, t, is given by the difference in moisture sources and sinks. These are typically taken as the evaporation rate into the air parcel, e, and the condensation rate into the air parcel, c. The horizontal and vertical wind components are $\mathbf{u} = (u, v)$ and ω, respectively.

$$\frac{\partial q}{\partial t} + u\frac{\partial q}{\partial x} + v\frac{\partial q}{\partial y} + \omega\frac{\partial q}{\partial p} = e - c. \tag{7.4}$$

Mathematically, the horizontal wind field defined on surfaces of constant pressure (p) is equivalent to the horizontal wind field defined on surfaces of constant geopotential height (z) - as shown by Equations 7.5a and 7.5b. There is no variation of height on a flat surface, so $(\partial z/\partial x)_p = 0$ and $(\partial z/\partial y)_p = 0$, meaning that the right-hand side terms disappear.

$$\left(\frac{\partial u}{\partial x}\right)_p = \left(\frac{\partial u}{\partial x}\right)_z + \cancel{\left(\frac{\partial z}{\partial x}\right)_p}\frac{\partial u}{\partial z}, \tag{7.5a}$$

$$\left(\frac{\partial v}{\partial y}\right)_p = \left(\frac{\partial v}{\partial y}\right)_z + \cancel{\left(\frac{\partial z}{\partial y}\right)_p}\frac{\partial v}{\partial z}. \tag{7.5b}$$

7.4.2 Mass conservation of water vapour

The continuity equation, an expression of the conservation of mass, is given in Equation 7.6 in pressure coordinates. This can be derived from first principles (e.g. Wallace and Hobbs (2006)), or shown by transforming from geometric to pressure coordinates.

$$\frac{\partial u}{\partial x} + \frac{\partial v}{\partial y} + \frac{\partial \omega}{\partial p} = 0. \tag{7.6}$$

7.4.3 Water vapour conservation in flux form

The flux form of Equation 7.4, representing the conservation of water vapour, is obtained by combining Equation 7.4 with the continuity equation (7.6), multiplied by a factor of q.

The result is Equation 7.7, where $\mathbf{u} = (u, v)$ is the horizontal wind field.

$$\frac{\partial q}{\partial t} + \underbrace{\mathbf{u} \cdot (\nabla q)}_{\substack{\text{horizontal} \\ \text{advection}}} + \underbrace{q \nabla \cdot (\mathbf{u})}_{\substack{\text{horizontal} \\ \text{convergence}}} + \underbrace{\omega \frac{\partial q}{\partial p} + q \frac{\partial \omega}{\partial p}}_{\text{vertical terms}} = \underbrace{e - c}_{\substack{\text{source} \\ -\text{sink}}}. \tag{7.7}$$

$$\frac{\partial q}{\partial t} = - \underbrace{\nabla \cdot (q\mathbf{u})}_{\substack{\text{horizontal} \\ \text{MFC}}} - \underbrace{\frac{\partial}{\partial p} (q\omega)}_{\substack{\text{vertical} \\ \text{MFC}}} + \underbrace{e - c}_{\substack{\text{source} \\ -\text{sink}}}. \tag{7.8}$$

The vector identity $\nabla \cdot (f\mathbf{F}) = \mathbf{F} \cdot (\nabla f) + f (\nabla \cdot \mathbf{F})$, for scalar field f and vector field $\mathbf{F}$, along with the product rule for partial derivatives, can be used to simplify Equation 7.7 to Equation 7.8. The advection and convergence terms are combined into moisture flux convergence (MFC) terms.

7.4.4   Change in water vapour mass for a fixed volume

The flux form of water vapour conservation (Equation 7.8) can be substituted into the equation for the change in moisture for a fixed volume (7.3). This gives Equation 7.9a, which can be further simplified to Equation 7.9b by application of the divergence theorem to the horizontal moisture flux convergence term, cancellation of the integral and derivative with respect to pressure in the vertical term and rewriting the vertical integrals of evaporation (e) and condensation (c) rates as surface evaporation (E) and precipitation (P). Further details regarding each of these terms are discussed below.

$$\frac{dQ}{dt} = -\frac{1}{g} \iiint_V \underbrace{\nabla \cdot (q\mathbf{u})}_{\substack{\text{horizontal} \\ \text{MFC}}} dx\ dy\ dp - \frac{1}{g} \iiint_V \underbrace{\frac{\partial}{\partial p} (q\omega)}_{\substack{\text{vertical} \\ \text{MFC}}} dx\ dy\ dp + \frac{1}{g} \iiint_V \underbrace{(e - c)}_{\substack{\text{source} \\ -\text{sink}}} dx\ dy\ dp,$$

$$\tag{7.9a}$$

$$= -\frac{1}{g} \iint_{S_i} q\mathbf{u} \cdot \mathbf{n}\ dS_i - \frac{1}{g} \iint_S (q_{\text{sfc}} \omega_{\text{sfc}})\ dS + \iint_S (E - P)\ dS. \tag{7.9b}$$

Equation 7.9b states that the change in mass of water vapour in a fixed column of the atmosphere is equal to the sum of the moisture flux across the vertical sides (S_i), the integrals of evaporation and precipitation over the ground surface (S) and the contribution from the vertical wind component in pressure coordinates over the ground surface (S). All terms are given in units of kg m^{-2}s^{-1}, which become kgs^{-1} on integrating over a surface. Moisture moving into the fixed volume is defined as positive and moisture moving out of the fixed volume is defined as negative. For example, evaporation, as a moisture source, is positive, whilst precipitation, as a moisture sink, is negative. The atmospheric column is assumed to have vertical sides and extends from the surface pressure (p_{sfc}) to the top of the atmosphere (p_{top}). Note that whilst the pressure at the top of the atmosphere should be taken as zero, the practice in weather models is define a model top of around 10–50 hPa, to avoid complications of dividing by zero in the numerical methods.

Evaporation and precipitation

The vertical integrals of the evaporation and condensation rates can be rewritten as evaporation, E, and precipitation, P:

$$\frac{1}{g} \int_{p_{\text{top}}}^{p_{\text{sfc}}} (e - c) \; dp = E - P. \tag{7.10}$$

Vertical boundary terms

At the top of the atmosphere, the vertical moisture flux convergence is zero. Then, the height integral of the vertical moisture flux convergence reduces to a surface term, $q_{\text{sfc}}\omega_{\text{sfc}}$, where the vertical velocity can be rewritten in terms of the horizontal wind field (Equation 7.11). The basis for this is discussed below:

$$\int_{p_{\text{top}}}^{p_{\text{sfc}}} \frac{\partial}{\partial p} (q\omega) \; dp = q_{\text{sfc}}\omega_{\text{sfc}} = q_{\text{sfc}} \left(\frac{\partial p_{\text{sfc}}}{\partial t} + \mathbf{u}_{\text{sfc}} \cdot \nabla p_{\text{sfc}} \right). \tag{7.11}$$

Vertical velocities in terms of pressure and geometric coordinates are related by the chain rule, as per Equation 7.12. At the surface, Equation 7.12 becomes Equation 7.13, where the subscript "sfc" denotes the value of the quantity at the surface.

$$\omega = \frac{\partial p}{\partial t} + \mathbf{u} \cdot \nabla p + w \frac{\partial p}{\partial z}. \tag{7.12}$$

$$\omega_{\text{sfc}} = \frac{\partial p_{\text{sfc}}}{\partial t} + \mathbf{u}_{\text{sfc}} \cdot \nabla p_{\text{sfc}} + w_{\text{sfc}} \frac{\partial p_{\text{sfc}}}{\partial z}. \tag{7.13}$$

The pressure tendency term ($\partial p_{\text{sfc}}/\partial t$) is of the order of 10 hPa per day (e.g. Wallace and Hobbs (2006)). Note that the advection terms, $\mathbf{u}_{\text{sfc}} \cdot \nabla p_{\text{sfc}}$ and $w_{\text{sfc}} (\partial p_{\text{sfc}}/\partial z)$, are even smaller. It is because of this that most authors entirely neglect the vertical boundary term at the surface. Here, the pressure tendency and horizontal advection terms are maintained, but the geometric vertical velocity term is neglected. Assuming that the surface is close to horizontal, the velocity perpendicular to the surface is zero and thus $w_{\text{sfc}} (\partial p_{\text{sfc}}/\partial z) = 0$. For the purposes of this chapter, the assumption of a horizontal surface is reasonable, as the aim is to diagnose a vertical flux several kilometers into the atmosphere. If the focus was regarding land-surface interactions or orographic effects, it may be more appropriate to retain the geometric vertical velocity term.

Horizontal moisture fluxes

The divergence theorem is applied to the volume integral of horizontal moisture flux convergence, to give the moisture flux across the surface. Here, the volume integral is a column from the ground to the top of the atmosphere, and the surface S_i refers to the sides of the column, as the integral consists solely of horizontal terms. The region is bounded by latitudes θ_1, θ_2, and longitudes ϕ_1, ϕ_2. The expression for the horizontal moisture fluxes can be expanded into components for north, south, west and east sides (Equation 7.14), which are abbreviated as per the terms in Equation 7.15. The radius of the Earth, r_E is

taken as 6371 km.

$$
-\frac{1}{g}\iint_{S_i} q\mathbf{u}\cdot\mathbf{n}\ dS_i = +\frac{r_E}{g}\int_{p_{\text{top}}}^{p_{\text{sfc}}}\int_{\phi_1}^{\phi_2} qv\cos\theta\ d\phi\ dp\Big|_{\theta_2} - \frac{r_E}{g}\int_{p_{\text{top}}}^{p_{\text{sfc}}}\int_{\phi_1}^{\phi_2} qv\cos\theta\ d\phi\ dp\Big|_{\theta_1}
$$

$$
+\frac{r_E}{g}\int_{p_{\text{top}}}^{p_{\text{sfc}}}\int_{\theta_1}^{\theta_2} qu\ d\theta\ dp\Big|_{\phi_1} - \frac{r_E}{g}\int_{p_{\text{top}}}^{p_{\text{sfc}}}\int_{\theta_1}^{\theta_2} qu\ d\theta\ dp\Big|_{\phi_2}, \tag{7.14}
$$

$$
= F_N - F_S + F_W - F_E. \tag{7.15}
$$

7.4.5   Numerical methods

Performing a moisture budget analysis on output from the WRF model requires certain numerical approximations to be made, which can introduce errors. These errors should be very small relative to the size of the individual moisture budget components. The approximations are listed below. Note that all quantities are given in the standard mass flux units of kg m^{-2}s^{-1}, which become kgs^{-1} after horizontally integrating. For quantities such as precipitation, which is not naturally given in standard mass flux units, we use the density of water, $\rho_w = 1000$ kg m^{-3}, to convert into the desired units. This ensures that terms are comparable with one another. A summary of numerical approximations is listed:

- Variables are vertically interpolated from model to pressure levels, ranging from 1000 to 50 hPa.

- p_{top} is taken as the model top, which is 50 hPa in the WRF model.

- Horizontal moisture fluxes are interpolated from the model grid (x, y) to lines of latitude and longitude.

- A function from the NumPy library in Python is used to determine central and one-side differences. Interior points are computed to second order accuracy and end points (forward or backward) to first order.

- Vertical integrals are calculated as per Equation 7.16:

$$
\int_{p_{\text{top}}}^{p_{\text{sfc}}} q\ dp \simeq \sum_{i=1}^{N} \frac{q_{i-1}+q_i}{2}\Delta p. \tag{7.16}
$$

- Area integrals are applied with equal weighting, possibly introducing slight errors at the boundaries.

- Data is 6-hourly. To convert fluxes to time units of per second, they are divided by a factor, $\Delta\tau = 21000$.

- Topographic gradients are assumed to be small, so that $dS \approx dx\ dy$.

Now, the horizontal integrals in Equation 7.9b can be rewritten using Equation 7.17, where A is the cross-sectional area of the column with vertical sides.

$$A = \iint_S dx\ dy. \tag{7.17}$$

Then, combining Equation 7.17 with Equations 7.11, 7.15 and 7.17, the moisture budget becomes:

$$\frac{d\overline{Q}}{dt} = \frac{1}{g} \int_{p_{\text{top}}}^{p_{\text{sfc}}} \frac{\partial \overline{q}}{\partial t}\ dp = \overline{F}_N - \overline{F}_S + \overline{F}_W - \overline{F}_E - \frac{\overline{q_{\text{sfc}}\omega_{\text{sfc}}}}{g} + \overline{E} - \overline{P}. \tag{7.18}$$

Note that overbars are used to denote quantities per unit of horizontal area, so that $\overline{Q}(t) = Q(t)/A$.

Evolution of mixing ratios

The microphysics scheme used in the configuration of the WRF model (as described previously in Section 6.2.2) defines six mixing ratios for water vapour, snow, rain, ice, graupel and cloud water. For the moisture budget, the sum of the mixing ratios is taken:

$$q = q_{\text{vapour}} + q_{\text{snow}} + q_{\text{rain}} + q_{\text{ice}} + q_{\text{graupel}} + q_{\text{cloud}}. \tag{7.19}$$
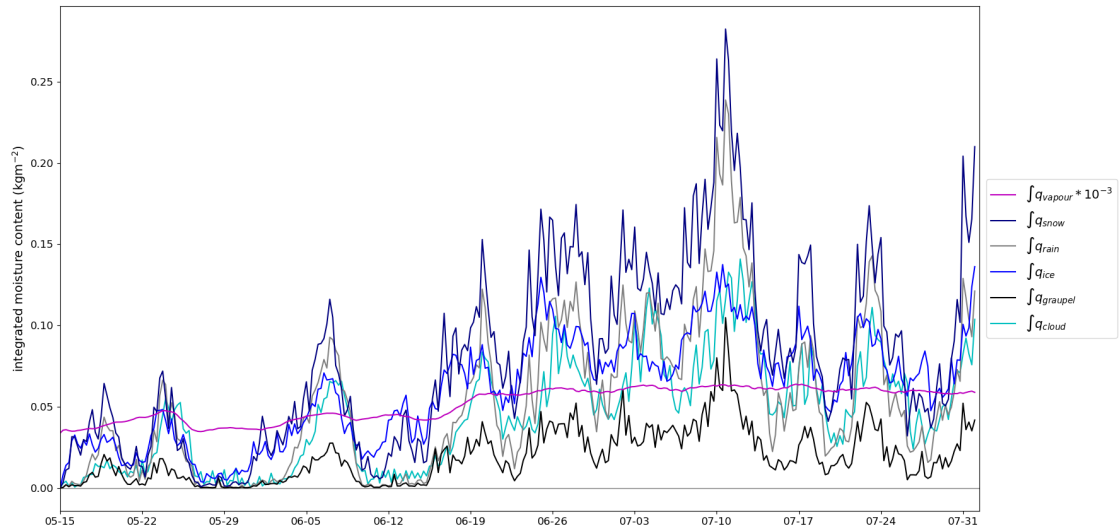
Figure 7.6: *Time series of integrated mixing ratios for water vapour (q_{vapour}), snow (q_{snow}), rain water (q_{rain}), ice (q_{ice}), graupel ($q_{graupel}$) and cloud water (q_{cloud}). Data from the 11 week simulation with the WRF model, averaged over the box shown in Figure 7.7.*

The evolution of each of these mixing ratios over India, vertically integrated over the height of the atmosphere, is considered in Figure 7.6. As expected, the key component is the water vapour mixing ratio, which is a thousand times greater than the other mixing

ratios (q_{vapour} is scaled to fit on the same axes). All the mixing ratio components increase from the 12th June, as the monsoon onsets. Peaks at about 6th June and 10th July, prior to and post onset respectively, indicate a synoptic event with precipitation.

7.5   Moisture budget analysis

The moisture budget analysis is applied over the area of India shown in Figure 7.7. The region, shown by the solid white square, lies within 10–30°N latitude and 70–90°E longitude. The bounding latitudes for calculation of the moisture fluxes become $\theta_1 = 10°N$, $\theta_2 = 30°N$ and the longitudes $\phi_1 = 70°E$, $\phi_2 = 90°E$. Moisture entering the region is defined as positive, and moisture leaving the region is negative. Figure 7.7 also illustrates the direction and sign of the moisture fluxes acting perpendicular to each side of the box. The moisture budget for north and south India is also considered (Subsection (7.5.2), over the north and south boxes in Figure 7.7, which are separated by the 20°N line of latitude.
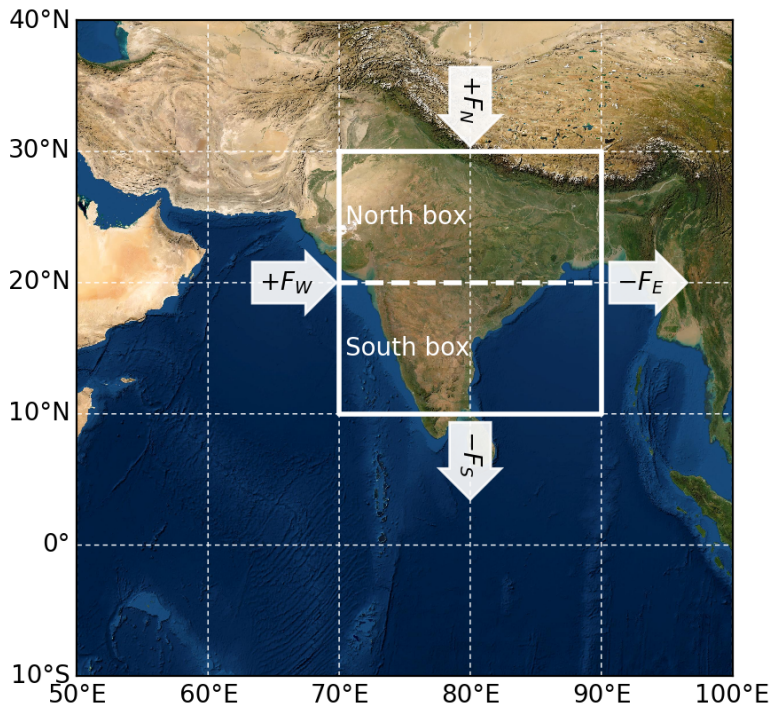
Figure 7.7: *Regions over which the moisture budget is calculated, including direction of fluxes at north, east, south and west sides.*

7.5.1   Indian region

The time-series of components calculated in the moisture budget analysis (as per Equation 7.18) is shown in Figure 7.8, where 7.8a uses 6-hourly data from the WRF model simulation and 7.8b shows the daily averaged data. Note that the term for the change

in the mass of water vapour in a fixed volume over time, dQ/dt, is used interchangeably with the change in precipitable water over a column of the atmosphere, ΔPW. The top subplots show the evolution of each component, including the side fluxes, evaporation, precipitation and vertical boundary term. The bottom subplots show the change in total column moisture (ΔPW) against the sum of the components, where terms representing movement of moisture into the volume are positive, and terms representing a loss of moisture from the volume are negative. The phrases total column moisture and precipitable water are used interchangeably. The anomaly is defined as the difference between these, as per Equation 7.20. Note that the negative anomaly is plotted to keep the time-series of the bottom plots consistent (i.e. oscillating in phase).

$$\text{anomaly} = \Delta PW - F_N + F_S - F_W + F_E - E + P. \tag{7.20}$$

The 6-hourly data (Figure 7.8a) results in a noisy plot where the trends are difficult to see, as many of the moisture budget components have a strong diurnal cycle which becomes more evident with sub-daily data. The differences between the change in total column moisture and the sum of other components is key to the aim of diagnosing a convective flux. In order to see the evolution of the bottom subplots more clearly, the data is averaged over each day (as per Figure 7.8b). For the remainder of this chapter, only the plots of daily averaged data are presented and discussed.

Considering the top subplot of Figure 7.8b, over the first two weeks of the simulation, the dominant components are the moisture fluxes to the north, west and east sides. Prior to onset, strong northwesterly winds are present at mid-levels, contributing to the north side flux, whilst moist south-westerlies at low levels make up a significant part of the west side flux. These south-westerly winds become more westerly as they pass over the southern peninsula, thus contributing to moisture leaving the moisture budget region via the east side flux. Both Figures 7.8a 7.8b show a calmer period between the end of May and the first week of June, with all components being contained within a narrow range. The south side flux, evaporation and vertical boundary term are relatively small compared to the precipitation throughout the length of the monsoon season. Just after 5th June, a sudden jump in the north, west & east side fluxes and the precipitation can be seen, consistent with the observed late onset date of 8th June at Kerala. The precipitation, north side flux and west side fluxes remain greater in magnitude than the other components until the start of July. After the 10th July, the north side flux becomes smaller and more comparable to the east side flux. The west side flux and the precipitation are the greatest magnitude terms over July, as would be expected during the full monsoon. Peaks of precipitation on the 26th June and the 10th July point to synoptic events bringing an influx of moisture from the north and west.

Examining the bottom subplot of Figure 7.8b, it can be seen that the change in total column moisture (ΔPW) matches reasonably well with the sum of the other components ($\sum F + E - P - q_{\text{sfc}}\omega_{\text{sfc}}$), in that it tracks each event peak by peak. The amplitude of
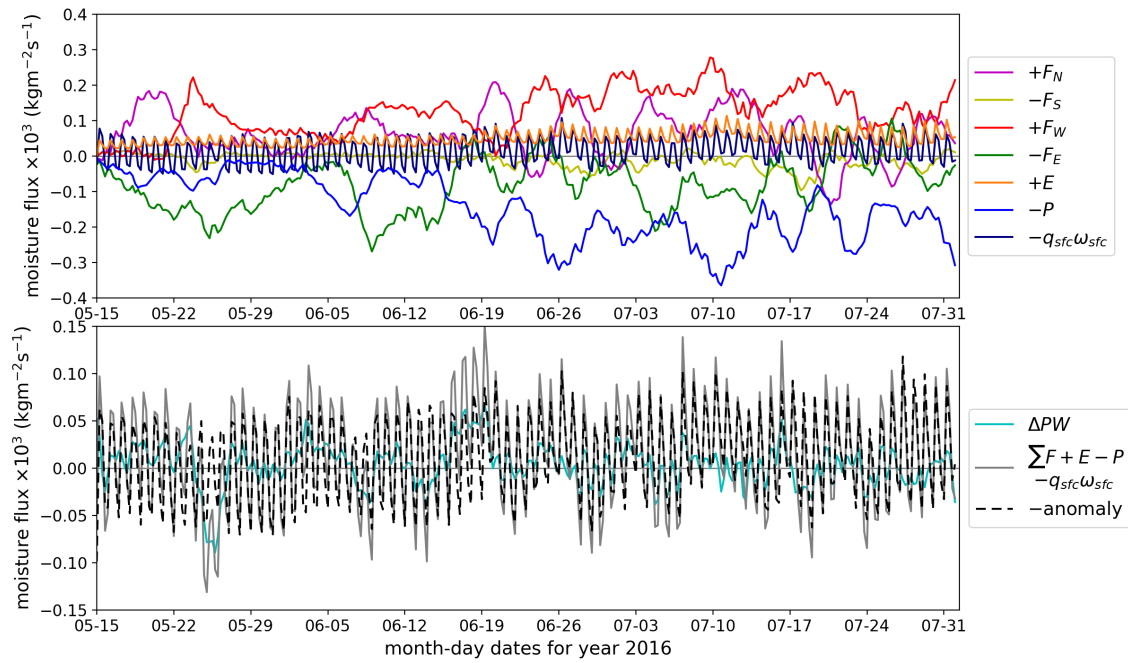
(a) *6-hourly data.*
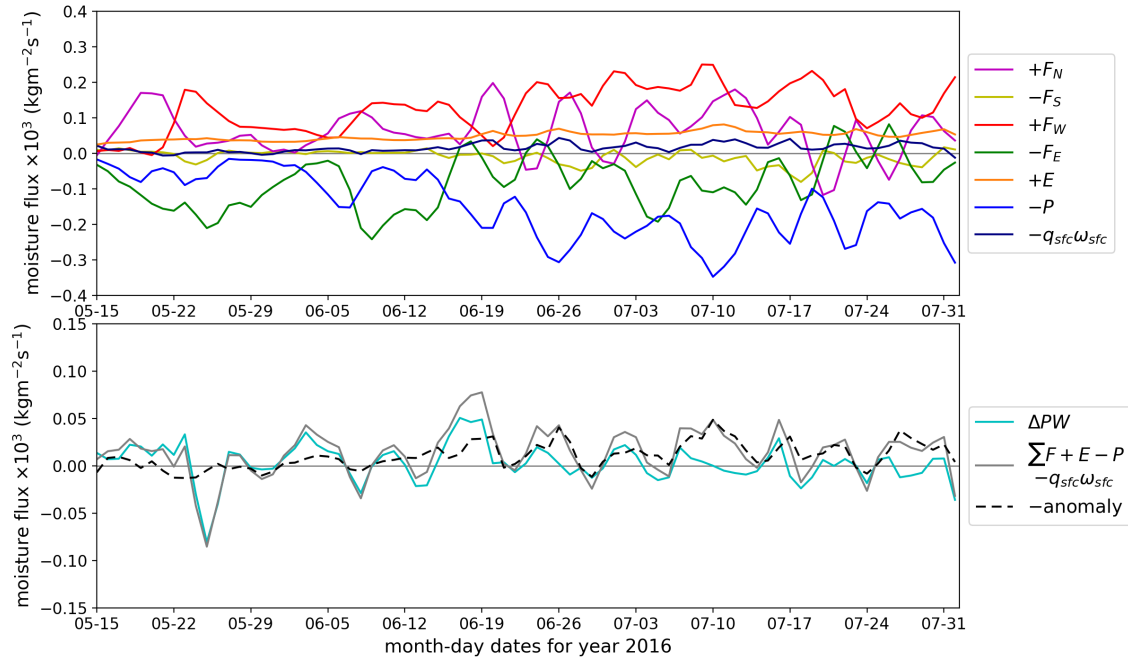
(b) *Daily averaged data.*

Figure 7.8: *Moisture budget components from 11 week simulation with the WRF model, over the box shown in Figure 7.7. Components have been interpolated to pressure levels.*

ΔPW is generally less than that of the component sum. The magnitude of the anomaly is approximately 15–25% compared to the magnitude of the side fluxes. Note that some difference between the change in total column moisture and the sum of the components entering/leaving the column is to be expected, given that mass is not necessarily conserved in numerical weather prediction models. For example, in the WRF model, negative mixing ratios are set to zero to maintain positive-definiteness of mass (i.e. non-negative mass values), which can lead to overestimates of mass (Shamrock et al., 2019). Additionally,

both within the WRF model time-stepping scheme and the moisture budget analysis, some error arises from the implementation of numerical techniques. For the purposes of this thesis, the anomaly is deemed within acceptable bounds to proceed with further analysis.
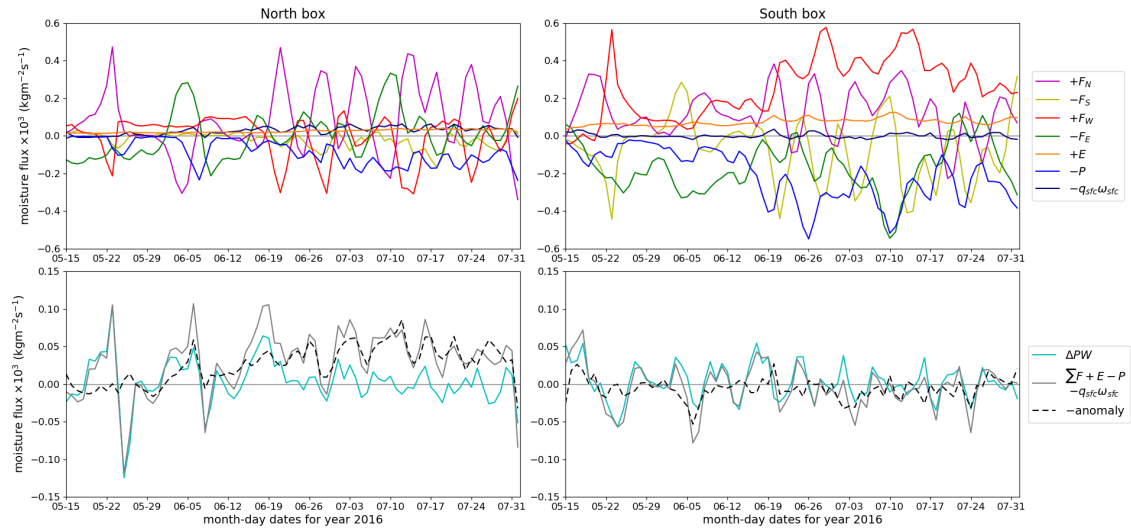
Figure 7.9: *Moisture budget components from 11 week simulation with the WRF model (daily averaged data), over the north & south boxes shown in Figure 7.7. Components have been interpolated to pressure levels.*

7.5.2   North & south regions

The moisture budget analysis is also applied over the north and south regions indicated in Figure 7.7, where the 20°N latitude line divides north and south. The results are given in Figure 7.9. Similarly to Figure 7.8, the side fluxes and precipitation show a sudden increase, although this occurs slightly later at 19th June. Over the north India region, the dominant fluxes after the 19th July are the north and west side fluxes. For the south region, the fluxes are generally of greater magnitude than for the north region, with the side fluxes and precipitation being the largest contributing components. The west side flux is greater in the south region, due to the development of the moist southwesterly monsoon flow prior to onset, which passes over the southern peninsula of India. The precipitation is lower over the north region than the south region, which would be expected given that part of northwest India is classified as desert. The precipitation peaks at 26th June and 10th July identified in Figure 7.8 are seen here over the south region, with corresponding peaks in the north and west side fluxes indicating an increase in moisture flux.

In terms of the anomaly (bottom subplots of Figure 7.9), the difference between the change in total column moisture and the sum of the moisture components is greater over the north region than the south region, particularly from mid June to late July. This indicates that the WRF model reproduces moisture advection over the south region more accurately than the north region. The anomaly over the north region merits further

investigation, as an explanation for the difference in ΔPW and $\sum F + E - P - q_{\mathrm{sfc}}\omega_{\mathrm{sfc}}$ could aid model development and improve performance.

7.5.3   Separating into two vertical layers

The moisture budget over the full height of the atmosphere has been considered over the full, north and south regions illustrated in Figure 7.7. Here, the moisture budget over two vertical layers of the atmosphere, separated at the 700 hPa level, is analysed. Note that the analysis was repeated with a level split at 600 hPa, but the results were indistinguishable and thus are not included.

$$\Delta PW_2 = F_{N_{L2}} - F_{S_{L2}} + F_{W_{L2}} - F_{E_{L2}} + F_C - P, \tag{7.21a}$$

$$\Delta PW_1 = F_{N_{L1}} - F_{S_{L1}} + F_{W_{L1}} - F_{E_{L1}} - F_C + E. \tag{7.21b}$$

The moisture budget for lower and upper layers of the atmosphere is outlined in Equations 7.21a–7.21b, where subscripts 1 and 2 refer to lower and upper layers, respectively. The fluxes follow the convention of being defined as positive for moisture entering the region and negative for moisture leaving the region. The side fluxes to the north, south, west and east are integrated from 1000–700 hPa for the lower layer and over 700–50 hPa for the upper layer. An additional term, representing the vertical convective flux (F_C), is included to account for the movement of moisture from the lower to the upper layer. Thus, it appears as a negative term in Equation 7.21b where it is removed, with the term in Equation 7.21a being correspondingly positive as the convective flux is added to the upper layer. The Equation for the moisture budget over the full height of the atmosphere (7.18) is recovered when the lower and upper layer Equations 7.21a–7.21b are summed, eliminating F_C.

Evaporation, as a surface process, is retained in the lower layer equation. The precipitation is removed from the upper layer and is assumed to have no contribution to the lower layer. This is reasonable given that precipitation mechanisms are contained within the upper layer, as the freezing level (approximately 500 hPa) is above the bottom boundary of the upper layer (700 hPa).
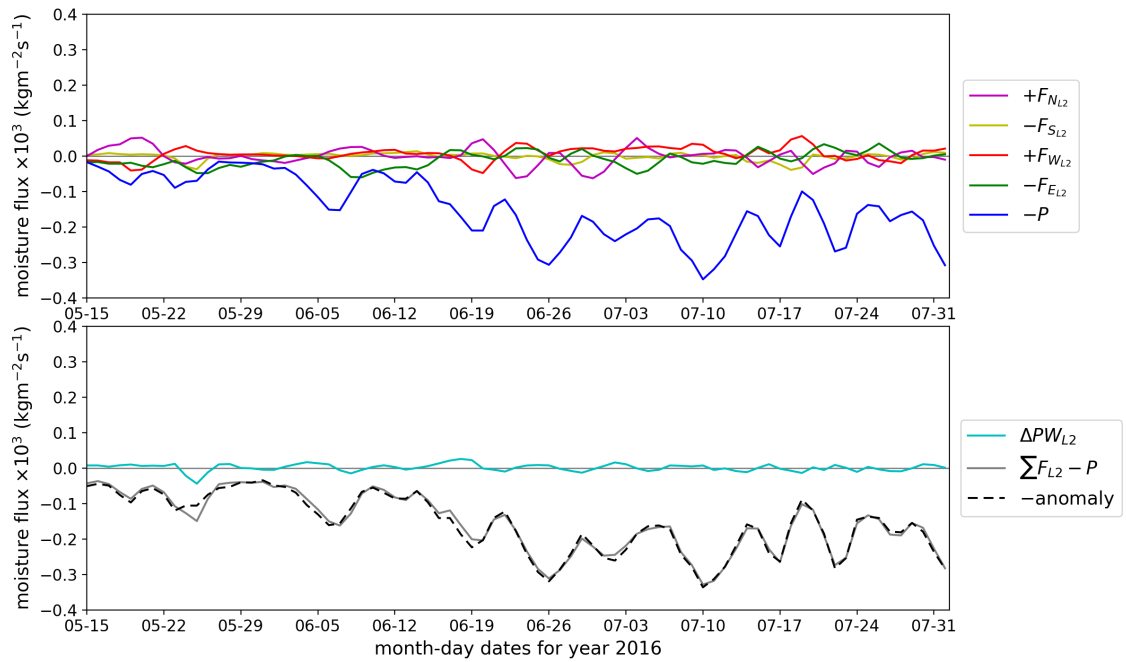
(a) *Upper layer.*
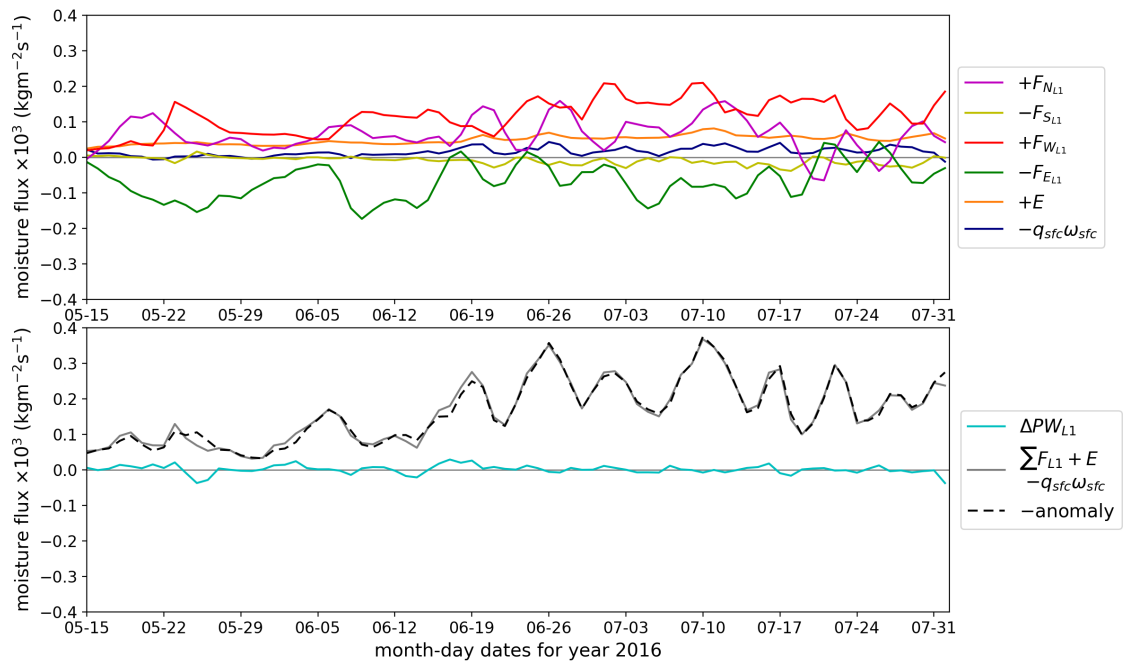
(b) *Lower layer.*

Figure 7.10: *Moisture budget components from 11 week simulation with the WRF model (daily averaged data), over the box shown in Figure 7.7. Components have been interpolated to pressure levels and split into two layers at 700 hPa.*
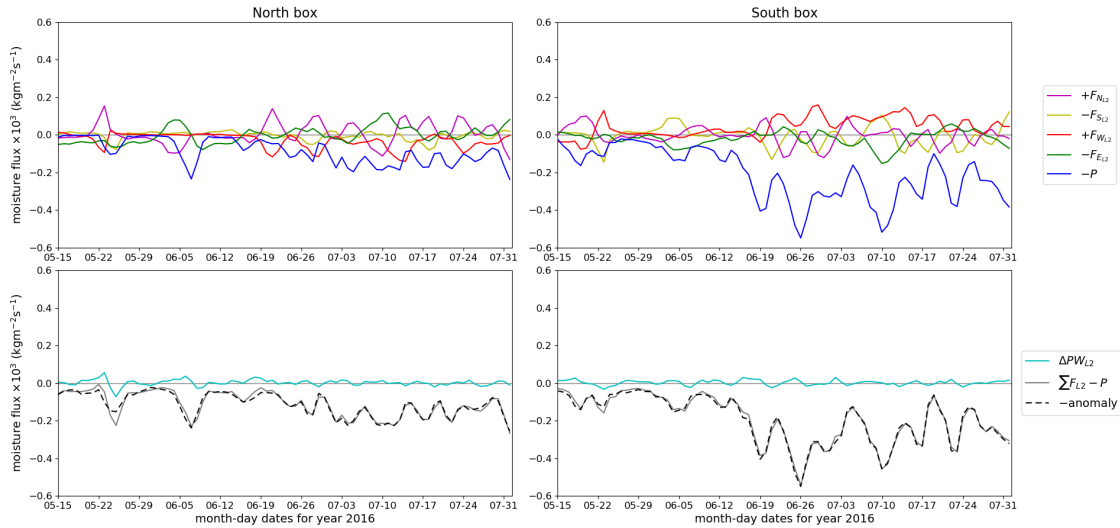
(a) *Upper layer.*
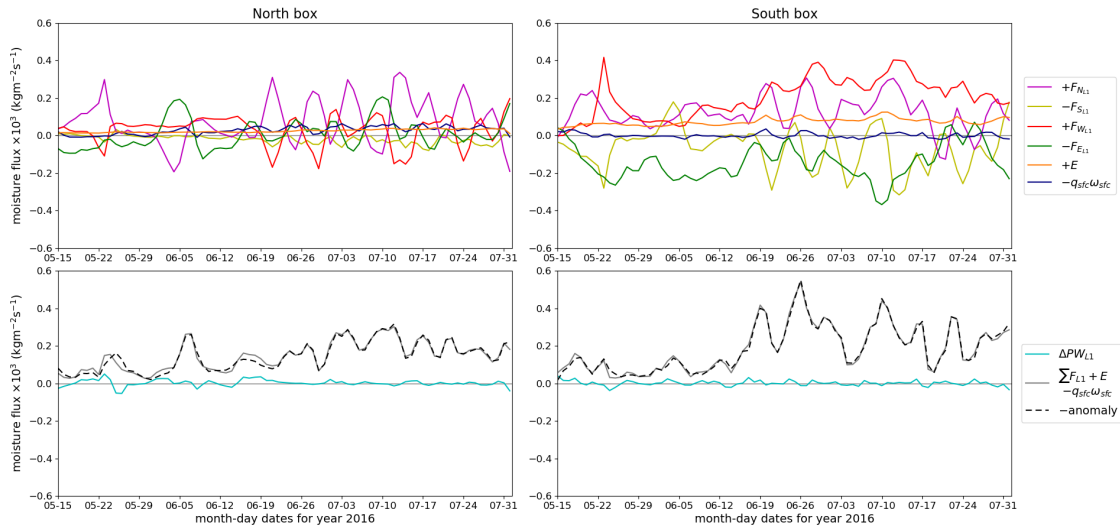
(b) *Lower layer.*

Figure 7.11: *Moisture budget components from 11 week simulation with the WRF model (daily averaged data), over the north & south boxes shown in Figure 7.7. Components have been interpolated to pressure levels and split into two layers at 700 hPa.*

Indian region

Figure 7.10 shows the evolution of moisture budget components over the upper layer (7.10a) and the lower layer (7.10b). The side fluxes are of greater magnitude in the lower layer, as would be expected. Moist inflow at low levels is a key driver of monsoon onset and thus the fluxes in the lower layer play a greater role than the fluxes in the upper layer. In the upper layer, the dominant component is the precipitation. Between the 12th and 19th of June, the precipitation flux increases significantly, reflecting one of the main differences from the pre-onset phase to the full monsoon. As previously, the side fluxes

show a step increase at around the 12th June, although this is more evident in the lower layer than the upper layer.

The change in total column moisture in both layers (ΔPW_{L2}, ΔPW_{L1}, cyan lines) fluctuates around zero. This is contrary to the expectation that both layers would moisten over time, as the monsoon onset progresses over India. The sum of fluxes in the upper layer ($\sum F_{L2} - P$, grey line) remains below the ΔPW_{L2} line, consistent with the prediction that there is a convective flux acting to move moisture from the lower to the upper layer. The difference between the change in total column moisture and the sum of the fluxes, labelled the anomaly, is attributed to the convective flux. In the lower layer, the sum of the moisture components ($\sum F_{L1} + E - q_{\mathrm{sfc}}\omega_{\mathrm{sfc}}$) is much greater than ΔPW_{L1}. Similarly to the upper layer, the difference between these (the anomaly) is taken as the vertical convective flux, F_C. If the convective flux is included in the analysis shown in Figure 7.10, it would be taken from the lower layer, reducing the height of the grey line ($\sum F_{L1} + E - q_{\mathrm{sfc}}\omega_{\mathrm{sfc}}$) relative to the cyan line (ΔPW_{L1}), and correspondingly added to the upper layer, increasing the height of the grey line ($\sum F_{L2} - P$) relative to the cyan line (ΔPW_{L2}). Note that the convective flux significantly increases in amplitude after the 19th June, in line with the side fluxes and synonymous with the transition of monsoon onset.

North & south regions

Here the moisture budget over two vertical layers of the atmosphere is considered for the north and south regions defined in Figure 7.7, with results for lower and upper layers presented in Figure 7.11. For the upper layer (7.11a), the key differences are the smaller magnitudes of precipitation and convective flux (indicated by the anomaly) for the north region, compared to the south region. The upper layer side fluxes are of comparable magnitudes for both regions, despite differences in sign. For example, the west side flux in the upper layer (red line) over the north region is generally negative, meaning moisture is leaving. Whereas over the south region, the west side flux is positive, signifying moisture entering the region.

In the lower layer (7.11b), the convective flux is more similar over the north and south regions than for the upper layer, although greater peaks for the south region are observed. The side fluxes in the lower layer for the south region are notably larger in magnitude than the north region.

7.6   Comparing convective timescales

Having applied the moisture budget analysis over two vertical layers in the atmosphere, the vertical convective flux between layers can be formally diagnosed (Subsection 7.6.1). Then, in Subsection 7.6.2, the relationship between the convective flux and the total column moisture in each layer is investigated. It is expected that there is some correlation between the convective flux and the difference in total column moisture, which can be used

to determine the convective timescale, T_c, for the WRF model. This will be compared with the assumed values of T_c from the dynamic lower layer model. Good agreement between the assumed and derived convective timescales would validate the theory behind the development of the dynamic lower layer model presented in Chapter 5.

7.6.1   Calculating the vertical convective flux

The vertical convective flux in each layer is determined by rearranging Equations 7.21a–7.21b:

$$F_{C_{L2}} = \Delta PW_2 - \left(F_{N_{L2}} - F_{S_{L2}} + F_{W_{L2}} - F_{E_{L2}} - P\right), \tag{7.22a}$$

$$-F_{C_{L1}} = \Delta PW_1 - \left(F_{N_{L1}} - F_{S_{L1}} + F_{W_{L1}} - F_{E_{L1}} + E\right). \tag{7.22b}$$

The convective fluxes derived individually from the lower and upper layers should equate, but some variation due to numerical approximations is anticipated. The derived convective fluxes from each layer are plotted (blue lines) in the top subplots of Figure 7.12 for the Indian region and Figure 7.13 for the north and south regions. Note that the sign of the lower layer convective flux has been flipped in order to simplify comparisons with the upper layer convective flux. The (negative) anomaly, as defined in Equation 7.20, over the full height of the atmosphere is also shown (black line). In order to have confidence in the diagnosed convective flux, it needs to be of a greater order than the anomaly between ΔPW and the moisture components over the whole height of the atmosphere. This is evident in the top plots of both figures (7.12, 7.13), with the convective fluxes derived from the lower and upper layers (blue lines) being of much greater magnitude than the anomaly. Additionally, the convective flux determined from the upper layer (light blue line) closely follows the convective flux determined from the lower layer (dark blue line). The exception is over the north region, where the convective flux from the lower layer is slightly larger than from the upper layer after monsoon onset (8th June). Possibly this is due to deficiencies in the WRF model regarding moisture advection over the north region. Generally, the differences between the derived convective fluxes are much smaller than the anomaly, meaning that the diagnosis of the convective fluxes is valid and further analysis can be proceeded with.

Going forward, the average of the convective flux from each layer is used, as per Equation 7.23. This is plotted on the bottom subplots of Figures 7.12 and 7.13 (blue line). The red and orange lines (PW_{L1}, PW_{L2}) show the evolution of the total column moisture, and the black line shows the difference in total column moisture between the layers. These three quantities have been scaled by $1/100$ in order to show on the same scale y-axis as the convective flux (F_C).

$$F_C = \frac{-\left(-F_{C_{L1}}\right) + F_{C_{L2}}}{2}. \tag{7.23}$$
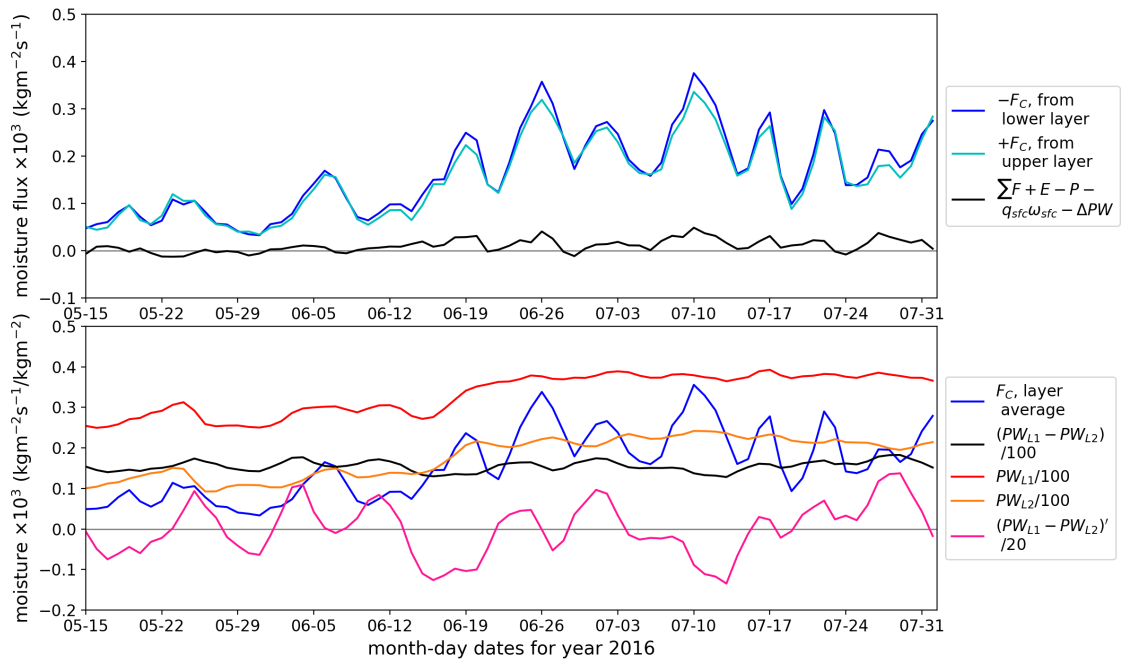
Figure 7.12: *Inferred vertical flux between upper and lower layers, split at 700 hPa. Daily averaged data from 11 week simulation with the WRF model, over the box shown in Figure 7.7.*
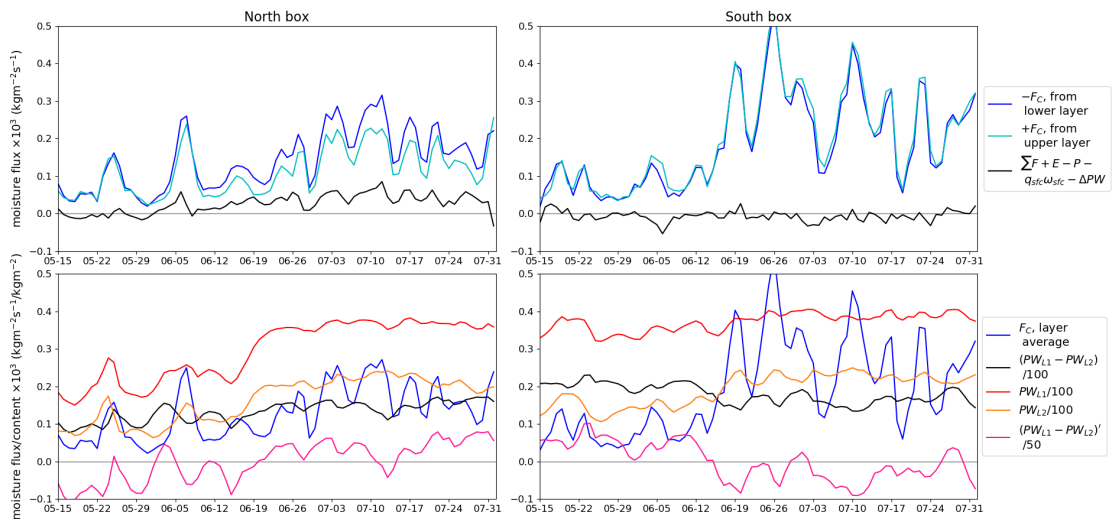
Figure 7.13: *Inferred vertical flux between upper and lower layers, split at 700 hPa. Daily averaged data from 11 week simulation with the WRF model, over the north & south boxes shown in Figure 7.7.*

Looking at the bottom subplot of Figure 7.12 for the Indian region, the total column moisture for the lower layer is greater than for the upper layer, as expected. This is also consistent with Section 7.2. There is much less fluctuation compared with the convective flux, although both the total column moisture for each layer and the convective flux show a step increase between 12th and 19th June as the monsoon onset progresses over India. The difference in total column moisture between the layers ($PW_{L1} - PW_{L2}$) remains fairly constant over the length of the simulation, hovering around 0.15×10^1 kg m^{-2}. It is difficult to see whether the convective flux and the difference in total column moisture between the layers relate, due to differences in scale. In order to emphasise the fluctuations in $PW_{L1} - PW_{L2}$, the deviation from the mean is plotted (pink line), as defined in Equation 7.24. Note that this is also scaled (by 20) to aid visual comparisons.

$$(PW_{L1} - PW_{L2})' = (PW_{L1} - PW_{L2}) - \overline{(PW_{L1} - PW_{L2})}. \tag{7.24}$$

Now comparing the convective flux with the deviation of the difference in total column moisture from the mean between layers, it can be seen that the pink line approximately follows the larger peaks of the blue line prior to onset. After about the 12th June, some of the peaks of the pink line correspond with peaks of the blue line, but other peaks of the blue line are correlated with troughs of the pink line. The relationship between the convective flux and the change in total column moisture between layers is investigated further in the following subsection.

Over the north region (bottom subplot of Figure 7.13), the integrated lower and upper layer moisture (PW_{L1}, PW_{L2}) both show a more sudden increase around 12th June, than for the south region or the entire Indian region. The difference in moisture content between layers, $PW_{L1} - PW_{L2}$, rises slightly for the north region over the length of the simulation, reflecting an increase in the lower layer moisture relative to the upper layer. For the south region, the difference reduces slightly around 12th June, indicating that the upper layer moisture increases at a faster rate than the lower layer moisture at onset. The pink line, representing the scaled deviation from the mean difference in total column moisture for each layer, increases from May–July in line with the convective flux over the north region. There appears to be some correlation, with the pink line following the blue line for the majority of the time period. By contrast, for the south region, the pink line only follows the blue line prior to the 12th June. After this, there is a significant change in magnitudes as the pink line becomes mostly negative and the blue line becomes greater in the positive y-direction. It is difficult to determine the correlation (if any) between the convective flux and the scaled deviation from the mean difference in total column moisture for the south region after onset.

7.6.2   Correlation of convective flux and moisture content

For a strong positive correlation between vertical convective flux and the difference in total column moisture between layers, statistical techniques can be applied to determine

a linear line of regression. Then, the gradient of this line gives the convective timescale, T_c, as noted in Equation 7.25.

$$T_c = \frac{PW_{L1} - PW_{L2}}{F_C}. \tag{7.25}$$

The expression for T_c from the WRF model is derived from the equivalent term in the idealised model, mentioned in Section 3.2.2 from Chapter 3.

Indian region

Scatter plots, presented in Figure 7.14, are used to examine the correlation between the convective flux (F_C) and the change in total column moisture between the layers over the Indian region. Figure 7.14a shows F_C against the difference, $PW_{L1} - PW_{L2}$ and Figure 7.14b shows F_C against the sum, $PW_{L1} + PW_{L2}$. The basis for the latter comes from the robust relationship demonstrated between precipitable water and column water vapour (e.g. Neelin et al. (2009)), as mentioned in Chapter 3. The data is split into two time periods, pre-onset and post-onset, which refer to before and after the 18th June.
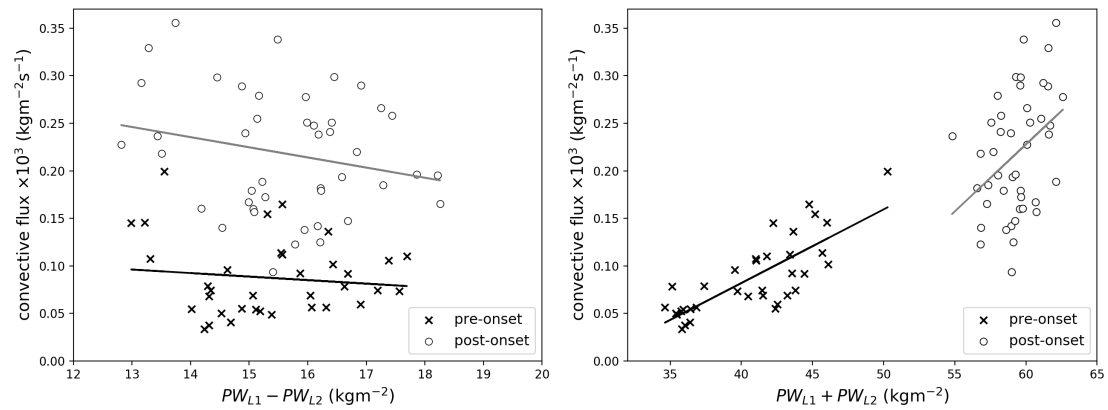
(a) F_C against the difference of PW_{layers}.   (b) F_C against the sum of PW_{layers}.

Figure 7.14: *Correlation of vertical convective flux with the change of the integrated moisture content in the lower and upper layers. Pre-onset refers to the period before 18th June, and post-onset the period after. Daily averaged data from 11 week simulation with the WRF model, over the box shown in Figure 7.7.*

Considering Figure 7.14a, there is not much (if any) correlation between the convective flux (F_C) and the difference in moisture content between layers ($PW_{L1} - PW_{L2}$), although there is less scatter for pre-onset period. The correlation coefficient (Table 7.1) reflects this, with the high p-values (> 0.05) meaning that there is little confidence in the relationship between the two variables. Although a linear regression line is shown for illustration purposes, it is not statistically meaningful and it would be unsuitable to use the calculated timescale values (T_c). There is much stronger correlation between the convective flux and the sum of the total column moisture between layers (Figure 7.14b). Pre-onset, the correlation coefficient is 0.784, indicating strong positive correlation. Post-onset, the correlation coefficient is lower, meaning weaker positive correlation. Both have p-values of

< 0.05, giving confidence in the hypothesis that the variables are related. The convective timescales are determined as 1.49 and 0.82 days, for pre-onset and post-onset, respectively. Empirically, it can be seen that for post-onset, the convective flux increases at a faster rate than the total moisture content over the layers, giving a regression line of steeper gradient. The slope corresponds with $1/T_c$, so a steeper line gives a smaller value of T_c.

Table 7.1: *Statistical parameters for correlation from scatter plots in Figure 7.14.*

Control run	T_c (days)	correlation coefficient	p-value
$PW_{L1} - PW_{L2}$ (pre-onset)	-3.12	-0.118	0.500
$PW_{L1} - PW_{L2}$ (post-onset)	-1.08	-0.224	0.144
$PW_{L1} + PW_{L2}$ (pre-onset)	1.49	0.784	0
$PW_{L1} + PW_{L2}$ (post-onset)	0.82	0.383	0.01

Despite very weak correlation between F_C and $PW_{L1} - PW_{L2}$, it is evident that the convective flux approximately doubles between pre-onset and post-onset, relative to $PW_{L1} - PW_{L2}$. This is representative of the observed increase in convective activity associated with the arrival of the monsoon. Also, if the convective flux doubles whilst $PW_{L1} - PW_{L2}$ remains constant, the convective timescale has to halve between pre-onset and post-onset (by Equation 7.25), similarly to the experiment with the dynamic lower layer model in Section 5.7. For Figure 7.14b, both the convective flux and the total column moisture over lower and upper layers increase from pre-onset to post-onset, although the convective flux increases at a greater rate than $PW_{L1} + PW_{L2}$ post-onset. Correspondingly, the convective timescale reduces between pre-onset and post-onset, meaning that more and/or shorter convective events occur after the monsoon has onset.

In the dynamic lower layer model, a range of $1/2 - 7$ days was assumed for T_c (Equation 3.5). The WRF model results suggest that T_c is towards the lower end of this range. Both models show that the convective timescale halves at monsoon onset, indicating a doubling of the vertical convective flux. The increase in convective activity leads to increased cloud development and precipitation in the real-world monsoon.

Another relationship that is investigated is the link between precipitation and the total column moisture for lower and upper layers. It would be expected that the dry intrusion over northwest India suppresses rainfall. To test this, a scatter plot of PW_{L1} against PW_{L2} is generated, where the points are proportional to the intensity of the rainfall. If the rainfall for a given lower layer moisture content (PW_{L1}) decreases with the upper layer moisture content (PW_{L2}), then it supports and quantifies the rainfall-suppression arguments of the dry intrusion. However, it is noted that PW_{L1} and PW_{L2} are not independent: they co-vary, which can make interpretation difficult. Figure 7.15 shows the scatter plot of PW_{L1} against PW_{L2}, where the size of the points reflects the intensity of rainfall and the darkening colour indicates increasing time from the start of the simulation.

It is not clear from Figure 7.15 that the rainfall increases with upper layer moisture content (PW_{L2}), for a given lower layer moisture content (PW_{L1}). However, the highest

rainfall occurrences (largest diameter points) are when the upper layer moisture content is high, relative to the lower layer moisture content. Possibly more significant is the timing of events (shading of points). This reflects that convective rainfall is a complex process and that there are changes associated with the evolving monsoon, for example, in terms of stability, land-surface state and surface fluxes. It is evident that the rainfall regimes evolve with time.
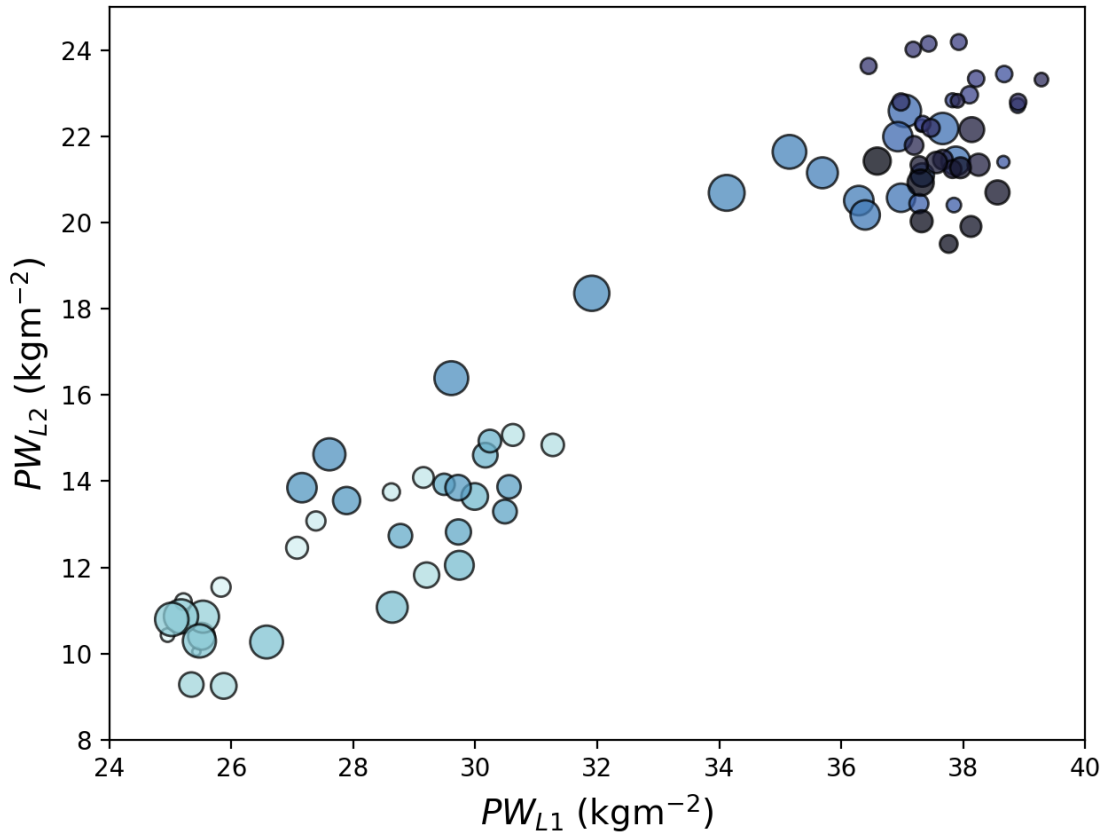
Figure 7.15: *Correlation between integrated moisture content in the lower and upper layers. Scatter point size is proportional to the intensity of precipitation and the darker colour shading indicates evolution of time. Daily averaged data from 11 week simulation with the WRF model, over the box shown in Figure 7.7.*

North & south regions

The correlation analysis is repeated for the north and south regions, with results given in Figure 7.16 and Table 7.2. For the north region, the correlation of F_C with both $PW_{L1} - PW_{L2}$ and $PW_{L1} + PW_{L2}$ (Figures 7.16a–7.16b) is reasonably similar to over the entire Indian region. There is perhaps some correlation pre-onset between F_C and $PW_{L1} - PW_{L2}$, but little/none after onset. Note that there is a shift between pre-onset and post-onset, with both the convective flux and the difference in layer moisture content increasing. This is in slight contrast to Figure 7.14a, where the convective flux increases relative to the difference in layer moisture content. Between F_C and $PW_{L1} + PW_{L2}$, the derived values of the convective timescale, T_c, are 1.88 and 0.76 days for before and

after onset (here taken as 18th June) respectively. This is comparable to the convective timescale over the entire Indian region and validates the theory in the derivation of the dynamic lower layer model.
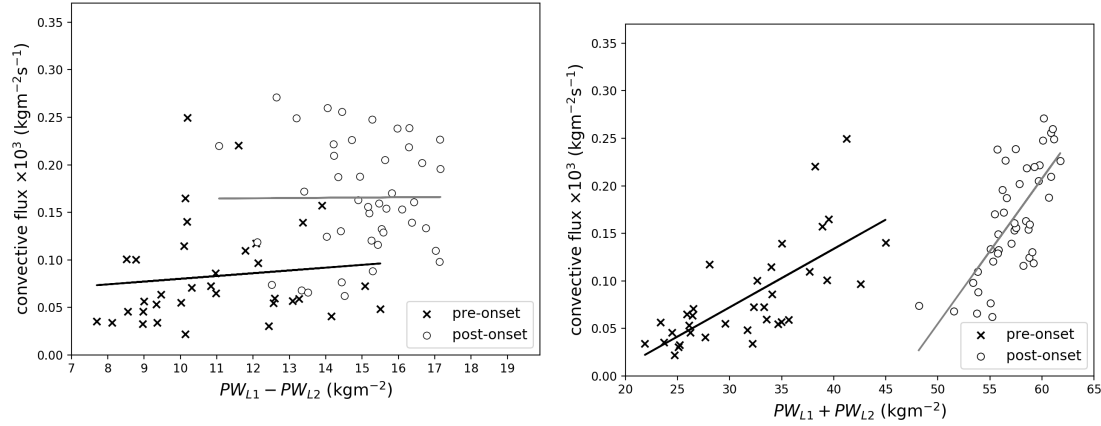
(a) F_C vs. the difference of PW_{layers}. North region.

(b) F_C vs. the sum of PW_{layers}. North region.
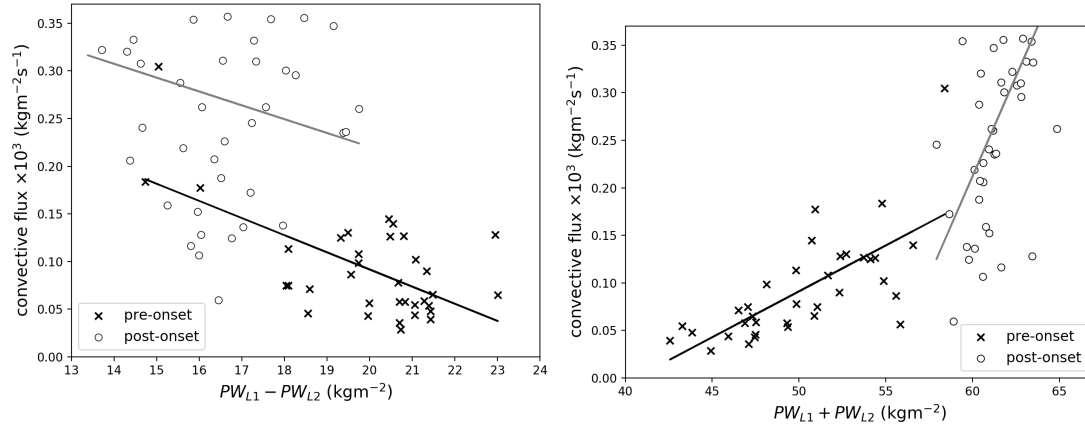
(c) F_C vs. the difference of PW_{layers}. South region.

(d) F_C vs. the sum of PW_{layers}. South region.

Figure 7.16: *Correlation of vertical convective flux with the change of the integrated moisture content in the lower and upper layers. Pre-onset refers to the period before 18th June, and post-onset the period after. Daily averaged data from 11 week simulation with the WRF model, over the north & south regions shown in Figure 7.7.*

Conditions are different for the south region. Looking at Figure 7.16c, at pre-onset, the convective flux is lower and the difference between moisture content in layers is greater than for the north or the combined regions. Moving to the post-onset phase, the values of convective flux against $PW_{L1} - PW_{L2}$ are more similar across the regions than for the pre-onset phase, although the convective flux values are slightly higher over the south than the north region. This would be expected, given that convective activity is greater towards southeast India. Another point to note is that the regression line between F_C and $PW_{L1} - PW_{L2}$ has a negative slope for the south region, possibly due to the role of the dry intrusion in suppressing rainfall. This is counter to the prediction that the convective flux is approximately proportional to $PW_{L1} - PW_{L2}$, and indicates that the initial model

parameterising the convective flux in terms of $PW_{L1} - PW_{L2}$ is not a good approximation. However, there is a large amount of scatter between the points in Figure 7.16c for both pre-onset and post-onset, with several points at low $PW_{L1} - PW_{L2}$ and high F_C influencing the pre-onset phase, so there is little confidence in the regression analysis. Figure 7.16d for the south region shows a similar pattern to the north and combined regions (Figures 7.14a, 7.16a), although the sum of the total moisture content over lower and upper layers is greater (i.e. x-axis values are higher). The derived convective timescales for F_C against $PW_{L1} + PW_{L2}$ are comparable to the north and combined regions, with values of 1.20 and 0.28 days before and after onset. The north region shows slightly longer convective timescales and the south region shows slightly shorter convective timescales than the combined region, which emphasises the higher rate of convective activity in the south, as seen in the real-world monsoon.

Table 7.2: *Statistical parameters for correlation from scatter plots in Figure 7.16.*

North region	T_c (days)	correlation coefficient	p-value
$PW_{L1} - PW_{L2}$ (pre-onset)	3.95	0.112	0.521
$PW_{L1} - PW_{L2}$ (post-onset)	44.4	0.006	0.968
$PW_{L1} + PW_{L2}$ (pre-onset)	1.88	0.712	0
$PW_{L1} + PW_{L2}$ (post-onset)	0.76	0.722	0
South region	T_c (days)	correlation coefficient	p-value
$PW_{L1} - PW_{L2}$ (pre-onset)	-0.64	-0.620	0
$PW_{L1} - PW_{L2}$ (post-onset)	-0.80	-0.224	0.144
$PW_{L1} + PW_{L2}$ (pre-onset)	1.20	0.708	0
$PW_{L1} + PW_{L2}$ (post-onset)	0.28	0.586	0

7.7   WRF experiment: impact of shallow & deep convection

Two additional simulations are undertaken with the WRF model, to examine the sensitivity of the convective timescale to aspects of the convective parameterisation scheme. The original simulation with no parameters changed is referred to as the control run. The first of the experiments switches off shallow and mid level convection in the Tiedtke cumulus parameterisation scheme, retaining deep convection. The second experiment switches off deep convection, but keeps shallow and mid level convection on. Similar experiments have been conducted by Shepherd and Walsh (2017); Pilon et al. (2016), for different applications. Shepherd and Walsh (2017) considers the effect of shallow convection and choice of cumulus parameterisation scheme on tropical cyclone simulations with the WRF model. Pilon et al. (2016) examines the roles of deep and shallow convection in simulations of the Madden-Julian Oscillation with the Model for Prediction Across Scales (MPAS), which is complementary to the WRF model.

Parker et al. (2016) argue that it is the shallow and mid level convection that control the monsoon onset. So with shallow and mid level convection switched off, it is predicted that there would be reduced moisture transport to the northwest, postponement of deep convection and possibly a delayed onset. However, it is not clear how the cumulus parameterisation scheme handles moisture advection with shallow or deep convection switched off. The shallow convection is often linked with the boundary layer scheme. Changing parameters in the cumulus scheme can have far-reaching implications and the interactions with other aspects of the WRF model are difficult to anticipate. Also note that these changes are imposed globally, meaning that they affect the convection everywhere in the domain, over ocean and land. There will be influences on the monsoon circulation due to remote changes, which will be very hard to assess and could have counter-intuitive effects on the onset of the Indian monsoon.

7.7.1   Results

The results of the simulations with shallow & mid level convection and deep convection switched off in turn, against the control run with the WRF model, are presented in this section. The plots of key variables are shown as the anomaly between the control run and the experiment runs with varying convection. The format of the figures is the same as in Chapter 6, with six panels represent daily snapshots over the monsoon season, from pre-onset to mid-onset to the full monsoon.

Figure 7.17 shows the anomaly of daily accumulated precipitation between each of the convective experimental runs and the control run. With shallow & mid level convection switched off (top row), the simulation more closely resembles the control run than the experiment with deep convection switched off. There is a dry bias over the Western Ghats over June to mid July, and a dry bias over the ocean south of India at mid July. The simulation with deep convection switched off generally shows more intense and less widespread precipitation than the control run. This is increasingly evident over the length

of the simulation. At 15th and 30th of June, the positively anomalous rainfall in the simulation with deep convection off is located slightly northwest compared with the control run, possibly indicating that the onset "front" is slightly ahead of time.

In terms of the relative humidity, the simulation with shallow & mid level convection switched off in particular shows dry biases over the ocean at the 850 hPa level, compared to the control run (Figure 7.18). Both experimental runs show a moist bias over the majority of India on 15th June, although it is slightly more widespread in the run with the shallow & mid level convection switched off. For the same date, there is also an anomalous northerly wind over India for both experimental runs. At the 500 hPa level (Figure 7.19), the simulation with deep convection switched off is significantly drier than the control and other experimental run. At 30th June, the simulation with shallow & mid level convection switched off has a dry bias over northwest India, indicating a stronger dry intrusion at mid levels than seen in the control run. With deep convection switched off, there is a similar dry bias but located further west and partially offshore. There is a also a wet bias over central India, compared to the control run.

Figures 7.20 and 7.21 show the vertical cross-sections of the moisture fields (q, rh) along transect 1. Considering firstly the water vapour mixing ratio, both experimental runs show a slight dry bias to the southeast at mid levels for 31st May, compared to the control run. By 15th June, both experimental runs show elevated values of water vapour mixing ratio at low levels, stretching from about 500–2300 km in the simulation with shallow & mid level convection switched off and from 1700-2300 km where deep convection is switched off. There is a dry bias over the mountains to the northwest of the transect for mid July, for both experimental runs. Secondly, examining the relative humidity field along transect 1, the greatest differences relative to the control run are around onset, from mid to late June. The simulation with shallow & mid level convection off has higher relative humidity in the range 1000–2000 km for nearly the full height of the atmosphere. Where deep convection is switched off, there is also a moist bias between 1000 and 2000 km, extending from the surface to about 400 hPa. By 30th June, the pattern has reversed and a region of lower relative humidity is seen at mid levels in both experimental runs, compared to the control run. Very generally, it seems that with shallow and mid level convection switched off, it is drier closer to the surface and more moist at higher levels. In contrast, in the simulation with deep convection switched off, it is more moist at low levels and becomes drier at upper levels, relative to the control run. It is difficult to analyse the differences in the simulations and it is not entirely clear how moisture is redistributed with either shallow or deep convection switched off.
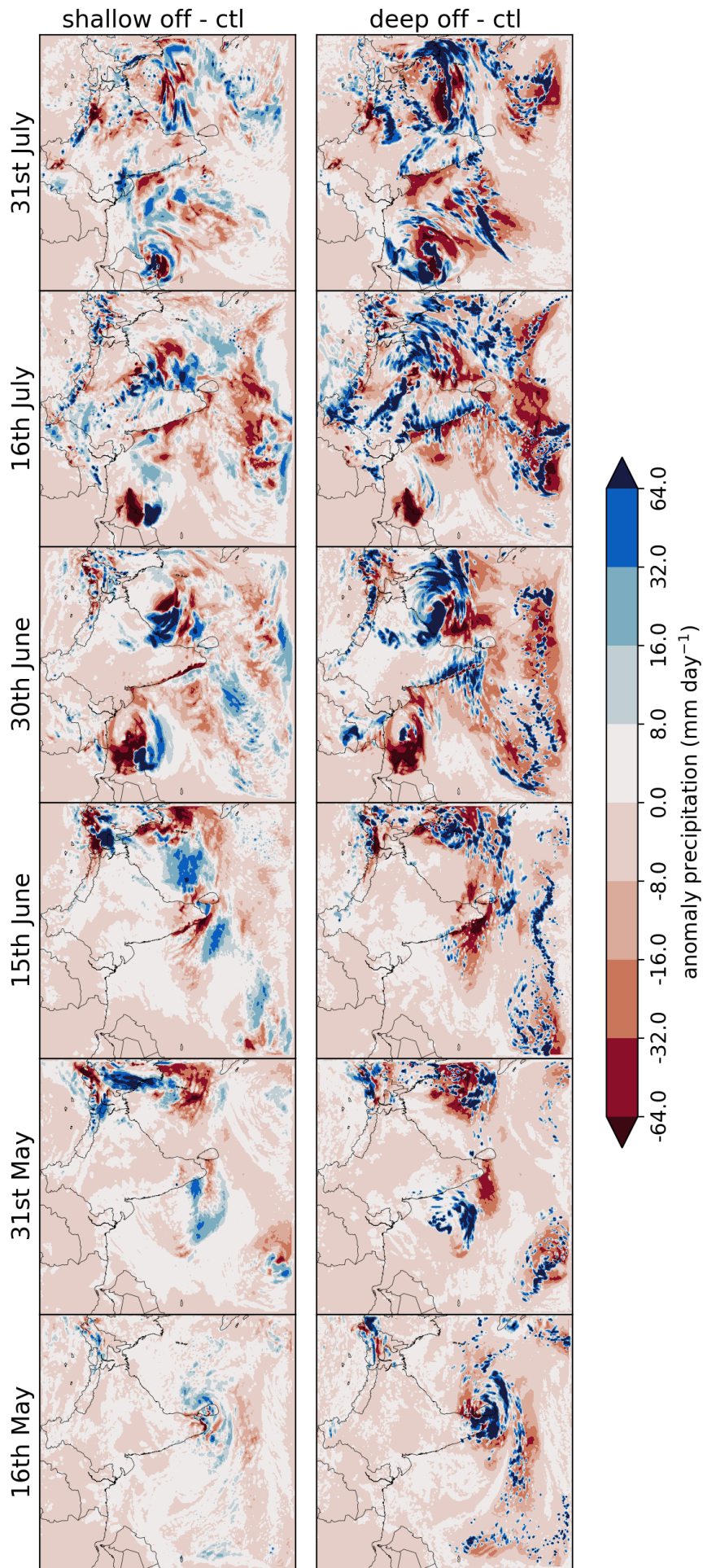
Figure 7.17: *Anomaly of daily accumulated precipitation (mm day^{-1}) for various dates from the 11 week simulations with the WRF model. Anomaly of shallow & mid level convection switched off (top), and deep convection switched off (bottom) with the control run.*
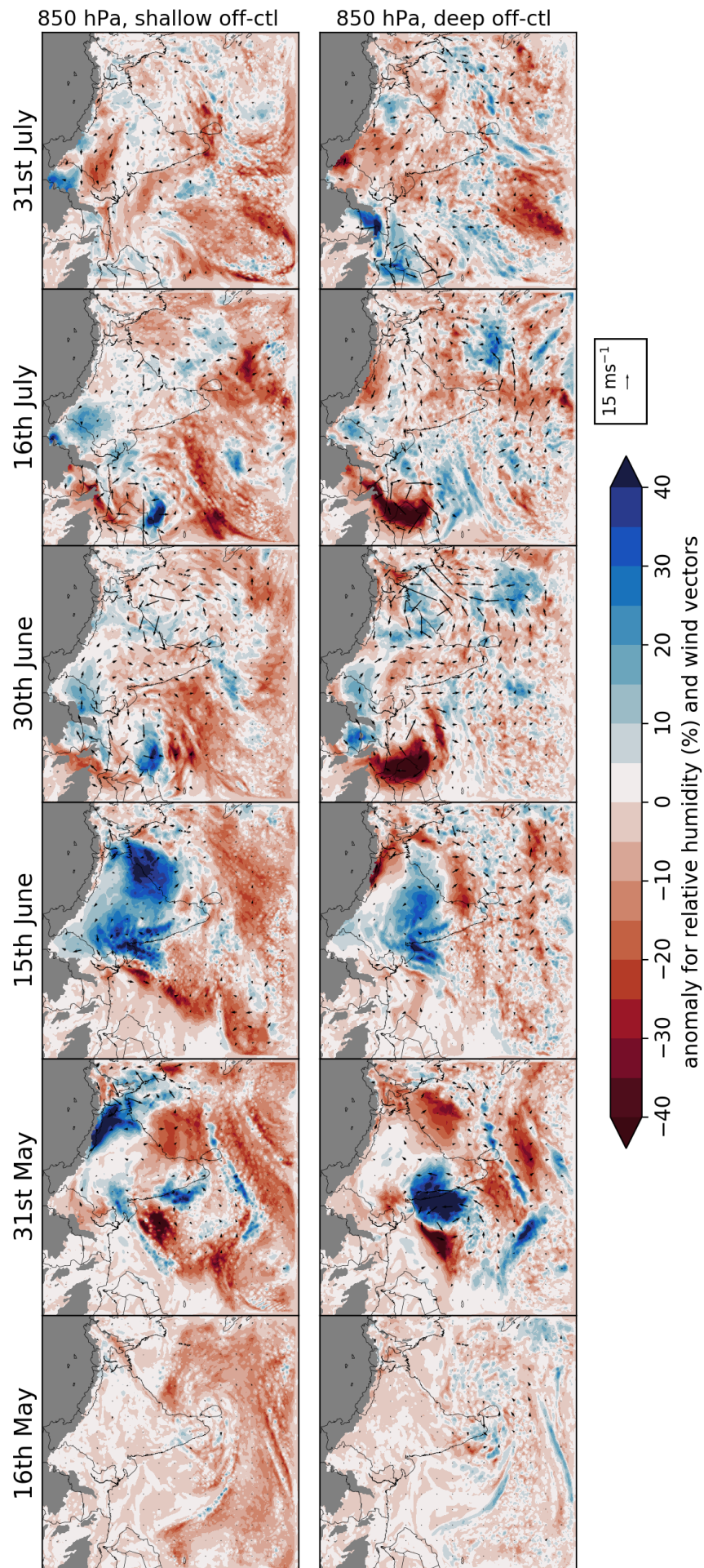
Figure 7.18: *Anomaly of relative humidity (shading, %) and wind (vectors, ms^{-1}) at the 850 hPa level, from the 11 week simulations with the WRF model. Anomaly of shallow & mid level convection switched off (top), and deep convection switched off (bottom) with the control run.*
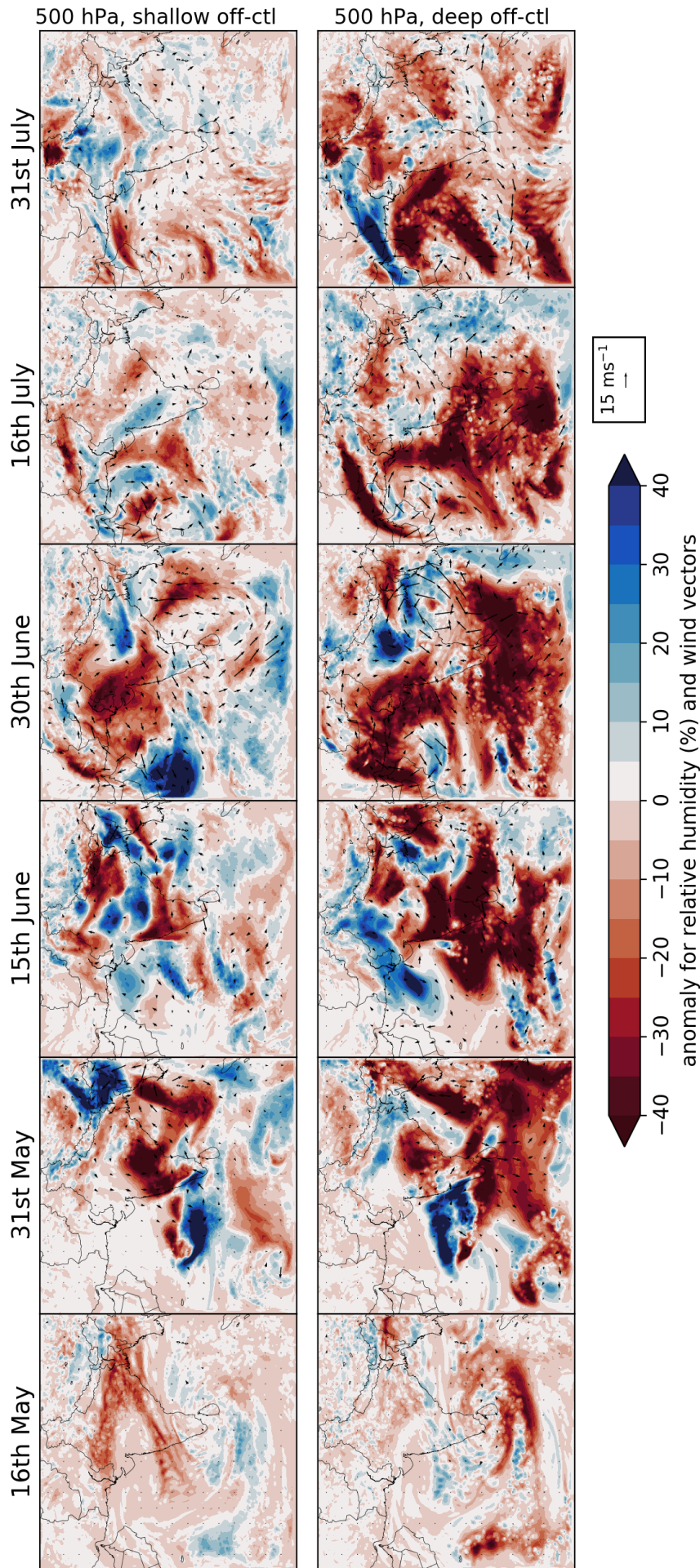
Figure 7.19: *Anomaly of relative humidity (shading, %) and wind (vectors, ms^{-1}) at the 500 hPa level, from the 11 week simulations with the WRF model. Anomaly of shallow & mid level convection switched off (top), and deep convection switched off (bottom) with the control run.*
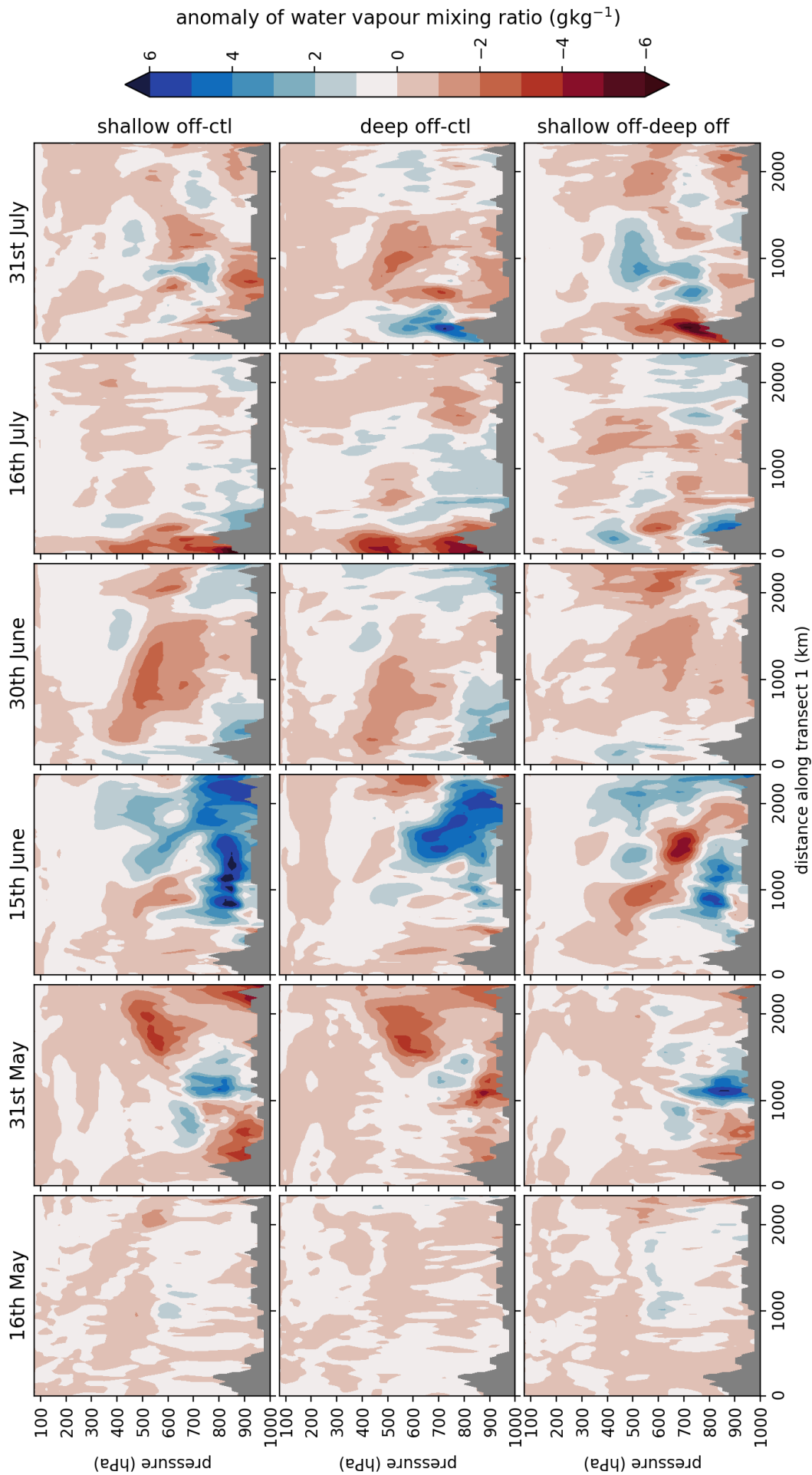
Figure 7.20: *Anomaly of water vapour mixing ratio (gkg^{-1}) along transect 1, from the 11 week simulations with the WRF model. Anomaly of control run and shallow & mid level convection switched off (top), control run and deep convection switched off (middle), and shallow & mid switched off and deep convection switched off (bottom).*
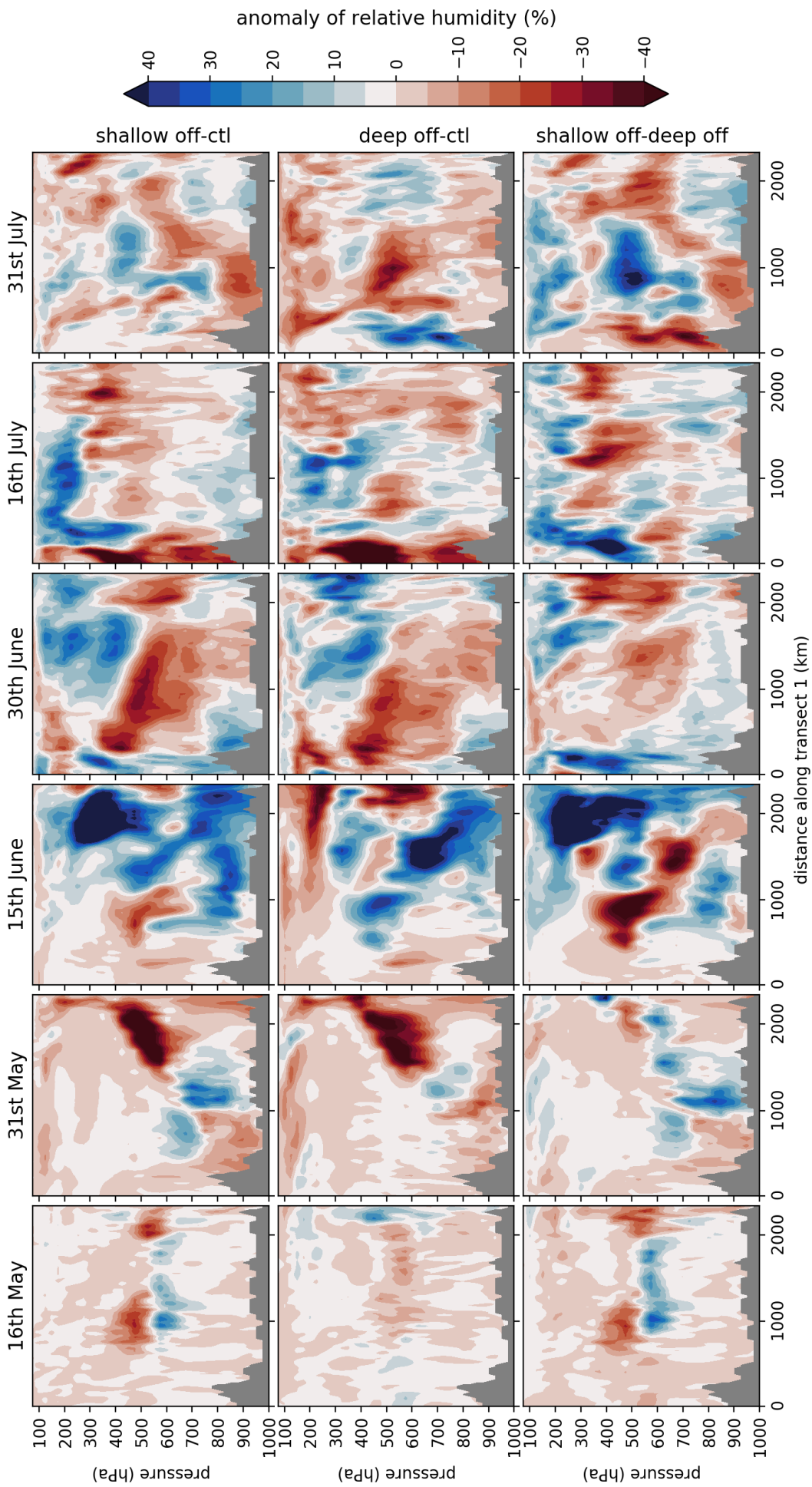
Figure 7.21: *Anomaly of relative humidity (shading, %) along transect 1, from the 11 week simulations with the WRF model. Anomaly of control run and shallow & mid level convection switched off (top), control run and deep convection switched off (middle), and shallow & mid switched off and deep convection switched off (bottom).*
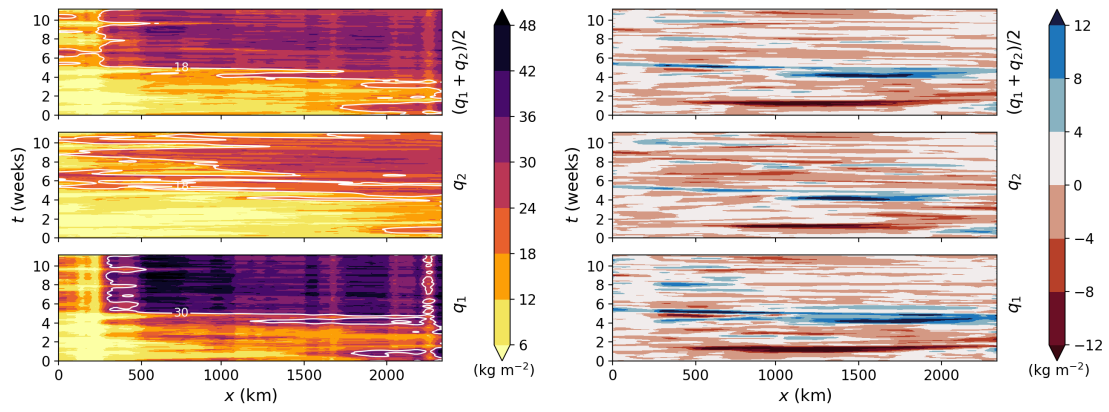
(a) *Shallow & mid level convection switched off..*

(b) *Shallow & mid level convection off - control run.*
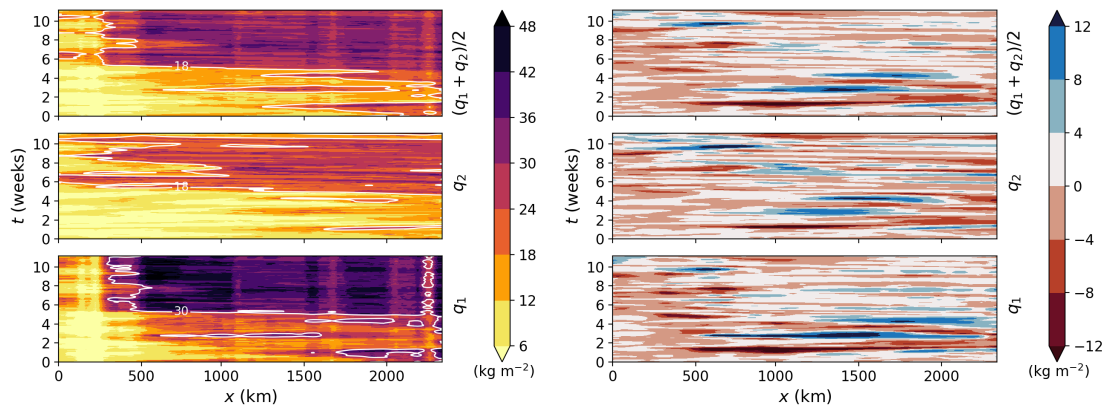
(c) *Deep convection switched off.*

(d) *Deep convection off - control run.*

Figure 7.22: *Evolution of column integrated water vapour mixing ratio (kg m^{-2}) over two vertical layers split at 700 hPa, along transect 1, from the WRF model simulation, with shallow & mid level convection switched off (top row) and deep convection switched off (bottom row). Note that contours have been smoothed for anomaly plots (right column).*

The evolution of water vapour mixing ratio over lower and upper layers of the atmosphere (split at 700 hPa) is considered in Figure 7.22 for simulations with the shallow & mid level convection switched off (top row) and deep convection switched off (bottom row). The left column shows the integrated water vapour mixing ratio against time for the lower, upper and combined layers, similarly to Section 7.2. It is difficult to distinguish the differences between Figures 7.22a and 7.22c, and with the control run shown in Figure 7.1a. Thus, the anomaly between the convective experimental runs and the control run is plotted (right column).

When the shallow & mid level convection is switched off, the lower and upper layers show a drying one week into the simulation from 500–2300 km, relative to the control run. Within 4–6 weeks, around the time of onset, there is a moist bias compared with the control simulation. This is more evident in the lower layer. Where deep convection is switched off, a slight dry bias is also observed for the lower and upper layers at around week 1. There is a slight moist bias just after weeks 2 and 4 in the lower and upper

layers, but it is less persistent than for the simulation with shallow & mid level convection switched off. The simulation with deep convection switched off shows a higher moisture content at the start of the run for both layers over central–southeast India, compared to the other simulations. This is possibly indicative of the important role played by shallow convection in moistening the lower troposphere prior to onset, although further analysis would be required to state this with confidence.

7.7.2   Moisture budget analysis

The moisture budget analysis is repeated for the simulations with the WRF model where shallow & mid level convection and deep convection are switched off independently. The similarity between the plots showing the evolution of the moisture budget components over the lower and upper layers for the experimental runs and the control run is such that not all the results are not presented here. Figure 7.23 shows the moisture budget applied to the Indian region over the full height of the atmosphere. Some differences are seen post-onset in terms of timing and amplitude of peaks regarding some of the fluxes and precipitation, compared to Figure 7.8b, but in this subsection the analysis is focused on diagnosing the vertical convective flux between layers, in order to derive a convective timescale.

Following Subsections 7.5.3 and 7.6.1, the moisture budget for both of the experimental simulations is analysed over two vertical layers of the atmosphere, splitting at the 700 hPa level. The vertical convective flux is diagnosed from lower and upper layers by taking the difference between the change in total column moisture and the sum of the components entering or leaving the column. The evolution of the convective flux and the total column moisture for each layer is considered in Figure 7.24. Both experimental runs follow the control run in that the convective flux more than doubles between 12th and 19th June. Figures 7.24a and 7.24b are comparable to Figure 7.12 (control run) pre-onset. Post-onset, each of the quantities (F_C, PW_{L1}, PW_{L2}) follow a similar trend, with peaks and troughs matching approximately in time, if not amplitude.
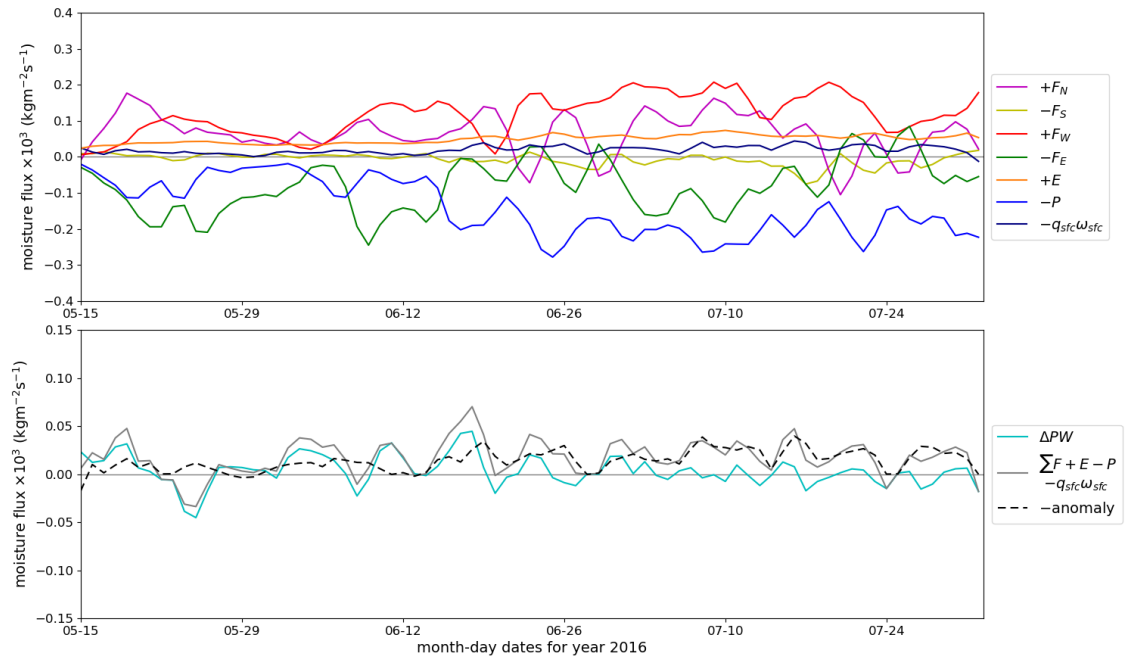
(a) *Shallow & mid level convection switched off.*
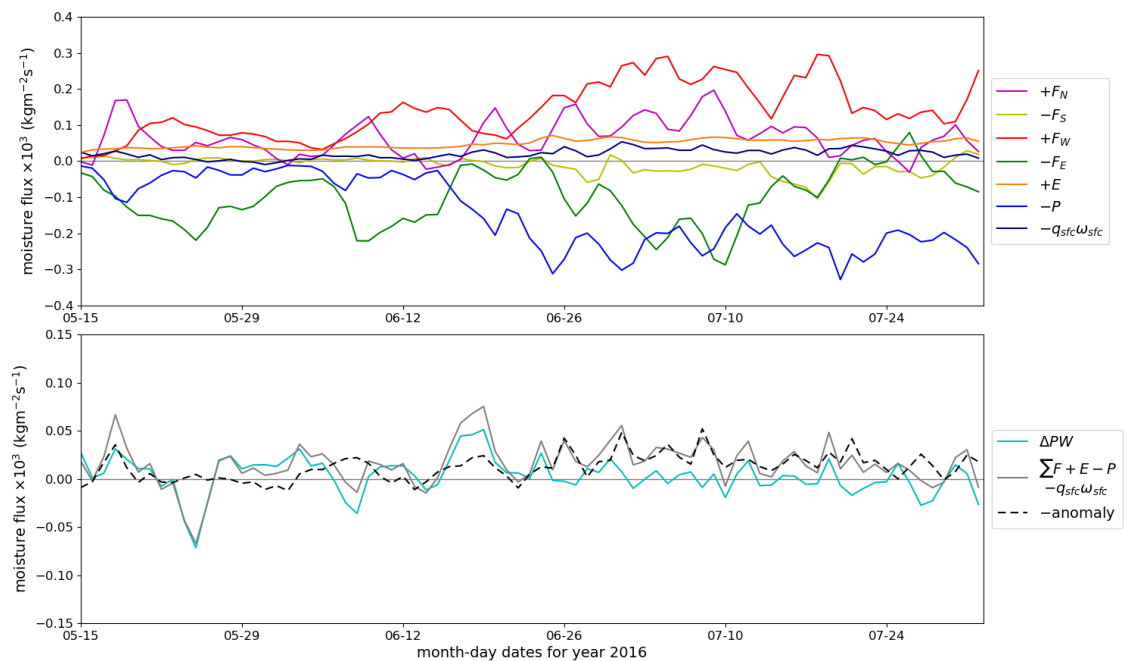
(b) *Deep convection switched off.*

Figure 7.23: *Moisture budget components from 11 week convective experimental simulations with the WRF model (daily averaged data), over the box shown in Figure 7.7. Components have been interpolated to pressure levels.*
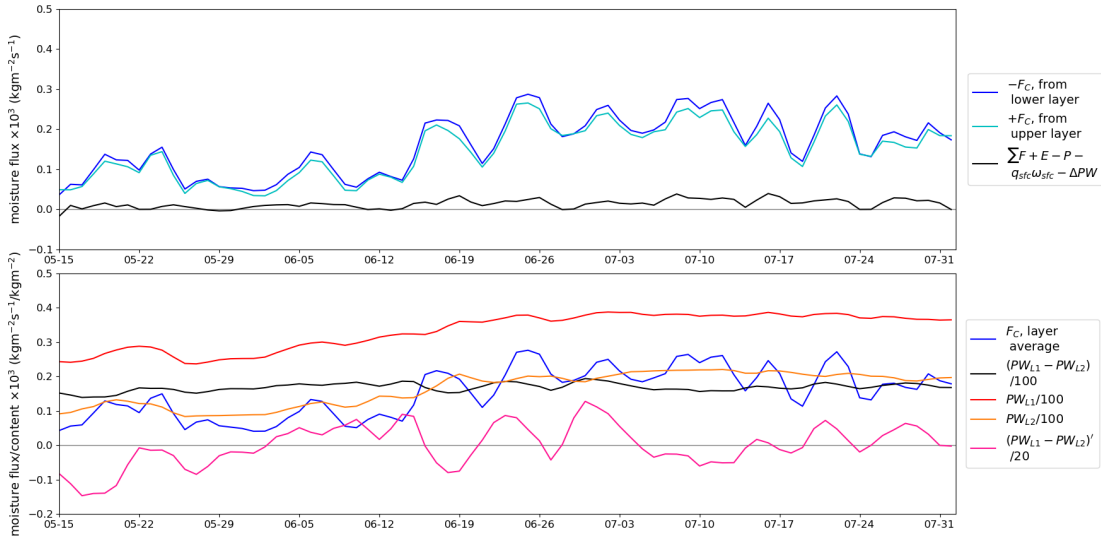
(a) *Shallow & mid level convection switched off.*
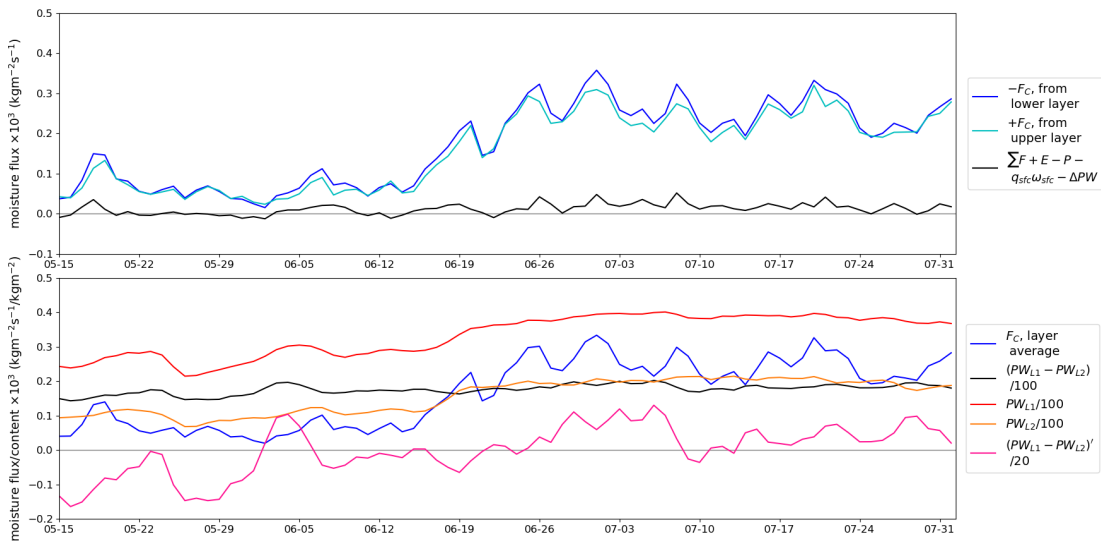
(b) *Deep convection switched off.*

Figure 7.24: *Inferred vertical flux between upper and lower layers, split at 700 hPa. Daily averaged data from 11 week simulation with the WRF model, over the box shown in Figure 7.7.*

7.7.3 Comparing convective timescales

The correlation between the convective flux and the difference and the sum of the integrated moisture content in the lower and upper layers is investigated. Following the method in Subsection 7.6.2, scatter plots of the relationships are shown in Figure 7.25, with the results of the regression analysis detailed in Table 7.3. As previously, there is little confidence in the correlation between F_C and $PW_{L1} - PW_{L2}$ for either of the experimental runs, although there is less scatter for the pre-onset phase compared with the post-onset phase. The correlation between F_C and $PW_{L1} + PW_{L2}$ is more robust, as indicated by the p-values being below 0.05. For the simulation with shallow & mid level convection switched off, the correlation coefficient is strongly positive pre-onset (0.758), and weakly positive post-onset (0.482). When instead the deep convection is switched off, the correlation between F_C and $PW_{L1} + PW_{L2}$ is weakly positive. Although the simulation with shallow & mid level convection switched off has comparable convective timescale values to the control run, with T_c halving after onset, the simulation with deep convection switched off has longer convective timescales of around 3 and 1.5 days for before and after onset. This is perhaps not surprising, given that deep convection plays a significant role in transferring moisture from lower to higher levels.

Table 7.3: *Statistical parameters for correlation from scatter plots in Figure 7.25.*

Shallow & mid level convection off	T_c (days)	correlation coefficient	p-value
$PW_{L1} - PW_{L2}$ (pre-onset)	-4.59	-0.071	0.687
$PW_{L1} - PW_{L2}$ (post-onset)	3.21	0.079	0.611
$PW_{L1} + PW_{L2}$ (pre-onset)	1.82	0.745	0
$PW_{L1} + PW_{L2}$ (post-onset)	0.92	0.482	0.001
Deep convection off	T_c (days)	correlation coefficient	p-value
$PW_{L1} - PW_{L2}$ (pre-onset)	-8.24	-0.600	0.732
$PW_{L1} - PW_{L2}$ (post-onset)	1.07	-0.217	0.157
$PW_{L1} + PW_{L2}$ (pre-onset)	3.37	0.448	0.007
$PW_{L1} + PW_{L2}$ (post-onset)	1.42	0.436	0.003

These timescale tests are consistent with the shallow & mid level convection having little effect on the vertical convective flux, which is perhaps unremarkable given that most of the shallow & mid level convection will occur in the lower layer, i.e. below 700 hPa. As noted above, it is the deep convection that has the greatest effect on the convective timescale. In terms of the dynamic lower layer model, the effect of switching off deep convection is comparable to the experiments in Section 5.7. Experiments with the idealised model are initialised with a longer T_c, representing little or no deep convection. Then the convective timescale is reduced, indicating the switching on of deep convection, facilitating increased moisture transport from the lower to the upper layer. An abrupt increase in deep convective events can act both to enhance monsoon onset locally, and delay its

progression to the northwest This is observed in the dynamic lower layer experiments, the WRF model simulation with deep convection switched off, supporting the results of Volonté et al. (2019).

(a) F_C against the difference of PW_{layers}.

(b) F_C against the sum of PW_{layers}.

(c) F_C against the difference of PW_{layers}.

(d) F_C against the sum of PW_{layers}.
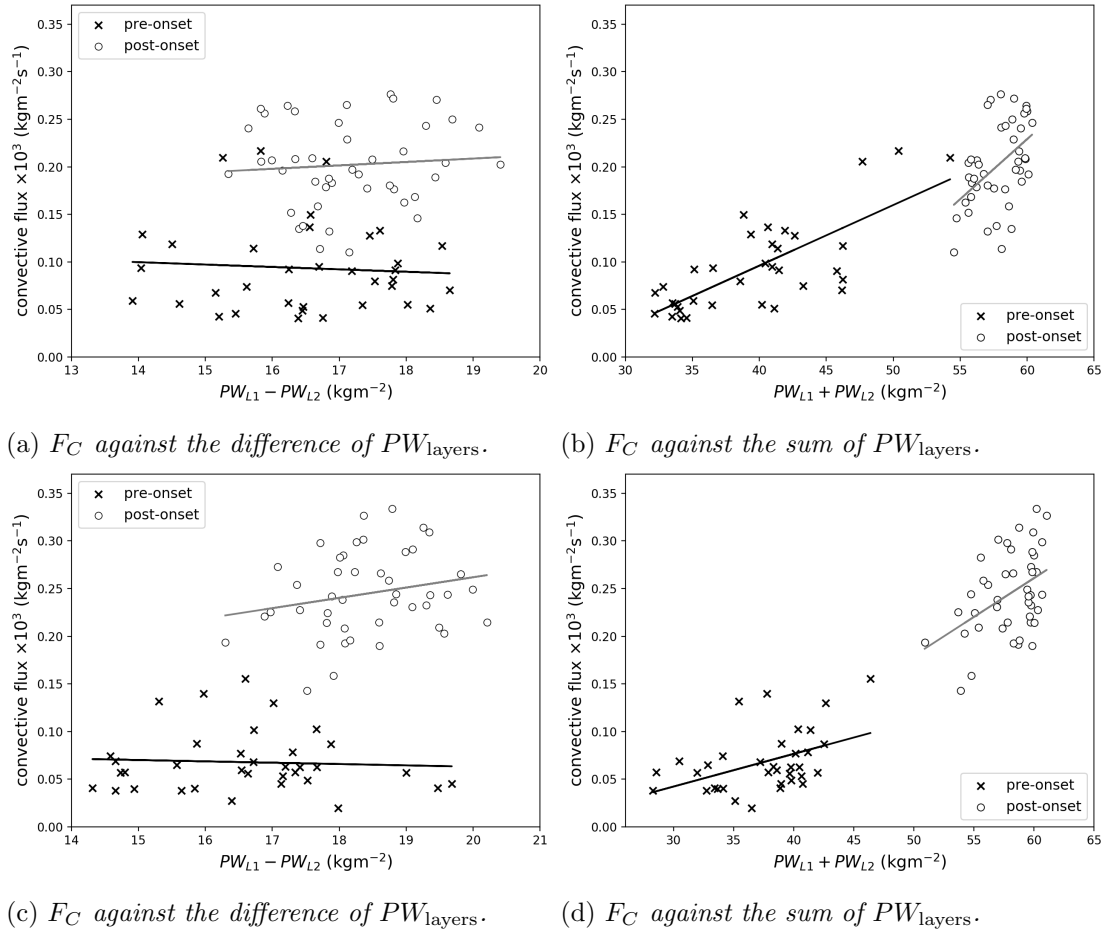
Figure 7.25: *Correlation of vertical convective flux with the change of the integrated moisture content in the lower and upper layers. Daily averaged data from 11 week simulation with the WRF model, over the box shown in Figure 7.7, with shallow & mid level convection switched off (top row) and deep convection switched off (bottom row).*

7.8   Conclusions

The framework of the idealised model presented in Chapter 5 has been used as a basis for evaluating aspects of the WRF model simulations, which allow testing of the theory and assumptions regarding the onset and progression of the monsoon. Prior to onset, both models show the moistening of the lower troposphere over southeast India (as in Parker et al. (2016); Menon et al. (2018)), and to a lesser extent, the moistening of the upper troposphere. The monsoon flux, i.e. the moist low level inflow from the Arabian Sea, has been shown to approximately double around onset. A reduction in the strength of the northwesterly wind at mid levels allows the monsoon onset to propagate to the northwest. A moisture budget analysis has been undertaken for the WRF model simulations, in

order to diagnose the vertical convective flux from the lower to the upper layer in the atmosphere, and thus derive a convective timescale from the correlation with moisture content in both the layers. The relationship between the convective flux and the difference of the total column moisture between the layers was examined. Although there was some weak correlation pre-onset, there was little confidence in the derived convective timescale values. The results with the WRF model demonstrate a robust relationship between the convective flux and the sum of the total column moisture over the layers, which are positively correlated for both pre-onset and post-onset phases. The convective timescales were of the order of 1–2 days pre-onset, then halving in the transition to post-onset. When deep convection is switched off, slighter longer timescales of 3.5 (pre-onset) and 1.5 (post-onset) days are noted. These values are consistent with the assumed convective timescales in the dynamic lower layer model, quantifying convective timescales in the real-world monsoon, which are difficult to observe. Figure 7.26 summarises the convective timescale values for various experiments undertaken with both the WRF model and the dynamic lower layer ("2-layer") model.
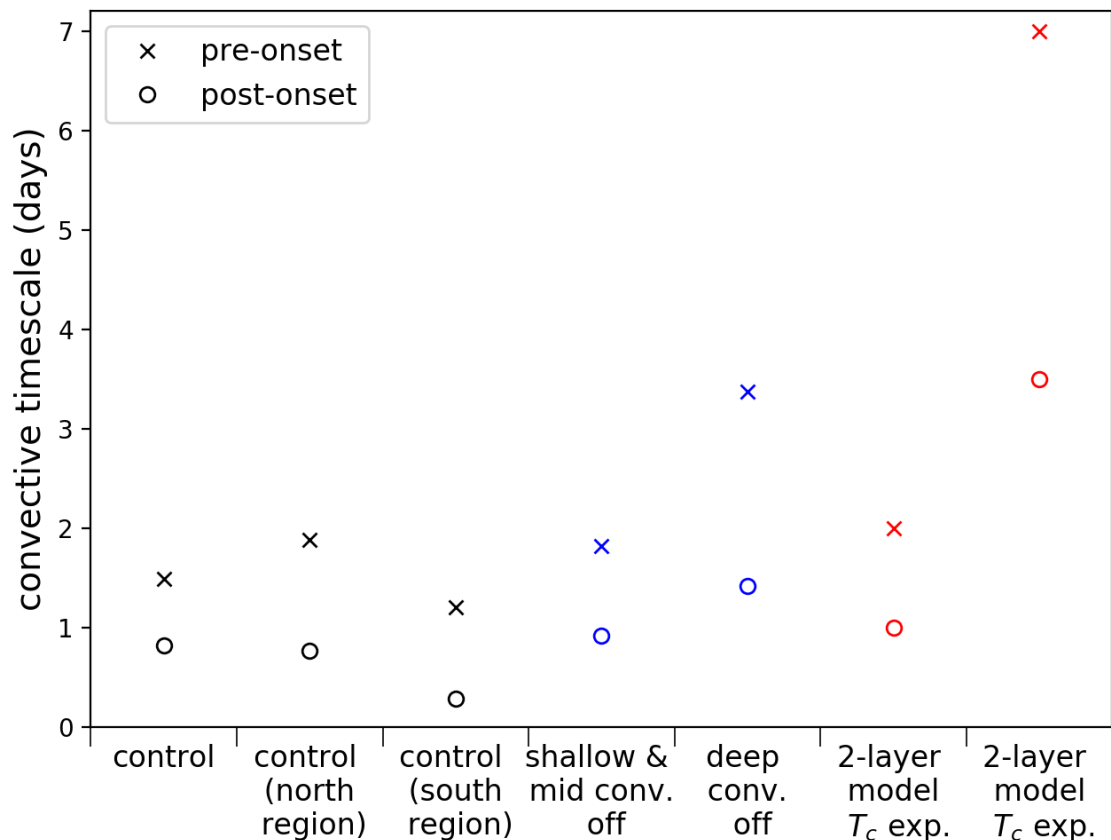
Figure 7.26: *Comparing convective timescales (T_c) between experiments with the WRF model (black & blue points) and the dynamic lower layer model (red points) for pre-onset and post-onset. Note that the T_c values derived from the WRF model are based on $PW_{L1} + PW_{L2}$, whilst T_c in the dynamic lower layer model is linked with $PW_{L1} - PW_{L2}$.*

Chapter 8

Conclusion

8.1 Summary of results

The Indian monsoon is a complex dynamical system that is difficult to forecast accurately. In particular, the timing, pattern and intensity of precipitation associated with the onset of the monsoon is hard to predict. Also, the mechanism by which the monsoon onset advances from southeast to northwest India, against the mean mid-level wind field, cannot be explained by simple moisture flux arguments. The physical mechanisms and interactions driving monsoon onset, and leading to precipitation events, are not well represented in weather and climate models, as they are often imperfectly parameterised. Processes such as low-level moist inflow, dry mid-level winds and rate of convection have been identified as playing key roles regarding the onset and progression of the Indian monsoon. Idealised modelling studies can increase understanding regarding the roles of these processes and allow testing of their effects on the Indian monsoon onset.

Here, several idealised models based on moisture dynamics are developed to explore the balance between low-level moist inflow, mid-level dry advection and the rate of convection on their effect on the onset and propagation of the Indian monsoon onset. In conjunction, simulations with a numerical weather prediction model are undertaken and analysed within the framework of the idealised models, to help test and quantify the theory behind monsoon onset in the context of the real-world system. The combination of examining the Indian monsoon onset from both a classical fluid dynamics and a meteorological perspective is particularly novel.

8.1.1 Two-layer model of moisture dynamics

A two-layer model of the atmosphere based on conservation laws was introduced in Chapter 3, describing a vertical transect running from northwest to southeast India (x-direction), along which the monsoon onset can propagate. The two-layer model and its simplified versions are the main theoretical tools used to investigate monsoon onset in this thesis (Chapters 4 and 5). In the lower layer, the evolution of moisture, $q_1(x, t)$, is determined by the horizontal wind field, including low-level moist inflow from the Arabian Sea, evapo-

ration from the surface and loss of moisture to the upper layer through a (parameterised) vertical convective flux. The upper layer moisture content, $q_2(x, t)$, is affected by the horizontal wind field, primarily northwesterly dry advection, the rate of convection, and the frequency of precipitation. To focus the two-layer model of moisture dynamics for testing monsoon onset theory, a simplified version is presented, which retains the key processes detailed below:

- Convection. This was included as a vertical moisture flux from the lower to the upper layer. Various simple parameterisations were deployed, with the standard choice being a down-gradient flux, $F = (q_1 - q_2)/T_c$, where T_c is a timescale for the convection to act and mix the layers. The suggested range for T_c was 1/2–7 days, but there is considerable uncertainty regarding the choice of this parameter.

- Moisture replenishment in the lower layer. This represents a combination of evaporation from a saturated surface, moist low-level winds (e.g. from over the surrounding oceans) and any addditional surface forcing, such as river inflow. Again, a simple parameterisation of this process was implemented, as a relaxation of the lower layer to a prescribed profile $q_e(x)$, where $q_e(x)$ is interpreted as an equilibrium state in the absence of convection. The relaxation occurs on a timescale T_m. It is not clear what the value of T_m should be, but as for the convective timescale, a range of 1/2–7 is selected.

- Advection in the upper layer. A northwesterly wind is imposed in the upper layer (u_2), consistent with observations of dry intrusions. Note that advection in the lower layer is neglected along the transect. At the northwestern boundary of the transect (where $x = 0$), a completely dry inflow was imposed, so that $q_2(x = 0, t) = 0$.

The resulting model consists of a pair of coupled partial differential equations which describe the evolution of the lower and upper layer moisture contents, $q_1(x, t)$ and $q_2(x, t)$. The simplicity of the model allows the relative roles of convection, low-level moisture replenishment and upper layer advection to be explicitly evaluated in the context of monsoon onset. This is a novel approach for studying and quantifying the effect of these key physical processes on the onset and progression of the Indian monsoon.

8.1.2   Fixed lower layer model

The simplest form of the two-layer model, which neglects surface processes and precipitation, has a fixed lower layer and is one-dimensional in space (Chapter 4). The timescale for the lower layer replenishment is assumed to be zero so that the lower layer moisture content is equivalent to the prescribed profile ($q_1 = q_e$), corresponding to instantaneous replenishment. The system reduces to a single partial differential equation, with parameters describing upper level advection and timescale of convection, with a forcing term relating to $q_e(x)$. Solutions can be determined analytically, giving more information about the

system and allowing the accuracy of a numerical scheme to be evaluated, which would be needed when additional complexity is incorporated. It has been demonstrated that this fixed lower layer model can reproduce a propagating monsoon onset "front", against an opposing upper layer wind, at a realistic speed. The results are noted in more specific detail below.

- An experiment was considered where the upper layer was initially dry ($q_2(x, t = 0) = 0$), corresponding to a configuration with either no convection (upper layer wind speed u_2 is finite, but $T_c = \infty$) or with upper layer advection so strong that the upper layer remained dry via the northwest boundary condition (T_c finite, but $u_2 = \infty$).

- The upper layer begins to moisten at immediately, when either the convection switches on (T_c) becomes finite) or advection is weakened (u_2 becomes finite). The evolution of q_2 then depends upon u_2, T_c, and the lower layer equilibrium profile $q_e(x)$.

- Several different prescribed profiles of $q_e(x)$ were tested, including $q_e(x) = 1$ (simplest option) and $q_e(x) = x$, which reflects the expected moisture gradient from northwest to southeast India.

- The upper layer moisture evolves towards a new equilibrium representing a balance between advection, acting to remove moisture, and convection, acting to add moisture. This equilibirum was characterised by a length-scale $u_2 T_c$, giving the distance that the upper layer moisture adjusts over, from zero to a moist equilibrium state. The length-scale is noted as the "monsoon length-scale", as it gives a bound on the possible extent of monsoon onset.

- A moisture front, interpreted as monsoon onset, can be observed to move along the transect from southeast to northwest India. An exact expression for the speed of the onset "front" can be derived from the analytical solutions. Calculated values are in the range 3–6 ms^{-1}, consistent with observed onset speeds.

- Results have been verified analytically and numerically.

It is noted that even the simplest version of the two-layer model, with a fixed lower layer, can lead to a monsoon onset that propagates from southeast to northwest India with a realistic speed. The experiments with this model are viewed as a transition from one equilibrium (dry) to a new equilibrium (moist), following a change in one of the meteorological processes, with either convection being intensified, or upper layer advection being reduced.

8.1.3   Dynamic lower layer model

The two-layer model with a dynamic lower layer (as presented in Chapter 3), which allows
evolution of moisture in both the upper and lower layers, is used to investigate the balance
between low layer moisture inflow, upper layer advection and vertical convective flux
(Chapter 5). There are parameters for the timescale of convection, T_c, and lower layer
moisture replenishment, T_m, which is now finite (compared to zero in the fixed lower layer
model).

- Experiments are similar to those in Chapter 4, but are now initialised at a state of
  equilibrium. Note that the steady-state solutions can be derived analytically from
  the system of partial differential equations.

- Once initialised, the system is perturbed by varying the rate of replenishment (T_m),
  the rate of convection (T_c), or the upper level advection (u_2) independently, to $\widetilde{T}_c$,
  $\widetilde{T}_m$, or $\widetilde{u}_2$. Changing each of these parameters induces a monsoon onset.

- Monsoon onset is arbitrarily defined as a threshold of the total moisture over both
  layers.

- Experiments with the dynamic lower layer model demonstrate that doubling the
  rate of low-level moisture flux (by halving T_m) or doubling the rate of convective
  activity (by halving T_c) produce a monsoon onset that propagates from southeast
  to northwest India. Decreasing the upper layer advection (u_2) allows the monsoon
  onset to progress at a faster speed to the northwest, whilst increasing the upper layer
  advection can result in a reverse onset which propagates in the opposite direction
  (i.e. to the southeast). This is representative of northwesterly dry intrusions, which
  are linked with active and break phases during the monsoon as they strengthen or
  weaken.

- A natural monsoon length-scale (L_{mon}) emerges as a combination of the timescales
  and upper layer wind speeds, so that $L_{\mathrm{mon}} = u_2 (T_c + T_m)$. Setting $T_m = 0$ recovers
  the length-scale found in Chapter 4.

- The dynamic lower layer model, representing an equilibrium state of the monsoon
  system, is associated with a particular monsoon length-scale (L_{mon_1}). As one of the
  processes, such as low-level moisture flux, upper layer wind or convective activity, is
  varied, the system reaches a new equilibrium which is linked with a different monsoon
  length-scale (L_{mon_2}). For a onset propagating from southeast to northwest India,
  $L_{\mathrm{mon}_1} > L_{\mathrm{mon}_2}$.

- Although analytical solutions are not easily derived for the time-evolving system,
  a combination of alternative methods including small-time solutions, scaling argu-
  ments and numerical solutions, allow the nature of the onset transition to be under-

stood. These have enabled expressions for the initial speed (ν) of the onset contour and an adjustment timescale (T_{adj}) to be derived.

- The calculated onset speeds are generally $< 5 \ \mathrm{ms}^{-1}$, comparable to observed speeds.

- The timescale of adjustment (T_{adj}), which is the time taken for the system to transition from one equilibrium (pre-onset) to a new equilibrium (post-onset). Generally, the dynamic lower layer model adjusts faster than the observed monsoon, on the order of 1–2 weeks compared with 6 weeks, and does not tend to progress over the full length of India, approximately 3000 km.

- It is interesting to note that for the experiments increasing low-level inflow (T_{m} to $\widetilde{T}_{\mathrm{m}}$) and varying upper layer advection (u_2 to $\widetilde{u}_2$), the adjustment timescale (T_{adj}) depends only on the combination of the replenishment and convective timescales, and not on the initial upper layer wind speed u_2.

- The system is more sensitive to changes in the timescale of moisture replenishment (T_{m}), than the convective timescale (T_{c}).

The dynamic lower layer model represents an Eulerian view of the evolution of key processes - low-level moist inflow, upper level advection and convection - along a vertical cross-section extending from northwest to southeast India. Each of these experiments, varying the processes noted above, reflect changes observed over India around the time of onset, May–June. Changing each of the key parameters causes the system to transition from one equilibrium (pre-onset) to a new equilibrium (post-onset). Considering the small-time solutions and using scaling arguments, explicit expressions for the onset speed and time of adjustment between equilibria can be derived. This means the relative importance of each parameter can be assessed. It is found that the adjustment timescale for varying the upper level advection is in fact independent of the upper level advection, and that the system is more sensitive to changes in the low-level moisture inflow than the rate of convection.

8.1.4   WRF model simulation

A numerical weather prediction model is selected to simulate the Indian monsoon, in order to test various assumptions and theory regarding monsoon onset. The WRF model is chosen, due to its flexibility and accessibility, and an 11 week simulation of the 2016 monsoon season is described in Chapter 6. Performance is validated against reanalysis and observational data, including from the INCOMPASS campaign during May–June of the year 2016. The WRF model simulation is reasonably accurate, reproducing the observed late onset, rapid progression to the northwest and large-scale circulation. It does not capture the observed monsoon depression over the Bay of Bengal at the end of June, but this is deemed of low significance in the context of this thesis.

8.1.5   Comparing models

The framework of the idealised dynamic lower layer model is used to quantify the WRF model simulation in a meaningful way in the context of the Indian monsoon. Parallels are drawn between key processes affecting monsoon onset, such as the evolution of the moisture content in each layer, low level moisture flux and upper layer advection. Further support is given to the theory that increased convective activity over southeast India leads to moistening of the lower troposphere, which enables the monsoon onset to progress to the northwest against the mean mid-level wind field (Parker et al., 2016; Menon et al., 2018). The results are summarised in detail below.

- Results from the dynamic lower layer model (Chapter 5) and the WRF model (Chapter 6) are contrasted using a novel framework, in order to increase understanding of key processes and their role in the onset of the Indian monsoon.

- Two atmospheric layers from the surface to 700 hPa and 700 hPa to 50 hPa (model top) are defined for the WRF model, giving lower and upper layers as in the idealised two-layer model. The sensitivity of the choice of boundary at 700 hPa has been tested, and found to make little difference to the results.

- The evolution of moisture over lower and upper layers is comparable in both models (Figure 7.3), with the lower layer containing more moisture than the upper layer and a moisture gradient being noted from northwest to southeast India. The adjustment times from pre-onset to post-onset are of a similar order, 1–2 weeks, although the idealised model does not show propagation over the full transect length ($\sim$2500 km) as in the WRF model.

- Low-level moisture flux is shown to approximately double at the time of onset in the WRF model, linking to the dynamic lower layer experiment where the timescale for moisture replenishment in the lower layer is decreased, thus increasing the moist inflow and initiating a monsoon onset.

- Advection in the upper layer is shown to play a key role in the results of both models. A lower northwesterly speed, indicating a weakening dry intrusion, allows the monsoon onset to advance to the northwest. The inverse statement is also true. Note that the progression of monsoon onset is not smooth or gradual, with bursts of dry northwesterly air, associated with the synoptic and large-scale circulation, affecting the rate of progression (Volonté et al., 2019).

- An equation for the moisture budget is derived in pressure coordinates, highlighting assumptions and numerical approximations which are often inadequately explained in the literature.

- A moisture budget analysis is undertaken for the WRF model simulation, in order to diagnose the vertical convective flux from the residual in the lower and upper layers.

- A convective timescale for the WRF model can be determined by correlating the convective flux with the moisture content in the layers, and performing a linear regression. The strongest relationship is between the convective flux and the sum of the moisture content in each layer, rather than with the difference in moisture content over layers.

- The analysis is repeated for additional simulations with the WRF model, to investigate the sensitivity to switching off the shallow & mid level convection and the deep convection independently. The sudden switch-on of deep convection is the basis for the dynamic lower layer model, where the convective timescale (T_c) is decreased, meaning enhancing convective activity.

- The derived convective timescales from the WRF model are of the order of 1–2 days prior to onset, and 1/2–1 day after onset. The assumed range of values for the dynamic lower layer model was 1/2–7 days. Switching off shallow & mid level convection had little effect on the convective timescale, as the shallow & mid level convection is contained within the lower layer, under 700 hPa. Longer convective timescales of 2–4 days were calculated for the simulation with deep convection switched off, which is not surprising given that deep convection is the dominant mechanism of moisture transport between lower and upper layers. It is difficult in practise to observe timescales of convection.

The combined approach of using an idealised model and a numerical weather prediction model has allowed quantification of the roles of low-level moisture inflow, upper layer advection and convection in terms of the onset and progression of the Indian monsoon. Additionally, values for the timescale of convection have been derived, which aids understanding of the timing of monsoon processes and can be used to inform convective parameterisation schemes in the context of model development.

8.2   Wider implications

The onset and progression of the Indian monsoon has been investigated using the novel approach of combining and contrasting results from an idealised mathematical model of moisture dynamics and a numerical weather prediction model. Key physical processes and their effect on the monsoon onset have been quantified. The role of the dry intrusion as the main factor determining the northward extent of the monsoon has been examined. The balance between the mid-level dry intrusion with low-level moist inflow and vertical convective flux is shown to control the onset. It is demonstrated that the low-level moist inflow acts to moisten the lower troposphere, encouraging shallow convection and enabling the monsoon onset to propagate to the northwest. Here, it has been shown that these balances are indeed dynamically consistent with the observed (and modelled) monsoon state, and inferences have been drawn about the sensitivity of the onset to certain physical

processes. This is in support of previous research (Parker et al., 2016; Menon et al., 2018; Volonté et al., 2019).

A method of diagnosing and quantifying the convective timescale has been demonstrated for the WRF model, outlining how the controlling factors of monsoon onset can be assessed in practise and across other models. These methods could be used to evaluate how the monsoon might change in a future climate, or as a result of particular synoptic changes in weather patterns in a given year.

The use of an idealised, two-layer model is shown to have great value in helping to evaluate simulations with numerical weather prediction models, which can be very difficult to interpret. The combined approach allows the relative importance and contribution of several key processes to be investigated and quantified. Here, the method is applied to the onset and progression of the Indian monsoon, but a similar framework could be developed to evaluate other meteorological events and phenomena.

8.3 Future work

Ideas for further research, beyond the scope of this thesis, are presented below. The novel approach of using an idealised model to evaluate a numerical weather model, in the context of the Indian monsoon, can be developed further. The two-layer model would be improved by including additional parameters or processes, which could then be compared with the WRF model, increasing understanding of mechanisms regarding monsoon onset and informing the next stage of improvements to be considered to the idealised model. The methods presented here could be adapted for use in applications other than the Indian monsoon, and also for evaluating different numerical weather prediction models.

8.3.1 Idealised modelling approach

The next stage would reconsider the dynamic lower layer model, including terms or simple parameterisations to represent physical processes, quantifying their effect on monsoon onset in the context of the model and the implications for the real-world system. A suggested list of improvements to the two-layer model is given below

- Explicit treatment of precipitation. This could be achieved by including a parameter P, which is removed from the upper layer once some critical threshold of moisture is reached.

- Inclusion of surface processes. A responsive land-surface incorporating simple parameterisations of soil moisture and evaporation could help test theories regarding their effect on the advance of the monsoon onset. Furthermore, an explicit representation of evaporation could be linked to a prescribed latitudinal temperature profile.

- Considering other parameterisations of convection, particularly in relation to $q_1 + q_2$, which was shown to have a robust relationship with the convection flux. More complex parameterisations incorporating critical switch-ons could also be studied. It is not clear how convection should be parameterised within a two-layer framework. Note that parameterisations in the idealised model would still be much simpler than convective parameterisation schemes in numerical weather prediction models.

- Extending the model to be two-dimensional in space, so that $q_1(x, y, t)$ and $q_2(x, y, t)$. This would allow cross-front variations to be examined, for instance, curvature in the moisture front. The observed monsoon onset follows curved isochrones, as shown in Figure 1.1.

- Adding some radiative effects, such as local cloud feedbacks. These might also link to surface evaporation.

The model would be built in stages, towards the full moisture model described by Equations 3.1a–3.1c, increasing understanding of the effect of the processes added in each model iteration, interpreted in terms of the real-world monsoon. Inclusion of all the suggestions listed above would result in a model that remains much less complex than existing numerical weather prediction models. It would continue to be less expensive computationally and numerical solutions would be easy to implement.

8.3.2 Using numerical weather prediction models

Ideas for future research using the WRF model and/or other numerical weather prediction models are detailed below.

- Repeat the moisture budget analysis and subsequent derivation of convective timescale for other numerical weather prediction models. This would further verify the derived values of the convective timescale and build a more complete picture of the realistic time range.

- Make a more precise "parameterisation" of the convective flux (F_c) in terms of q_1 and q_2, going beyond the dependence on $q_1 - q_2$ and $q_1 + q_2$ that has already been considered. This could be used as input for the two-layer modelling work, and the resulting effects upon monsoon onset investigated.

- Examine simulations of the WRF model using different convective parametersation schemes, switching off shallow and/or deep convection where the scheme allows. Here, the (new) Tiedtke cumulus scheme has been selected, but the analysis could be repeated with the Kain-Fritsch scheme or the Betts-Miller-Janjic scheme, for example. The impact on the diagnosed convective flux would be inspected, and any systematic patterns (in terms of dependence of F_c on $q_1 - q_2$ or $q_1 + q_2$) would become evident.

- Conduct further analysis or devise experiments to derive the timescale of moisture replenishment at low-levels, T_m.

- Consider different domains over India, both larger and smaller, and the effect on the results of the moisture budget analysis.

The novel approach of using an idealised model to evaluate a numerical weather prediction model, in order to test aspects of the mechanisms behind the onset and propagation of the Indian monsoon, can be applied to increase understanding of other meteorological events. The methods developed within this thesis can be further refined and adapted beyond the context in which they are presented, with the aim of improving the representation of physical processes in numerical weather predication models.

Bibliography

Ashfaq, M., Rastogi, D., Mei, R., Touma, D., and Leung, L. R. (2017). Sources of errors in the simulation of south Asian summer monsoon in the CMIP5 GCMs. *Climate Dynamics*, 49(1-2):193–223.

Bamzai, A. S. and Shukla, J. (1999). Relation between Eurasian snow cover, snow depth, and the Indian summer monsoon: An observational study. *Journal of Climate*, 12(10):3117–3132.

Banacos, P. C. and Schultz, D. M. (2004). Moisture flux convergence: its history and application in convective initiation forecasting. In *22nd Conference on Severe Local Storms, 4-8th October 2004, Hyannis, Massachusetts, USA*.

Barton, E. J., Taylor, C. M., Parker, D. J., Turner, A. G., Belušić, D., Böing, S. J., Brooke, J. K., Harlow, R. C., Harris, P. P., Hunt, K., Jayakumar, A., and Mitra, A. K. (2019). A case-study of land–atmosphere coupling during monsoon onset in northern India. *Quarterly Journal of the Royal Meteorological Society*.

Basu, S., Iyengar, G. R., and Mitra, A. K. (2002). Impact of a Nonlocal Closure Scheme in a Simulation of a Monsoon System over India. *Monthly Weather Review*, 130(1):161–170.

Bechtold, P. (2015). Atmospheric moist convection. Lecture notes for ECMWF.

Beljaars, A. C. M. (1994). The parametrization of surface fluxes in large-scale models under free convection. *Quarterly Journal of the Royal Meteorological Society*, 121(522):255–270.

Birch, C. E., Parker, D. J., Marsham, J. H., Copsey, D., and Garcia-Carreras, L. (2014). A seamless assessment of the role of convection in the water cycle of the West African monsoon. *Journal of Geophysical Research: Atmospheres*, 119(6):2890–2912.

Birch, C. E., Roberts, M. J., Garcia-Carreras, L., Ackerley, D., Reeder, M. J., Lock, A. P., and Schiemann, R. (2015). Sea-breeze dynamics and convection initiation: the influence of convective parameterization in weather and climate model biases. *Journal of Climate*, 28(20):8093–8108.

Bollasina, M. A. and Benedict, S. (2004). The role of the Himalayas and the Tibetan Plateau within the Asian monsoon system. *Bulletin of the American Meteorological Society*, 85(7):1001–1004.

Bollasina, M. A. and Ming, Y. (2013a). The general circulation model precipitation bias over the southwestern equatorial Indian Ocean and its implications for simulating the South Asian monsoon. *Climate dynamics*, 40(3-4):823–838.

Bollasina, M. A. and Ming, Y. (2013b). The role of land-surface processes in modulating the Indian monsoon annual cycle. *Climate Dynamics*, 41(9):2497–2509.

Bollasina, M. A. and Nigam, S. (2011). The summertime "heat" low over Pakistan/northwestern India: evolution and origin. *Climate Dynamics*, 37(5):957–970.

Bombardi, R. J., Pegion, K. V., Kinter, J. L., Cash, B. A., and Adams, J. M. (2017). Sub-seasonal predictability of the onset and demise of the rainy season over monsoonal regions. *Frontiers in Earth Science*, 5:14.

Boos, W. R., Hurley, J. V., and Murthy, V. S. (2015). Adiabatic westward drift of Indian monsoon depressions. *Quarterly Journal of the Royal Meteorological Society*, 141(689):1035–1048.

Boos, W. R. and Kuang, Z. (2010). Dominant control of the South Asian monsoon by orographic insulation versus plateau heating. *Nature*, 463(7278):218–222.

Bordoni, S. and Schneider, T. (2008). Monsoons as eddy-mediated regime transitions of the tropical overturning circulation. *Nature Geoscience*, 1(8):515–519.

Bouchut, F., Lambaerts, J., Lapeyre, G., and Zeitlin, V. (2009). Fronts and nonlinear waves in a simplified shallow-water model of the atmosphere with moisture and convection. *Physics of Fluids*, 21(11):116604.

Cadet, D. and Ovarlez, H. (1976). Low-level air flow circulation over the Arabian Sea during the summer monsoon as deduced from satellite-tracked superpressure balloons. Part I: Balloon trajectories. *Quarterly Journal of the Royal Meteorological Society*, 102(434):805–816.

Chadwick, R., Good, P., Martin, G., and Rowell, D. P. (2015). Large rainfall changes consistently projected over substantial areas of tropical land. *Nature Climate Change*, 6(2):177–181.

Chakraborty, A., Nanjundiah, R. S., and Srinivasan, J. (2009). Impact of African orography and the Indian summer monsoon on the low-level Somali jet. *International Journal of Climatology*, 29(7):983–992.

Charnock, H. (1955). Wind stress on a water surface. *Quarterly Journal of the Royal Meteorological Society*, 81(350):639–640.

Chen, T. (2009). Monsoon depression: Formation mechanism, propagation property, water vapor budget, and its impact on the interannual variation of the northeast Indian monsoon rainfall (invited). *AGU Fall Meeting Abstracts*, 1:7. Provided by the SAO/NASA Astrophysics Data System.

Chou, C. (2003). Land-sea heating contrast in an idealized Asian summer monsoon. *Climate Dynamics*, 21(1):11–25.

Clark, C. O., Cole, J. E., and Webster, P. J. (2000). Indian Ocean SST and Indian summer rainfall: Predictive relationships and their decadal variability. *Journal of Climate*, 13(14):2503–2519.

Collins, M., AchutaRao, K., Ashok, K., Bhandari, S., Mitra, A. K., Prakash, S., Srivastava, R., and Turner, A. (2013). Observational challenges in evaluating climate models. *Nature Climate Change*, 3(11):940–941.

Collins, M., An, S.-I., Cai, W., Ganachaud, A., Guilyardi, E., Jin, F.-F., Jochum, M., Lengaigne, M., Power, S., Timmermann, A., Vecchi, G., and Wittenberg, A. (2010). The impact of global warming on the tropical Pacific Ocean and El Niño. *Nature Geoscience*, 3(6):391–397.

Copernicus Climate Change Service (2017). ERA5: Fifth generation of ECMWF atmospheric reanalyses of the global climate. *Copernicus Climate Change Service Climate Data Store (CDS)*. Accessed 05/05/2020. Available from: https://cds.climate.copernicus.eu/cdsapp#!/home.

Dearden, C. (2018). *Email to Lucy G. Recchia*, 26 november.

Dirmeyer, P. A., Cash, B. A., Kinter, J. L., Jung, T., Marx, L., Satoh, M., Stan, C., Tomita, H., Towers, P., Wedi, N., Achuthavarier, D., Adams, J. M., Altshuler, E. L., Huang, B., Jin, E. K., and Manganello, J. (2012). Simulating the diurnal cycle of rainfall in global climate models: Resolution versus parameterization. *Climate dynamics*, 39(1-2):399–418.

Douville, H. (2002). Influence of soil moisture on the Asian and African monsoons. Part II: Interannual variability. *Journal of Climate*, 15(7):701–720.

Douville, H., Chauvin, F., and Broqua, H. (2001). Influence of soil moisture on the asian and african monsoons. Part i: Mean monsoon and daily precipitation. *Journal of Climate*, 14(11):2381–2403.

Dudhia, J. (2019). *WRF Tutorial Presentations - Physics* [online]. Accessed 27/02/2020. Available from: https://www2.mmm.ucar.edu/wrf/users/supports/tutorial.html.

Dyer, A. J. and Hicks, B. B. (1970). Flux-gradient relationships in the constant flux layer. *Quarterly Journal of the Royal Meteorological Society*, 96(410):715–721.

Ethé, C., Basdevant, C., Sadourny, R., Appu, K., Harenduprakash, L., Sarode, P. R., and Viswanathan, G. (2002). Air mass motion, temperature, and humidity over the Arabian Sea and western Indian Ocean during the INDOEX intensive phase, as obtained from a set of superpressure drifting balloons. *Journal of Geophysical Research: Atmospheres*, 107(D19):2156–2202.

Fasullo, J. (2004). A stratified diagnosis of the Indian monsoon—Eurasian snow cover relationship. *Journal of Climate*, 17(5):1110–1122.

Fasullo, J. and Webster, P. J. (2003). A hydrological definition of Indian monsoon onset and withdrawal. *Journal of Climate*, 16(19):3200–3211.

Findlater, J. (1969). A major low-level air current near the Indian Ocean during the northern summer. *Quarterly Journal of the Royal Meteorological Society*, 95(404):362–380.

Findlater, J. (1974). The low-level cross-equatorial air current of the western Indian Ocean during the northern summer. *Weather*, 29(11):411–416.

Fitzpatrick, R. G. J., Bain, C. L., Knippertz, P., Marsham, J. H., and Parker, D. J. (2016a). On what scale can we predict the agronomic onset of the West African monsoon? *Monthly Weather Review*, 144(4):1571–1589.

Fitzpatrick, R. G. J., Parker, D. J., and Willetts, P. D. (2016b). Assessing the level of spatial homogeneity of the agronomic Indian monsoon onset. *Geophysical Research Letters*, 43(22).

Fletcher, J. K., Parker, D. J., Turner, A. G., Menon, A., Martin, G. M., Birch, C. E., Mitra, A. K., Mrudula, G., Hunt, K. M. R., Taylor, C. M., Houze, R. A., Brodzik, S. R., and Bhat, G. S. (2018). The dynamic and thermodynamic structure of the monsoon over southern India: New observations from the INCOMPASS IOP. *Quarterly Journal of the Royal Meteorological Society*.

Fornberg, B. (1998). *A Practical Guide to Pseudospectral Methods*. Cambridge University Press.

Friedl, M. A., McIver, D. K., Hodges, J. C. F., Zhang, X. Y., Muchoney, D., Strahler, A. H., Woodcock, C. E., Gopal, S., Schneider, A., Cooper, A., Baccini, A., Gao, F., and Schaaf, C. (2002). Global land cover mapping from MODIS: algorithms and early results. *Remote sensing of Environment*, 83(1-2):287–302.

Gadgil, S. (2003). The Indian monsoon and its variability. *Annual Review of Earth and Planetary Sciences*, 31(1):429–467.

Gadgil, S. and Gadgil, S. (2006). The Indian Monsoon, GDP and Agriculture. *Economic and Political Weekly*, 41(47):4887–4895.

Galvin, J. F. P. (2008). The weather and climate of the tropics: Part 6 - Monsoons. *Weather*, 63(5):129–137.

Gbode, I. E., Dudhia, J., Ogunjobi, K. O., and Ajayi, V. O. (2019). Sensitivity of different physics schemes in the WRF model during a West African monsoon regime. *Theoretical and Applied Climatology*, 136(1):733–751.

Geen, R., Bordoni, S., Battisti, D. S., and Hui, K. L. (2020). The Dynamics of the Global Monsoon: Connecting Theory and Observations. *Earth and Space Science Open Archive*, page 50.

George, G., Rao, D. N., Sabeerali, C. T., Srivastava, A., and Rao, S. A. (2016). Indian summer monsoon prediction and simulation in CFSv2 coupled model. *Atmospheric Science Letters*, 17(1):57–64.

Gilchrist, A. (1977). The simulation of the Asian summer monsoon by general circulation models. *pure and applied geophysics*, 115(5-6):1431–1448.

Gill, A. E. (1980). Some simple solutions for heat-induced tropical circulation. *Quarterly Journal of the Royal Meteorological Society*, 106(449):447–462.

Godbole, R. V. (1973). Numerical simulation of the Indian summer monsoon. *Indian Journal of Meteorology and Geophysics*, 24:1–14.

Goswami, B. B. and Goswami, B. N. (2017). A road map for improving dry-bias in simulating the South Asian monsoon precipitation by climate models. *Climate Dynamics*, 49(5-6):2025–2034.

Guinness World Records (2017). *Guinness World Records* [online]. Accessed 18/05/2017. Available from: http://www.guinnessworldrecords.com.

Hahn, D. G. and Manabe, S. (1975). The role of mountains in the South Asian monsoon circulation. *Journal of the Atmospheric Sciences*, 32(8):1515–1541.

Hahn, D. G. and Shukla, J. (1976). An apparent relationship between Eurasian snow cover and Indian monsoon rainfall. *Journal of Atmospheric Sciences*, 33(12):2461–2462.

Hannachi, A. and Turner, A. G. (2013). 20th century intraseasonal Asian monsoon dynamics viewed from Isomap. *Nonlinear Processes in Geophysics*, 20(5):725–741.

Hartley, A. J., Parker, D. J., Garcia-Carreras, L., and Webster, S. (2016). Simulation of vegetation feedbacks on local and regional scale precipitation in West Africa. *Agricultural and Forest Meteorology*, 222:59–70.

Holloway, C. E. and Neelin, J. D. (2009). Moisture Vertical Structure, Column Water Vapor, and Tropical Deep Convection. *Journal of the Atmospheric Sciences*, 66(6):1665–1683.

Holloway, C. E. and Neelin, J. D. (2010). Temporal Relations of Column Water Vapor and Tropical Precipitation. *Journal of the Atmospheric Sciences*, 67(4):1091–1105.

Holloway, C. E., Woolnough, S. J., and Lister, G. M. S. (2012). Precipitation distributions for explicit versus parametrized convection in a large-domain high-resolution tropical case study. *Quarterly Journal of the Royal Meteorological Society*, 138(668):1692–1708.

Hong, S.-Y. and Lim, J.-O. J. (2006). The WRF Single-Moment 6Class Microphysics Scheme (WSM6). *Journal of the Korean Meteorological Society*, 42(2):129–151.

Hong, S.-Y., Noh, Y., and Dudhia, J. (2006). A New Vertical Diffusion Package with an Explicit Treatment of Entrainment Processes. *Monthly Weather Review*, 134(9):2318–2341.

Hong, S.-Y. and Pan, H.-L. (1996). Nonlocal Boundary Layer Vertical Diffusion in a Medium-Range Forecast Model. *Monthly Weather Review*, 124(10):2322–2339.

Hoskins, B. J. and Rodwell, M. J. (1995). A model of the Asian summer monsoon. Part I: The global scale. *Journal of the Atmospheric Sciences*, 52(9):1329–1340.

Houze, Jr, R. A. (1982). Cloud clusters and large-scale vertical motions in the tropics. *Journal of the Meteorological Society of Japan*, 60(1):396–410.

Houze, Jr, R. A., Wilton, D. C., and Smull, B. F. (2007). Monsoon convection in the Himalayan region as seen by the TRMM precipitation radar. *Quarterly Journal of the Royal Meteorological Society*, 133(627):1389–1411.

Hunt, K. M. R. and Parker, D. J. (2016). The movement of Indian monsoon depressions by interaction with image vortices near the Himalayan wall. *Quarterly Journal of the Royal Meteorological Society*, 142(698):2224–2229.

Hunt, K. M. R., Turner, A. G., Inness, P. M., Parker, D. E., and Levine, R. C. (2016a). On the structure and dynamics of Indian monsoon depressions. *Monthly Weather Review*, 144(9):3391–3416.

Hunt, K. M. R., Turner, A. G., and Parker, D. E. (2016b). The spatiotemporal structure of precipitation in Indian monsoon depressions. *Quarterly Journal of the Royal Meteorological Society*, 142(701):3195–3210.

Hurley, J. V. and Boos, W. R. (2015). A global climatology of monsoon low-pressure systems. *Quarterly Journal of the Royal Meteorological Society*, 141(689):1049–1064.

Iacono, M. J., Delamere, J. S., Mlawer, E. J., Shephard, M. W., Clough, S. A., and Collins, W. D. (2008). Radiative forcing by long-lived greenhouse gases: Calculations with the AER radiative transfer models. *Journal of Geophysical Research: Atmospheres*, 113(D13).

India Meteorological Department (2016). *Government of India* [online]. Accessed 07/11/2016. Available from: http://www.imd.gov.in.

Jaswal, A. K., Singh, V., and Bhambak, S. R. (2012). Relationship between sea surface temperature and surface air temperature over Arabian Sea, Bay of Bengal and Indian Ocean. *Journal Indian Geophysical Union*, 16(2):41–53.

Jayakumar, A., Abel, S. J., Turner, A. G., Mohandas, S., Sethunadh, J., O'Sullivan, D., Mitra, A. K., and Rajagopal, E. N. (2019). Performance of the NCMRWF convection-permitting model during contrasting monsoon phases of 2016 INCOMPASS field campaign. *Quarterly Journal of the Royal Meteorological Society*.

Johnson, S. J., Turner, A., Woolnough, S., Martin, G., and MacLachlan, C. (2017). An assessment of Indian monsoon seasonal forecasts and mechanisms underlying monsoon interannual variability in the Met Office GloSea5-GC2 system. *Climate Dynamics*, 48(5-6):1447–1465.

Joseph, P. V. and Sijikumar, S. (2004). Intraseasonal variability of the low-level jet stream of the Asian summer monsoon. *Journal of Climate*, 17(7):1449–1458.

Joseph, P. V., Sooraj, K. P., and Rajan, C. K. (2016). The summer monsoon onset process over South Asia and an objective method for the date of monsoon onset over Kerala. *International Journal of Climatology*, 26(13):1871–1893.

Karmacharya, J., Levine, R. C., Jones, R., Moufouma-Okia, W., and New, M. (2015). Sensitivity of systematic biases in South Asian summer monsoon simulations to regional climate model domain size and implications for downscaled regional process studies. *Climate Dynamics*, 45(1):213–231.

Kelmanson, M. A. (2019). *Notes on partial differential equations, discussed with Lucy G. Recchia*, 19 July.

Kent, T., Bokhove, O., and Tobias, S. (2017). Dynamics of an idealized fluid model for investigating convective-scale data assimilation. *Tellus A: Dynamic Meteorology and Oceanography*, 69(1).

Kripalani, R. H., Kulkarni, A., and Sabade, S. S. (2003). Western Himalayan snow cover and Indian monsoon rainfall: A re-examination with INSAT and NCEP/NCAR data. *Theoretical and Applied Climatology*, 74(1):1–18.

Krishnamurthy, V. and Kirtman, B. P. (2003). Variability of the Indian Ocean: Relation to monsoon and ENSO. *Quarterly Journal of the Royal Meteorological Society*, 129(590):1623–1646.

Krishnamurti, T. N., Thomas, A., Simon, A., and Kumar, V. (2010). Desert air incursions, an overlooked aspect, for the dry spells of the Indian summer monsoon. *Journal of the Atmospheric Sciences*, 67(10):3423–3441.

Kumar, K. K., Hoerling, M., and Rajagopalan, B. (2005). Advancing dynamical prediction of indian monsoon rainfall. *Geophysical Research Letters*, 32(8).

Kumar, M. R. R. and Sadhuram, Y. (1989). Evaporation over the Arabian Sea during two contrasting monsoons. *Meteorology and Atmospheric Physics*, 41(2):87–97.

Kumar, S. P., Muraleedharan, P. M., Prasad, T. G., Gauns, M., Ramaiah, N., De Souza, S. N., Sardesai, S., and Madhupratap, M. (2002). Why is the Bay of Bengal less productive during summer monsoon compared to the Arabian sea? *Geophysical Research Letters*, 29(24).

Lau, K. M., Kim, K. M., and Yang, S. (2000). Dynamical and boundary forcing characteristics of regional components of the Asian summer monsoon. *Journal of Climate*, 13(14):2461–2482.

Lenton, T. M., Held, H., Kriegler, E., Hall, J. W., Lucht, W., Rahmstorf, S., and Schellnhuber, H. J. (2008). Tipping elements in the Earth's climate system. *Proceedings of the national Academy of Sciences*, 105(6):1786–1793.

Levine, R. C., Turner, A. G., Marathayil, D., and Martin, G. M. (2013). The role of northern Arabian Sea surface temperature biases in CMIP5 model simulations and future projections of Indian summer monsoon rainfall. *Climate dynamics*, 41(1):155–172.

Lim, E.-P. and Hendon, H. H. (2017). Causes and predictability of the negative Indian Ocean Dipole and its impact on La Niña during 2016. *Scientific reports*, 7(1):1–11.

Lu, B., Ren, H.-L., Scaife, A. A., Wu, J., Dunstone, N., Smith, D., Wan, J., Eade, R., MacLachlan, C., and Gordon, M. (2018). An extreme negative Indian Ocean Dipole event in 2016: dynamics and predictability. *Climate Dynamics*, 51(1–2):89–100.

Lucas-Picher, P., Christensen, J. H., Saeed, F., Kumar, P., Asharaf, S., Ahrens, B., Wiltshire, A. J., Jacob, D., and Hagemann, S. (2011). Can regional climate models represent the Indian monsoon? *Journal of Hydrometeorology*, 12(5):849–868.

Luo, H. and Yanai, M. (1983). The large-scale circulation and heat sources over the Tibetan Plateau and surrounding areas during the early summer of 1979. Part I: Precipitation and kinematic analyses. *Monthly Weather Review*, 111(5):922–944.

Luo, H. and Yanai, M. (1984). The large-scale circulation and heat sources over the Tibetan Plateau and surrounding areas during the early summer of 1979. Part II: Heat and moisture budgets. *Monthly Weather Review*, 112(5):966–989.

Maheskumar, R. S., Narkhedkar, S. G., Morwal, S. B., Padmakumari, B., Kothawale, D. R., Joshi, R. R., Deshpande, C. G., Bhalwankar, R. V., and Kulkarni, J. R. (2014). Mechanism of high rainfall over the Indian west coast region during the monsoon season. *Climate dynamics*, 43(5-6):1513–1529.

Martin, G. M., Brooks, M. E., Johnson, B., Milton, S. F., Webster, S., Jayakumar, A., Mitra, A. K., Rajan, D., and Hunt, K. M. R. (2019). Forecasting the monsoon on daily to seasonal time-scales in support of a field campaign. *Quarterly Journal of the Royal Meteorological Society*.

Martin, G. M., Klingaman, N. P., and Moise, A. F. (2017). Connecting spatial and temporal scales of tropical precipitation in observations and the MetUM-GA6. *Geoscientific Model Development*, 10(1):105.

Martin, G. M., Milton, S. F., Senior, C. A., Brooks, M. E., Ineson, S., Reichler, T., and Kim, J. (2010). Analysis and Reduction of Systematic Errors Through a Seamless Approach to Modeling Weather and Climate. *Journal of Climate*, 23(22):5933–5957.

Masunaga, H. and Sumi, Y. (2017). A toy model of tropical convection with a moisture storage closure. *Journal of Advances in Modeling Earth Systems*, 9(1):647–667.

McColl, K. A., Alemohammad, S. H., Akbar, R., Konings, A. G., Yueh, S., and Entekhabi, D. (2017). The global distribution and dynamics of surface soil moisture. *Nature Geoscience*, 10(2):100–104.

McGregor, G. R. and Nieuwolt, S. (1998). *Tropical climatology: an introduction to the climates of the low latitudes.* John Wiley & Sons Ltd, Chichester, England, 2 edition.

Medina, S., Houze, R. A., Kumar, A., and Niyogi, D. (2010). Summer monsoon convection in the Himalayan region: Terrain and land cover effects. *Quarterly Journal of the Royal Meteorological Society*, 136(648):593–616.

Menon, A., Turner, A. G., Martin, G., and MacLachlan, C. (2018). Modelling the moistening of the free troposphere during the northwestward progression of Indian monsoon onset (accepted). *Quarterly Journal of the Royal Meteorological Society*.

Mishra, V., Kumar, D., Ganguly, A. R., Sanjay, J., Mujumdar, M., Krishnan, R., and Shah, R. D. (2014). Reliability of regional and global climate models to simulate precipitation extremes over India. *Journal of Geophysical Research: Atmospheres*, 119(15):9301–9323.

Mitra, A. K., Bohra, A. K., Rajeevan, M. N., and Krishnamurti, T. N. (2009). Daily Indian Precipitation Analysis Formed from a Merge of Rain-Gauge Data with the TRMM TMPA Satellite-Derived Rainfall Estimates. *Journal of the Meteorological Society of Japan*, 87A:265–279.

Mitra, A. K., Momin, I. M., Rajagopal, E. N., Basu, S., Rajeevan, M. N., and Krishnamurti, T. N. (2013). Gridded daily Indian monsoon rainfall for 14 seasons: Merged TRMM and IMD gauge analyzed values. *Journal of Earth System Science*, 122(5):1173–1182.

Monin, A. S. and Obukhov, A. M. (1954). Osnovnye zakonomernosti turbulentnogo peremeshivanija v prizemnom sloe atmosfery (basic laws of turbulent mixing in the atmosphere near the ground). *Akademii Nauk SSSR Geofizicheskii Institut Trudy*, 24(151):163–187.

Muller, C. J., Back, L. E., O'Gorman, P. A., and Emanuel, K. A. (2009). A model for the relationship between tropical precipitation and column water vapor. *Geophysical Research Letters*, 36(16).

Muller, C. J. and O'Gorman, P. A. (2011). An energetic perspective on the regional response of precipitation to climate change. *Nature Climate Change*, 1(5):266–271.

National Center for Atmospheric Research (2020). *WPS V4 Geographical Static Data Downloads Page* [online]. Accessed 23/03/2020. Available from: https://www2.mmm.ucar.edu/wrf/users/download/.

National Centers for Environmental Prediction, National Weather Service, National Oceanic and Atmospheric Administration, and U.S. Department of Commerce (2015). NCEP GDAS/FNL 0.25 Degree Global Tropospheric Analyses and Forecast Grids. *Research Data Archive at the National Center for Atmospheric Research, Computational and Information Systems Laboratory.* Accessed 15/11/2019. Available from: https://doi.org/10.5065/D65Q4T4Z.

Neelin, J. D., Peters, O., and Hales, K. (2009). The transition to strong convection. *Journal of the Atmospheric Sciences*, 66(8):2367–2384.

Nieuwolt, S. (1977). *Tropical climatology.* John Wiley & Sons Ltd.

Noh, Y., Cheon, W. G., Hong, S. Y., and Raasch, S. (2003). Improvement of the K-profile Model for the Planetary Boundary Layer based on Large Eddy Simulation Data. *Boundary-layer meteorology*, 107(2):401–427.

O'Gorman, P. A. (2015). Precipitation extremes under climate change. *Current climate change reports*, 1(2):49–59.

Otkin, J. A. and Greenwald, T. J. (2008). Comparison of WRF Model-Simulated and MODIS-Derived Cloud Data. *Monthly Weather Review*, 136(6):1957–1970.

Park, S. and Hong, S.-Y. (2004). The role of surface boundary forcing over south Asia in the Indian summer monsoon circulation: A regional climate model sensitivity study. *Geophysical Research Letters*, 31(12).

Parker, D. J., Willetts, P., Birch, C., Turner, A. G., Marsham, J. H., Taylor, C. M., Kolusu, S., and Martin, G. M. (2016). The interaction of moist convection and mid-level dry air in the advance of the onset of the Indian monsoon. *Quarterly Journal of the Royal Meteorological Society*, 142(699):2256–2272.

Paulson, C. A. (1970). The Mathematical Representation of Wind Speed and Temperature Profiles in the Unstable Atmospheric Surface Layer. *Journal of Applied Meteorology*, 9(6):857–861.

Pilon, R., Zhang, C., and Dudhia, J. (2016). Roles of deep and shallow convection and microphysics in the MJO simulated by the Model for Prediction Across Scales. *Journal of Geophysical Research: Atmospheres*, 121(18):10–575.

Powers, J. G., Klemp, J. B., Skamarock, W. C., Davis, C. A., Dudhia, J., Gill, D. O., Coen, J. L., Gochis, D. J., Ahmadov, R., Peckham, S. E., Grell, G. A., Michalakes, J., Trahan, S., Benjamin, S. G., Alexander, C. R., Dimego, G. J., Wang, W., Schwartz, C. S., Romine, G. S., Liu, Z., Snyder, C., Chen, F., Barlage, M. J., Yu, W., and Duda, M. G. (2017). The Weather Research and Forecasting Model: Overview, System Efforts, and Future Directions. *Bulletin of the American Meteorological Society*, 98(8):1717–1737.

Privé, N. C. and Plumb, R. A. (2007a). Monsoon Dynamics with Interactive Forcing. Part I: Axisymmetric Studies. *Journal of the Atmospheric Sciences*, 64(5):1417–1430.

Privé, N. C. and Plumb, R. A. (2007b). Monsoon Dynamics with Interactive Forcing. Part II: Impact of Eddies and Asymmetric Geometries. *Journal of the Atmospheric Sciences*, 64(5):1431–1442.

Rácz, Z. and Smith, R. K. (1999). The dynamics of heat lows. *Quarterly Journal of the Royal Meteorological Society*, 125(553):225–252.

Rajeevan, M., Gadgil, S., and Bhate, J. (2010). Active and break spells of the Indian summer monsoon. *Journal of Earth System Science*, 119(3):229–247.

Raju, P. V. S., Mohanty, U. C., and Bhatla, R. (2005). Onset characteristics of the southwest monsoon over India. *International journal of climatology*, 25(2):167–182.

Rao, K. G. and Goswami, B. N. (1988). Interannual variations of sea surface temperature over the Arabian Sea and the Indian monsoon: A new perspective. *Monthly Weather Review*, 116(3):558–568.

Rodwell, M. J. (1993). *Dynamics of the Indian Monsoon*. PhD thesis, University of Reading.

Rodwell, M. J. and Hoskins, B. J. (1995). A model of the Asian summer monsoon. Part II: Cross-equatorial flow and PV behavior. *Journal of the Atmospheric Sciences*, 52(9):1341–1356.

Romatschke, U., Medina, S., and Houze Jr., R. A. (2010). Regional, Seasonal, and Diurnal Variations of Extreme Convection in the South Asian region. *Journal of Climate*, 23(2):419–439.

Sadhuram, Y. and Kumar, M. R. R. (1988). Does evaporation over the Arabian Sea play a crucial role in moisture transport across the West coast of India during an active monsoon period? *Monthly Weather Review*, 116(2):307–312.

Saha, K. (1970). Air and water vapour transport across the equator in western Indian Ocean during northern summer. *Tellus*, 22(6):681–687.

Sahana, A. S., Pathak, A., Roxy, M. K., and Ghosh, S. (2018). Understanding the role of moisture transport on the dry bias in indian monsoon simulations by CFSv2. *Climate Dynamics*, pages 1–15.

Saini, R., Barlow, M., and Hoell, A. (2011). Dynamics and thermodynamics of the regional response to the Indian monsoon onset. *Journal of Climate*, 24(22):5879–5886.

Schewe, J., Levermann, A., and Cheng, H. (2012). A critical humidity threshold for monsoon transitions. *Climate of the Past*, 8(2):535–544.

Schiro, K. A. and Neelin, J. D. (2019). Deep Convective Organization, Moisture Vertical Structure, and Convective Transition Using Deep-Inflow Mixing. *Journal of the Atmospheric Sciences*, 76(4):965–987.

Schneider, T., Bischoff, T., and Haug, G. H. (2014). Migrations and dynamics of the intertropical convergence zone. *Nature*, 513:45–53.

Seager, R. and Henderson, N. (2013). Diagnostic Computation of Moisture Budgets in the ERA-Interim Reanalysis with Reference to Analysis of CMIP-Archived Atmospheric Model Data. *Journal of Climate*, 26(20):7876–7901.

Shamrock, W. C., Klemp, J. B., Dudhia, J., Gill, D. O., Liu, Z., Berner, J., Wang, W., Powers, J. G., Duda, M. G., Barker, D. M., and Huang, X.-Y. (2019). A Description of the Advanced Research WRF Model Version 4. Technical report, National Center for Atmospheric Research, Boulder, Colorado, USA. NCAR/TN-556+STR.

Shenoi, S. S. C., Shankar, D., and Shetye, S. R. (2002). Differences in heat budgets of the near-surface Arabian Sea and Bay of Bengal: Implications for the summer monsoon. *Journal of Geophysical Research: Oceans*, 107(C6):5–1–5–14.

Shepherd, T. J. and Walsh, K. J. (2017). Sensitivity of hurricane track to cumulus parameterization schemes in the WRF model for three intense tropical cyclones: impact of convective asymmetry. *Meteorology and Atmospheric Physics*, 129(4):345–374.

Shukla, J. (1975). Effect of Arabian Sea-surface temperature anomaly on Indian summer monsoon: A numerical experiment with the GFDL model. *Journal of the Atmospheric Sciences*, 32(3):503–511.

Shukla, J. and Misra, B. M. (1977). Relationships between sea surface temperature and wind speed over the central Arabian Sea, and monsoon rainfall over India. *Monthly Weather Review*, 105(8):998–1002.

Sperber, K. R., Annamalai, H., Kang, I.-S., Kitoh, A., Moise, A., Turner, A., Wang, B., and Zhou, T. (2013). The asian summer monsoon: an intercomparison of CMIP5 vs. CMIP3 simulations of the late 20th century. *Climate Dynamics*, 41(9-10):2711–2744.

Sperber, K. R. and Palmer, T. N. (1996). Interannual tropical rainfall variability in general circulation model simulations associated with the Atmospheric Model Intercomparison Project. *Journal of Climate*, 9(11):2727–2750.

Sperber, K. R., Slingo, J. M., and Annamalai, H. (2000). Predictability and the relationship between subseasonal and interannual variability during the Asian summer monsoon. *Quarterly Journal of the Royal Meteorological Society*, 126(568):2545–2574.

Srinivasan, J. (2001). A simple thermodynamic model for seasonal variation of monsoon rainfall. *Current Science*, 80(1):73–77.

Stensrud, D. J. (2009). *Parameterization Schemes: Keys to Understanding Numerical Weather Prediction Models*. Cambridge University Press.

Stephens, G. L., L'Ecuyer, T., Forbes, R., Gettlemen, A., Golaz, J.-C., Bodas-Salcedo, A., Suzuki, K., Gabriel, P., and Haynes, J. (2010). Dreary state of precipitation in global models. *Journal of Geophysical Research: Atmospheres*, 115(D24).

Subrahmanyam, M. V., Murty, K. P. R. V., and Pushpanjali, B. (2014). Sea Surface Temperature and Findlater Jet Variations over Arabian Sea During Summer Monsoon. *Journal of Climatology & Weather Forecasting*, 2(2).

Sun, B.-Y. and Bi, X.-Q. (2019). Validation for a tropical belt version of WRF: sensitivity tests on radiation and cumulus convection parameterizations. *Atmospheric and Oceanic Science Letters*, 12(3):192–200.

Taylor, C. M., Gounou, A., Guichard, F., Harris, P. P., Ellis, R. J., Couvreux, F., and De Kauwe, M. (2011). Frequency of Sahelian storm initiation enhanced over mesoscale soil-moisture patterns. *Nature Geoscience*, 4(7):430–433.

Taylor, C. M., Parker, D. J., and Harris, P. P. (2007). An observational case study of mesoscale atmospheric circulations induced by soil moisture. *Geophysical Research Letters*, 34(15).

Tewari, M., Chen, F., Wang, W., Dudhia, J., LeMone, M. A., Mitchell, K., Ek, M., Gayno, G., Wegiel, J., and Cuenca, R. H. (2004). Implementation and verification of the unified Noah land surface model in the WRF model (Formerly Paper Number 17.5). In *Proceedings of the 20th Conference on Weather Analysis and Forecasting/16th Conference on Numerical Weather Prediction, 12-15th January 2004, Seattle, Washington, USA*.

The GLOBE Task Team, Hastings, D. A., Dunbar, P. K., Elphingstone, G. M., Bootz, M., Murakami, H., Maruyama, H., Masaharu, H., Holland, P., Payne, J., Bryant, N. A., Logan, T. L., Muller, J. P., Schreier, G., and MacDonald, J. S. (1999). The Global Land One-kilometer Base Elevation (GLOBE) Digital Elevation Model, Version 1.0. *National Oceanic and Atmospheric Administration, National Geophysical Data Center*. Accessed 30/03/2020. Available from: http://www.ngdc.noaa.gov/mgg/topo/globe.html.

Tompkins, A. M. and Craig, G. C. (1998). Time-scales of adjustment to radiative-convective equilibrium in the tropical atmosphere. *Quarterly Journal of the Royal Meteorological Society*, 124(552):2693–2713.

Troen, I. B. and Mahrt, L. (1986). A simple model of the atmospheric boundary layer; sensitivity to surface evaporation. *Boundary-Layer Meteorology*, 37(1):129–148.

Turner, A. G. and Annamalai, H. (2012). Climate change and the South Asian summer monsoon. *Nature Climate Change*, 2(8):587–595.

Turner, A. G., Bhat, G. S., Martin, G. M., Parker, D. J., Taylor, C. M., Mitra, A. K., Tripathi, S. N., Milton, S., Rajagopal, E. N., Evans, J. G., Morrison, R., Pattnaik, S., Sekhar, M., Bhattacharya, B. K., Madan, R., Govindankutty, M., Fletcher, J. K., Willetts, P. D., Menon, A., Marsham, J. H., the INCOMPASS team, Hunt, K. M. R., Chakraborty, T., George, G., Krishnan, M., Sarangi, C., Belušić, D., Garcia-Carreras, L., Brooks, M., Webster, S., Brooke, J. K., Fox, C., Harlow, R. C., Langridge, J. M., Jayakumar, A., Böing, S. J., Halliday, O., Bowles, J., Kent, J., O'Sullivan, D., Wilson, A., Woods, C., Rogers, S., Smout-Day, R., Tiddeman, D., Desai, D., Nigam, R., Paleri, S., Sattar, A., Smith, M., Anderson, D., Bauguitte, S., Carling, R., Chan, C., Devereau, S., Gratton, G., MacLeod, D., Nott, G., Pickering, M., Price, H., Rastall, S., Reed, C., Trembath, J., Woolley, A., Volonté, A., and New, B. (2019). Interaction of convective organization with monsoon precipitation, atmosphere, surface and sea: The 2016 INCOMPASS field campaign in India. *Quarterly Journal of the Royal Meteorological Society*.

University Corporation for Atmospheric Research (2020). *WRF-ARW Online Tutorial* [online]. Accessed 26/02/2020. Available from: https://www2.mmm.ucar.edu/wrf/OnLineTutorial/index.php.

Vecchi, G. A. and Harrison, D. E. (2004). Interannual Indian Rainfall Variability and Indian Ocean Sea Surface Temperature Anomalies. *Earth's Climate*, pages 247–259.

Volonté, A., Turner, A. G., and Menon, A. (2019). Airmass analysis of the processes driving the progression of the Indian summer monsoon. *Quarterly Journal of the Royal Meteorological Society*.

Walker, J. M. (1972). The monsoon of Southern Asia: A review. *Weather*, 27(5):178–189.

Walker, J. M., Bordoni, S., and Schneider, T. (2015). Interannual Variability in the Large-Scale Dynamics of the South Asian Summer Monsoon. *Journal of Climate*, 28(9):3731–3750.

Wallace, J. M. and Hobbs, P. V. (2006). *Atmospheric Science: An Introductory Survey*, volume 92. Elsevier.

Wang, W., Bruyère, C., Duda, M., Dudhia, J., Gill, D., Kavulich, M., Werner, K., Chen, M., Lin, H.-C., Michalakes, J., Rizvi, S., Zhang, X., Berner, J., Munoz-Esparza, D., Reen, B., Ha, S., and Fossell, K. (2019). *ARW Version 4 Modelling System User's Guide.* National Center for Atmospheric Research, Boulder, Colorado, USA.

Webb, E. K. (1970). Profile relationships: The log-linear range, and extension to strong stability. *Quarterly Journal of the Royal Meteorological Society*, 96(407):67–90.

Webster, P. J. and Chou, L. C. (1980). Seasonal structure of a simple monsoon system. *Journal of the Atmospheric Sciences*, 37(2):354–367.

Willetts, P. D., Marsham, J. H., Birch, C. E., Parker, D. J., Webster, S., and Petch, J. (2017). Moist convection and its upscale effects in simulations of the Indian monsoon with explicit and parametrized convection. *Quarterly Journal of the Royal Meteorological Society*, 143(703):1073–1085.

Yanai, M., Esbensen, S., and Chu, J.-H. (1973). Determination of bulk properties of tropical cloud clusters from large-scale heat and moisture budgets. *Journal of the Atmospheric Sciences*, 30(4):611–627.

Yang, D.-S. and Krishnamurti, T. N. (1981). Potential vorticity of monsoonal low-level flows. *Journal of the Atmospheric Sciences*, 38(12):2676–2695.

Yoon, J.-H. and Chen, T.-C. (2005). Water vapor budget of the Indian monsoon depression. *Tellus A*, 57(5):770–782.

Zangvil, A., Portis, D. H., and Lamb, P. J. (2001). Investigation of the large-scale atmospheric moisture field over the midwestern United States in relation to summer precipitation. Part I: Relationships between moisture budget components on different timescales. *Journal of climate*, 14(4):582–597.

Zhang, C. and Wang, Y. (2017). Projected Future Changes of Tropical Cyclone Activity over the Western North and South Pacific in a 20-km-Mesh Regional Climate Model. *Journal of Climate*, 30(15):5923–5941.

Zhang, C., Wang, Y., and Hamilton, K. (2011). Improved Representation of Boundary Layer Clouds over the Southeast Pacific in ARW-WRF Using a Modified Tiedtke Cumulus Parameterization Scheme. *Monthly Weather Review*, 139(11):3489–3513.

Zhang, D. and Anthes, R. A. (1982). A High-Resolution Model of the Planetary Boundary Layer—Sensitivity Tests and Comparisons with SESAME-79 Data. *Journal of Applied Meteorology*, 21(11):1594–1609.

Zhang, Z., Chan, J. C. L., and Ding, Y. (2004). Characteristics, evolution and mechanisms of the summer monsoon onset over Southeast Asia. *International Journal of Climatology*, 24(12):1461–1482.

Appendix A

Solving the dynamic lower layer system analytically

An attempt is made to solve the system of partial differential equations, 5.1a, 5.1b (repeated here for convenience), analytically, with $\Phi = 1$. The variable of most interest is the upper layer moisture, $q_2(t, x)$, hence solution for $q_2(t, x)$ is sought first. Then, a solution for the lower layer moisture, $q_1(t, x)$, can be derived.

$$\frac{\partial q_2}{\partial t} + u_2 \frac{\partial q_2}{\partial x} = +\frac{1}{T_c}(q_1 - q_2), \tag{5.1a}$$

$$\frac{\partial q_1}{\partial t} = -\frac{1}{T_c}(q_1 - q_2) - \frac{1}{T_m}(q_1 - q_e). \tag{5.1b}$$

To begin, Equation 5.1a is rearranged in terms of q_1. Expressions for q_1 and $\partial q_1/\partial t$ can then be substituted into Equation 5.1b, thus eliminating q_1.

$$q_1 = \left(\frac{\partial q_2}{\partial t} + u_2 \frac{\partial q_2}{\partial x} \right) T_c + q_2, \tag{A.2}$$

$$\frac{\partial q_1}{\partial t} = \left(\frac{\partial^2 q_2}{\partial t^2} + u_2 \frac{\partial^2 q_2}{\partial t \partial x} \right) T_c + \frac{\partial q_2}{\partial t}. \tag{A.3}$$

On simplifying, there is a second order partial differential equation for q_2 in two variables (t, x), where $q_e = q_e(x)$.

$$\frac{\partial^2 q_2}{\partial t^2} + u_2 \frac{\partial^2 q_2}{\partial t \partial x} + \frac{\partial q_2}{\partial t} \left(\frac{2}{T_c} + \frac{1}{T_m} \right) + u_2 \frac{\partial q_2}{\partial x} \left(\frac{1}{T_c} + \frac{1}{T_m} \right) + \frac{q_2}{T_c T_m} = \frac{q_e(x)}{T_c T_m}. \tag{A.4}$$

Equation A.4 has constant coefficients (u_2, T_c, T_m) and is non-homogeneous. Considering the coefficients of the second order derivatives, it can be seen that Equation A.4 is hyperbolic, as $b^2 - ac = u_2^2 > 0$, where a is the coefficient of $\partial^2 q_2/\partial t^2$, b is the coefficient of $\partial^2 q_2/\partial t \partial x$ and c is the coefficient of $\partial^2 q_2/\partial x^2$.

Using the method of characteristics, the roots of $as^2 - bs + c = 0$ are found, where a, b, c are the coefficients of the second order derivatives, as before. Two distinct real roots emerge, $s_+ = 0$ (positive root) and $s_- = u_2$ (negative root). The aim is to employ a change of variables $X, Y = x - s_{+,-}t$, in order to reduce the number of second order

221

derivatives in Equation A.4.

$$X = x - u_2 t, \tag{A.5a}$$

$$Y = x. \tag{A.5b}$$

Calculating the derivatives with the change of variables defined in Equations A.5a, A.5b:

$$\frac{\partial q_2}{\partial t} = \frac{\partial q_2}{\partial X}\frac{\partial X}{\partial t} + \frac{\partial q_2}{\partial Y}\frac{\partial Y}{\partial t} = -u_2\frac{\partial q_2}{\partial X},$$

$$\frac{\partial q_2}{\partial x} = \frac{\partial q_2}{\partial X}\frac{\partial X}{\partial x} + \frac{\partial q_2}{\partial Y}\frac{\partial Y}{\partial x} = \frac{\partial q_2}{\partial X} + \frac{\partial q_2}{\partial Y},$$

$$\frac{\partial^2 q_2}{\partial t^2} = u_2^2\frac{\partial^2 q_2}{\partial X^2},$$

$$\frac{\partial^2 q_2}{\partial t\partial x} = -u_2\left(\frac{\partial^2 q_2}{\partial X^2} + \frac{\partial^2 q_2}{\partial X\partial Y}\right).$$

Thus Equation A.4 is transformed to Equation A.6, the canonical form, which contains only the mixed derivative and lower order terms.

$$\frac{\partial^2 q_2}{\partial X\partial Y} + \frac{1}{u_2}\frac{\partial q_2}{\partial X}\left(\frac{1}{T_c}\right) - \frac{1}{u_2}\frac{\partial q_2}{\partial Y}\left(\frac{1}{T_c} + \frac{1}{T_m}\right) - \frac{q_2}{u_2^2 T_c T_m} = -\frac{q_e(Y)}{u_2^2 T_c T_m}. \tag{A.6}$$

This can be simplified further, removing the first order derivatives. Let $q_2 = re^{-(\beta X + \alpha Y)}$, where β is the coefficient of $\partial q_2/\partial Y$ and α is the coefficient of $\partial q_2/\partial X$.

$$\alpha = \frac{1}{u_2}\left(\frac{1}{T_c}\right),$$

$$\beta = -\frac{1}{u_2}\left(\frac{1}{T_c} + \frac{1}{T_m}\right),$$

$$q_2 = re^{-(\beta X + \alpha Y)},$$

$$\frac{\partial q_2}{\partial X} = \left(\frac{\partial r}{\partial X} - \beta r\right)e^{-(\beta X + \alpha Y)},$$

$$\frac{\partial q_2}{\partial Y} = \left(\frac{\partial r}{\partial Y} - \alpha r\right)e^{-(\beta X + \alpha Y)},$$

$$\frac{\partial^2 q_2}{\partial X\partial Y} = \left(\frac{\partial^2 r}{\partial X\partial Y} - \alpha\frac{\partial r}{\partial X} - \beta\frac{\partial r}{\partial Y} + \alpha\beta r\right)e^{-(\beta X + \alpha Y)}.$$

Substituting these terms into Equation A.6 gives:

$$\frac{\partial^2 r}{\partial X\partial Y} + \frac{r}{u_2^2 T_c^2} = -\frac{q_e(Y)\cdot e^{(\beta X + \alpha Y)}}{u_2^2 T_c T_m}, \quad \text{where} \quad \begin{cases} \alpha = \dfrac{1}{u_2}\left(\dfrac{1}{T_c}\right), \\[2mm] \beta = -\dfrac{1}{u_2}\left(\dfrac{1}{T_c} + \dfrac{1}{T_m}\right). \end{cases} \tag{A.8}$$

To construct a Green's function for $r(X, Y; \xi, \eta)$, it is required that:

(i) $\dfrac{\partial^2}{\partial X \partial Y} + \dfrac{r}{u_2^2 T_c^2} = 0,$ (A.9a)

(ii) $\dfrac{\partial r}{\partial X} = 0$ on $Y = \eta,$ (A.9b)

(iii) $\dfrac{\partial r}{\partial Y} = 0$ on $X = \xi,$ (A.9c)

(iv) $r = 1$ at $(\xi, \eta).$ (A.9d)

Following notes by Kelmanson (2019), a new independent variable is taken,
$z = k\left[(X - \xi)(Y - \eta)\right]^m$, where k and m are to be determined. Then:

$$\frac{\partial r}{\partial X} = mk(X - \xi)^{m-1}(Y - \eta)^m \frac{dr}{dz},$$

$$\frac{\partial r}{\partial Y} = mk(X - \xi)^m(Y - \eta)^{m-1} \frac{dr}{dz},$$

$$\frac{\partial^2 r}{\partial X \partial Y} = m^2 k^2 (X - \xi)^{2m-1}(Y - \eta)^{2m-1} \frac{d^2 r}{dz^2} + m^2 k (X - \xi)^{m-1}(Y - \eta)^{m-1} \frac{dr}{dz}.$$

These expressions can be simplified by choosing $m = 1/2$, so
$z = k\left[(X - \xi)(Y - \eta)\right]^{1/2}$. Substituting these derivatives into the homogeneous form of
Equation A.8:

$$\frac{k^2}{4} \frac{d^2 r}{dz^2} + \frac{k^2}{4z} \frac{dr}{dz} + \frac{r}{u_2^2 T_c^2} = 0.$$

Now putting $k = \dfrac{2}{u_2 T_c}$, the expression becomes Bessel's equation.

$$\frac{d^2 r}{dz^2} + \frac{1}{z} \frac{dr}{dz} + r = 0. \tag{A.10}$$

The solution to Bessel's equation (A.10) is $r = J_0(z)$, where $z = \dfrac{2}{u_2 T_c}\left[(X - \xi)(Y - \eta)\right]^{1/2}$.
Thus, the complementary solution to Equation A.8 is:

$$r_c = J_0\left[\frac{2}{u_2 T_c}(X - \xi)^{1/2}(Y - \eta)^{1/2}\right]. \tag{A.11}$$

To find the particular integral, r_p, for Equation A.8, a function $r_p = pe^{(\beta X + \alpha Y)}$ is tried,
where p is to be determined. Substituting r_p for r in Equation A.8, which can be rearranged
to determine an expression for p, and thus the particular integral, r_p can be written.

$$p = \frac{-q_e(Y) T_c}{T_m\left(u_2^2 T_c^2 + 1\right)},$$

$$r_p = \frac{-q_e(Y) T_c}{T_m\left(u_2^2 T_c^2 + 1\right)} e^{(\beta X + \alpha Y)}. \tag{A.12}$$

The general solution to Equation A.8, by the Principle of Superposition ($r = r_c + r_p$), is then:

$$r(X,Y;\xi,\eta) = J_0\left[\frac{2}{u_2 T_c}(X - \xi)^{1/2}(Y - \eta)^{1/2}\right] - \frac{q_e(Y)T_c}{T_m\left(u_2^2 T_c^2 + 1\right)}e^{(\beta X + \alpha Y)},$$

(A.13)

$$\text{where} \quad \alpha = \frac{1}{u_2}\left(\frac{1}{T_c}\right) \quad \text{and} \quad \beta = \frac{1}{u_2}\left(\frac{1}{T_c} + \frac{1}{T_m}\right).$$

Recalling that $q_2 = re^{(\beta X + \alpha Y)}$, $X = x - u_2 t$ and $Y = x$, the general solution is rewritten in terms of the original variables (t, x). From Equation A.2, an expression for q_1 can be derived. Thus, the general solution for the system of equations 5.1a, 5.1b, for q_2 and q_1 is:

$$q_2(t,x;\xi,\eta) = J_0(z)e^{-(\beta t + \alpha x)} - \frac{q_e(x)T_c}{T_m\left(u_2^2 T_c^2 + 1\right)},$$

(A.14a)

$$q_1(t,x;\xi,\eta) = T_c e^{-(\beta t + \alpha x)}\left[\left(\frac{1}{T_c} - \beta - \alpha\right)J_0(z) + \frac{\partial J_0(z)}{\partial t} + u_2\frac{\partial J_0(z)}{\partial x}\right]$$

$$+ \frac{T_c\left(u_2 T_c q_e'(x) - q_e(x)\right)}{T_m\left(u_2^2 T_c^2 + 1\right)},$$

(A.14b)

$$\text{where} \quad z = \frac{2}{u_2 T_c}(t - \xi)^{1/2}(x - \eta)^{1/2}, \quad \alpha = \frac{1}{u_2}\left(\frac{1}{T_c}\right) \quad \text{and} \quad \beta = \frac{1}{u_2}\left(\frac{1}{T_c} + \frac{1}{T_m}\right).$$

Note that this analysis is incomplete as boundary and initial conditions have not been taken into account. For instance, it should be that $q_2 = 0$ at $x = 0$, which is not clear from Equation A.14a. This appendix in intended to give an idea of how the dynamic lower layer system might be solved, rather than providing explicit solutions.

Appendix B

Boundary layer solutions

In order to satisfy the lateral boundary condition on the upper layer, a solution for the boundary layer region close to $x = 0$ must also be determined. This "inner" solution is matched with the "outer" solution derived in Subsection 5.2.1 (Equations 5.6a–5.6b), to give a complete description of the system's early state, satisfying all boundary and initial conditions (Equations 5.3a–5.3c).

A small parameter ε is introduced, where $\varepsilon \ll 1$. It can be seen empirically that the width of the boundary layer near $x = 0$ is proportional to time, so x and t can be rewritten with the expressions $X = x/\varepsilon$ and $T = t/\varepsilon$. Firstly, this scaling in ε is applied to t only, since this should be an alternative way of deriving the standard outer solution. Then, the scaling is applied to both t and x to find the inner solution.

Scaling in t

Rewriting the system of equations for dynamic lower layer model (5.1a, 5.1b), taking $\Phi = 1$, with scaling for t and multiplying through by ε:

$$\frac{\partial q_2}{\partial T} + \varepsilon u_2 \frac{\partial q_2}{\partial x} = +\frac{\varepsilon}{T_{\mathrm{c}}}(q_1 - q_2), \tag{B.1a}$$

$$\frac{\partial q_1}{\partial T} = -\frac{\varepsilon}{T_{\mathrm{c}}}(q_1 - q_2) - \frac{\varepsilon}{T_{\mathrm{m}}}(q_1 - q_{\mathrm{e}}). \tag{B.1b}$$

The variables are rewritten as series:

$$q_2 = q_{20}(x, T) + \varepsilon q_{21}(x, T) + \varepsilon^2 q_{22}(x, T) + \dots$$

$$q_1 = q_{10}(x, T) + \varepsilon q_{11}(x, T) + \varepsilon^2 q_{12}(x, T) + \dots$$

Then, the series for q_1 and q_2 are substituted into Equations B.1a, B.1b, and solved for orders of ε: $O(1)$, $O(\varepsilon)$ and $O(\varepsilon^2)$. On integrating $q_{ij}(x, T)$ with respect to T, the constant of integration will be denoted by $\tilde{q}_{ij}(x)$.

$\underline{O(1)}$

$$\frac{\partial q_{20}}{\partial T} = 0 \quad \Rightarrow \quad q_{20} = \tilde{q}_{20}(x).$$

$$\frac{\partial q_{10}}{\partial T} = 0 \quad \Rightarrow \quad q_{10} = \tilde{q}_{10}(x).$$

$\underline{O(\varepsilon)}$

$$\frac{\partial q_{21}}{\partial T} = \frac{1}{T_c} \left(q_{10} - q_{20} \right) - u_2 \frac{\partial q_{20}}{\partial x} = \frac{1}{T_c} \left(\tilde{q}_{10} - \tilde{q}_{20} \right) - u_2 \tilde{q}_{20}',$$

$$q_{21} = \frac{T}{T_c} \left(\tilde{q}_{10} - \tilde{q}_{20} \right) - T u_2 \tilde{q}_{20}' + \tilde{q}_{21}(x).$$

$$\frac{\partial q_{11}}{\partial T} = -\frac{1}{T_c} \left(q_{10} - q_{20} \right) - \frac{1}{T_m} \left(q_{10} - q_e(x) \right) = -\frac{1}{T_c} \left(\tilde{q}_{10} - \tilde{q}_{20} \right) - \frac{1}{T_m} \left(\tilde{q}_{10} - q_e(x) \right),$$

$$q_{11} = -\frac{T}{T_c} \left(\tilde{q}_{10} - \tilde{q}_{20} \right) - \frac{T}{T_m} \left(\tilde{q}_{10} - q_e(x) \right) + \tilde{q}_{11}(x).$$

$\underline{O(\varepsilon^2)}$

$$\frac{\partial q_{22}}{\partial T} = \frac{1}{T_c} \left(q_{11} - q_{21} \right) - u_2 \frac{\partial q_{21}}{\partial x},$$

$$= -\frac{2T}{T_c^2} \left(\tilde{q}_{10} - \tilde{q}_{20} \right) - \frac{T}{T_c T_m} \left(\tilde{q}_{10} - q_e(x) \right) + \frac{1}{T_c} \left(\tilde{q}_{11} - \tilde{q}_{21} \right) - u_2 \tilde{q}_{21}'$$

$$- \frac{T u_2}{T_c} \left(\tilde{q}_{10}' - 2 \tilde{q}_{20}' \right) + T u_2^2 \tilde{q}_{20}'',$$

$$q_{22} = -\frac{T^2}{T_c^2} \left(\tilde{q}_{10} - \tilde{q}_{20} \right) - \frac{T^2}{2 T_c T_m} \left(\tilde{q}_{10} - q_e(x) \right) + \frac{T}{T_c} \left(\tilde{q}_{11} - \tilde{q}_{21} \right)$$

$$- T u_2 \tilde{q}_{21}' - \frac{T^2 u_2}{2 T_c} \left(\tilde{q}_{10}' - 2 \tilde{q}_{20}' \right) + \frac{T^2 u_2^2}{2} \tilde{q}_{20}'' + \tilde{q}_{22}(x).$$

$$\frac{\partial q_{12}}{\partial T} = -\frac{1}{T_c} \left(q_{11} - q_{21} \right) - \frac{1}{T_m} \left(q_{11} \right),$$

$$= \frac{T}{T_c} \left(\frac{2}{T_c} + \frac{1}{T_m} \right) \left(\tilde{q}_{10} - \tilde{q}_{20} \right) + \frac{T}{T_m} \left(\frac{1}{T_c} + \frac{1}{T_m} \right) \left(\tilde{q}_{10} - q_e(x) \right)$$

$$- \tilde{q}_{11} \left(\frac{1}{T_c} + \frac{1}{T_m} \right) + \frac{1}{T_c} \tilde{q}_{21} - \frac{T u_2}{T_c} \tilde{q}_{20}',$$

$$q_{12} = \frac{T^2}{T_c} \left(\frac{1}{T_c} + \frac{1}{2 T_m} \right) \left(\tilde{q}_{10} - \tilde{q}_{20} \right) + \frac{T^2}{2 T_m} \left(\frac{1}{T_c} + \frac{1}{T_m} \right) \left(\tilde{q}_{10} - q_e(x) \right)$$

$$- T \tilde{q}_{11} \left(\frac{1}{T_c} + \frac{1}{T_m} \right) + \frac{T}{T_c} \tilde{q}_{21} - \frac{T^2 u_2}{2 T_c} \tilde{q}_{20}' + \tilde{q}_{12}(x).$$

The series approximations for q_1 and q_2 for the scaling in t are:

$$q_2 = \tilde{q}_{20} + \varepsilon \left[\frac{T}{T_c} (\tilde{q}_{10} - \tilde{q}_{20}) - T u_2 \tilde{q}'_{20} + \tilde{q}_{21} \right] + \varepsilon^2 \left[-\frac{T^2}{T_c^2} (\tilde{q}_{10} - \tilde{q}_{20}) - \frac{T^2}{2 T_c T_m} (\tilde{q}_{10} - q_e(x)) \right.$$

$$\left. + \frac{T}{T_c} (\tilde{q}_{11} - \tilde{q}_{21}) - T u_2 \tilde{q}'_{21} - \frac{T^2 u_2}{2 T_c} (\tilde{q}'_{10} - 2\tilde{q}'_{20}) + \frac{T^2 u_2^2}{2} \tilde{q}''_{20} + \tilde{q}_{22} \right] + \ldots$$

$$\text{(B.2a)}$$

$$q_1 = \tilde{q}_{10} + \varepsilon \left[-\frac{T}{T_c} (\tilde{q}_{10} - \tilde{q}_{20}) - \frac{T}{T_m} (\tilde{q}_{10} - q_e(x)) + \tilde{q}_{11} \right] + \varepsilon^2 \left[\frac{T^2}{T_c} \left(\frac{1}{T_c} + \frac{1}{2 T_m} \right) (\tilde{q}_{10} - \tilde{q}_{20}) \right.$$

$$\left. + \frac{T^2}{2 T_m} \left(\frac{1}{T_c} + \frac{1}{T_m} \right) (\tilde{q}_{10} - q_e(x)) - T \tilde{q}_{11} \left(\frac{1}{T_c} + \frac{1}{T_m} \right) + \frac{T}{T_c} \tilde{q}_{21} - \frac{T^2 u_2}{2 T_c} \tilde{q}'_{20} + \tilde{q}_{12} \right] + \ldots$$

$$\text{(B.2b)}$$

Thus, equations B.2b, B.2a are consistent with "outer" equations 5.6b and 5.6a, providing that the constants of integration $\tilde{q}_{21}, \tilde{q}_{11}, \tilde{q}_{22}, \tilde{q}_{12}$ etc. are taken as zero.

Scaling in t and x

The issue of the behaviour near $x = 0$, particularly in q_2, is now considered. Scaling for t and x, Equations 5.1a, 5.1b for the dynamic lower layer model are rewritten and multiplied through by ε:

$$\frac{\partial q_2}{\partial T} + u_2 \frac{\partial q_2}{\partial X} = \frac{\varepsilon}{T_c} (q_1 - q_2) H(T), \quad \text{(B.3a)}$$

$$\frac{\partial q_1}{\partial T} = -\frac{\varepsilon}{T_c} (q_1 - q_2) H(T) - \frac{\varepsilon}{T_m} (q_1 - q_e H(X)). \quad \text{(B.3b)}$$

As before, the variables are rewritten as series, then substituted into Equations B.3a, B.3b, and solved for orders of ε. The Taylor series for q_e is justified because $\varepsilon X \ll 1$ when X is of order 1. The lateral boundary condition is $q_2(X=0, T) = 0$.

$$q_2 = q_{20}(X, T) + \varepsilon q_{21}(X, T) + \varepsilon^2 q_{22}(X, T) + \ldots$$

$$q_1 = q_{10}(X, T) + \varepsilon q_{11}(X, T) + \varepsilon^2 q_{12}(X, T) + \ldots$$

$$q_e(\varepsilon X) = q_e(0) + \varepsilon X q'_e(0) + \varepsilon^2 X^2 \frac{q''_e(0)}{2} + \ldots$$

When required, the variables X, T will be transformed with $\xi = X$, $\eta = X - u_2 T$ to simplify the partial differential equation. Using the Chain Rule, the partial derivatives in X and T become:

$$\frac{\partial}{\partial T} = \frac{\partial \xi}{\partial T} \frac{\partial}{\partial \xi} + \frac{\partial \eta}{\partial T} \frac{\partial}{\partial \eta} = -u_2 \frac{\partial}{\partial \eta}$$

$$\frac{\partial}{\partial X} = \frac{\partial \xi}{\partial X} \frac{\partial}{\partial \xi} + \frac{\partial \eta}{\partial X} \frac{\partial}{\partial \eta} = \frac{\partial}{\partial \xi} + \frac{\partial}{\partial \eta}$$

$\underline{O(1)}$

$$\frac{\partial q_{20}}{\partial T} + u_2 \frac{\partial q_{20}}{\partial X} = 0 \quad \Rightarrow \quad u_2 \frac{\partial q_{20}}{\partial \xi} = 0 \quad \Rightarrow \quad q_{20}(\xi, \eta) = \tilde{q}_{20}(\eta),$$

$$q_{20}(X, T) = \tilde{q}_{20}(X - u_2 T).$$

$$\frac{\partial q_{10}}{\partial T} = 0 \quad \Rightarrow \quad q_{10}(X, T) = \tilde{q}_{10}(X).$$

$\underline{O(\varepsilon)}$

$$\frac{\partial q_{21}}{\partial T} + u_2 \frac{\partial q_{21}}{\partial X} = \frac{1}{T_c}(q_{10} - q_{20}) = \frac{1}{T_c}\left(\tilde{q}_{10}(X) - \tilde{q}_{20}(X - u_2 T)\right),$$

$$\frac{\partial q_{21}}{\partial \xi} = \frac{1}{u_2 T_c}\left(\tilde{q}_{10}(\xi) - \tilde{q}_{20}(\eta)\right),$$

$$q_{21}(\xi, \eta) = \frac{1}{u_2 T_c}\left(\int \tilde{q}_{10}(\xi) \, d\xi - \xi \tilde{q}_{20}(\eta)\right) + \tilde{q}_{21}(\eta),$$

$$q_{21}(X, T) = \frac{1}{u_2 T_c}\left(\int \tilde{q}_{10}(X) \, dX - X \tilde{q}_{20}(X - u_2 T)\right) + \tilde{q}_{21}(X - u_2 T).$$

$$\frac{\partial q_{11}}{\partial T} = -\frac{1}{T_c}(q_{10} - q_{20}) - \frac{1}{T_m}\left(q_{10} - q_e(0)\right),$$

$$= -\frac{1}{T_c}\left(\tilde{q}_{10}(X) - \tilde{q}_{20}(X - u_2 T)\right) - \frac{1}{T_m}\left(\tilde{q}_{10}(X) - q_e(0)\right),$$

$$q_{11}(X, T) = -\frac{1}{T_c}\left(T\tilde{q}_{10}(X) - \int \tilde{q}_{20}(X - u_2 T) \, dT\right) - \frac{T}{T_m}\left(\tilde{q}_{10}(X) - q_e(0)\right) + \tilde{q}_{11}(X).$$

The series approximations for q_1 and q_2 for the scaling in x and t are:

$$q_2(X, T) = \tilde{q}_{20}(X - u_2 T) + \varepsilon\left[\frac{1}{u_2 T_c}\left(\int \tilde{q}_{10}(X) \, dX - X \tilde{q}_{20}(X - u_2 T)\right)\right.$$

$$\left. + \tilde{q}_{21}(X - u_2 T)\right] + \dots \qquad \text{(B.4a)}$$

$$q_1(X, T) = \tilde{q}_{10}(X) + \varepsilon\left[-\frac{1}{T_c}\left(T\tilde{q}_{10}(X) - \int \tilde{q}_{20}(X - u_2 T) \, dT\right)\right.$$

$$\left. - \frac{T}{T_m}\left(\tilde{q}_{10}(X) - q_e(0)\right) + \tilde{q}_{11}(X)\right] + \dots$$

$$\text{(B.4b)}$$

The analysis would be simplified by applying boundary conditions such as $q_1(X, T{=}0) = q_e$ and $q_2(X, T{=}0) = 0$, corresponding to an initially dry upper layer (as in Chapter 4). However, it is more desirable to keep generalised initial conditions to be consistent with Chapter 5. The next stage in the analysis would involve matching the "inner" and "outer" solutions (possibly at $X = T$) to give small-time solutions that are valid even close to $x = 0$. The boundary layer matching is not presented here.